Ministry of Education and Science of Ukraine
Sumy State University

JOURNAL OF ENGINEERING SCIENCES

Scientific Journal

Volume 9, Issue 2 (2022)

ISSN 2312-2498 (print)
ISSN 2414-9381 (online)

Founded in 2014

Journal of Engineering Sciences is an open-access peer-reviewed scientific journal. It covers urgent issues of up-to-date high-tech production in developing new engineering trends and future technologies. The general topics of the journal include manufacturing, mechanical, and chemical engineering. The publication language is English. The editorial board is represented by scientists from different international research institutions covering the journal's topics and evaluating all the submitted articles. The system of double-blinded review provides a high-quality presentation of articles. The editorial policy, including submission, review, acceptance, and publication of articles, is entirely transparent.

The journal was founded in 2014. It is published by Sumy State University of Ministry of Education and Science of Ukraine under the support of the International Association for Technological Development and Innovations.

ISSN 2312-2498 (print)
ISSN 2414-9381 (online)

The journal is intended for a wide range of scientists, researchers, practitioners, and others interested in manufacturing, mechanical, and chemical engineering. All the publications in the journal are free of articles processing charges (APCs) and articles submission charges.

Recommended for publication
by the Academic Council of Sumy State University,
(order No. 0103-I of 13.02.2023)

The journal is the scientific professional edition of Ukraine (Category "B") in Engineering Sciences ordered by the Ministry of Education and Science of Ukraine, November 7, 2018, No. 1218.

Partners:

– International Association for Technological Development and Innovations, http://iatdi.org;
– Ministry of Education and Science of Ukraine, https://mon.gov.ua;
– Faculty of Mechanical Engineering and Management, Poznan University of Technology (Poland), https://www.put.poznan.pl;
– Faculty of Manufacturing Technologies with a seat in Prešov, Technical University of Košice (Slovakia), http://www.fvt.tuke.sk;
– Faculty of Mechanical Engineering of University of West Bohemia (Czech Republic), http://www.fst.zcu.cz.

Editorial Board: 2, Rymskogo-Korsakova St., 40007, Sumy, Ukraine; Apt. M-211
Contact Phone: +380-993-845-740
E-mail: jes@teset.sumdu.edu.ua
Website: http://jes.sumdu.edu.ua

State registration certificate of the print mass-media No. 20499-10299 PR.

JOURNAL OF ENGINEERING SCIENCES

Volume 9, Issue 2 (2022)

TOPICS

Manufacturing Engineering:

- Machines and Tools;
- Technical Regulations and Metrological Support;
- Materials Science.

Mechanical Engineering:

- Dynamics and Strength of Machines;
- Computational Mechanics.

Chemical Engineering:

- Processes in Machines and Devices;
- Energy Efficient Technologies;
- Environmental Protection.

STATISTICS

- **Publication frequency:** biannually (2 issues per year)
- **Acceptance rate:** 25 %
- **Timeline:**
  - days from submission of the manuscript to first decision: 30
  - days from acceptance of the article to publication online: 14
- **Editorial Board:**
  - members: 66
  - institutions: 46
  - countries: 25

JOURNAL OF ENGINEERING SCIENCES

Volume 9, Issue 2 (2022)

CONTENTS

MANUFACTURING ENGINEERING

Technical Regulations and Metrological Support

Materials Science

MECHANICAL ENGINEERING

Dynamics and Strength of Machines

Computational Mechanics

CHEMICAL ENGINEERING

JOURNAL OF ENGINEERING SCIENCES

Volume 9, Issue 2 (2022)

JOURNAL OF ENGINEERING SCIENCES

Volume 9, Issue 2 (2022)

Denysenko, Y. O., Pop, G. M., Sushko V. V., Korniienko, A. O., Husar I. (2022). Ensuring accurate characteristics of the pipe-piston installation. Journal of Engineering Sciences, Vol. 9(2), pp. B1-B6, doi: 10.21272/jes.2022.9(2).b1

Ensuring Accurate Characteristics of the Pipe-Piston Installation

Denysenko Y. O.[1][0000-0002-9816-2862], Pop G. M.[2][0000-0002-0557-368X], Sushko V. V.[3], Korniienko, A. O.[1], Husar I.[2]

[1] Sumy State University, University, 2, Rymskogo-Korsakova St., Sumy 40007, Ukraine;
[2] Technical University of Cluj-Napoca, 18, Memorandumului St., Cluj-Napoca 400114, Romania;
[3] State Enterprise "Sumy Regional Scientific and Production Center for Standardization, Metrology and Certification", 101, Kharkivska St., Sumy 40007, Ukraine

Article info:
Submitted: April 11, 2022
Accepted for publication: August 28, 2022
Available online: September 3, 2022

***Corresponding email:**
y.denisenko@tmvi.sumdu.edu.ua

Abstract. The study aims to increase the efficiency of the use of the pipe-piston unit by ensuring the reliability of the measurement results based on the development of calibrating technique for the pipe-piston installation. Theoretical research is based on using the principles of system and process approaches. To solve the scientific problem, the fundamental provisions of statistical methods and experimental methods were used; methods of mathematical modeling of estimation of measurement uncertainties. Based on the results of the work, the normative document "Metrology. Installations of a standard pipe-piston. Calibration technique". The approach to controlling metrological characteristics of the pipe-piston installation, based on estimating the uncertainty of measurements during its calibration, was further developed. Application of the proposed approach allows one to control the metrological characteristics directly on site without disrupting the working product's accounting process and increasing the pipe-piston installation's efficiency by an increase in the reliability of measurements and ensuring repeatability.

Keywords: methods, calibration, pipe-piston installation, uncertainty, verification.

1 Introduction

The economies of many countries, including Ukraine, are based mainly on natural resources. Available natural resources are the key to the country's competitiveness in the world market. Therefore, a reliable system of accounting and control of the use of such resources is an essential factor in the efficient and economical use of nature.

Today in our area, the pipe-piston test installation (production of "Energoinvest. Measuring systems") is designed to control the characteristics and verification of measuring instruments of volume and mass at the place of operation without violating the process of accounting for the working product.

Legislation of Ukraine in the field of metrology has changed in recent years. According to the Resolution of the Cabinet of Ministers of 04.06.2015 № 374 [2], the pipe-piston installation was not included in the List of categories of legally regulated measuring equipment subject to periodic verification, so it belongs to the gages. According to the procedure for calibration of legally regulated measuring equipment in operation and registration of its results (Order of the Ministry of Economy of 08.02.2016 № 193), the gages used during the verification must be calibrated.

The purpose of the work is to increase the efficiency of the pipe-piston installation by ensuring the reliability of measurement results based on the development of calibration techniques for the pipe-piston installation.

2 Literature Review

Consumption - the amount of liquid, gas, or bulk (mass, volume, or weight) transported or supplied per unit time across the cross-section [3].

When measuring the volume of liquid (gas) flowing through the cross-section, determine the volume consumption when measuring mass flow.

Volume flow rate is the volume of liquid that passes through a given area per unit of time.

Usually, the liquid (gas) consumption is measured by a flowmeter and to measure the amount of a substance – by a quantity counter (counter).

For verification, calibration, and control of measuring equipment's characteristics of volume and weight on a

place of operation without disturbance of process of the account of a working product, the pipe-piston installation (further PPI) is used.

Bilateral PPIs have been most widely used in industries where high flow measurement accuracy is required. The main advantage of bilateral PPI compared to unidirectional PPI is that in the bilateral design of PPI, the volume of the measuring section is taken as the passage of the piston in both directions, thus compensating for the error of detectors, thereby increasing measurement reliability and improving repetition.

The experimental installation under consideration it is a two-sided stationary pipe-piston test installation with a capacity of 550 m3 / h.

Operating conditions have a fairly wide range, namely: ambient temperature from minus 50 to 65 °C; the average value of humidity is 80% (possibly for a short time up to 100%); the maximum pressure in PPI to 4 MPa.

The main components of the PPI are shown in Figure 1.

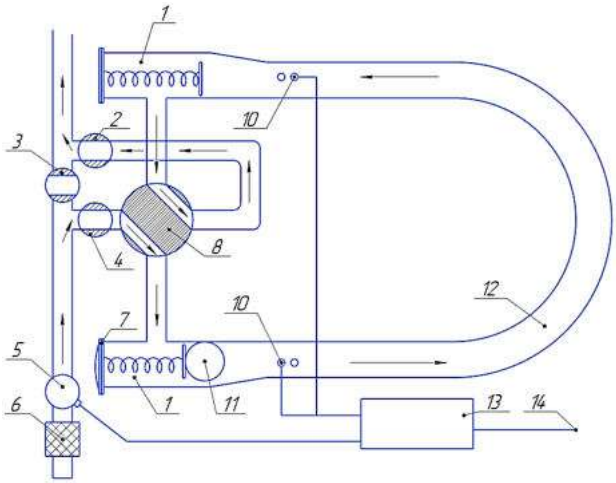

Figure 1 - Scheme of bilateral PPI: 1 – shock absorber; 2, 4 – shut-off valves; 3 – the valve on the main pipeline; 5 – flow meter; 6 – filter; 7 – cover; 8 – four-way valve with a drive that acts as a switch of fluid flow through the loop; 9, 10 – bullet passage detectors; 11 – polyurethane ball; 12 – loop made of steel pipe coated in the middle with epoxy resin to obtain the high-quality, smooth and constant diameter of the pipeline; 13 – pulse counter; 14 – power

The general view of the experimental setup is shown in Figure 2.

PPI is a two-way installation with flow control by a four-way valve, a ball polyurethane piston, and a calibrated area with an internal polymer coating. The calibrated area is made of pipes and taps calibrated for inner diameter. The calibrated area is limited by detectors that detect the passage of the ball piston.

The inner surface of the installation is thoroughly cleaned and covered with a thin layer of special synthetic resin to protect against corrosion and reduce friction when moving the ball.

During the flow transducer test, the ball piston inside the starting chamber starts moving toward the opposite starting chamber. Once in the acceleration section of the PPI, the ball piston completely covers the inner section of the PPI and moves with the fluid at a constant speed.

Figure 2 – General view of the calibrated area between detectors: Experimental setup

Continuous calibration of the flowmeter is carried out by draining the liquid to the auxiliary loop of the pipeline of a certain length, in which a polyurethane ball is installed, and the flow of liquid passes past four sensors of the ball. With the help of bullet passage sensors, switches are triggered, which start and stop the meter connected to the test flow meter. The volume of the calibrated part of the pipe between the sensors of the ball passage is accurate. By comparing it with the value on the flowmeter, it is possible to determine the calibration factor under normal operating conditions. Next, the piston enters the opposite chamber of the PPI and remains there until the position of the four-way valve changes, which causes a change in the direction of fluid flow inside the PPI to the opposite. The flow captures the ball piston, and the measurement process is repeated.

Therefore, PPI has a complexity of design and operation. The reliability of the system of accounting and control of the use of natural resources depends on its metrological characteristics, so the urgent task is to increase the reliability and repeatability of measurements based on the study and improvement of the regulatory framework.

The study of the requirements of international regulations on the application or confirmation of metrological characteristics of PPI did not reveal such.

The technical regulation [7] of measuring instruments, developed based on Directive 2014/32 / EC of the European Parliament and of the Council of 26.02.2014, entered into force on 24.02.2016. The effect of this Technical Regulation of measuring instruments extends to the following categories of measuring equipment (hereinafter – ME), which relate only to: water meters; gas meters and volume conversion devices; active electricity meters; heat meters; measuring systems for continuous and dynamic measurement of liquids other than water; automatic weighing devices; taximeters; material measures; size measuring instruments; exhaust gas analyzers.

The legislation does not provide for the verification of standards. The law [4] does not include such an important but specific category of ME as gages in the sphere of legislative regulation. Gages of any accuracy must be calibrated. The essence of calibration is to determine the characteristics, for this purpose, a comparison with the relevant gauge, and not to determine the suitability for using ME. This is reflected in the normative legal act "Procedure for verification of legally regulated measuring instruments in operation and registration of its results", approved by order of the Ministry of Economic Development and Trade of Ukraine No. 193 of 08.02.2016 [5]: "For the gages used during the calibration, the measurement uncertainty limits that these gages must provide must be specified. The ratio between the measurement uncertainty that provides the gages and the maximum permissible error of the ME to be verified is not less than one to three".

According to the Procedure for calibration of secondary and working gages, item 4, II "Calibration of working gages is carried out according to calibration methods contained in national standards or developed by contractors considering national standards harmonized with relevant international and European standards and documents adopted by international and regional organizations in metrology".

Thus, there is currently a scientific and practical problem to ensure reliable control over the measurement of volume outside the legal field, the solution of which will control the measurement of volume by measuring equipment and protect the rights of consumers.

3 Research Methodology

At the beginning of the development of the PPI calibration methodology, it is advisable to investigate its verification procedure according to the requirements of P81 / 24.99-1999 "Recommendation. Metrology. Pipe-piston installations. A typical method of verification by installations based on ОГВ scales or gauges".

Depending on the capacity determination method used, different sets of verification tools are used when performing the PPI calibration. The method of determining the capacity of the PPI is based on the fact that the water displaced from the PPI when moving the piston calibrated area from one detector to another, sent to a special storage tank, and measured its volume. The volume of water is measured by draining it from the storage tank, indirectly (using scales and hydrometers) or directly (meter).

The following methods and means of PPI verification have been established, such as a calibration unit based on ОГВ scales with storage capacity and flow switch;

calibration unit based on meters with storage capacity and flow switch; calibration unit based on ОГВ scales or meters with storage capacity with piston stop; calibration unit based on meters with piston stop (without storage tank); calibration unit based on meters without stopping the piston and without storage capacity; (compact prover) test unit based on meters without piston stop and a storage tank.

The manufacturer foresaw the need for such calibration units, which were built on site of PPI operation (Figure 3). It includes:

- meter type M1R - 1000, capacity 1000 l, scale from 984 l to 1009 l, division price 0.2 l; extended uncertainty of 0.2 l; 1st category (Figure 3, a);
- D400 type scales range from 100 kg to 1500 kg; extended uncertainty of 0.05 kg (Figure 4 b, c).

Figure 3 – Test installation (general view)

a b

Figure 4 – Reference meter (a) and weighing device (b)

Considering the PPI's available equipment and the provision of reference equipment, a method with a calibration installation based on meters with a piston stop (with storage capacity) was chosen.

Before verification, the following preparatory work must be carried out: checking the availability of certificates of verification or prints of calibration marks on them; checking the value of the diameter and condition of the surface (degree of wear) of the ball pistons PPI, which is verified, according to the operating documentation; checking the correctness of installation and connections of PPI, means of verification and auxiliary equipment according to the operating documentation on PPI and means of verification; checking the tightness of PPI, connecting pipes and valves. The test is performed by

external inspection at the selected value of the test flow and pressure at the outlet of the PPI not less than 0.1 MPa.

Tests during a trial by testing installations based on meters with a piston stop are carried out as follows. Water is fed into the meter from below. The storage tank's capacity exceeds not less than (1.2–1.5) times the maximum capacity of the PPI to be verified.

Check the KE valve manually from the control unit by closing and opening it several times. The test is considered to have passed if the valve has to close again when the piston approaches the second detector. Since our installation is two-way, the above operations are performed while moving the piston in the opposite direction.

Determining the capacity of PPI, reduced to normal conditions (temperature 20 °C, absolute pressure 101.3 kPa). For two-way PPI, the capacity is determined separately for each direction of movement of the piston.

For an experimental PPI with two pairs of detectors, the capacity is determined by each pair of detectors.

The temperature (pressure) at the inlet and outlet is equal to the average value of the two measurements - after opening the valve and closing it. The difference between the readings of the thermometers at the inlet and outlet of the PPI should not exceed 0.2 °C. Using thermometers and manometers with visual reading allows it to record the temperature and pressure once during the piston's passage.

Choose the capacity of the meter based on the capacity of the PPI, which is verified, so that when measuring the volume of water, get the smallest integer number of fillings of the meter. It is allowed to use meters of different capacities. If the meter has a scale on the neck, predetermine the amount of water to be poured so that the water level was within the scale in all measurements. Pour a certain amount of water into the meter from the storage tank. If the meter does not have a scale, it is filled to the mark of nominal capacity.

When verifying the bilateral PPI, the above operations are performed in the direction of piston's movement.

After passing the piston of the calibrated area in one direction and taking measurements, open the valves and move the piston further to the receiving chamber, then change the direction of movement.

Determine the capacity of the PPI under test conditions using a meter according to formula:

$$V = K_T \times \sum_{j=1}^{r} V_{ij}; j = 1...r \quad (1)$$

For bilateral PPI:

$$V_i = V_{i_{(1-2)}} + V_{i_{(2-1)}} \text{ and } V_i = V_{i_{(1-3)}} + V_{i_{(3-1)}} \quad (2)$$

$$\bar{V} = \frac{\sum_{i=1}^{n} V_i}{n} \quad (3)$$

The value of PPI capacity under standard conditions:

$$V_o = \bar{V} \cdot K_{tpm} \quad (4)$$

where K_{tpm} – the value of the coefficient taking into account the temperature and water pressure on the PPI tank and the volume of water in the PPI:

$$K_{tp,m} = 1 + \beta(t_y - t_{om}) - 3\alpha_T(t_y - 20) + 3\alpha_M(t_{om} - 20) - FP_y - \frac{0,95}{E} \cdot \frac{D}{S} \cdot P_y \quad (5)$$

where β – the coefficient of volumetric expansion of the fluid; a_T – coefficient of linear expansion of PPI wall material; a_M – the coefficient of linear expansion of the material of the meter; F – the coefficient of compressibility of the liquid, 1/MPa; P_y – average pressure in PPI for one measurement, MPa; D – inner diameter of the calibrated section of PPI, mm; E – modulus of elasticity of PPI wall material, MPa; S – PPI wall thickness, mm.

The standard deviation of the random component of the error is determined by the formula:

$$S_o^o(\Delta) = \sqrt{\frac{\sum_{i=1}^{n}(V_{oi} - V_o)^2}{n-1}} \cdot \frac{100}{V_o}, \quad (7)$$

where $V_o = \frac{\sum_{i=1}^{n} V_{oi}}{n}$.

Must comply with the condition: $S_0 \le 0.015\%$ – for PPI of the 1st category; $S_0 \le 0.030\%$ – for PPI of the 2nd category.

4 Results

As a result of research, the method of calibration of MK.RU.XX.0XX: 2021 "Metrology. Gage pipe-piston installations. Calibration Method", which applies to PPI type 550-64-40, which corresponds to the operating documentation on them and establishes the content and procedure for their calibration. If this technique is used to calibrate other installations according to the customer's special requirements (at certain points in the range, in special operating conditions), it is necessary to assess its suitability.

As the State Enterprise implemented the proposed methodology "Sumy Regional Scientific and Production Center for Standardization, Metrology and Certification", this section provides the content of the methodology and the main scientific results.

When using the proposed method, there is a requirement to use the following documents: instructions for operation of the installation to be calibrated; guidelines for the operation of gages and ancillary equipment used in the calibration of the installation; standards of calibration of standards, and instructions on labor protection.

The following operations must be done during calibration: (1) external review, (2) functional check, (3) definition of metrological characteristics, (4) estimation of measurement uncertainties, (5) establish traceability of measurements, (6) registration of calibration results.

Estimating measurement uncertainties during installation calibration is carried out according to the requirements of EA 4/02.

To build a model equation, it is necessary to identify the primary sources of uncertainty in measuring the volume of liquid by installations *Vi*. After considering these sources, the model equation will take the form:

$$V_i = V_o + \Delta_e + \Delta_d + \Delta_o + \Delta_s + \Delta_v, \quad (8)$$

where V_o – data from the gauge; Δ_e – component due to the expanded uncertainty of the standard; Δ_d – component due to the drift of metrological characteristics of the standard; Δ_o – components due to the error of reading the readings of the installation and the standard operator; Δ_s – component due to the influence of random factors; Δ_v – component due to fluid flowing through the seal of the sphere.

Extended uncertainty U_e of the standard is indicated in the certificate (certificate) of calibration of the gauge together with the value of the coverage factor k (k = 2). The uncertainty component of the standard, which is taken into account in the budget of uncertainties ue, is estimated by the formula:

$$u_e = \frac{U_e}{k} \quad (9)$$

Extended uncertainty u_d, due to the drift of metrological characteristics of the gauge, is estimated by the formula (type B, uniform distribution law):

$$u_d = \frac{\Delta V_м \cdot \Delta\tau}{T \cdot \sqrt{3}}, \quad (10)$$

where $\Delta V_м$ – change of metrological characteristic of the gauge (meter) for the previous inter-calibration interval T;

$\Delta\tau$ – the time interval that has elapsed since the last calibration.

The component of uncertainty due to the accuracy of reading impressions u_o is equal to (type B, uniform distribution law):

$$u_o = \frac{d}{m \cdot \sqrt{3}}, \quad (11)$$

where m – the share of the scale division that distinguishes the operator (m = 2 for digital indicators).

To estimate the uncertainty of the measurement due to the contribution of random factors, n repeated measurements of the value must be performed by the same verifier under the same conditions, the results of which we obtain a statistical estimate of the standard deviation:

$$CKB = u_s = \sqrt{\frac{\sum_{i=1}^{n}\left(V_i - \overline{V}\right)^2}{n \cdot (n-1)}} \quad (12)$$

The number of repeated measurements must be at least three.

To assess the measurement's uncertainty due to fluid flow through the installation's seals, perform the operations described in p. 6.4 P81 / 24.99 and determine the relative deviation of the capacity of the installation Δnp.

Given the normal distribution law, the measurement uncertainty due to fluid flows through the seals of the installation u_v, estimated by the formula:

$$u_v = \frac{\Delta_{np}}{2} \quad (13)$$

The sources of uncertainty are independent of each other, so the values of the correlation coefficients are zero.

The uncertainty budget method requires to be made as shown in Table 1.

Table 1 – Calculation results

Input value	Estimation of input value	Standard uncertainty	Probability distribution	Coef-ficient of influence	Contri-bution to uncertainty
V_o	X,XXX	u_s	Normal	C_s	$C_s \cdot u_s$
Δ_e	0	u_e	Normal	C_e	$C_e \cdot u_e$
Δ_d	0	u_d	Uniform	C_d	$C_d \cdot u_d$
Δ_o	0	u_o	Uniform	C_o	$C_o \cdot u_o$
Δ_v	0	u_v	Normal	C_v	$C_v \cdot u_v$
Initial value	Estimation of the initial value	Standard total uncer-tainty	Confi-dential confidence	Cove-rage ratio	Advanced uncertainty
V_i	Y,YYY	$u(V)$ =	p =	k =	$U(V)$ =
			Deviation of installation readings		
			ΔV =		

The formula calculates the total standard measurement uncertainty when calibrating the installation:

$$u(V) = \sqrt{(C_e \cdot u_e)^2 + (C_d \cdot u_d)^2 + (C_o \cdot u_o)^2 + (C_s \cdot u_s)^2 + (C_v \cdot u_v)^2} \quad (14)$$

The formula estimates the expanded uncertainty for the confidence interval:

$$U(V) = k \cdot u(V), \quad (15)$$

where k – coverage ratio with p=0,95.

The formula estimates the relative extended uncertainty:

$$U(v) = \frac{U(V)}{V_i} \cdot 100 \quad (16)$$

The deviation of the value of the capacity of the installation from the value obtained during the pre-calibration will be estimated by the formula:

$$\Delta V = V_{np} - V_0 \quad (17)$$

The calibration technique also establishes requirements for the traceability of measurements and registration of their results. The requirements for establishing the recommended inter-calibration interval are also specified.

5 Conclusions

Based on the conducted research for carrying out control of the definition of indicators of expense and metrological characteristics and verification of means of measurements of volume and weight on a place of

operation without disturbance of process of the account of a working product that in the majority of measurements.

It is established that there are currently no methodological documents regulating the calibration procedure of these working standards.

The result of the work is the proposed Calibration technique "Metrology. Installations are standard pipe-piston. Calibration technique". Implementing this technique allows you to control the metrological characteristics directly on site without disrupting the accounting process of the working product and increase the efficiency of PPI by increasing the reliability of measurements and ensuring repeatability.

6 Acknowledgments

The scientific results have been partially obtained within the research project "Ful-fillment of tasks of the perspective plan of development of a scientific direction "Technical sciences" Sumy State University" ordered by the Ministry of Education and Science of Ukraine (State Reg. No. 0121U112684).

The research was partially supported by the Research and Educational Center for Industrial Engineering (Sumy State University) and International Association for Technological Development and Innovations.

References

1. Tai, B., Stephenson, D., Shih, A. (2011). Improvement of surface flatness in face milling based on 3-D holographic laser metrology. *International Journal of Machine Tools & Manufacture*, Vol. 51(6), pp. 483–490. doi: 10.1016/j.ijmachtools.2011.02.006.
2. Wu, W.G, Yu, Q.X., Chang, X., Pang, S.Q. (2004) Design Theory and Experiment of the Step Face Milling Cutter Based on Free Cutting. *Advances in Grinding and Abrasive Processes,* Vol. 259–2, pp. 132–136. doi: 10.4028/www.scientific.net/KEM.259-260.132
3. Ramakrishnan, S., Wysk, R. (2002) Optimization of The Length of Travel in Face Milling Operations for Flat Surfaces. *Transactions of The North American Manufacturing Research Institute of SME*, Vol. XXX, pp. 431–438.
4. Hadad, M., Ramezani, M. (2016) Modeling and analysis of a novel approach in machining and structuring of flat surfaces using face milling process. *International Journal of Machine Tools and Manufacture,* Vol. 05, pp. 32–44. doi: 10.1016/j.ijmachtools.2016.03.005
5. Ivanov, V., Dehtiarov, I., Pavlenko, I., Kosov, M., Hatala, M. (2020) Technological assurance and features of fork-type parts machining. *Advances in Design, Simulation and Manufacturing II. DSMIE 2019. Lecture Notes in Mechanical Engineering,* pp. 114–125. doi: 10.1007/978-3-030-22365-6_12
6. Taurit, G.E. (1981) Machining Large Parts. *Tekhnika*.
7. Kushnirov, P., Zhyhylii, D., Ivchenko, O., Yevtukhov, A., Dynnyk, O. (2020) Investigation of the dynamic state of adjustable milling heads. *Advances in Design, Simulation and Manufacturing II. DSMIE 2019. Lecture Notes in Mechanical Engineering,* Vol. II, pp. 169–179. doi: 10.1007/978-3-030-22365-6_17
8. Ivanov, V., Dehtiarov, I., Pavlenko, I., Kosov, I., Kosov, M. (2019) Technology for complex parts machining in multiproduct manufacturing. *Management and Production Engineering Review*, Vol. 10(2), pp. 25–36. doi: 10.24425/mper.2019.129566
9. Ivanov, V., Dehtiarov, I., Zaloga, V., Kosov, I., Savchuk, V. (2020) Increasing Productivity of Connecting Rods Machining. *In: Ivanov, V., Trojanowska, J., Pavlenko, I., Zajac, J., Peraković, D. (eds) Advances in Design, Simulation and Manufacturing III. DSMIE 2020. Lecture Notes in Mechanical Engineering*, Vol. III, pp. 264–275. doi: 10.1007/978-3-030-50794-7_26
10. Hlembotska, L., Melnychuk, P., Balytska, N., Melnyk, O. (2018) Modelling the loading of the nose-free cutting edges of face mill with a spiral–stepped arrangement of inserts. *Eastern Eur. J. Enterp. Technol*, Vol. 1(91), pp. 46–54.
11. Lishchenko, N. V., Larshin, V. P., Pitel, J. (2020) Vibrational impact on milled surface irregularities. *Journal of Engineering Sciences*, Vol. 7(1), pp. A8–A16. doi: 10.21272/jes.2020.7(1).a2
12. Permyakov, A., Dobrotvorskiy, S., Dobrovolska, L., et al. (2019) Computer modelling application for predicting of the passing of the high-speed milling machining hardened steel. *In: Ivanov, V., et al. (eds.) Advances in Design, Simulation and Manufacturing. DSMIE-2018. Lecture Notes in Mechanical Engineering*, pp. 135–145. doi:10.1007/978-3-319-93587-4_15
13. Klimenko, S. (2017) Improvement of performance of finishing of details with a cutting tool. *J. Zhytomyr State Technol. Univ* Vol. 2(88), pp. 56–66.
14. Ivanov, V., Pavlenko, I. (2017) Comprehensive analysis of the mechanical system system "fixture–workpiece". *Journal of Engineering Science*, Vol. 4(1), pp. A1–A10.
15. Ivanov, V. (2018) Process-Oriented Approach to Fixture Design. *In: Ivanov, V. et al. (eds) Advances in Design, Simulation and Manufacturing. DSMIE 2018. Lecture Notes in Mechanical Engineering*, pp. 42–50. Springer, Cham. doi: 10.1007/978-3-319-93587-4_5.
16. Coromant, S.: Cutter path and chip formation in milling, https://www.sandvik.coromant.com/en-gb/knowledge/milling/pages/cutter-path-and-chip-formation.aspx, last accessed 15/05/2021.

JOURNAL OF ENGINEERING SCIENCES

Volume 9, Issue 2 (2022)

Majewski A., Merkisz-Guranowska A., Czarnota K. (2022). Flow management of first-time orders: a dental office case study. Journal of Engineering Sciences, Vol. 9(2), pp. B7-B16, doi: 10.21272/jes.2022.9(2).b2

Flow Management of First-Time Orders: A Dental Office Case Study

Majewski A.[1], Merkisz-Guranowska A.[2][0000-0003-2039-1806], Czarnota K.[3]

[1] Analyst, Trainer at Oboda Consulting & Training Group, 5C/159, Kazimierza Wielkiego St., 61-863 Krakow, Poland;
[2] Faculty of Civil and Transport Engineering, Institute of Transport, Poznan University of Technology, 60-965 Poznan, Poland;
[3] Individual Dental Practice Kinga Czarnota, 66-400 Gorzów Wielkopolski, Poland

Article info:
Submitted: September 19, 2022
Accepted for publication: December 8, 2022
Available online: December 12, 2022

***Corresponding email:**
agnieszka.merkisz-guranowska@put.poznan.pl

Abstract. The article presents the importance of managing the flow of first-time patients in a dental practice. Three main areas of difference between the popular linear model of dental office operation on the market and the author's model of an integrated multi-specialist dental team were analyzed. Performance indicators for working with first-time patients illustrating the ability to manage the flow of patients in the office, communicate with patients, build patient awareness of oral health conditions, and harness patients' potential for treatment are presented and discussed. It was proven that with the fuller utilization of patients' potential for treatment, a noticeable effect is a simultaneous increase in the profitability of the dental practice, which, with an entirely ethical process based solely on diagnosed dental problems, makes both profitable.

Keywords: quality assessment, performance measure, efficiency level, flow management, performance indicators.

1 Introduction

Management is the deliberate making, by selected individuals, of decisions and actions leading to the achievement of set goals using available methods.

Management is directing external resources and tasks not personally but through others [1]. In the case of treating first-time patients, external resources include the potential for treatment in these patients. And these services of external should, and even need to be managed. Flow Management serves to achieve the overriding purpose in the dental practice of restoring the patient's oral health and is accomplished by managing the flow of patients, creating opportunities for access to resources held by the recipient of the medical service, and making optimal use of internal resources, which are the available working hours of dentists. Employees play crucial in the realization of these points. Knowing and understanding the whole process, seeing the so-called big picture, have a sense of good work organization, belonging to a collective task, in which they have a significant part, a real influence on its course, and thus a sense of agency. This eliminates and prevents the effect of focusing solely on that task. In a dental office, no tasks are disconnected; one always follows the other. Flow management supports seemingly separated activities as an integrated process united by tasks, in which some activities influence and get feedback from others. When considering the flow process of first-time patients, the author relied on his research supplemented by analysis and interpretation of indicators of the functioning of the dental practices surveyed.

A first-time patient is often referred to as a person receiving services for the first time at a particular office. It is permissible to use an additional identification, in which first-time patients are also treated, those patients who, for various reasons, have interrupted the treatment they started and for at least the last four years have not used the services of the practice. Their oral health situation has most likely changed significantly, and previous diagnoses and recommendations have become obsolete. In building a competitive advantage in the market for medical services, dental office managers, in addition to striving for the highest quality of medical services and reducing costs, look for methods to improve their position in the market competition, leading to a steady increase in the number of patients served and change in the structure of the procedures performed to more complex and higher-value ones. Managers usually undertake promotional activities to differentiate the practice and attract more first-time patients. At the same time, they focus on managing medical factors, i.e., purchasing modern dental equipment, using high-quality dental materials, and introducing

innovative medical methods and procedures. With the equalization of access to specialized medical equipment, the increase in ease of movement around the world in the wake of globalization, the ability to attend foreign conferences, rapid access to the latest scientific discoveries, and the development of the Internet instant flow of information and the possibility of online consultations with other specialists, the previous factors determining the market position of the practice have lost their value. Meaningful differences in access to knowledge and equipment have blurred and are no longer crucial to distinguishing a practice in the market for medical services. The increase in the number of medical entities has led to an increase in the number of practice managers looking for new areas and tools to build a practice's competitive position in the dental services market.

2 Literature Review

While Stankiewicz calls competition a phenomenon whose participants compete in pursuit of similar purposes [2], Adamkiewicz-Drwiłło also calls the ability to create development trends, increase productivity and expand markets [3]. In the market for dental services, competition mostly means competition in reaching new patients, but it is also less common competition for the scope of treatment undertaken by patients.

According to Drucker, the moment when a manager can identify emerging opportunities in his environment will occur when he realizes his values and the advantage he can achieve through them [4]. The publication highlights the critical opportunity presented by properly leveraging first-time patientsc role in building a dental practice's competitive advantage in the marketplace.

Creating a relationship with a new patient in practice by forging a pathway for them to move between specialists enables them to completely restore their oral health and thus benefit from a broader range of treatment, and after treatment is completed, maintaining a lasting relationship between the patient with the hygiene practice and, as a result, increase the number of recommendations given by the patient and increase his satisfaction level.

Curing the patient is the primary objective of dental teams built based on skills and qualifications, which Kopalinski, according to the literature, defines as education, aptitude, and preparation for the profession [5]. It remains indisputable that a doctor's medical expertise is the basis of his work with patients, and the quality of the medical procedures used is the most essential medical factor affecting patient satisfaction with treatment.

Simultaneously, it is worth noting that skillful planning and supervision of the patient's flow in the office increases the likelihood of completing biological treatment and allows for building his readiness for prosthetic treatment and changes in the aesthetics of the smile [6].

Many currently managing dental offices fail to see the opportunities that come with more fully utilizing the potential to treat patients and focus only on attracting new patients for treatment.

A study led by Min-Gyeong attempted to identify factors influencing patients' intention to use the same dental office again [7].

A similar narrative was taken by Park et al., who last year published the results of a study in which they focused on finding factors that cause patients to visit again in dental offices, which can ultimately affect the profitability of medical facilities [8].

Both studies did not pay enough attention to how the practice's revenue is affected by the use of capacity to treat first-time patients and the change in the number of procedures performed during a single patient visit to the dental office.

3 Research Methodology

3.1 A linear mathematical model

According to our observations and audit surveys of dental practices, a linear model of dental office operation dominates the market for dental services. Its main feature is the realization of the patient's treatment by a single dentist. Such a linear type of structure Foltyn defined as classic centralized [9].

In this model, all examinations, medical procedures, and treatments for a single patient are carried out by a dentist, to whom a dental receptionist refers the patient, and to whom the patient is then made all subsequent appointments and comprehensively treated by him. This makes it so that one dentist performs treatments from areas of different specialties. The patient is referred for specialized treatments and consultations to other dentists only in extreme cases involving the risk of permanent damage to health or following the need for medical procedures beyond the medical knowledge and skills of the treating the patient.

This is partly a consequence of the standard method of accounting for doctors' cooperation with the dental practice's owner. It is based on a percentage commission fee on the value of each procedure performed. And is mainly due to historical tinctures in terms of one doctor's management of the patient in the treatment process, and the fear of transferring the treatment to another specialist with remuneration for future procedures. Such an arrangement results in the patient being treated by a single stomatologist and limits patient access to doctors of different specialties.

Figure 1 shows the handling of a first-time patient in a linear model, in which this one is signed up for an appointment with the first available dentist.

He or she is treated to the extent requested by the patient, without the doctor attempting to discuss any remaining dental problems that the patient did not know about before the appointment. This is often due to fear of the risk of equating the dentist with a salesman who offers the patient solutions that the patient does not need. This is because an important awareness-building stage is skipped, and the patient is moved to the stage of proposing solutions.

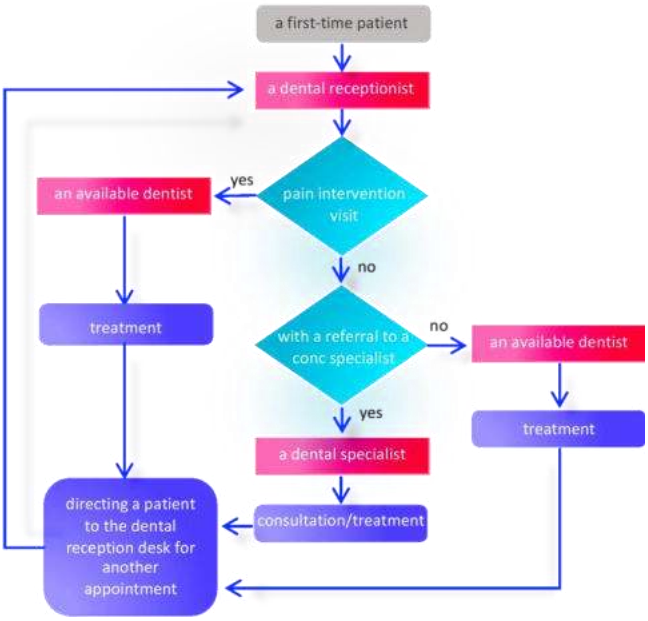

Figure 1 - A linear flow management model

It makes the patient, not understanding the risk and impact of periodontal disease on the health of the entire body, consider the solutions as unnecessary.

Communication with the patient, which skips the stages leading to acceptance of the treatment plan, results in narrowing the scope of treatments provided in the dental office and indirectly jeopardizes the patient's health by influencing the patient to remain unaware of the current state of his oral health [6].

3.2 An integrated model

Competing with the linear model is the integrated model of the multi-specialty team.

In this model, not only is the patient's flow controlled at every stage of his contact with the dental office but also the way of thinking about the treatment process is different, which, in addition to the mission behind the idea of helping the sick. It does not exclude the conduct of medical activities inseparable from the sale of medical services. In dentistry, there are no classical sales. The dentist and the medical team do not focus on creating patient needs that did not exist before. Sales in this model are not made by offering patients additional treatments or services.

It follows the process of building patients' awareness of their current dental problems and possible medical procedures and solutions. With these, it will be possible to restore oral health completely. The integrated model for managing patient services in a multi-specialty dental office is shown in Figure 2.

It assumes that the treatment process is carried out with the full participation of the team's medical potential. Each dentist is characterized by a different skill level in building motivation for treatment in the patient's consciousness.

There are differences between them in their ability to skillfully lead conversations that create a patient's vision of a possible final health and aesthetic outcome.

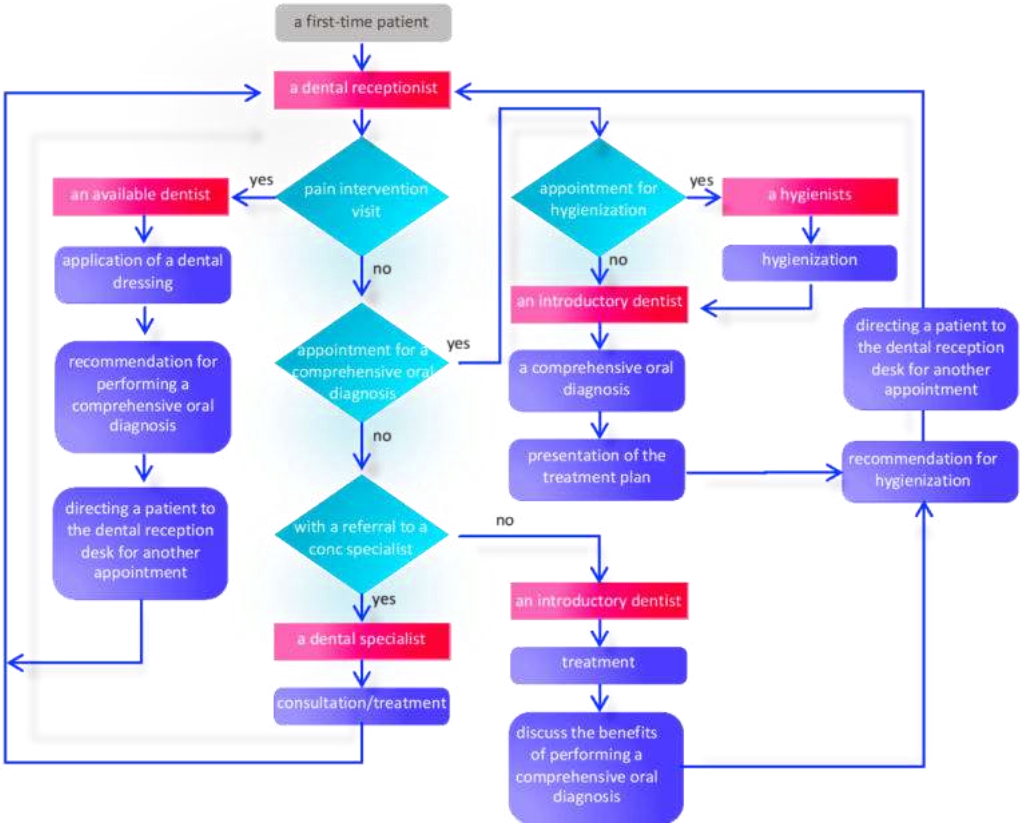

Figure 2 - An integrated model

It depends on dentist's interpersonal skills. Most often, the first of the dental practice is the dentist owner who defines and begins the introduction and what's more, is also the person the most involved in the process and focused on practical implementation. He performs a comprehensive oral health examination and conducts discussions with patients, during which mechanisms are set in motion to motivate them to start, continue and complete treatment.

Due to the highest level of soft skills and abilities of a doctor to talk to patients, he realizes his main task - to handle first-time patients and patients with irregular visits who have not yet opted for treatment leading to the restoration of total oral health. The introductory doctor creates a comprehensive treatment plan, which he presents and discusses in detail with the patient.

The patient is then coordinated by the introductory doctor of dental, who plans the course of treatment in the dental office and directs the flow and sequence of the patient's visits with subsequent specialists required to fully restore oral health or achieve the desired aesthetics of the smile.

When creating the plan, he consults substantively with the other specialists on the team. Upon the doctor's recommendation, the first-time patient benefits from a hygienization procedure, thus reducing the risk of a dental problem going undiagnosed due to being obscured by sediment or tartar.

3.3 Experimental studies

In one case in the survey, the author asked patients how much influence a recommendation given to a patient by a doctor has on their decision to use the services of a hygiene office.

The question was constructed as a single-choice option on a scale of 1 to 5, with a score of 1 indicating the most negligible influence and five showing the most significant impact. A total of 262 respondents from a group of 343 patients gave the highest rating of 5 or 4.

The percentage distribution of responses is shown in Figure 3.

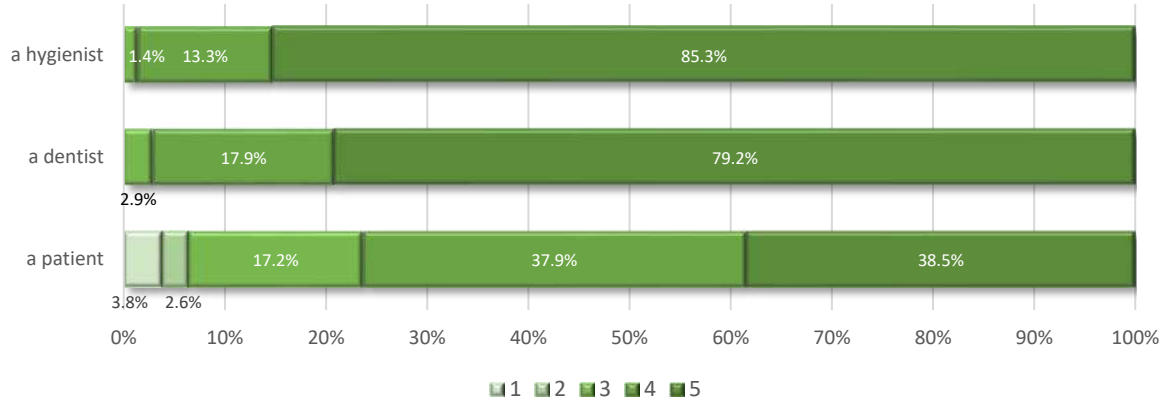

Figure 3 - Distribution of responses

The highest ratings from the surveyed groups were given by hygienists, whose work is primarily derived from recommendations provided by doctors and are fully aware of their influence on patients' choice of services at the hygiene office.

The answers given show the relevance of the measures taken by doctors in this regard. The dentist's omission of the hygiene stage when discussing the course of health restoration excludes it from the comprehensive treatment process.

During treatment, according to the multi-specialty team model, the patient for the next stage of treatment goes to dentists who focus exclusively on treatments directly related to their specialty. The patient is scheduled for consecutive appointments, a planned sequence of treatments carried out by doctors with the most significant expertise and experience in a particular field. In this model, assigning individual treatment stages to doctors who specialize in a specific area of dentistry allows them to focus their ongoing work on their chosen area of treatment and develop their medical skills. In this way, they reduce the time required to perform procedures while continuing to strive for an expert level in their specialty. In addition to the obvious benefit to patients, who gain access to specialized medical care, there is also an advantage that dental practitioners, and dental implantologists, gain from this model.

Thanks to the multi-specialty team model, they gain access to patients who are determined to receive implants. They can put their theoretical knowledge into practice and continue to hone their skills. After each stage of treatment is completed, the patient returns to the introductory doctor, who holistically guides the process, acting as a source of medical information and maintaining a constant level of patient motivation for further treatment.

4 Results

4.1 Comparison of the developed models

In terms of first-time handling patients, there are three key areas of activity that differentiate the linear model from the integrated multi-specialty team model: managing the flow of patients, building patients' awareness of their current dental problems and the consequences of negligent

treatment and possible solutions; performing more treatments during a single visit.

The use of the chosen model follows the decisions of the managers. A linear model of dental office operation based on the constant acquisition of first-time patients can effectively operate in the market. This is because some patients expect to start treatment immediately and focus exclusively on solving the current problem through symptomatic treatment. However, in this model, ensuring the continuous purchase of new patients requires constantly undertaking expensive promotional activities. This often entails managers accepting lower profitability for the practice or charging above-market prices for services. Meanwhile, the multi-specialty model involves building a lasting relationship with patients and treating patients in a broader range than the original one. It is a less costly tool, as it relies primarily on the ability of the introductory doctor to build patient motivation for treatment and coordinate the implementation of the process of treatment.

In the first area of difference between the models related to referring first-time patients for a comprehensive examination before treatment. It should be noted that a patient who does not experience pain most of the time is unaware of his dental problems. He does not undertake treatment in this area because he does not know that it is required. A study conducted by

Suchodolski shows that of 100 teeth with inflammatory lesions, 95 remain asymptomatic [10]. Diagnosis of health problems is possible when a comprehensive oral diagnosis is performed. For there to be an opportunity to do a dental check-up and build his awareness of the current state of oral health, it is necessary to control the patient's flow in the dental office and arrange by registration first for an appointment during which such a comprehensive oral examination will be performed. Except in situations where the symptom is severe pain disabling cognitive processes, a first-time patient should always be scheduled by dental registration for a visit during which a comprehensive examination will be performed in the first part of the visit, and treatment will be provided in the second part of the meeting to the extent expected by the patient.

When a first-time patient is reported to be in pain, the dental registration clerk arranges an emergency visit with one of the available conservative dentists. Since this is an unscheduled visit, it is short and takes place between treatments or as the last visit. The main purpose of this visit is to relieve pain, apply a dressing and refer the patient to the registrar, with whom he will schedule a scheduled treatment appointment. Suppose the doctor performing the interventional procedure is not also the introductory doctor. In that case, he only initiates a conversation about performing a detailed oral examination and the knowledge that the patient will receive as a result. Once the dressing has been applied, the doctor directs the patient to the registration desk to schedule a scheduled visit. At that point, the registration staff initiates discussions about the patient's participation in the visit, during which a comprehensive oral examination will be performed, followed by hygienization for complete access to information about the current state of the teeth.

Interestingly, in the linear model, where no patient flow control is used, patients are not ultimately dissatisfied with the service and treatment. Patients unaware of their existing dental problems receive treatment to the extent they come to the dental office. They get what they expect, so their satisfaction remains high because when evaluating the office, according to Rudawska, the patient also considers the relationship that connects him with the doctor and verifies it with previous expectations [11]. Therefore, it remains to be determined which of the activities was performed incorrectly since patients and all participating dental office employees and doctors believe that everything was completed correctly. Performing a comprehensive examination opens up the prospect of treatment while directing the patient according to his expectation, and making only an appointment during which treatment will be processed prevents the doctor from having

a conversation that builds his understanding of the nature and direction of further treatment. The interventional-only treatment leaves the patient unaware of the current situation in the oral cavity, exposes him to possible complications in the future, and reduces the chance of maintaining his teeth for life.

The conventional approach to the dental registrar's tasks is understood as enrolling for treatment those who contact the dental practice and are determined to make an appointment, providing face-to-face service to those who come to the medical facility, and billing payment for treatments. In the integrated model, the dental registration staff, who do not take active steps to acquire new patients on their own as the front line of patient contact, participate in selling the practice's services in the full sense of the word. This is because dental receptionists sell patients the time in the dentist's office, during which they will have access to the doctor's expertise. The way that this process takes place determines how many patients will receive the dentist's specialized care. When we are looking for an answer to the question of how to increase the profitability and efficiency of a dental practice, a range of possibilities can be pointed out to managers. These include defining and focusing on the extension of services with the most significant economic justification, reorganizing the flow of patients between specialists, actively acquiring patients via the Internet, developing the number of procedures performed during a single visit, changing the structure of the work performed, changing the scope of activities of the patient's caregiver, and using tools related to pricing. These measures can only be effective if the patient comes to the appointment. It should be known that this will not happen if contact with the dental practice is ineffective at the registration level. When listing the qualities and competencies that a good dental receptionist clerk should have (friendly, courteous, professional, able to recommend a dentist to patients and answer all incoming calls), managers rarely point to the overriding competency of professional phone service, which is the ability to sign up a new patient for an appointment, especially for a

comprehensive oral health check. All first-time patients, regardless of whether they are enrolled by registration for a comprehensive oral examination or, outside the established procedure, directly for treatment, are made an appointment with an introductory dentist for a visit on one of the days in the medical calendar reserved for first-time handling patients. An exception is made for visits by first-time patients with severe pain. The doctor does not perform a comprehensive oral examination during such a visit but afterward presents the patient with the resulting benefits and offers to perform it at the next visit.

The second area of difference between the models involves building patient awareness of their current dental problems, the consequences of negligent treatment, and possible solutions. In the linear model of dental office management, communication with the patient is carried out in terms of providing baseline information to questions asked by patients and meeting verbalized needs. The zone of expectations, which the patient does not indicate as important, remains outside the interest of the staff. What's more, in dental offices working in the linear model, there is a lack of interest on the part of the staff in scheduling another appointment if the patient has not asked for it himself. The patient service standards currently used in dental offices focus on implementing procedures and clearly presenting patient expectations rather than performing anticipatory measures that increase the level of care shown to the patient by the staff throughout the treatment process.

Meanwhile, in the integrated model, the dentist's tasks, in addition to treatment, also include providing patients with information related to health-promoting prevention and explaining the consequences of neglecting to maintain oral hygiene on the entire body's health. Our research shows that 91 % of patients expect their doctor to motivate them to continue treatment, 7 % have no opinion on this, and only about 1.5 % do not want to be motivated. The average patient's decisions on treatment methods for objective reasons cannot be based on his medical knowledge because he does not have it. For this reason, there is a need for a dentist to recommend solutions. There is, therefore, a parallel space for educational activities and the expectation of their fulfillment by the dentist. Another difference is the location of leading the conversation with the patient. As in the case of gynecological examinations, the conversation should not occur while the patient is on the dental unit, although this is common practice in the linear model. This is different in the integrated model, where the best place to have a conversation about the range of treatment, prognosis for a cure, and possible solutions is in the space where the patient is outside the immediate environment of the dental chair. In the integrated model, additional emphasis is placed on creating the right technical conditions to enable effective two-way communication.

If the layout of the furniture in the room allows it, the conversation between the doctor with the patient should be conducted at a desk or a table. The dental unit is not an appropriate place for a conversation that opens the patient to solutions, as many people with pain and lack of comfort associate it.

The literature [12] points out that inadequate communication between doctor and patient can harm the patient's health. However, the transmission of a message and the patient's understanding of its content is not the same as the activation of processes in which they will decide about treatment. For this reason, effective communication should be considered, one after which the patient will follow the doctor's medical recommendations, not just understand the content he or she is conveying. This means viewing communication with the patient as a process of constructing consciousness and motivation for treatment regarding his current dental problems and building his awareness of the negative consequences of neglecting treatment. Communication should be focused on creating a negative emotional status in the patient that will result in his ability to act and continue the treatment process.

As Shah notes, poor health awareness is associated with a higher risk of life-limiting diseases for patients, and practitioner-level health consciousness interventions can positively impact health behaviors and health outcomes in individuals with low levels of health care knowledge [13]. Building a patient's willingness to apply medical solutions enables the patient to be fully healed and thus creates space for the dentist to put his medical knowledge into practice, continue to develop his skills, and further gain professional experience. A patient who understands the consequences of stopping treatment and the causes and consequences of the development of periodontal disease, including their negative impact on the entire body, acquires an openness to treatment. Then the prices of the medical therapies cease to be of primary importance and do not block his health care decision.

Area three of the differences between the models relates to the approach to the number of procedures performed per visit. Increasing this number affects the efficiency of the process by reducing the daily number of patients served, fewer required room disinfection and preparation of instrument sets and materials dedicated to each patient, and fewer non-medical processes related to billing for payments for procedures and scheduling visits in doctors' calendars. Also, from the patient's point of view, performing several procedures during a single visit makes economic sense. It involves a reduction in the time needed for commuting, returning, and parking, as well as the fees associated with them, and most importantly, it reduces treatment time. Treating adjacent teeth allows for a single dose of anesthesia, which is essential for patients with an aversion to injections. The dental receptionist can use all these arguments when scheduling a visit with a patient and recommending that the patient be explicitly enrolled for a visit during which more extensive treatment will be provided.

Concerns have been encountered among dentists and managers about the advisability of performing several procedures during a single visit. Information gathered from those who use this method of making appointments confirms that these fears are unfounded. Implementing this

solution benefits practice owners, the patient, and the doctor. It reduces nervousness in the waiting room and reduces the likelihood of delays in the punctuality of starting appointments. Significantly from the managers' perspective, it reduces the possibility of situations that create unplanned gaps in visit schedules, during which dental staff remains idle, continuing to generate costs, and dentists have unscheduled, unpaid breaks. Because of this, offering patients longer visits, during which a more significant number of procedures are performed, makes greater use of the time potential of each of the dental units available in practice.

For this process to function correctly, it is necessary to apply the principles of a unified message directed to the patient. This begins at the registration level when proposing such a solution to the patient and continues during communication with the dentist. Dental assistants also confirm the validity of such a solution during patient contact. The statistical patient is not familiar with detailed medical and non-medical procedures. He cannot accurately assess what is good for him, acts intuitively, and expects recommendations. Suppose he receives consistent information at each level of the visit about the standard used in the office, which includes treatment of several teeth in one visit. In that case, he will consider this standard binding and follow the recommendations received.

4.2 Performance indicators

Based on the analysis of data extracted from 341 monthly periods from 65 different dental offices, covering for a single office a range of at least three consecutive months from the period from January 2017 to August 2022, practice performance indicators were developed to measure current states and compare performance between team members and offices. Their purpose is added to support managers in building conclusions based on managerial decisions. They allow compiling the results of analyzed people and processes in a way that generates a response presented as a percentage or quantifiable numerical value.

To make it possible to compare parameters between establishments of different sizes, the author of the study used indicators depicting the functioning of the dental practice concerning a universal unit, for which he took one dental unit analyzed over one month. This method of converting parameters makes it possible to juxtapose data from offices of different scales of operation by reducing them to a common denominator and presenting indicator levels in terms of "per dental unit", also referred to interchangeably by the phrase "per dental chair". In addition, clustering and analysis of data from the same months in different years were applied. The results allowed the construction of average indicators depicting areas specific to the operation of the studied offices.

A wide variety of indicators can measure the evaluation of the performance of a dental practice. For effective management, the manager must select the key ones that, in his opinion, will allow comparing the implementation with expectations and often also with the market. One of the assessments of the quality of a practice's, dentist's, or non-medical staff's performance is efficiency, including effectiveness in working with first-time patients. The performance level indicators assessed the quality of patient communication carried out by the dental team. They represent the efficiency of the conversations held with the patient at the registration stage, the ability of dentists to build patient awareness of the current health situation leading to the emergence of the patient's motivation to start and continue comprehensive treatment, and the doctor's ability to recommend hygiene treatments to patients.

The first measure from this level is the WUKP indicator of "continuation of treatment of first-time patients", which most graphically shows the doctor's ability to work with the patient beyond the dental unit, i.e., the office's ability to retain the patient and begin the process of treating him comprehensively instead of just treating him symptomatically. The dentist's communication with the patient in terms of presenting and discussing their current oral health situation is a key moment in which there is an opportunity to build patient awareness and stimulate motivation to treatment continuation. This indicator illustrates the extent to which such conversations are effectively held with patients and indicates how first-time patients are managed at the practice. It helps determine whether the facility is attempting to seek to treat patients beyond their initial need or treating only within the patient's reported problems and focused on the constant search for new, more first-time patients. This measure can be referred to as a "return rate" of new patients or an indicator of a patient's "ability to retain" in dental practice.

To calculate it, the function $f(WUKP_{\mathrm{m}})$ was used:

$$f(WUKP_m) = \frac{sum\ of\ first\ time\ patients\ continuing\ treatment_m}{sum\ of\ first\ time\ patients_m} \cdot 100\ \% = \frac{\frac{\sum_{n=1}^{n}\left(\left(\frac{M_n}{u_n}\right)_m\right)}{n_m}}{\frac{\sum_{n=1}^{n}\left(\left(\frac{K_n}{u_n}\right)_m\right)}{n_m}} \cdot 100\ \%, \quad (1)$$

where *WUKP* – the indicator of continuation of treatment in first-time patients; *u* – the number of dental units in the office; *K* – the number of first-time patient visits during the period; *M* – the number of first-time patients continuing treatment (minimum 4 visits); *m* – month (from 1 to 12); *n* – number of data (monthly periods).

It was also assumed, as first-time patients continuing treatment, those patients who had a minimum of four consecutive office visits within six months of their first-time visit, regardless of the scope range to which they referred and related it to the number of all first-time patients of the period.

The average monthly values of this indicator, calculated as the ratio of the number of average monthly follow-ups of first-time patients to the monthly number of visits of all first-time patients, are shown in Figure 4, where its level is illustrated against the number of total patients.

The average value of the "continuation of treatment of first-time patients" indicator calculated from all the periods studied, rather than as an average of monthly averages, takes the value at 42 %. The lowest observed value of one studied period is 1 %, and the highest is 95 %.

The indications of this measure do not reflect work with the same group of patients since they refer to measurements for different time intervals. The information on the continuation of treatment occurs in the following six months differently than in the case of hygienization or examination, which is carried out during or immediately after the initial visit.

An indicator analyzed over a longer period of time can be treated as ongoing information that is a consequence of previous actions.

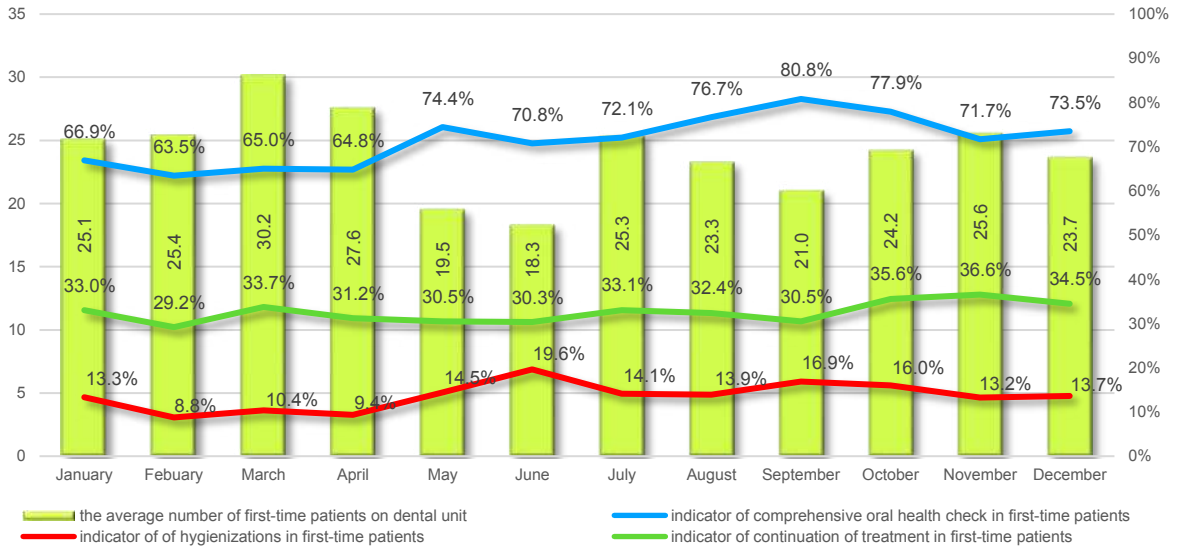

Figure 4 - Performance indicators

The return rate of first-time patients gives feedback to doctors about the effectiveness of their non-medical activities since it is the dentist, of all those in contact with the patient, who has the most significant influence on the patient's decisions to continue treatment.

The second measure of the efficiency level in managing first-time patients is WUBP's indicator of "comprehensive oral health check in first-time patients".

It represents the effectiveness of a dental receptionist's work in referring new patients for a comprehensive examination rather than referring them directly for treatment. Information related to the following can also be used to comprehensively assess the effectiveness of dental registrars' work related to the number of incoming calls answered and responses to uncompleted contact attempts, the availability of the dental office to the patient, the time spent on telephone or email and social messaging service, and the average length of face-to-face calls. All the indicators provide the manager with the necessary information about the structure and daily activity of registration. However, analyzing them in detail, it should be emphasized that the most important of them is the efficiency in conducting calls that lead to an appointment that begins with a comprehensive examination of the patient's oral health, and the measure of just this indicator is crucial in assessing the registrar's efficiency. The level of this indicator is calculated using the function $f(WUBP_m)$:

$$f(WUBP_m) = \frac{sum\ of\ comprehensive\ oral\ health\ check\ in\ first\ time\ patients_m}{sum\ of\ first\ time\ patients_m} \cdot 100\ \% = \frac{\frac{\sum_{n=1}^{n}\left(\left(\frac{B_n}{u_n}\right)_m\right)}{n_m}}{\frac{\sum_{n=1}^{n}\left(\left(\frac{K_n}{u_n}\right)_m\right)}{n_m}} \cdot 100\ \%, \quad (2)$$

where *WUBP* – comprehensive oral health check in first-time patients; *u* – number of dental units in the office; *K* – number of first-time patient visits during the period; *B* – number of comprehensive oral health checks in first-time patients (first-time screening patients); *m* – month (from 1 to 12); *n* – number of data (monthly periods).

It suggests the ability of the dental practice to obtain comprehensive treatment plans instead of performing only interventional treatment. During the period under review, it reaches an average value of 51 %, and its smallest value is 1.7 %. The value of this indicator close to 100 % indicates the dental practice's use of patient flow standards, in which all first-time patients are referred for a comprehensive oral diagnosis as part of their first visit.

The third performance measure of WUHP's work with first-time patients illustrates the percentage of hygienizations performed on first-time patients. Together with the "follow-up of first-time patients" indicator and the "examinations in first-time patients" indicator, it is shown in Figure 4.

It is related to the management of first-time patients in terms of the degree of hygienizations performed. It illustrates the dentists' ability to motivate first-time patients to use the hygiene office.

The function $f(WUHP_m)$ is used to calculate it:

$$f(WUHP_m) = \frac{sum\ of\ hygienizations\ in\ first\ time\ patients_{\mathrm{m}}}{sum\ of\ first\ time\ patients_{\mathrm{m}}} \cdot 100\ \% = \frac{\frac{\sum_{n=1}^{n}\left(\left(\frac{H_n}{u_n}\right)m\right)}{n_m}}{\frac{\sum_{n=1}^{n}\left(\left(\frac{K_n}{u_n}\right)m\right)}{n_m}} \cdot 100\ \%, \quad (3)$$

where *WUHP* – an indicator of hygienizations in first-time patients; *u* – number of dental units in the office; *K* – number of first-time patients during the period; *B* – number of hygienizations in first-time patients; *m* – month (from 1 to 12); *n* – number of data (monthly periods).

Its average value is 19 %, with the highest value taken in a single period being 61 % and the lowest being 1.2 %.

The WUWP indicator, which depicts the percentage of first-time patient visits in the number of total visits, is used to evaluate the potential of the dental office to carry out the treatment. The values of the gauge are calculated using the function $f(WUWP_m)$:

$$f(WUWP_m) = \frac{sum\ of\ first\ time\ patients_m}{sum\ of\ total\ patients_m} \cdot 100\ \% = \frac{\frac{\sum_{n=1}^{n}\left(\left(\frac{K_n}{u_n}\right)m\right)}{n_m}}{\frac{\sum_{n=1}^{n}\left(\left(\frac{L_n}{u_n}\right)m\right)}{n_m}} \cdot 100\ \%, \quad (4)$$

where *WUWP* – the indicator of the ratio of first-time patients to total patients; *u* – the number of dental units in the office; *K* – the number of first-time patient visits during the period; *L* – the number of total patients during the period; *m* – month (from 1 to 12); *n* – number of data (monthly periods).

The average monthly level of this indicator is shown in Figure 5.

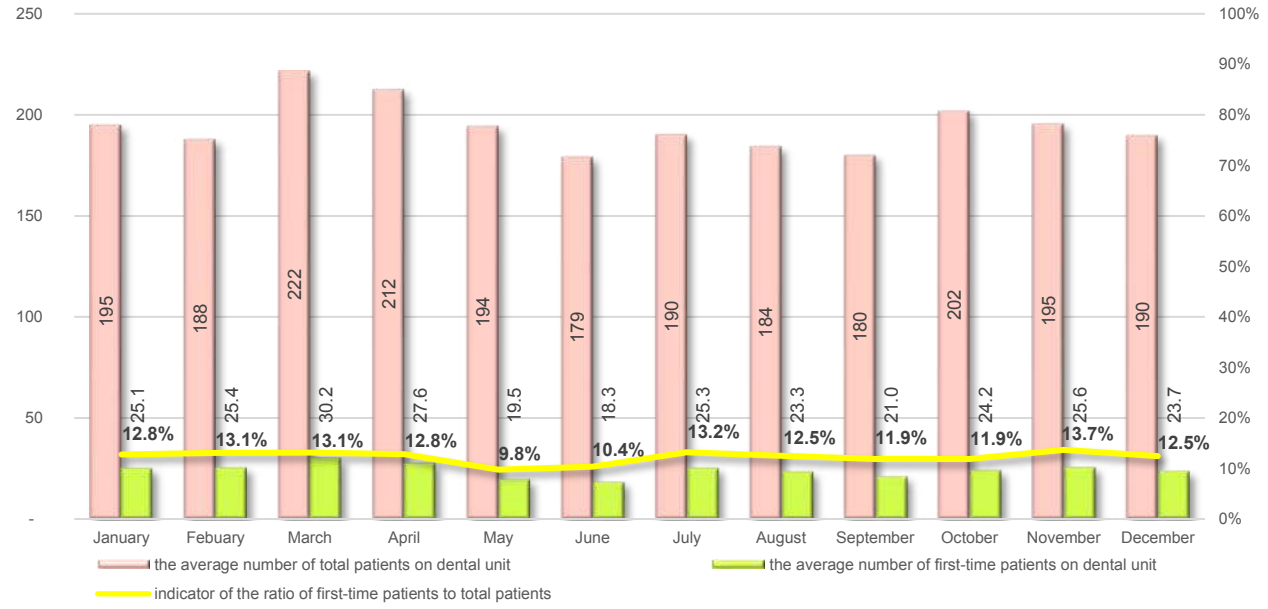

Figure 5 - Ratio of first-time patient visits in total patient visits

The gauge illustrates the current capacity of the dental practice to generate an influx of new patients. It is a consequence of the number of referrals by patients because of promotional activities aimed at attracting new patients.

This indicator indirectly depicts the evaluation of the dental practice by current patients and the number of recommendations they give to their closest and most familiar people. It makes it possible to make a preliminary prediction of the future number of total patients and first-time patients by determining trends of change.

It is the yardstick for evaluating the management model chosen in the practice's management model. Its high values indicate a focus on activities attracting many first-time patients and not taking advantage of their potential for treatment. Values below 5 % suggest lower levels of patient satisfaction and limited recommendation for dental practice. On average, the ratio of first-time patient visits to total visits is 12 %, taking an average monthly figure of 25 new patients per dental unit. This ratio reached 62 % among the surveyed facilities and the lowest at 3 %.

5 Discussion

Understanding the interpenetration of processes in the dental office seems crucial when using an integrated model of first-time patient management, in which the patient receives information and recommendations that are maintained in the same narrative. There is no discrepancy between advice from the dental registration, recommendations from the dentist, and information provided by the hygienist. The entire team is centered around convergent patient service procedures that guarantee repeatable processes and provide the patient with a sense of security and stability. This creates a professional image of the dental team, which gives the patient full access to the resources in the dental office and guarantees the use of uniform communication.

Simultaneously, the patient's level of satisfaction is derived from repeatedly exceeding his original expectations with which he came to the dental office. This satisfaction influences the recommendations given by patients, both the number of recommendations and their commitment when referring the dental practice to others. This is important for the dental practice's growth and affects future profitability, as the author''s research shows that for 85 % of patients, the dental office's choice follows a recommendation from family or friends.

Kesy argues that the permanent qualities of competence are complicated to change and sometimes impossible [14]. Therefore, matching the tasks performed by dental receptionists and dental assistants with their natural predispositions in terms of working with patients is essential.

Bukowska-Pietrzynska rightly notes that the entire dental office staff, not just the dentist, is responsible for the patient's overall assessment of the quality of service [15]. Therefore, when recruiting new people and developing the competence of the existing dental team members, their individual acquired qualities should be considered, which can be developed.

6 Conclusions

Some patients' decisions will be influenced by the potential negative consequences of not treating them years from now; others will be affected by arguments about the importance of smile aesthetics in building a professional image. The dentist's role is to select the communication with a patient in a way that will most enable the key information to reach them. Patient ignorance leads to a lack of action taken. Awareness and understanding of the disease processes occurring in the oral cavity and their adverse effects on the function of the heart, kidneys, and other internal organs if the patient ignores the need for treatment, need not, but can result in the initiation of comprehensive treatment.

If the patient is unaware of his problems or does not understand them, he will undoubtedly take no action, but if he has knowledge and awareness, he may begin treatment. Activities in each of the three areas discussed, in an integrated model carried out under the principles of Flow Management, serve the recipient of services and, as a result, enable the patient to restore his oral health in the shortest possible time. It is true that following the fuller utilization of patients' potential for treatment, a noticeable effect is a simultaneous increase in the profitability of the dental practice, which, with an entirely ethical process based solely on diagnosed dental problems, makes both sides a winner.

References

1. Suchodolski, L. (2020). Endodoncja w czasach implantów. *Forum Stomatologii Praktycznej*, Vol. 57 [in Polish].
2. Stoner, J.A.F., Freeman, R.E., Gilbert, D.R. (2001). *Kierowanie*. PWE, Warszawa, Poland [in Polish].
3. Adamkiewicz-Drwiłło, H.G. (2002). *Uwarunkowania Konkurencyjności Przedsiębiorstwa*. Wydawnictwo Naukowe PWN, Warszawa, Poland [in Polish].
4. Drucker, P.F. (1999). *Managing Oneself*. Harvard Business School Publishing, Massachusetts, USA.
5. Kopaliński, W. (1994). *Słownik Wyrazów Obcych i Zwrotów Obcojęzycznych z Almanachem*. PWN, Warszawa, Poland [in Polish].
6. Majewski, A., Czarnota, K., Oboda, M. (2022). The role of dental registration employees in the sale of medical services. *PSI Implant Dentistry*, Vol. 2(26).
7. Min-Gyeong, J. (2017). Convergence analysis on the determinants of reuse intention in patients visiting a dentist. *Journal of Convergence for Information Technology*. Vol. 7(4).
8. Rudawska, I. (2005). Jakość relacji pacjent-profesjonalista w sektorze usług medycznych. *Problemy Jakości*, Vol. 3 [in Polish].
9. Fołtyn, H. (2013). *Klasyczne i Nowoczesne Struktury Organizacji*. Wydawnictwo Key Text, Warszawa, Poland [in Polish].
10. Park, S., Kim, H.-K.., Choi, M., Lee, M. (2021). Factors affecting revisit intention for medical services at dental clinics. *PLoS ONE*. Vol. 16(5).
11. Shah, S. (2021). *Health Literacy and How to Communicate Effectively with Patients to Elicit a Long-Term Behavioural Change*. Elsevier, Cardiff, UK.
12. Dworzański, W., Dworzańska, A., Burdan, F. (2012). Istota relacji lekarz – pacjent w budowaniu wizerunku placówki medycznej. *Polski Merkuriusz Lekarski*, Vol. 187 [in Polish].
13. Stankiewicz, M. J. (2005). *Konkurencyjność Przedsiębiorstwa. Budowanie Konkurencyjności Przedsiębiorstwa w Warunkach Globalizacji*. Dom Organizatora, Toruń [in Polish].
14. Kęsy, M. (2008). *Kompetencje Zawodowe Młodych*. WUJ, Kraków, Poland [in Polish].
15. Bukowska-Piestrzyńska, A. (2012). Jakość obsługi pacjenta a konkurencyjność gabinetu stomatologicznego. *Przedsiębiorczość i Zarządzanie*, Vol. 13 [in Polish].

JOURNAL OF ENGINEERING SCIENCES

Volume 9, Issue 2 (2022)

Javanbakht T. (2022). Analysis of nanoparticles characteristics with TOPSIS for their manufacture optimization. Journal of Engineering Sciences, Vol. 9(2), pp. C1-C8, doi: 10.21272/jes.2022.9(2).c1

Analysis of Nanoparticles Characteristics with TOPSIS for Their Manufacture Optimization

Javanbakht T.

Department of Chemistry and Biochemistry, Department of Physics, Concordia University, Richard J. Renaud Science Complex, 7141 Sherbrooke St. West, Montreal, Quebec, Canada H4B 1R6;
Department of Computer Science, University of Quebec in Montreal, 201 President Kennedy St., Montreal, Quebec H2X 3Y7, Canada

Article info:
Submitted: April 7, 2022
Accepted for publication: July 27, 2022
Available online: August 2, 2022

***Corresponding email:**
tjavanbakht@yahoo.ca

Abstract. The present study focuses on the comparative analysis of superparamagnetic iron oxide nanoparticles (SPIONs) characteristics with the TOPSIS method. The prediction of the characteristics of SPIONs is required for better manufacturing of these nanoparticles. Although the characteristics of these nanoparticles have been investigated, no research has been done on their comparison in order to determine which one of their surface functionalities would be more appropriate for their diverse applications. The objective of this study was to analyze the characteristics of SPIONs without or with surface charge with a prediction model and TOPSIS in order to determine the best nanoparticles. Moreover, the effect of inappropriate consideration of their cost criterion on their ranks was explored with the modified TOPSIS. This analysis showed that the characteristics of SPIONs such as antibiofilm activity, hemocompatibility, activity with hydrogen peroxide, rheological properties, and the labour of their chemical synthesis could affect their ranking. Neutral SPIONs, negatively charged SPIONs, and positively charged SPIONs were ranked as the first, second, and third candidates, respectively. However, the improvement of the activity of positively charged SPIONs with hydrogen peroxide showed an increase to 0.3 instead of 0.2, which resulted in a better rank of these nanoparticles in comparison with that of the same nanoparticles in the first analysis series. One of the advantages of this study was to determine the impact of the characteristics of SPIONs on their ranking for their manufacturing. The other advantage was getting the information for further comparative study of these nanoparticles with the others. The results of this work can be used in manufacturing engineering and materials science.

Keywords: SPIONs, chemical activity, biological properties, rheological properties, TOPSIS, industrial growth, manufacturing engineering.

1 Introduction

Superparamagnetic iron oxide nanoparticles (SPIONs) have diverse applications such as magnetic drug targeting, magnetic hyperthermia, photocatalytic applications, etc. For most materials science and engineering applications, these nanoparticles are suspended in water [1–3]. The characteristics of SPIONs that were first studied in recent investigations have been as follows: antibiofilm activity, hemocompatibility, activity with hydrogen peroxide, rheological properties, and labour for their chemical synthesis in the lab [4–8].

The antibiofilm activity and hemocompatibility studies of SPIONs require the assessment of these nanoparticles with biological materials, which are bacterial biofilms and blood cells (ex.: red blood cells and platelets), respectively [4, 5, 9–14]. These analyses of SPIONs have allowed the development of their applications in materials science and biomedical engineering [15–20].

The Technique for Order of Preference by Similarity to Ideal Solution (TOPSIS) is a decision-making method that allows optimizing and ranking candidates. This method has been widely used to analyze candidates, such as electronic devices, cognitive entities, etc. Hwang and Yoon developed TOPSIS in 1981 to determine solutions from a finite set of alternatives [21, 22]. TOPSIS ranks candidates according to their distances from their ideal solutions with the consideration of their profit and cost criteria [21–26].

This paper considers these characteristics of SPIONs: antibiofilm activity, hemocompatibility, activity with hydrogen peroxide, rheological properties, and labour for

their chemical synthesis. The first four properties of these nanoparticles are positive because their increase is beneficial for their biomedical and engineering applications, whereas the last one is negative because less labour would be more appropriate in order to spend less time and energy on the chemical synthesis of these nanoparticles. Therefore, in this study, the first four indicated properties were considered as profit criteria and the last one as cost criterion.

TOPSIS has been used to analyze the properties of some materials and those of human beings according to their traits [27–32]. It has also been used to rank manufactured devices and instruments [33–38].

The analysis of the characteristics of SPIONs for optimizing their manufacture with TOPSIS has not been reported yet. This paper's results can be used to improve the applications of these nanoparticles in materials science and biomedical engineering.

2 Research Methodology

2.1 Preparation of SPIONs

The neutral, positively charged, and negatively charged SPIONs studied in this work were the nanoparticles prepared according to the protocols described in previous studies [4, 5, 6, 7, 39].

2.2 TOPSIS method

The TOPSIS code that Chakravorty developed in 2016 (https://github.com/Glitchfix/TOPSIS-Python/blob/master/topsis.py) was used for this analysis.

The numerical analysis with TOPSIS was carried out on two groups of characteristics of SPIONs; positive and negative characteristics were considered profit and cost, respectively.

The steps of the TOPSIS method were as below [40–46] :

Step 1: Creation of a normalized decision matrix

The normalized R decision matrix was created in step 1 according to the formula below:

$$r_{ij} = \frac{X_{ij}}{\sqrt{\sum_{l}^{m} = 1^{x_{ij}^2}}}$$

Step 2: Creation of a weighted normalized decision matrix V

This matrix was created using the formula below:

$$v_{ij} = w_j . r_{ij}$$

Step 3: Determination of the positive ideal solution (A^+) and the negative ideal solution (A^-)

The positive ideal solution (A^+) and negative ideal solution (A^-) were calculated with the TOPSIS method as described previously [40, 41, 42].

Step 4: Calculation of the separation distance from the positive ideal solution S^+ and the other distance from the negative ideal solution S^- for each candidate

These distances were calculated using the formulas below:

$$D_j^* = \sqrt{\sum_{i=1}^{n} (v_{ij} - v_i^*)^2}, j = 1,...,J.$$

$$D_j^- = \sqrt{\sum_{i=1}^{n} (v_{ij} - v_i^-)^2}, j = 1,...,J.$$

Step 5: Calculation of the similarity coefficients using the proximity relative to the ideal solution

The candidates' similarity coefficients were calculated with the formula below:

$$C_j^* = \frac{D_j^-}{D_j^* + D_j^-}, j = 1,...,J.$$

The ranking according to the value of closeness coefficient (C_j^*) was described previously [47–54].

2.3 Modification of TOPSIS

The TOPSIS code was modified with the formulas below according to the Lukasiewicz's type disjunction:

self.evaluation_matrix[self.row_size-2][self.column_size-1]=self.evaluation_matrix[self.row_size-2][self.column_size-1] + 0.6

self.evaluation_matrix[self.row_size-3][self.column_size-1]=self.evaluation_matrix[self.row_size-3][self.column_size-1] + 0.6

if self.evaluation_matrix[self.row_size-2][self.column_size-1]>1:

self.evaluation_matrix[self.row_size-2][self.column_size-1]=1

if self.evaluation_matrix[self.row_size-3][self.column_size-1]>1:

self.evaluation_matrix[self.row_size-3][self.column_size-1]=1

These lines added to the first step in the TOPSIS code will add the value of 0.6 to the mean values of the membership degrees of the properties of neutral and positively charged SPIONs in the last column (labour of chemical synthesis), the first and second rows of Table 1. As the previous values of these membership degrees were 0.4, their summation with 0.6 will give 1.0, and the maximal value according to Lukasiewicz's type disjunction is 1.0. Therefore, these modifications in the TOPSIS code will make the values of 1.0 for these membership degrees in Table 1.

3 Results and Discussion

The results obtained in this study are included in the steps below:

1. Determine the mean values of triangular fuzzy membership degrees of candidates' characteristics.

The terms and corresponding triangular fuzzy values of the membership degrees of the characteristics of SPIONs and their mean values are shown in Table 1. The information about SPIONs as three candidates, C-1, C-2, and C-3, with their different characteristics, is presented in the table. Antibiofilm activity, hemocompatibility, activity with hydrogen peroxide, and rheological properties, which positively affect the candidates' properties as they reveal the efficiency of their activity, are profit criteria. The last one, the labour of their chemical synthesis, has a negative effect on this output as less labor for their manufacture is desired. So, this characteristic is considered a cost criterion. The mean values of fuzzy membership degrees of the candidates' characteristics according to the chosen terms (low, medium, or high) are indicated in the table.

Table 1 – Terms and their corresponding triangular fuzzy values of membership degrees of characteristics of SPIONs and their mean values

Candidates/ criteria	antibiofilm activity	hemocompatibility	activity with hydrogen peroxide	rheological properties	labour of their chemical synthesis
C-1	medium	medium	low	high	medium
C-2	medium	medium	low	medium	medium
C-3	low	low	high	medium	high

Candidates/ criteria	antibiofilm activity	hemocompatibility	activity with hydrogen peroxide	rheological properties	labour of their chemical synthesis
neutral SPIONs	0.3, 0.4, 0.5	0.4, 0.5, 0.6	0.2, 0.3, 0.4	0.7, 0.8, 0.9	0.3, 0.4, 0.5
pos-SPIONs	0.4, 0.5, 0.6	0.4, 0.5, 0.6	0.1, 0.2, 0.3	0.4, 0.5, 0.6	0.3, 0.4, 0.5
neg-SPIONs	0.2, 0.3, 0.4	0.1, 0.2, 0.3	0.7, 0.8, 0.9	0.4, 0.5, 0.6	0.6, 0.7, 0.8

Candidates/ criteria	antibiofilm activity	hemocompatibility	activity with hydrogen peroxide	rheological properties	labour of their chemical synthesis
neutral SPIONs	0.4	0.5	0.3	0.8	0.4
pos-SPIONs	0.5	0.5	0.2	0.5	0.4
neg-SPIONs	0.3	0.2	0.8	0.5	0.7

2. Determine the weights of alternatives for each criterion.

Table 2 shows the weight of alternatives for each criterion.

As the sums of weight values were more than 1.0, they were normalized in the TOPSIS code used for this analysis.

3. Determine the values in the criteria matrix.

The next step is obtaining the data of the criteria matrix.

Table 2 – The weights of alternatives for criteria

Alternatives /Values	antibiofilm activity	hemocompatibility	activity with hydrogen peroxide	rheological properties	labour of their chemical synthesis
C1-C3	0.5	0.5	0.5	0.5	0.5

Table 3 shows the criteria matrix in which the words "True" and "false" indicate the profit and cost criteria, respectively. In this matrix, antibiofilm activity, hemocompatibility, activity with hydrogen peroxide and rheological properties are profit criteria for SPIONs, whereas labour of their chemical synthesis is a cost criterion for these nanoparticles, respectively.

Table 3 – Criteria matrix

Alternatives /Values	antibiofilm activity	hemocompatibility	activity with hydrogen peroxide	rheological properties	labour of their chemical synthesis
C1-C3	True	True	True	True	False

4. Normalization step for fuzzy membership degrees and weights.

The results of the vector normalization performed on the fuzzy membership degrees of the characteristics of SPIONs as well as those of the normalization carried out on their weights, are represented in Tables 4 and 5, respectively.

Table 4 – The normalized decision matrix

Candidates/ criteria	antibiofilm activity	hemocompatibility	activity with hydrogen peroxide	rheological properties	labour of their chemical synthesis
neutral SPIONs	0.565685	0.680414	0.341882	0.749269	0.444444
pos-SPIONs	0.707107	0.680414	0.227921	0.468293	0.444444
neg-SPIONs	0.424264	0.272166	0.911685	0.468293	0.777778

Table 5 – The weighted normalized decision matrix

Candidates/ criteria	antibiofilm activity	hemocompatibility	activity with hydrogen peroxide	rheological properties	labour of their chemical synthesis
neutral SPIONs	0.113137	0.136083	0.068376	0.149854	0.088889
pos-SPIONs	0.141421	0.136083	0.045584	0.093659	0.088889
neg-SPIONs	0.084853	0.054433	0.182337	0.093659	0.155556

5. Determine the values of the best alternative and the worst alternative.

Table 6 shows the values of the best alternative and the worst alternative.

6. Determine the distances from the alternatives.

Table 7 shows the values of the distances from the best and the worst alternatives represented with (d_i^*) and (d_i^-), respectively.

Table 6 – The best alternative (A^+) and the worst alternative (A^-)

Candidates/ criteria	antibiofilm activity	hemocompatibility	activity with hydrogen peroxide	rheological properties	labour of their chemical synthesis
A^+	0.141421	0.136083	0.182337	0.149854	0.088889
A^-	0.084853	0.054433	0.045584	0.093659	0.155556

7. Determine the values of the similarity coefficients.

Table 8 shows the similarity coefficients (CC_i) and the rankings of the candidates according to their worst similarity.

Table 7 – The distances between the best and the worst alternatives

Candidates	d_i^+	d_i^-
neutral SPIONs	0.117418	0.124854
pos-SPIONs	0.147849	0.119629
neg-SPIONs	0.132170	0.136753

The improvement of the activity of positively charged SPIONs with hydrogen peroxide can increase to 0.3. In this case, we obtain a better ranking for these nanoparticles than those of the same nanoparticles in the first analysis series.

Table 8 – The similarity coefficients and the ranking of the candidates

Candidates	CC_i	ranking
neutral SPIONs	0.515346	1
pos-SPIONs	0.447249	3
neg-SPIONs	0.508520	2

The improvement of the activity of positively charged SPIONs with hydrogen peroxide can increase to 0.3. In this case, we obtain a better ranking for these nanoparticles than those of the same nanoparticles in the first analysis series. Tables 9 and 10 show the mean values of triangular fuzzy membership degrees of the characteristics of SPIONs and the results obtained with TOPSIS following this modification.

The only difference in the data of tables 9 and 1 concerns the mean value of the triangular fuzzy membership degree of the activity of positively charged SPIONs changed from 0.2 to 0.3.

Table 9 – The mean values of triangular fuzzy membership degrees of the characteristics of SPIONs

Candidates/ criteria	antibiofilm activity	hemocompatibility	activity with hydrogen peroxide	rheological properties	labour of their chemical synthesis
neutral SPIONs	0.4	0.5	0.3	0.8	0.4
pos-SPIONs	0.5	0.5	0.3	0.5	0.4
neg-SPIONs	0.3	0.2	0.8	0.5	0.7

The weights of each alternative for each criterion and the values in the criteria matrix were used in this second series of analyses as presented in Tables 2 and 3.

Tables 11, 12, and 13 show the weighted normalized decision matrix, the best alternative (A^+) and the worst alternative (A^-), and the distances from the best alternative (d_i^*) and the worst alternative (d_i^-) for the candidates, respectively.

Table 10 – The normalized decision matrix

Candidates/ criteria	antibiofilm activity	hemocompatibility	activity with hydrogen peroxide	rheological properties	labour of their chemical synthesis
neutral SPIONs	0.565685	0.680414	0.331295	0.749269	0.444444
pos-SPIONs	0.707107	0.680414	0.331295	0.468293	0.444444
neg-SPIONs	0.424264	0.272166	0.883452	0.468293	0.777778

Table 11 – The weighted normalized decision matrix

Candidates/ criteria	antibiofilm activity	hemocompatibility	activity with hydrogen peroxide	rheological properties	labour of their chemical synthesis
neutral SPIONs	0.113137	0.136083	0.066259	0.149855	0.088889
pos-SPIONs	0.141421	0.136083	0.066259	0.093659	0.088889
neg-SPIONs	0.084853	0.054433	0.176690	0.093659	0.093659

Table 12 – The best alternative (A^+) and the worst alternative (A^-)

Candidates/ criteria	antibiofilm activity	hemocompatibility	activity with hydrogen peroxide	rheological properties	labour of their chemical synthesis
A^+	0.141421	0.136083	0.176690	0.149854	0.088889
A^-	0.084853	0.054433	0.066259	0.093659	0.155556

Table 13 – The distances from the best alternative and the worst alternative for candidates

Candidates	d_i^+	d_i^-
neutral SPIONs	0.113996	0.122756
pos-SPIONs	0.123907	0.119629
neg-SPIONs	0.132170	0.110432

Table 14 – The similarity coefficients and the ranking of the candidates

Candidates	CC_i	ranking
neutral SPIONs	0.518500	1
pos-SPIONs	0.491216	2
neg-SPIONs	0.455196	3

The comparison of Tables 8 and 14 shows that the ranking of SPIONs is affected after the change in the mean value of triangular fuzzy membership degree of the reactivity of positively charged SPIONs with hydrogen peroxide from 0.2 to 0.3. In the first ranking before this modification, these nanoparticles were ranked in the third

place, whereas they appeared in the second place after this modification.

Fuzzy logic is a non-classical logic with applications in sciences and engineering [55–59]. A prediction model called the model of the tree has been applied for the improvement of these applications [60]. This model can be used to determine the number of profit and cost criteria and predict the impact of inappropriate consideration of the nanoparticles' characteristics on their ranks. The application of fuzzy logic in this model was explained previously [60]. The fuzzy logic disjunction operator is an important operator in this logic that can determine the effect of the simultaneous consideration of entities. Lukasiewicz's type disjunction can be used in fuzzy matrices [61, 62].

In another analysis series, Lukasiewicz's type disjunction was used to determine the impact of the simultaneous consideration of the labour for the chemical synthesis of SPIONs. This analysis was aimed to determine the effect of the inappropriate consideration and underestimation of this criterion for these nanoparticles. Suppose the manufacturer who synthesizes these nanoparticles while comparing with other nanoparticles considers that the labour for the preparation of neutral SPIONs and positively charged SPIONs is not high. In that case, the confusion in consideration of their manufacturing procedure due to the confusion of categories and inconsistency in his epistemic beliefs on their characteristics can change the ranks of these nanoparticles. If the membership degrees for the labor required for the preparation of other nanoparticles are as high as 0.6 or more, the summation of the fuzzy degree memberships of this criterion for these two types of SPIONs and those of other nanoparticles would be 1.0 or greater than 1.0. The maximal value of Lukasiewicz's type disjunction is 1.0. So, the value of 1.0 will appear as the maximum value in the output of TOPSIS.

Tables 15 and 16 show the mean values of the triangular fuzzy membership degrees of the characteristics of SPIONs and the output of modified TOPSIS after their consideration with other nanoparticles.

Table 15 – The mean values of triangular fuzzy membership degrees of the characteristics of SPIONs after consideration with other nanoparticles

Candidates/ criteria	antibiofilm activity	hemocompatibility	activity with hydrogen peroxide	rheological properties	labour of their chemical synthesis
neutral SPIONs	0.4	0.5	0.3	0.8	1.0
pos-SPIONs	0.5	0.5	0.2	0.5	1.0
neg-SPIONs	0.3	0.2	0.8	0.5	0.7

Table 16 – The similarity coefficients and the ranking of the candidates according to the worst similarity

Candidates	CC_i	ranking
neutral SPIONs	0.461011	3
pos-SPIONs	0.394185	1
neg-SPIONs	0.554313	2

As shown in Table 16, the positively charged SPIONs and negatively charged SPIONs are ranked in the first and second positions, respectively, whereas the neutral SPIONs are ranked in the third position. This is due to Lukasiewicz's type disjunction in the TOPSIS code and the summation of the degrees of membership of SPIONs and other nanoparticles.

As TOPSIS has been used to optimize manufacturing processes [63–66], the modification of this algorithm with the fuzzy disjunction operator, as explained in this work can help investigate the impact of the confusion of categories when the criteria for the manufacture of materials are selected. Fuzzy logic also has other operators such as conjunction operator and implication operator. These operators can also be implemented in the TOPSIS code to determine the other situations affecting the manufacturing processes [67–73].

Other non-classical logic, such as modal logic and computability logic [74], can also be used in the TOPSIS analysis, including the issues explained in this paper for the optimization of nanoparticle manufacture.

In recent years, several nanomaterials and biomaterials' physicochemical and biological properties have been investigated [75–80]. These works have revealed the properties and activities of these materials for their manufacture as well as their applications in diverse fields of science and engineering [81–85]. Further investigations are required for the analysis of the properties of these materials with TOPSIS.

4 Conclusions

The properties of nanoparticles are diverse and require being ranked to determine which of these nanoparticles has the best characteristics in comaprison with the others. This paper presents the characteristics of SPIONs, and their impact on ranking these nanoparticles has been explained. The results obtained in this study show that neutral SPIONs have a better rank of positively charged and negatively charged nanoparticles. Moreover, improving the activity of positively charged SPIONs with hydrogen peroxide can affect their rank. These results are promising for the manufacture of the next generations of SPIONs. Moreover, they can be helpful in a comparative study of these nanoparticles with the other ones. The results can be applied in the comparative optimization of the manufacturing procedures of these nanoparticles.

5 Acknowledgment

The author would like to thank Shivanjan Chakravorty for the code of TOPSIS.

References

1. Kalidasan, V., Liu, X.L., Li, Y., Sugumaran, P.J., Liu, A.H., Ren, L., Ding, J. (2018). Examining the effect of ions and proteins on the heat dissipation of iron oxide nanocrystals, *RSC Adv.*, Vol. 8, pp. 1443–1450. doi: 10.1039/C7RA11472A.
2. Wang, X., Xing, X., Zhang, B., Liu, F., Cheng, Y., Shi, D. (2014). Surface engineered antifouling optomagnetic SPIONs for bimodal targeted imaging of pancreatic cancer cells, *International Journal of Nanomedicine*, Vol. 9, pp. 1601–1615. doi: 10.2147/IJN.S58334.
3. Wang, J., Zhang, B., Wang, L., Wang, M., Gao, F. (2015). One-pot synthesis of water-soluble superparamagnetic iron oxide nanoparticles and their MRI contrast effects in the mouse brains, *Materials Science and Engineering: C*, Vol. 48(1), pp. 416–423. doi: 10.1016/j.msec.2014.12.026.
4. Javanbakht, T., Laurent, S., Stanicki, D., Wilkinson, K.J. (2016). Relating the surface properties of superparamagnetic iron oxide nanoparticles (SPIONs) to their bactericidal effect towards a biofilm of *Streptococcus mutans*, *Plos One*. doi: 10.1371/journal.pone.0154445.
5. Javanbakht, T., Hachem, A., Laurent, S., Sacher, E., Merhi, Y., Yahia, L'H. (2014). Comparative study of the influences of surface functionality and corona protein adsorption on the hemocompatibility of magnetite nanoparticles, Society for Biomaterials, p. 445.
6. Javanbakht, T., Laurent, S., Stanicki, D., Frenette, M. (2020). Correlation between physicochemical properties of superparamagnetic iron oxide nanoparticles and their reactivity with hydrogen peroxide, *Canadian Journal of Chemistry*, Vol. 98(10), pp. 601–608. https://doi.org/10.1139/cjc-2020-0087.
7. Javanbakht, T., Laurent, S., Stanicki, D., Salzmann, I. (2021). Rheological properties of superparamagnetic iron oxide nanoparticles, *Journal of Engineering Sciences*, Vol. 8(1), pp. C29-C37. doi: 10.21272/jes.2021.8(1).c4.
8. Mireles, L.-K., Sacher, E., Yahia, L'H., Laurent, S., Stanicki, D. (2016). Washing effect on superparamagnetic iron oxide nanoparticles, *Data in Brief*, Vol. 7, pp. 1296–1301. doi: 10.1016/j.dib.2016.03.104.
9. Arias, L.S., Pessan, J.P., Vieira, A.P.M. de Lima, T.M.T., Delbem, A.C.B., Monteiro, D.R. (2018). Iron oxide nanoparticles for biomedical applications: a perspective on synthesis, drugs, antimicrobial activity, and toxicity, *Antibiotics*, Vol. 7(46). doi: 10.3390/antibiotics7020046.
10. Ranmadugala, D., Ebrahiminezhad, A., Manley-Harris, M., Ghasemi, Y., Berenjian, A. (2017). The effect of iron oxide nanoparticles on *Bacillus subtilis* biofilm, growth and viability, *Process Biochemistry*, Vol. 62, pp. 231–240. doi: 10.1016/j.procbio.2017.07.003.
11. Haney, C., Rowe, J.J., Robinson, J.B. (2012). SPIONs increase biofilm formation by Pseudomonas aeruginosa, *Journal of Biomaterials and Nanobiotechnology*, Vol. 03(04), pp. 508–518. doi: 10.4236/jbnb.2012.324052.
12. Szekeres, M., Illés, E., Janko, C., Farkas, K. (2015). Hemocompatibility and biomedical potential of poly(gallic acid) coated iron oxide nanoparticles for theranostic use, *Journal of Nanomedicine and Nanotechnology*, Vol. 2(6), 1000252. doi: 10.4172/2157-7439.1000252.
13. Janko, C., Zaloga, J., Pöttler, M., Dürr, S., Eberbeck, D., Tietze, R., Lyer, S. Alexiou, C. (2017). Strategies to optimize the biocompatibility of iron oxide nanoparticles – "SPIONs safe by design", *Journal of Magnetism and Magneric Materials*, Vol. 431(1), pp. 281–284.
14. Blok S.L.J., Engels, G.E. (2016). *In vitro* hemocompatibility testing: The importance of fresh blood, *Biointerphases*, Vol. 11(2), 029802. doi: 10.1116/1.4941850.
15. Yeh, Y.-C., Huang, T.-H., Yang, S.-C., Chen, C.-C., Fang, J.-Y. (2020). Nano-based drug delivery or targeting to eradicate bacteria for infection mitigation: A review of recent advances, *Front. Chem.*, Vol. 8, 286. doi: 10.3389/fchem.2020.00286.
16. Armijo, L.M., Wawrzyniec, S.J., Kopciuch, M., Brandt, Y.I., Rivera, A.C., Withers, N.J., Cook, N.C., Huber, D.L., Monson, T.C., Smyth, H.D.C., Osinski, M. (2020). Antibacterial activity of iron oxide, iron nitride, and tobramycin conjugated nanoparticles against Pseudomonas aeruginosa biofilms, *Journal of Nanobiotechnology*, Vol. 18(35). doi: 10.1186/s12951-020-0588-6.
17. Vieira, A.P.M., Arias, L.S., Neto, F.N.S., Kubo, A.M., Lima, B.H.R., de Camargo, E.R., Pessan, J.P., Delbem, A.C.B., Monteiro, D.R. (2019). Antibiofilm effect of chlorhexidine-carrier nanosystem based on iron oxide magnetic nanoparticles and chitosan, *Colloids and Surfaces B: Biointerfaces*, Vol. 174, pp. 224–231. doi: 10.1016/j.colsurfb.2018.11.023.
18. Vallabani, N.V.S., Vinu, A., Singh, S., Karakoti, A. (2020). Tuning the ATP-triggered pro-oxidant activity of iron oxide-based nanozyme towards an efficient antibacterial strategy, *Journal of Colloid and Interface Science*, Vol. 567, pp. 154–164. doi: 10.1016/j.jcis.2020.01.099.
19. Maruthupandy, M., Muneeswaran, T., Anand, M., Quero, F. (2020). Highly efficient multifunctional graphene/chitosan/magnetite nanocomposites for photocatalytic degradation of important dye molecules, *International Journal of Biological Macromolecules*, Vol. 153, pp. 736–746. doi: 10.1016/j.ijbiomac.2020.03.045.
20. Saraswathy, A., Nazerr, S.S., Nimi, N., Santhakumar, H., Suma, P.R., Jibin, K., Victor, M., fernandez, F.B., Amurugam, S., Shenoy, S.J., Varma, P.R.H., Jayasree, R.S. (2021). Asialoglycoprotein receptor targeted optical and magnetic resonance imaging and therapy of liver fibrosis using pullulan stabilized multi-functional iron oxide nanoprobe, *Scientific Reports*, Vol. 11, 18324. doi: 10.1038/s41598-021-97808-0.
21. Hwang, C.L., Yoon, K. (1981). *Multiple attribute decision making: Methods and applications*, Springer-Verlag, New York.

22. Vithalani AA, Vithalani CH. (2017). Application of combined TOPSIS and AHP method for spectrum selection in cognitive radio by channel characteristic evaluation, *International Journal of Electronics and Communication Engineering*, Vol. 10(2), pp. 71–79.
23. Sangchini, E.K., Naliavn, O.A., Tahmasebipour, N. (2017). Application of TOPSIS method in evaluation and prioritization of social stability in rural areas, *Journal of Applied Sciences and Environmental Manage*, Vol. 21(1), pp. 49–56. doi: 10.4314/jasem.v21i1.6.
24. Yadav, V., Karmakar, S., Kalbar, P.P., Dikshit, A.K. (2019). Pytops: A Python based tool for TOPSIS, *SoftwareX*, Vol. 9, pp. 217–222. doi: 10.1016/j.softx.2019.02.004.
25. Zulqarnain, R.M., Saeed, M., Ahmad, N., Dayan, F., Ahmad, B. (2020). Application of TOPSIS method for decision making, *International Journal of Scientific Research in Mathematical and Statistical Sciences*, Vol. 7(2), pp. 76–81.
26. Motia, S., Reddy, S.R.N. (2020). Application of TOPSIS method in selection of design attributes of decision support system for fertilizer recommendation, *Journal of Information and Optimization Sciences*, pp. 1689–1704.
27. Indahingwati, A., Barid, M., Wajdi, N., Susilo, D. E., Kurniasih, N., & Rahim, R. (2018). Comparison analysis of TOPSIS and fuzzy logic methods on fertilizer selection, *International journal of engineering and technology*, Vol. 7(2.3), pp. 109–114.
28. Jumarni, R. F., & Zamri, N. (2018). An integration of fuzzy TOPSIS and fuzzy logic for multi-criteria decision making problems, *International journal of engineering and technology*, Vol. 7(2), pp. 102–106.
29. Javanbakht T, Chakravorty, S. (2022). Prediction of human behavior with TOPSIS, *Journal of Fuzzy Extension and Applications*, Vol. 3(2), pp. 109–125.
30. Wieckowski, J., Sałabun, W. (2020). How to handling with uncertain data in the TOPSIS technique? *Procedia Computer Science*, Vol. 176, pp. 2232–2242.
31. Roghanian, E., Sheykhan, A., Abendankashi, E.S. (2014). An application of fuzzy TOPSIS to improve the process of supply chain management in the food industries: A case study of protein products manufacturing company, *Decision Science Letters*, Vol. 3(1), pp. 17–26.
32. Huang, W., Huang, Y.Y. (2012). Research on the performance evaluation of Chongqing electric power supply bureaus based on TOPSIS, *Energy Procedia*, Vol. 14, pp. 899–905.
33. Barrios, M.A.O. et al. (2016). An AHP-Topsis integrated model for selecting the most appropriate tomography equipment, *International Journal of Information Technology and Decision Making*, Vol. 15(4), pp. 861–885. doi: 10.1142/S021962201640006X.
34. Abdel-Basset, M. et al. (2019). A group decision making framework based on neutrosophic TOPSIS approach for smart medical device selection, *Journal of Medical Systems*, Vol. 43, 38.
35. Mustapha, M.T. et al. (2021). Application of fuzzy TOPSIS in the sterilization of medical devices, in *Applications of Multi-Criteria Decision-Making Theories in Healthcare and Biomedical Engineering*, I. Ozsahin, D. Ozsahin, B. Uzun (Eds.), Elsevier, pp. 197–216. doi: 10.1016/B978-0-12-824086-1.00013-X.
36. Trivedi, A. et al. (2019). Fuzzy TOPSIS multi-criteria decision making for selection of electric molding machine, in *Innovations in Computer Science and Engineering*, Springer, pp. 325–332.
37. Lata, S. et al. (2021). Selection of machine tool by using FUZZY TOPSIS method, *AIP Conference Proceedings*, 2341, 020015.
38. Foubert, B., Mitton, N. (2021). RODENT: A flexible TOPSIS based routine protocol for multi-technology devices in wireless sensor networks, *ITU Journal on Future and Evolving Technologies*, 7.
39. Javanbakht T, Laurent S, Stanicki D, David E. (2019). Related physicochemical, rheological, and dielectric properties of nanocomposites of superparamagnetic iron oxide nanoparticles with polyethyleneglycol, *Journal of Applied Polymer Science*, Vol. 136, pp. 48280–48290.
40. Korbryn, A. (2016). A data pre-processing model for the TOPSIS method, *Fobia Oecnomica Stetinensia*, pp. 219–235. doi: 10.1515/foli-2016-0036.
41. Rahim, R. et al. (2018). TOPSIS method application for decision support system in internal control for selecting best employees, *2nd International Conference on Statistics, Mathematics, Teaching and Research*, Vol. 1028, 012052. doi:10.1088/1742-6596/1028/1/012052.
42. Zhongyou, X. (2012). Study on the application of TOPSIS method to the introduction of foreign players in CBA games, *International Conference on Medical Physics and Biomedical Engineering*, Vol. 33, 2034–2039.
43. Ahariea, E. et al. (2019). A TOPSIS-based approach for wind turbines ranking with negative performance and different weighting strategies, *E3S Web of Conferences*, 85, 03003. doi:10.1051/e3sconf/20198503003.
44. Alinezhad, A., Amini, A. (2011). Sensitivity analysis of TOPSIS technique : The results of change in the weight of one attribute on the final ranking of alternatives, *Journal of Optimization in Industrial Engineering*, Vol. 7, pp. 23–28.
45. Alemiardakani, A. (2014). *Enhancing impact characterization and multi-criteria design optimization of glass fiber reinforced polypropylene laminates*, PhD thesis, The University of British Columbia.
46. Singh, H., Singh, J. (2014). Attribute based analysis, evaluation and selection of nanocomposite using MADM-TOPSIS approach, *Journal of Academia and Industrial Research*, Vol. 3(1), pp. 21–30.
47. Fuse, K. et al. (2021). Integration of fuzzy AHP and fuzzy TOPSIS methods for wire electric discharge machining of titanium (Ti6Al4V) alloy using RSM, *Materials*, Vol. 14(23), 7408.
48. Ponugoti, U. et al. (2019). Optimizing cutting parameters in hard turning of AISI 52100 steel using topsis approach, *Journal of Mechanical and energy Engieering*, Vol. 3(43), pp. 227–232. doi: 10.30464/jmee.2019.3.3.227.
49. Yadav, S. et al. (2019). A novel hybrid TOPSIS-PSI approach for material selection in marine applications, *Sådhanå*, Vol. 44(3). doi: 10.1007/s12046-018-1020-x.
50. Nguyen, V.C. et al. (2021). Cutting parameter optimization in finishing milling of Ti-6Al-4V titanium alloy under MQL condition using TOPSIS and ANOVA analysis, *Engineering, Technology and Applied Science Research*, Vol. 11(1):6775–6780.

51. Falqi, I.I. et al. (2019). Siliceous concrete materials management for sustainability using fuzzy-TOPSIS approach, *Applied Sciences*, Vol. 9(17), 3457. doi: 10.3390/app9173457.
52. Dialey, S. et al. (2017). PSI and TOPSIS based selection of process parameters in WEDM, *Periodica Polytechnica Mechanical Engineering*, Vol. 61(4), pp. 255–260. doi: *10.3311*/PPme.10431.
53. Singh, T. Agrawal, V.P. (2014). Attribute based specification, comparison and selection of nanoactuator elements, *International Journal of Advanced Engineering and Nano Technolog*, Vol. 1(6), pp. 1–14.
54. Mittal, K., Tewari, P.C., Khanduja, D. (2017). On the right approach to selecting a quality improvement project in manufacturing industries, *Operation Research and Decisions*, pp. 105–124. doi: 10.5277/ord170106.
55. Harris, J. (2005). Fuzzy logic applications in engineering science in *Intelligent Systems, Control and Automation : Science and Engineering*, Springer.
56. Bien, Z., Min, K.C. (1995). Fuzzy logic and its applications to engineering, information sciences, and intelligent systems, in *Theory and Decision Library D*, TDLD, 16.
57. Gupta, A.K. (2021). Fuzzy logic and their application in different areas of engineering science and research : A survey, *International Journal of Scientific Research in Science and Technology*, Vol. 8(2), pp. 71–75. doi: 10.32628/IJSRST218212.
58. Ram, M. (2018). A*dvanced fuzzy logic approaches in engineering science*, IGI Global, Hershey, PA, USA.
59. Ross. T.J. (Ed.) (1994). *Fuzzy logic with engineering applications*, McGraw-Hill Education.
60. Javanbakht, T. (2020). *Être et Pensée*, S. Robert & J.P. Beaudin (Eds.), Bouquinbec, Montreal.
61. Javanbakht, T. (2016). *Logique floue et arborescence comme outils de modélisation des catégories en tant que prototypes*, Thesis, University of Quebec in Montreal.
62. Muthuraji, T., Sriram, S. (2017). Reduction of an intuitionistic fuzzy matrix to fuzzy matrix with some algebraic properties, *Annals of Fuzzy Mathematics and Informatics*, Vol. 13(4), 475–483.
63. Shukla, A. et al. (2017). Applications of TOPSIS algorithm on various manufacturing processes: A review, *Materials Today: Proceedings*, Vol. 4(4), 5320-5329. doi: 10.1016/j.matpr.2017.05.042.
64. Raja, S., Rajan, A.J. (2022). A decision-making model for selection of the suitable FDM machine using fuzzy TOPSIS, *Mathematical Problems in Engineering*, 7653292. doi: 10.1155/2022/7653292.
65. Samala, T. et al. (2022). A systematic simulation-based multi-criteria decision-making approach for the evaluation of semi–fully flexible machine system process parameters, *Electronics*, Vol. 11, 233. doi: 10.3390/electronics11020233.
66. Mabkhot, M.M. et al. (2020). An ontology-based multi-criteria decision support system to reconfigure manufacturing systems, *IISE Transactions*, Vol. 52(1).
67. Oh, K.W., Bandler, W. (1987). Properties of fuzzy implication operators, *International Journal of Approximate Reasoning*, Vol. 1, pp. 273–28.
68. Khaliq, A., Ahmad, A. (2010). *Fuzzy logic and approximate reasoning*, Thesis, Blekinge Institute of Technology.
69. Espin-Andrade, R.A. et al. (2015). Archimedean-compensatory fuzzy logic systems, *International Journal of Computational Intelligence Systems*, Vol. 8, pp. 54–62.
70. Emami, M.R. (1997). *Systematic methodology of fuzzy-logic modeling and control and application to robotics*, Thesis, University of Toronto.
71. Chen, X., Hu, Z., Sun, Y. (2022). Fuzzy logic based logical query answering on knowledge graphs, *AAAI Technical Track on Data Mining and Knowledge Management*, Vol. 36(4). doi: 10.1609/aaai.v36i4.20310.
72. Smets, P., Magre, P. (1987). Implication in fuzzy logic, *International Journal of Approximate Reasoning*, Vol. 1, pp. 327–347.
73. Ying, M. (2002). Implication operators in fuzzy logic, *IEEE Transactions on Fuzzy Systems*, Vol. 10(1), pp. 88–91, doi: 10.1109/91.983282.
74. Yao, Y.Y. (1998). A comparative study of fuzzy sets and rough sets, *Information Sciences*, Vol. 109(1–4), pp. 227–242. doi: 10.1016/S0020-0255(98)10023-3.
75. Gatoo, M.A. et al. (2014). Physicochemical properties of nanomaterials: Implication in associated toxic manifestations, *Toxicity of Nanomaterials*, 498420. doi: 10.1155/2014/498420.
76. Ghane-Motlagh B, Javanbakht T, Shoghi F, Wilkinson KJ, Martel R, Sawan M. (2016). Physicochemical properties of peptide-coated microelectrode arrays and their in vitro effects on neuroblast cells, *Materials Science and Engineering C*, Vol. 68, pp. 642–650.
77. Javanbakht T, Ghane-Motlagh B, Sawan M. (2020). Comparative study of antibiofilm activity and physicochemical properties of microelectrode arrays, *Microelectronic Engineering*, 229:111305.
78. Javanbakht T, Sokolowski W. (2015). Thiol-ene/acrylate systems for biomedical shape-memory polymers, *Shape Memory Polymers for Biomedical Applications*, pp. 157–166.
79. Djavanbakht T, Carrier V, André JM, Barchewitz R, Troussel P. (2000). Effets d'un chauffage thermique sur les performances de miroirs multicouches Mo/Si, Mo/C et Ni/C pour le rayonnement X mou, *Journal de Physique IV*, France, Vol. 10, pp. 281–287.
80. Javanbakht T, David E. (2020). Rheological and physical properties of a nanocomposite of graphene oxide nanoribbons with polyvinyl alcohol, *Journal of Thermoplastic Composite Materials*, 0892705720912767.
81. Javanbakht T, Hadian H, Wilkinson KJ. (2020). Comparative study of physicochemical properties and antibiofilm activity of graphene oxide nanoribbons, *Journal of Engineering Sciences*, Vol. 7(1), pp. C1–C8.
82. Navya, P.N., Daima, H.K. (2016). Rational engineering of physicochemical properties of nanomaterials for biomedical applications with nanotoxicological perspectives, *Nano Convergence*, 1.
83. Javanbakht T, Bérard A, Tavares J.R. (2016). Polyethylene glycol and poly (vinyl alcohol) hydrogels treated with photo-initiated chemical vapor deposition, *Canadian Journal of Chemistry*, Vol. 94(9), pp. 744–750.
84. Javanbakht T, Raphael W, Tavares J.R. (2016). Physicochemical properties of cellulose nanocrystals treated by photo-initiated chemical vapour deposition (PICVD), *The Canadian Journal of Chemical Engineering*, Vol. 94(6), pp. 1135–1139.
85. Afolalu, S.A. et al. (2020). Overview Of physicochemical and surface properties of nanoparticles for engineering applications, *IOP Conference Series: Earth and Environmental Science*, Vol. 665, 012049.

JOURNAL OF ENGINEERING SCIENCES

Volume 9, Issue 2 (2022)

Okwesileze I. A., Okafor O. C., Atanmo P. N., Ekengwu I. E., Uyaelumuo E. I. (2022). Carburization-based optimization of AISI 8620 steel using rice husks and charcoal as carburizers. Journal of Engineering Sciences, Vol. 9(2), pp. C9-C16, doi: 10.21272/jes.2022.9(2).c2

Carburization-Based Optimization of AISI 8620 Steel Using Rice Husks and Charcoal as Carburizers

Okwesileze I. A.[1], Okafor O. C.[2], Atanmo P. N.[1], Ekengwu I. E.[3], Uyaelumuo E. I.[1]

[1] Chukwuemeka Odumegwu Ojukwu University, Uli, Nigeria;
[2] Grundtvig Polytechnic, Oba Nigeria;
[3] Nnamdi Azikiwe University, Awka, Nigeria

Article info:
Submitted: October 6, 2022
Accepted for publication: December 9, 2022
Available online: December 12, 2022

***Corresponding email:**
obiora.okafor@grundtvigpolytechnic.com

Abstract. This study was centered on improving the mechanical properties of AISI 8620 steel using the carburization technique. The failure in service conditions of many steel components such as cams, gears, and shafts necessitated the research as it demands that they possess both high wear-resistant surfaces and tough shock-resistant cores. Standard test samples prepared from the steel material were subjected to a pack carburization process using rice husk and charcoal as carburizers, and the energizer – calcium trioxocarbonate (IV) at temperatures of 800, 850, 900, and 950 °C, and held for 60, 90, and 120 minutes. The samples were quenched in water and tempered at 500 °C for 60 minutes. After the pack hardening process, the test samples were subjected to tensile, impact, and hardness tests. From the data obtained, ultimate tensile strength (UTS), Hardness, Young's Modulus, engineering strain, and impact strength were calculated. The case and core hardness of the carburized samples were noted, and an optical microscope was used to observe the microstructural features of the case-hardened, quenched, and tempered samples. The responses (mechanical properties of steel) were optimized using response surface methodology to obtain the optimum carburizing conditions-temperature and holding time. Results showed that the sample's microhardness core and microhardness case increased from 253 to 327 HV and from 243 to 339 HV as the holding time increased from 60 to 120 minutes, indicating an appreciable increase in the mechanical property of the samples. The optimum carburizing conditions were at a temperature of 885 °C and a holding time of 120 minutes. Hence, the carburization of AISI 8620 steel using rice husk and charcoal as carburizers improved the steel material's case, core, and mechanical properties.

Keywords: materials science, carburization, rice husks, charcoal, steel, optimization.

1 Introduction

Carburization is one of the case hardening methods in which carbon layer formation is induced on the surface of a substance in order to improve the strength and hardness properties. Carburizing temperature boundary is within 850-950 °C. Carburization is employed on materials that cannot be hardened appreciably by hardening process, like low carbon steel. Hardenability is a property of steel that measures the depth and distribution of hardness obtained by quenching from the austenizing temperature. The ratio of transformation of austenite to martensite is the deciding factor for hardenability. Steel with high hardenability forms thick layers of martensite. In many engineering applications, it is desirable that steel being used should have a good surface hardness value in order to resist wear and tear. The hardened surface is required to possess a soft and tough core to aid in shock absorption process. Surface hardening processes other than carburizing are: Cyaniding, Nitriding, induction hardening and flame hardening.

Steel materials with high carbon content of around 0.8 % are hard, but brittle, and therefore cannot be used in machine parts such as gears, sleeves and shafts that are exposed to dynamic bending and tensile stresses during operation [1]. A steel material with carbon content as high as 1.0 % is very hard to machine by cutting operations such as turning or drilling [1]. These concerns are solved by using low carbon steel materials such as AISI 8620, AISI 1020, etc. and subjecting them to some surface modification operations like carburizing, boronizing, nitriding, ion nitriding, etc. In addition, most

of the failures of some mechanical elements or components subjected to cyclic motions are caused by fatigue, as such, the fatigue performance of materials has prime importance for the design of structures which are subject to cyclic loading [2]. The surfaces of machine parts or components are the most susceptible zones to fatigue and tribomechanical failures, and fatigue cracks are generally initiated at the surface [3]. Therefore, there is a high incremental stress profile generation and distribution across the surfaces of machine parts under cyclic loading or a tribological condition. Hence, strengthening of the surface materials of such machine part or component is very imperative in enhancing fatigue life and tribomechanical characteristics of the material. The application of mechanical or thermo-chemical surface treatment like case carburizing, boronizing, etc. strengthens the surfaces of the steel material and in-turn initiates residual compressive stresses at the surface that would hinder fatigue crack development and propagation.

Therefore, this study was centered on the determination of the carburizing potential of rice husks and charcoal, as an agricultural residue, to provide carbon to the surface of a specimen of AISI/SAE 8620 mild steel when it is heat treated by pack carburizing. The consequent effects of carburizing operation on the tribo-mechanical properties of AISI 8620 steel were also studied. The optimum carburizing conditions (temperature and holding time) that yielded the best response characteristics of the carburized sample were obtained using optimization technique.

2 Literature Review

The determination of the effects of carburizing conditions (temperature and holding time) and the carburizing substances on the tribo-mechanical properties of the base material has been a research focus. These factors and their various combinations propose different mechanical properties and carbon-inducement percentage on the surface layer of the material- low carbon steel. Based on this, studies have been carried out inquest of improving the surface hardness of low carbon steel material and the determination of the consequent effects of the process. To this effect, Oluwafemi et al [4] used palm-shell as carburizing substance to pack carburize AISI 1020 steel. They used a treatment temperature ranging from 800 to 950 °C and holding time of 60, 90, and 120 minutes. The result obtained showed a microstructural pattern of a hardened steel specimen, thereby attesting that there was an inducement of carbon on the surface. Also, Istiroyah et al [5] employed charcoal gotten from coconut shell and rice husk at a temperature of 600°C to carburize AISI 316L steel. They use a treatment temperature of 400 °C and a soaking time of 480 minutes. The results obtained proved that carbon distribution in the steel carburized with coconut shell was better than that of rice husk. In addition, Siti et al [6] studied the effects of paste carburizing treatment on mechanical properties of ASTM A516 low carbon steel. Tensile test, hardness test (Rockwell) and microstructural examination were conducted on the carburized sample. The paste carburizing treatment was carried out at temperature of 700, 750, and 800 ℃ for 6 hours holding time. The results depicted that paste carburized samples provide significant improvement on both tensile strength and hardness values compared to uncarburized samples. This was associated with the formation of hard carburized surface-layer on the substance. Increasing the carburizing temperature profoundly improved both hardness and tensile strength, as the results of deeper carburized layer produced. Paste carburizing was found to induce formation of carburized layer at shorter time and lower temperature compared to pack carburizing method.

3 Research Methodology

3.1 Material description

The base material employed in this study was AISI 8620 steel and pack carburizing method was used in assessing the surface hardening potential of an agricultural residue- rice husk and charcoal.

The steel material was sourced locally and was analyzed using atomic absorption spectrometer (AAS). It was cut and machined to standard test sample sizes according to American Society for Testing and Materials (ASTM) standard specifications using a lathe machine. Carburization was done using heat treatment furnace. The tensile test was conducted using Computer Controlled Electro-Hydraulic Servo Universal Tensile Testing Machine (Model HLCS-600). Metallurgical microscope (Model Olympus PMG-3) was used to study the microstructures while micro-hardness testing machine (Model UH930) was employed to measure the micro-hardness while impact testing machine (Model UI820) was used to ascertain the impact strength of the steel material.

The method employed in this study includes: the determination of the percentage composition of the locally sourced AISI 8620 steel material, elemental analysis (%) carburizing materials, pack carburizing method application, design of experiment, mechanical tests and optimization.

3.2 Chemical analysis of AISI 8620 steel

AISI 8620 steel was sourced locally and analyzed using atomic absorption spectrometer (AAS). It was cut and machined to standard test sample sizes according to American society for testing and material (ASTM) standard specifications using a lathe machine. The AISI 8620 steel was polished with a polishing machine for it to bring out the best results. It was placed in the spectrometer machine and spark was introduced to give the result shown in Table 1.

Table 1 – The compositional build of AISI 8620 steel sample

Elements	C	Si	Mn	Mo
Average content	0.200	0.165	0.750	0.158
Elements	Cr	Ni	Fe	P
Average content	0.450	0.470	97.886	0.0295

The sparking was done two to three times after which the average was taken.

3.3 Chemical composition of carburizing materials

The chemical compositions of rice husks were obtained through the following procedures: samples of rice husks were handpicked and washed clean to avoid impurities and sand. The rice husks were chemically treated with sodium hydroxide (NaOH) solution, neutralized with acetic acid and finally washed with distilled water and sun-dried. 2 kg of rice husks was measured and 1 kg of charcoal in the proportion of 7:3.

A grinding machine was used to reduce the size of the rice husks and charcoal individually and sieved to a standard sieve size of 450 µm to get uniform size. Mixture of rice husks/charcoal were melted and sparked in an extrusion machine at temperature of 120-150 °C and screw speed of 50 rpm to obtain the chemical analysis of rice husks/charcoal. The chemical compositions of the carburizing materials are shown in Table 2.

Table 2 – Chemical composition of the carburizing materials

Material	Elemental Analysis (%)				
	C	H	O	N	S
Rice husk	41.13	3.37	35.3	0.33	–
Charcoal	72.31	2.43	–	1.16	1.05

3.4 Pack carburization technique

Pack carburizing method was employed in this study. Carbon powder (derived from the carburizers) was mixed properly with an energizer (calcium carbonate) in the proportion of 7:3 after which the first set of samples was buried in the mixture inside a rectangular steel box. Clay mixed with Bentonite and moderate water was used to seal the rectangular steel box tightly to prevent carbon (11) oxide from escaping and in turn not allowing unwanted furnace gas from re-entering the steel box. The steel box was then charged into the furnace and allowed to heat to temperatures of 750, 800, 850, and 900 °C, respectively. At each temperature the test specimen was soaked for one, two and three hours respectively according to the experimental design. The steel box was removed from the furnace with the help of tongs at each temperature and then the specimen was quenched in water at ambient temperature. The mixture configurations of the applied carburizers in the development of the test samples are shown in Table 3.

Table 3 – Mixture composition for pack carburizing operation

Mixture code	carburizing material	Amount of, g	Amount of energizer $CaCO_3$, g
MC1	charcoal	500	–
MC2		500	333.3
MC3	rice husk	500	–
MC4		500	333.3

3.5 Design of experiment

The Design Expert 11.0 software was employed for the experimental design. In quest of finding the optimum factor combination that would yield the best response characteristics of carburized AISI 8620 steel, response surface methodology tool was applied.

The input factors were temperature (°C) and holding time (minutes). The response variables employed in the experimental design were ultimate tensile strength (MPa), strain (%), modulus of elasticity (MPa), impact strength (J), micro hardness case (H), and micro hardness core (H).

A total of 12 runs/simulations were obtained from the experimental design and were meticulously followed while performing the experiment. The mathematical inequality used in designing the experiment is described thus: temperature – in a range of 800-950 °C; holding time – 60-120 minutes.

The ultimate tensile strength, strain, modulus of elasticity, impact strength and hardness (case and core structures) of pack carburized steel samples all determined using the appropriate machines. The microstructural characteristics of the produced samples of carburized steel were ascertained by first polishing the samples and etching them with 2 % Nital solution.

4 Results and Discussion

4.1 Microstructural analysis

Figure 1 a reveals the optical micrograph of the base (non-carburized) AISI 8620 steel material used.

It depicts steel in the state of supply. The structure observed is a matrix of ferrite and pearlite which are the characteristic constituents that yielded the chemical composition of the material steel as indicated in Table 1.

Figures 1 b-e correspond to the specimens that is heat treated using the carburizing mixtures indicated in Table 3. The figures show from the core to the surface, a progressive increment in the amount of pearlite. This amount remaining in the core equals the amount observed in the image of the specimen without heat treatment (Figure 1 a). This progressive increment in the proportion of pearlite shows that both the rice husk and the charcoal allowed the introduction of carbon (diffusion) into the steel specimen, showing an increment in the amount of carbon until certain distance from the surface (case depth). The case depth, as observed, was greater in the specimens that contained energizer material in its composition (Figures 1 c, e).

In this way, as stipulated in the literature [7] is contrasted with respect to the potentiating effect of the energizer in the increase of the diffusion rate of the carbon in heat treatment of pack carburizing. The results also showed that the carbon diffusion was more intense in the specimens that were heat treated with charcoal (Figures 1 b, c), the expected result, taking into account that the percentage of carbon in this, was higher by 43 % to the percentage present in the rice husk. In addition, it can be seen that in the specimens that were carburized with charcoal (MC1 and MC2) a greater percentage of carbon was obtained in this zone. Although, in the Figures 1 b, d, no uniform thickness of the diffused carbon was observed compared to Figures 1 c, e. It does not indicate that the carbon content did not increase at the surface of these specimens, it is sufficient to compare with Figure 1 a for a clearer view of the increase in the carbon contents of these specimens.

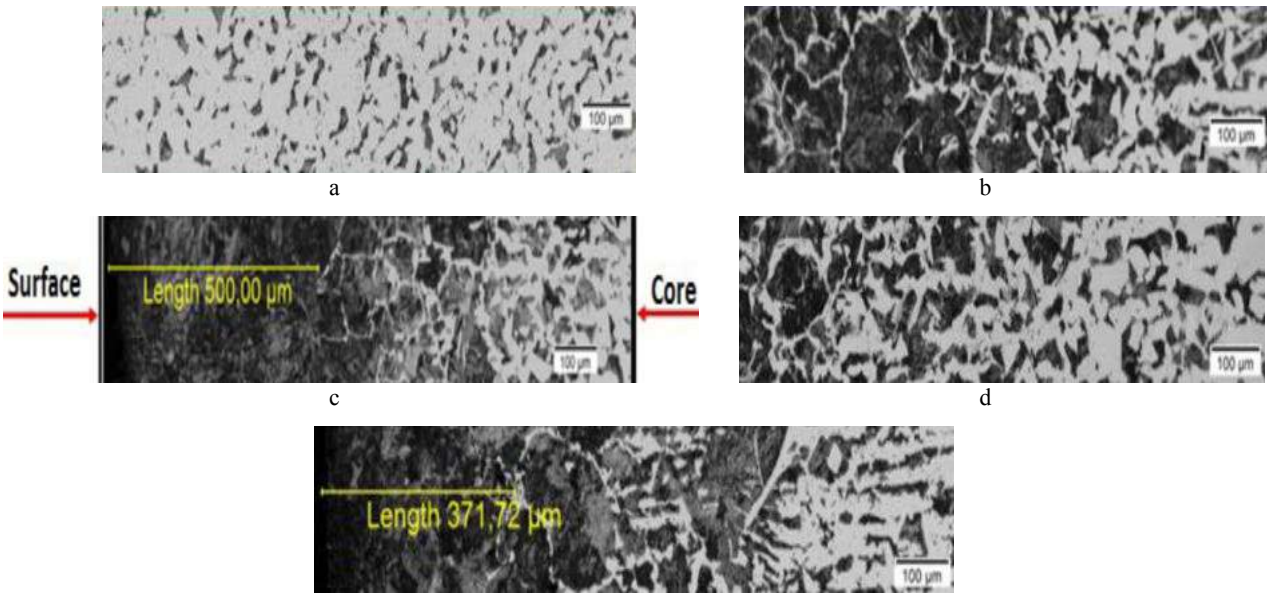

Figure 1 – Optical micrograph of AISI 8620 mild steel specimen: a – uncarburized base material; b – carburized specimen with MC1; c – carburized specimen with MC2; d – carburized specimen with MC3; e – carburized specimen with MC4

4.2 Core micro hardness

Figure 2 depicts the variations of micro hardness of the carburized steel at its case and core parts under the effects of carburizing temperatures and holding time.

From Figure 2 a, it can be clearly seen that for all the holding time (60, 90, and 120 minutes), the micro hardness of the case dropped between carburizing temperatures of 800 to 850 °C and increased between temperatures of 850-900 °C. This was as a result of the distortion produced in the atomic structure of the samples and the material's adjustment to accommodate the treatment induced on it; as such, the micro hardness of the case was expected to drop at the earlier stage of the carburizing operation and rise after the atomic adjustments of the material in order to accommodate the treatment. Sequel to that, the inducement of some carbon percentage which led to the observed increase in micro hardness of the sample affirmed the explained distortion and adjustment of the atomic structure of the sample.

Also, a decrease in the case hardness of the sample was observed at a holding time of 60 minutes between temperatures of 900-950 °C while a continuous rise in the hardness of the case occurred at holding time of 90mins and 120 minutes, with a peak value reached at 120mins and 950 °C. This was so because, high carburizing temperatures allows for high hardness values of samples. The material needs to be transformed completely to austenite owing to its great affinity for carbon. Such if achieved, causes a large amount of carbon percentage to be induced into the material and consequently leads to the actualization of higher hardness values of the material.

Figure 2 b revealed the effect of carburizing temperature and holding time on the core micro hardness of the samples. From Figure 2 b, it was observed that all the samples carburized at 800, 850, and 900 °C followed the same trend beginning from high hardness value at the core when soaked for 60 minutes (316 HV) and decreased at 90 minutes holding time (207 HV), but increases as the holding time is increased to 120 minutes (230 HV).

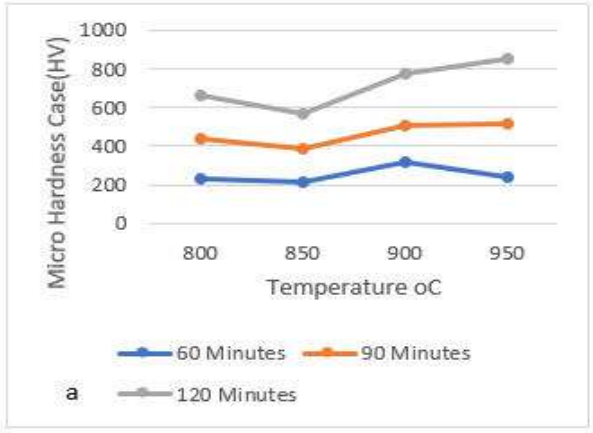

a

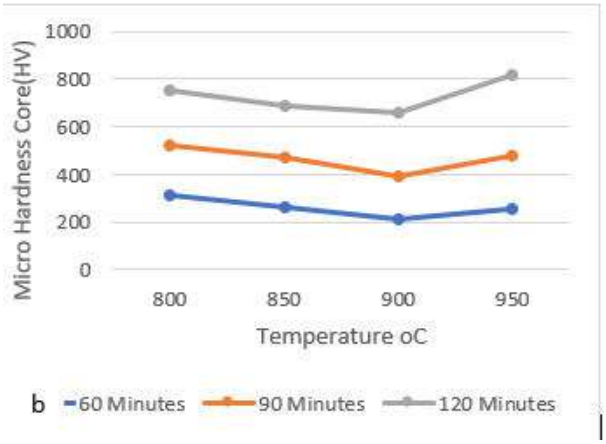

b

Figure 2 – Effect of carburizing temperatures and holding time on the case micro hardness (a) and the core micro hardness (b)

Thus, attaining the respective peak hardness values at 120 minutes holding time. The uniform fall in the values of micro hardness of the core for holding time of 60, 90, and 120 minutes could be attributed to the distortions and adjustments of large volumes of atoms present at the core

of the samples which required an increased condition of carburizing operations (temperature and holding time) before accommodating the treatments induced into it.

Sequel to that, owing to the large volume of the core, the transformation of the material completely to austenite would take longer time and treatment temperature compared to the case. Increased hardness of the core occurred after its continuous decrease to the temperature of 900 °C. Beyond 900 °C, a uniform rise of micro hardness of the core was observed because of the transformation to Austenite which has great affinity for carbon.

4.3 Ultimate tensile strength, engineering strain, and Young's modulus

Figure 3 shows the effects of carburizing temperature and holding time of the ultimate tensile strength and strain properties of AISI 8620 steel material.

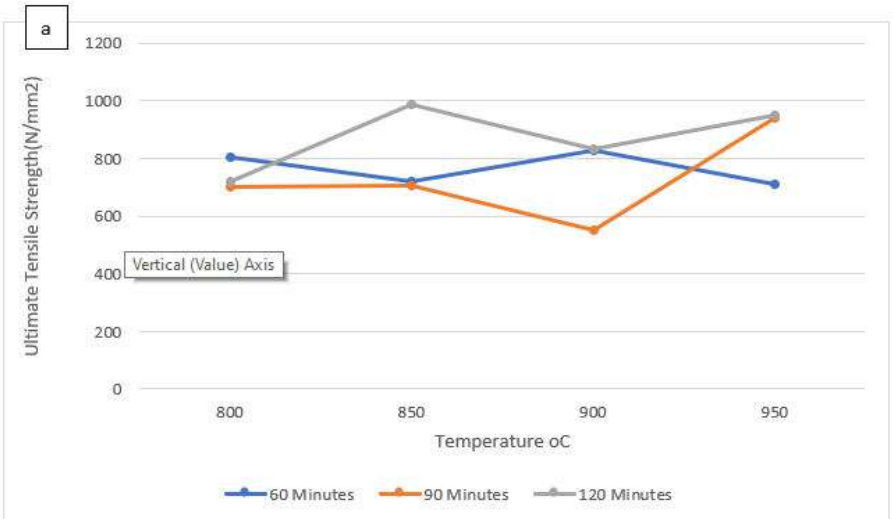

a

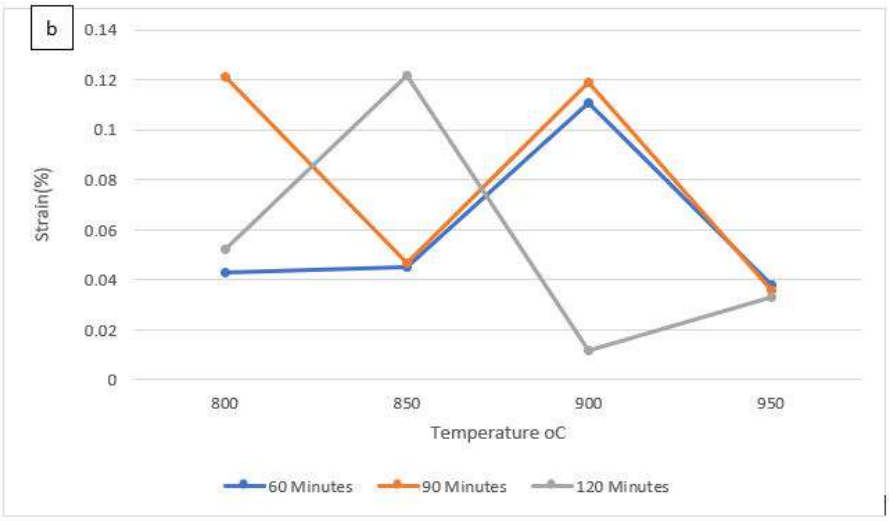

b

Figure 3 – Effect of carburizing temperatures and holding time on the ultimate tensile strength (a) and the engineering strain (b)

From Figure 3 a, the highest value of ultimate tensile strength was obtained at a carburizing temperature of 850 °C and holding time of 120 minutes. This was followed by carburizing conditions of 950 °C temperature and 90 minutes holding time. The lowest value of ultimate tensile strength was gotten at a carburizing temperature of 900 °C and holding time of 90 minutes. These observed characteristics of the material could be attributed to the distortion and rearrangement of the material's atoms during the carburization of operation.

In addition, Figure 3 b depicts the influence of carburizing temperature and holding time on the strain property of the steel specimen. From Figure 3 b, maximum strain values of the material were obtained at carburizing temperatures and holding time of: 800 °C for 90 minutes, 850 °C for 120 minutes, and 900 °C for 90 minutes.

These notable strain characteristics of the material delineate high ductility parameter of AISI 8620 steel at the stated carburization conditions. Moreso, the lowest strain values were obtained at carburizing temperatures and holding time of: 800 °C for 60 minutes, 850 °C for 90 minutes, and largely, 900 °C for 120 minutes. Therefore, the material has low ductility property at these carburization conditions.

Figure 4 depicts the effects of carburizing temperature and holding time on the impact strength and elastic modulus of AISI 8620 steel material respectively.

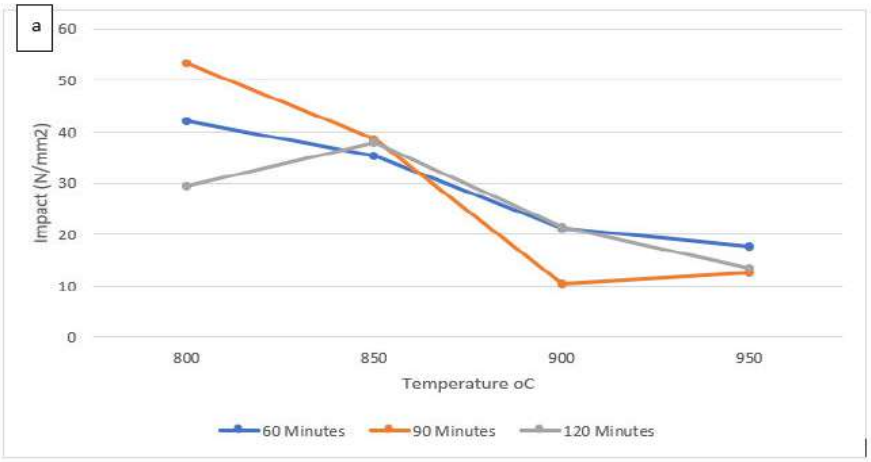

a

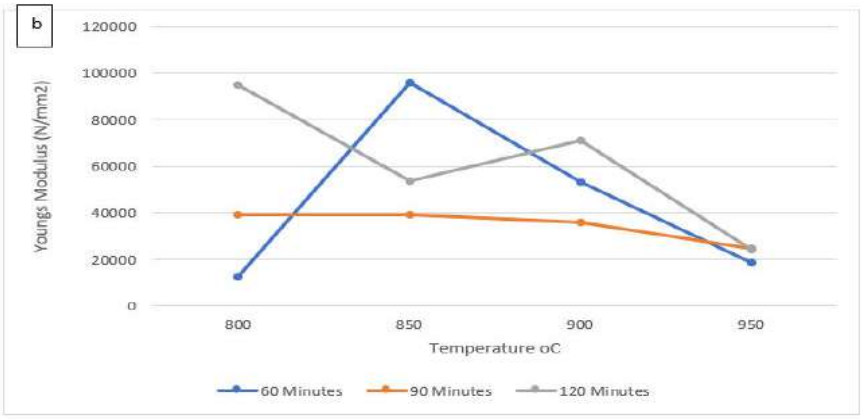

b

Figure 4 – Effect of carburizing temperatures and holding time on impact strength (a) and Young's modulus (b)

From Figure 4 a, the highest value of impact strength was obtained at a carburizing temperature of 800 °C and holding time of 90 minutes. Also, the lowest value was gotten at a temperature of 900 °C and holding time of 90 minutes.

In addition, Figure 4 b presents the lowest value of elastic modulus achieved at a carburizing temperature of 800 °C and holding time of 60 minutes. While higher values of elastic modulus were obtained at 800 and 850 °C carburizing temperatures for holding time of 120 and 60 minutes, respectively.

These bahavioural characteristics of the steel material could be explained through the study of iron-carbon phase diagram for the steel specification as reported by [8].

4.4 Optimization of the responses

The optimum operating temperature and holding time that would yield the best response values were obtained using numerical optimization technique.

Figure 5 shows the plot of desirability against temperature and holding time.

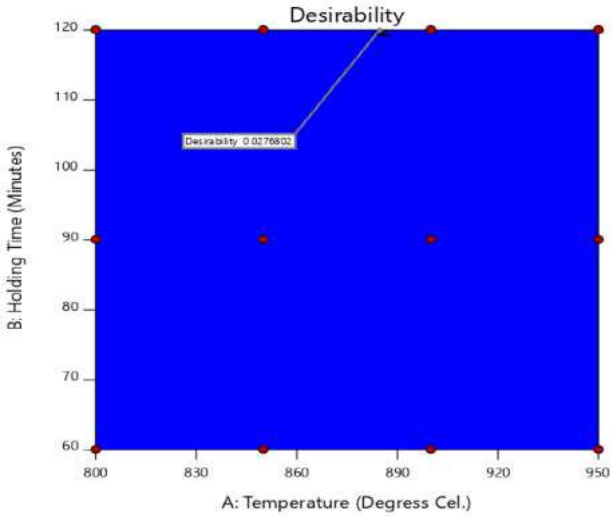

Figure 5 – Desirability for holding time against temperature

From Figure 5, the highest desirability value of 0.028 was obtained for factor combination of temperature at 885 °C and holding time of 120 minutes.

In addition, Figure 6 shows the contour plot of the response variable- ultimate tensile strength having the holding time plotted against the temperature.

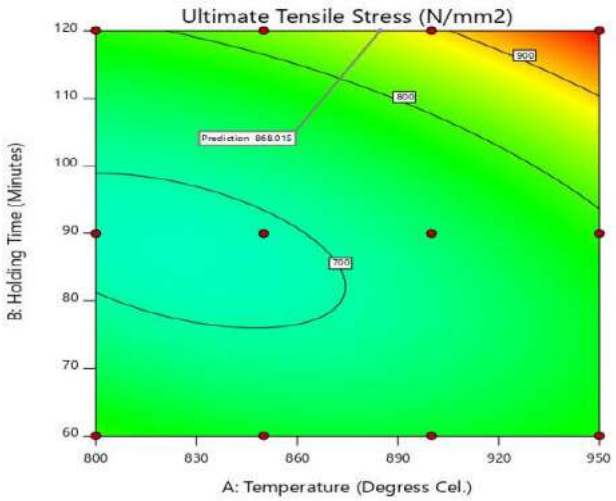

Figure 6 – Ultimate tensile strength for holding time against temperature

From Figure 6, it can be deduced that at the optimal factor combination of temperature 885 °C and holding time of 120 minutes, the predicted value of ultimate tensile strength of carburized AISI 8620 was 868 MPa.

This predicted value of ultimate tensile strength is well suited when matched with the other values observed from Figure 3 a.

Figure 7 shows the contour plot of the strain induced on the material at the optimal points of temperature and holding time, 885 °C and 120 minutes, respectively.

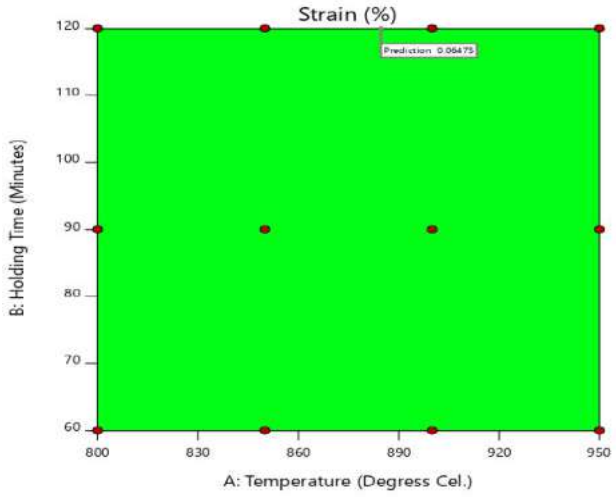

Figure 7 – Strain for holding time against temperature

From Figure 7, it can be inferred that the optimum holding time and temperature for strain minimization in carburized AISI 8620 were 120 minutes and 885 and 725 °C, respectively.

A strain value of about 0.06 % at these optimum factor combinations was predicted. An induced strain value of 0.06 % is good when compared with others shown in Figure 3 b.

Figure 8 shows the contour plot of Young's modulus for holding time and temperature.

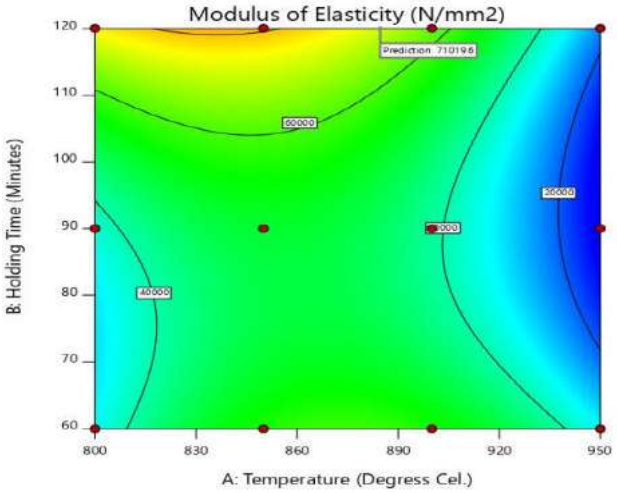

Figure 8 – Holding time against temperature

From Figure 8, it is evident that the optimum factor combination for a good yield of the response parameter- Young ' s modulus is at a temperature 885 °C and holding time of 120 minutes. A response prediction of $7.1 \cdot 10^4$ MPa was obtained at this optimum point or design point.

Figure 9 shows the contour plot of the response parameter, impact strength. It attests to the optimum factor combination of temperature 885 °C and holding time of 120 minutes. The impact strength at this design point was 24.1 J.

Figure 9 – Impact strength for holding time against temperature

Figure 10 shows the contour plots of the responses: micro hardness case and micro hardness core. From Figure 10 a, the optimum or design point for obtaining the best value of the response was at the factor combinatorial point of temperature 885 °C and holding time of 120 minutes. A predicted value of micro hardness case about 241.3 H was gotten at this design point.

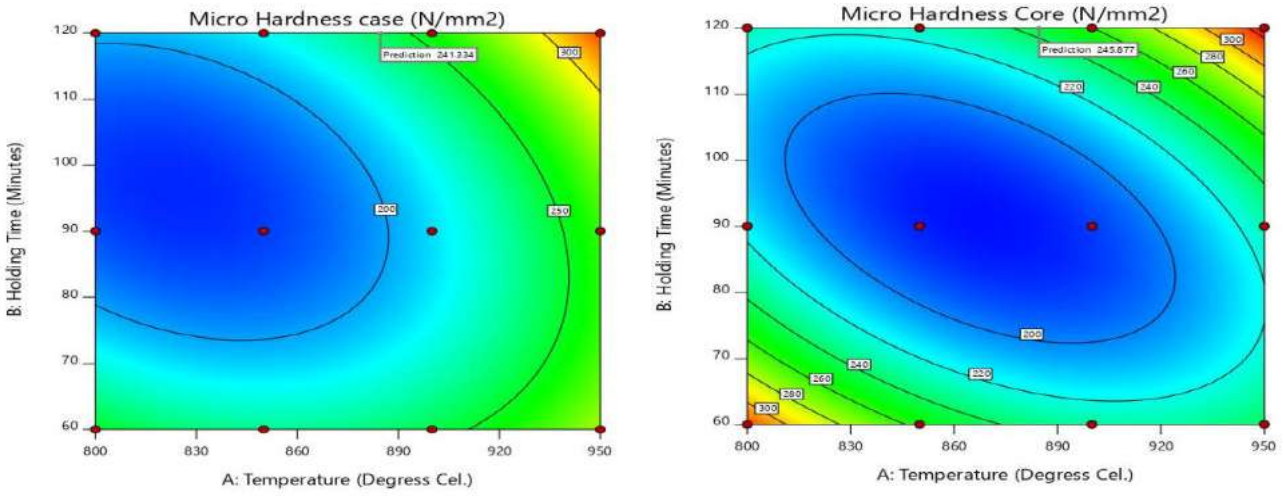

a b

Figure 10 – Micro hardness case (a) and core (b) for holding time against temperature

Furthermore, Figure 10 b gave the optimum value of micro hardness core of carburized AISI 8620 of 245.9 H at the optimal or design point. This value is well suited when compared with others as shown in Figure 2 b.

Therefore, at the gotten optimal factor combination, the overall best response characteristics was obtained. The summary of optimal factor combination for better response characteristics is shown in Table 4.

Table 4 – Summary of optimal factor combination (temperature of 885 °C and holding time of 120 minutes)

Response	Mean	Median	StdDev	SE Mean	95 % CI low	95 % CI high	95 % TI low	95 % TI high
Ultimate tensile stress	868.015	867.950	132.433	81.504	668.517	1067.38	56.1749	1679.73
Strain	0.06475	0.06475	0.04082	0.0118	0.03881	0.0907	–0.11945	0.24895
Modulus of elasticity	71019.6	71019.6	25147.9	15477.0	33148.8	108890	–83130.2	225169
Impact strength	24.1136	24.1136	7.52327	3.45442	16.2992	31.9281	–14.1004	62.3277
Micro hardness case	241.334	241.334	43.1072	26.5298	176.417	306.25	–22.9017	505.569
Micro hardness core	245.877	245.877	16.4321	10.1129	221.132	270.623	145.153	346.602

5 Conclusions

The mechanical properties of low carbon steel material are improved by carburization process through the influence of the carburizing factors- carburizing temperature, carburizers and holding time. More so, from this study, the three carburizers employed in the process in the ratio of 75 % wt. : 25 % wt. strongly influenced the mechanical properties of the low carbon steel material.

The optimum conditions for carburizing low carbon steel material (AISI 8620) for good response characteristics are: temperature of 885 °C and holding time of 120 minutes as obtained from the numerical optimization performed. In addition, the presence of carbon-enriched skin (austenite to martensite) in the test samples can be inferred from the microstructural change and the good increase in hardness in most of the samples.

References

1. Zbigniew, Z., Sisson, R. D. (2016). Development of nitrogen-hydrocarbon atmospheric carburizing and process control methods. *Journal of Materials Engineering and Performance*, Vol. 10(7), pp. 1-37.
2. Kenan, G., Mehmet, D. (2017). Effect of case depth on fatigue performance of AISI 8620 carburized steel. *International Journal of Fatigue*, Vol. 21, pp. 207-212.
3. Fuchs, H. O., Stephens, R. I. (2015). *Metal Fatigue in Engineering*, John Wiley, New York, USA, pp. 231-239.
4. Balusamy, T., Sankara Narayanan, T. S. N., Ravichandran, K., Song Park, I., Lee, M. H. (2013). Pack boronizing of AISI H11 tool steel: Role of surface mechanical attrition treatment. *Vacuum*, Vol. 97, pp. 36-43, doi: 10.1016/j.vacuum.2013.04.006.
5. Oluwafemi, O. M., Oke, S. R., Otunniyi, I. O., Aramide, F. O. (2015). Effect of carburizing temperature and time on mechanical properties of AISI/SAE 1020 steel using carbonized palm Kernel Shell. *Leonardo Electronic Journal of Practices and Technologies*, Vol. 14(27), pp. 41-56.
6. Istiroyah, M. A., Saroja, G., Ghufron, M., Juwono, A. M. (2017). Characteristics of low temperature carburized austenitic stainless steel. *International Conference on Chemistry and Material Science*, Vol. 299, 012048, doi: 10.1088/1757-s.
7. Siti, K. A., Bulan, A., Ahmed, J., Syazuan, A. L., Salmiah, K., Mohd, F. I., Muhd, M. A. (2013). Mechanical properties of paste carburized ASTM A516 steel. *The Malaysian International Tribology Conference 2013, MITC2013*, Vol. 68, pp. 525-530.
8. Aramide, F. O., Ibitoye, S. A., Oladede, I. O., Borode, J. O. (2009). Effects of carburization time and temperature on the mechanical properties of carburized mild steel, using activated carbon as carburizer. *Mat. Res.*, Vol. 12(4), pp. 483-487.
9. Li, W., Sun, Z., Zhang, Z., Deng, H., Sakai, T. (2015). Influence of case-carburizing and micro-defect on competing failure behaviors of Ni–Cr–W steel under gigacycle fatigue. *International Journal of Fatigue*, Vol. 72, pp. 66-74.
10. Hussein, N. (2017). Material Science and Engineering. *International Energy and Environment Foundation (IEEF)*, pp. 172-187.

JOURNAL OF ENGINEERING SCIENCES

Volume 9, Issue 2 (2022)

Verbovyi A., Khomenko V., Neamtu C., Pavlenko V., Simonovskiy V., Pavlenko I. (2022). Rotor dynamics of turbocompressor based on the finite element analysis and parameter identification approach. Journal of Engineering Sciences, Vol. 9(2), pp. D1-D5, doi: 10.21272/jes.2022.9(2).d1

Rotor Dynamics of Turbocompressor Based on the Finite Element Analysis and Parameter Identification Approach

Verbovyi A.[1][0000-0002-7805-4733], Khomenko V.[1], Neamtu C.[2][0000-0003-0899-0451], Pavlenko V.[3], Simonovskiy V.[1], Pavlenko I.[0000-0002-6136-1040]

[1] Sumy State University, 2, Rymskogo-Korsakova St., 40007 Sumy, Ukraine;
[2] Technical University of Cluj-Napoca, 28, Memorandumului St., 400114 Cluj-Napoca, Romania;
[3] Machine Building College of Sumy State University, 17, Shevchenko Ave., 40011 Sumy, Ukraine

Article info:
Submitted: September 5, 2022
Accepted for publication: November 23, 2022
Available online: November 29, 2022

***Corresponding email:**
a.verbovoy@omdm.sumdu.edu.ua

Abstract. The article is devoted to improving methods for designing a finite element model of rotor dynamics. For this purpose, numerical implementation of the authors' computer program "Critical frequencies of the rotor" was developed based on the computer algebra system MathCAD. As a result of the scientific work, a refined mathematical model of rotor dynamics using finite beam elements was created. This model considers the dependence of the radial stiffness characteristics of the bearing supports on the values of the critical frequencies. The reliability of the mathematical model was justified by the permissible differences of the obtained results within 2% compared with the results of finite element analysis using the ANSYS software. The theorem was also proven by the mutual location of the spectra of the natural and critical frequencies. Overall, the proposed scientific approach reduces preparation and machine time compared to numerical modeling using the ANSYS software without losing the accuracy of the calculations.

Keywords: centrifugal machine, process innovation, critical frequency, finite element analysis, Campbell diagram.

1 Introduction

Rotary machines belong to the largest class of power machines [1]. During the operational process, polyharmonic disturbances act on the rotor in the form of forces and moments of inertia of unbalanced masses. They cause forced oscillations of the rotor.

In most cases, the technical level of such machines is assessed by their vibroacoustic characteristics determined by the vibration state of the rotor [2]. Therefore, the rotordynamic problems are of significant practical importance, and the range of these tasks is predetermined by the number of constructive types of rotor machines, their features, and operating conditions.

Among rotary machines, high-pressure multistage centrifugal pumps and compressors are characterized by permanently increasing operating parameters (e.g., speed, pressure) that lead to a single unit's capacity.

The pressure in centrifugal machines is proportional to the square of the rotor speed. Therefore, an increase in the rotation speed turns out to be the most rational way of achieving high pressures. As a result, high-pressure centrifugal machines are usually high-speed. And for such machines, the rotordynamic problems are particularly relevant [3].

The reasons for the unsatisfactory vibration state of the rotor are imbalance and misalignment, force and temperature deformations of the housing and its individual elements, loss of dynamic stability, structural and technological defects, wear of gap seals, supports, drive couplings [4, 5].

Increased vibrations are accompanied by operations close to critical frequencies. The calculation of the latter cannot guarantee a reliable detuning from resonance due to the lack of reliable data on the stiffness of the supports and the impact of randomly variable factors [6].

Up-to-date trends in studying the dynamics of rotary systems are mainly based on computer programs that implement finite element analysis [7].

To solve such problems, 2D and 3D finite elements are used [8, 9].

Calculating rotor dynamics, e.g., using numerical modeling using the ANSYS software, is time-consuming. This is mainly due to the time for the preparation of initial data. It also requires a lot of machine time.

According to those mentioned above, the work aims to improve the vibration state of the rotor system by creating a reliable model for evaluating the dynamic state.

The main research objectives are as follows:

– development of a refined mathematical model of free and forced oscillations of the rotor considering the predetermined dependence of the stiffness of the supports on the frequency of rotation of the rotor;

– parameter identification of the coefficients for the dependence of the stiffness of the bearing supports;

– simulation of rotor dynamics for a multistage centrifugal compressor 225GC2-135/12-50M1245 using the program "Critical frequencies of the rotor" realized in the computer algebra system MathCAD;

– verification of the reliability of the finite element model in the ANSYS software;

Research methods include numerical simulation of free oscillations of the rotor using the finite element analysis and parameter identification approach comprehensively.

2 Research Methodology

2.1 Design scheme

The object of research is the free oscillations of a flexible rotor of a centrifugal compressor 225GC2-135/12-50M1245 (Figure 1). Its technical parameters are summarized in Table 1.

a

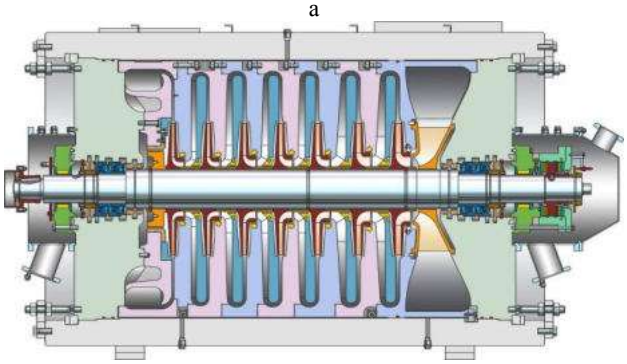

b

Figure 1 – General view (a) and cross-section (b) of the turbocompressor

Table 1 – Technical parameters

Parameter	Value
Normal performance, m^3/s	25.0
Inlet pressure, MPa	1.20
Outlet pressure, MPa	4.95
Polytropic efficiency, %	70.0
Rotor speed, rpm	8920
Nominal power, MW	7.33
Inlet gas temperature, °C	28.1

To further study rotor dynamics, it is necessary to create its calculation model. A beam finite element model was compiled using the authors' program "Critical frequencies of the rotor" [10] (Figure 2a).

Figure 2b presents 3D finite element model created in the ANSYS software.

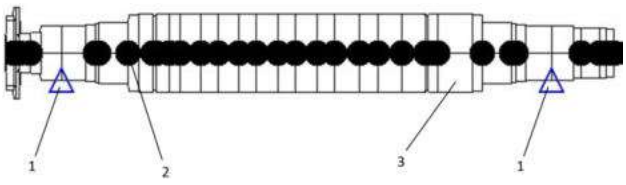

a

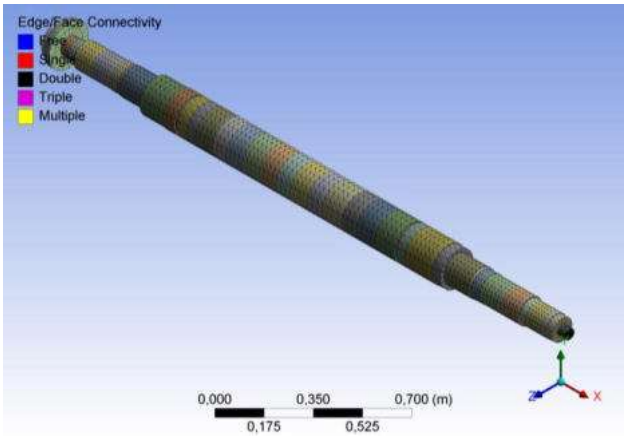

b

Figure 2 – Design models in MathCAD (a) and ANSYS (b): 1 – radial supports; 2 – local masses; 3 – finite elements

2.2 Program description

The program "Critical frequencies of the rotor" is based on the finite element method. It is intended to evaluate the critical and eigenfrequencies of radial oscillations of rotors. The calculation results in the value of critical frequencies and forms of oscillations.

The program was created using the computer algebra system MathCAD.

The input data required are density and Young's modulus of the material, lengths of sections, inner and outer diameters, added masses of mounting parts, and rigidity of bearing supports and gap seals.

The matrix equations of free oscillations of a rotating rotor can be presented in the following form:

$$\bar{M}\ddot{\bar{U}} + \bar{K}\bar{U} = 0, \quad (1)$$

where $\bar{U} = (x_1, \vartheta_1, x_2, \vartheta_2, \ldots, x_{n+1}, \vartheta_{n+1})$ – column-vector of deflections and angles of rotation for sections at the joints of finite elements.

Local matrices $\bar{K}_i$ and $\bar{M}_i$ by the dimension of 4×4 have a standard form according to the fundamentals of beam's oscillations [11, 12].

The formation of global matrices $\bar{K}$ and $\bar{M}$ by local matrices $\bar{K}_i$, $\bar{M}_i$ for $i = (1, n+1)$ is based on the algorithm, which uses the conditions of the junctions for all the sections [13].

The calculation of critical rotor frequencies is based on the numerical determination of the eigenvalues λ of the following equation:

$$det[\bar{K} - \lambda\bar{M}] = 0. \quad (2)$$

The program for calculating free oscillations consists of the following stages:

1) calculation of coefficients for stiffness and inertia matrices;

2) solving the frequency equation (2) and finding a given number of eigenfrequencies;

3) calculation of the mode shapes of free oscillations corresponding to their frequencies.

2.3 Mathematical model of bearing stiffness

In this work, it is proposed to approximate the dependence of the stiffness of the supports on the frequency of rotation of the rotor by the following analytical formula:

$$c(\omega) = c_0 + (c_{max} - c_0)(1 - e^{-k\omega}), \quad (3)$$

where c_0 – initial stiffness, N/m; c_{max} – maximum stiffness, N/m; ω – operating speed, rad/s; k – time parameter, s.

Such a model has the following advantages compared with the polynomial approximation. Firstly, instead of an infinite increase in stiffness, it asymptotically approaches its maximum value.

Secondly, when approaching this value, the stiffness gradient asymptotically approaches zero.

These facts are because parameter k has the following physical meaning:

$$\frac{dc(\omega)}{d\omega} = k[c_{max} - c(\omega)]. \quad (4)$$

According to the quasilinear parameter identification approach, the unknown parameter k in expression (1) can be evaluated by minimizing of the following least square error:

$$R(k) = \sum_{n=1}^{N}\left[k\omega_n - ln\left(\frac{c_{max} - c_0}{c_{max} - c_n}\right)\right]^2 \to min, \quad (5)$$

where n – a number of the experimental point; N – the total number of the experimental dataset; ω_n – n-th operating speed, rad/s; c_n – experimentally obtained stiffness, N/m.

The last condition is satisfied for values of k, at which the following derivative equals a zero value:

$$\frac{dR(k)}{dk} = 2\sum_{n=1}^{N}\left[k\omega_n - ln\left(\frac{c_{max} - c_0}{c_{max} - c_n}\right)\right]\omega_n = 0. \quad (6)$$

Finally, the following regression dependence can be obtained:

$$k = \frac{\sum_{n=1}^{N}\omega_n ln\left(\frac{c_{max} - c_0}{c_{max} - c_n}\right)}{\sum_{n=1}^{N}\omega_n^2}. \quad (7)$$

Thus, the determination of the unknown parameter k requires preliminary experimental determination of stiffnesses c_0 and c_{max}.

3 Results

3.1 MathCAD simulations

The calculation of eigenfrequencies involves calculating dangerous speeds during the rotor's constant rotation at its operating frequency. For the considered case study, such a frequency equals 934 rad/s.

The stiffness of the bearings was also assumed to be constant and equal to the stiffness at the operating speed ($c_p = 2.94 \cdot 10^8$ N/m).

Remarkably, critical frequencies are dangerous for the rotor during its acceleration to the operating mode. For their calculation, it is necessary to consider that the bearings have different stiffness at different rotation frequencies, which depends on the values of the natural frequencies of the rotor.

The program "Critical frequencies of the rotor" allows setting directly the dependence of the rigidity of the rotor supports on the frequency of its rotation.

Using the dataset of JSC "Sumy NPO" (Sumy, Ukraine), the following values were evaluated: $c_0 = 1.77 \cdot 10^8$ N/m and $c_{max} = 1.51 \cdot 10^9$ N/m.

Therefore, according to formula (7), the evaluated time parameter $k = 1.0 \cdot 10^{-4}$ s.

The program "Critical frequencies of the rotor" outputs the result in the form of natural frequency values and their corresponding forms. Figure 3 presents screenshots from the program with calculation results for the investigated rotor.

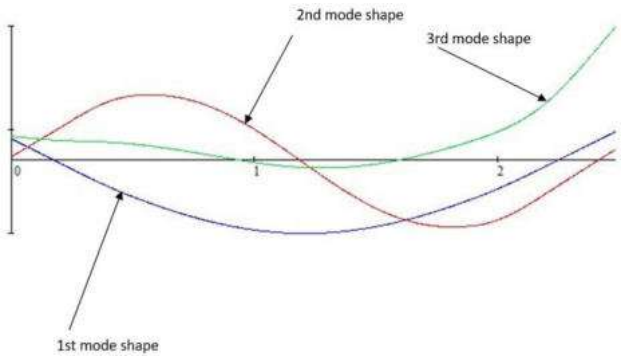

a

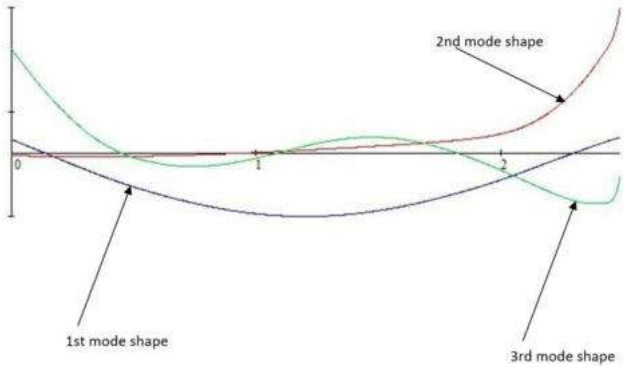

b

Figure 3 – Natural (a) and critical (b) frequencies of the rotor

3.2 ANSYS simulations

As a result of numerical simulations using the ANSYS software, Figure 4 presents mode shapes of free oscillations of the rotor at the corresponding frequencies.

Unfortunately, ANSYS does not allow directly evaluating the critical frequencies as is possible in the program "Critical frequencies of the rotor".

In general, the calculation of critical frequencies using the ANSYS software is like the calculation of eigenfrequencies. The only difference is that it is necessary to consider the property of bearings to change their stiffness depending on the rotation frequency non-linearly. However, the modal analysis ignores the initial model's nonlinearities [14].

During the simulations, the stiffness of the bearings was calculated in the range of rotation frequencies from 0 to 3000 rad/s with a step of 250 rad/s.

Then, changing the stiffness of the bearings in ANSYS, the eigenfrequencies of the rotor at the corresponding frequencies of its rotation were found as a Campbell diagram(Figure 5).

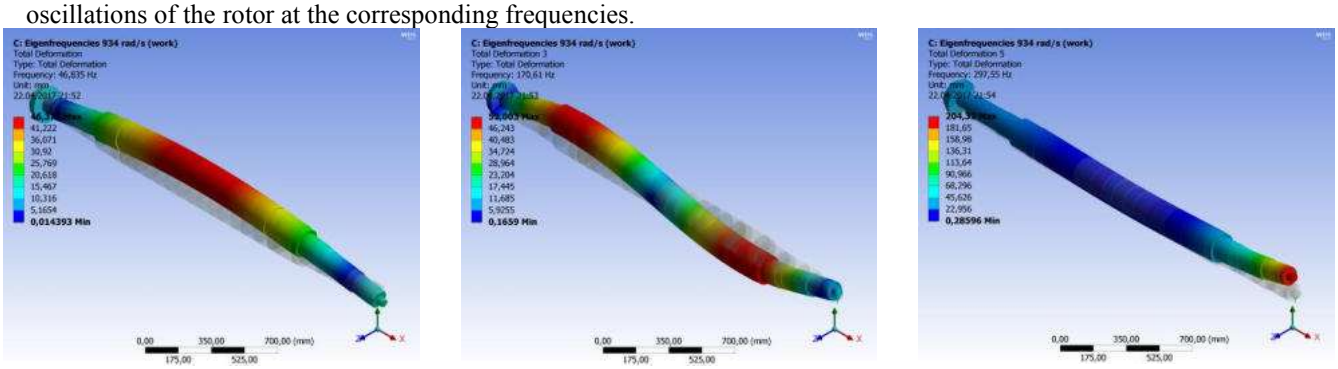

a b c

Figure 4 – 1st (a), 2nd (b), and 3rd (c) mode shapes of free oscillations of the rotor

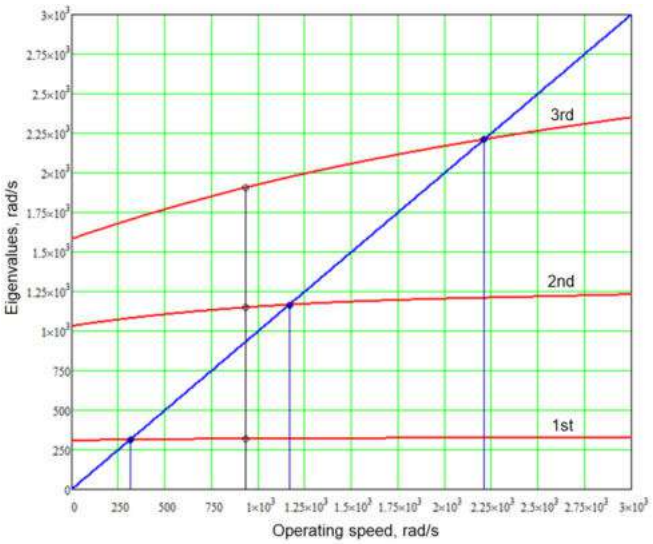

Figure 5 – Campbell diagram

The essence of Campbell's method for calculating the critical frequencies of the rotor is that the ordinates of the points of intersection of the bisector on the diagram drawn from the origin of the coordinates with the eigenfrequency curves are equal to the critical frequencies of the rotor.

Remarkably, the Campbell diagram serves as visual proof of the theorem on the mutual location of the spectra of critical and eigenfrequencies [15]. Particularly, critical frequencies below the operating speed are lower than the corresponding eigenfrequencies. Vice versa, critical frequencies above the operating speed are higher than the corresponding eigenfrequencies.

3.3 Comparison of the results

To confirm the reliability of the mathematical model of the rotor dynamics created in the program "Critical frequencies of the rotor", it is necessary to compare the results obtained in it with the data of numerical simulation in the ANSYS software. Such a comparison is presented in Table 3. It shows values of critical and eigenfrequencies evaluated by both the MathCAD and ANSYS software, as well as the percentage difference between the obtained results.

Table 2 – Comparison of the calculation results

No.	Natural frequencies, rad/s		Relative deviation, %	Критичні частоти, рад/с		Relative deviation, %
	ANSYS	MathCAD		ANSYS	MathCAD	
1	318.8	318	0.25	312.9	312	0.28
2	1125.0	1148	1.97	1140.0	1164	2.06
3	1867.0	1906	2.04	2150.0	2210	2.72

4 Conclusions

As a result of the work, a refined mathematical model of rotor dynamics using finite beam elements was created. This model considers the dependence of the rigidity of the radial supports of the rotor on the frequency of its rotation. The reliability of the mathematical model is confirmed by the permissible differences of the obtained results within 3%, as well as by the observance of the theorem on the mutual location of the spectra of natural and critical frequencies.

This indicates that using the working file "Critical frequencies of the rotor" of the computer algebra system MathCAD is more appropriate for solving similar problems. This is due to the possibility of directly considering (in an arbitrary analytical form) the dependence of bearing stiffnesses on the frequency of rotation of the rotor.

Additionally, the calculation using the proposed method reduces the preparation and machine time by order of magnitude compared to the numerical simulation in the ANSYS software without losing the accuracy of the calculations.

The obtained results can be further applied to study centrifugal machines' rotordynamic stability under fractional-order internal friction.

5 Acknowledgment

The research was carried out at the Research and Educational Center for Industrial Engineering within the R&D project "Fulfillment of tasks of the perspective plan of development of a scientific direction "Technical sciences" Sumy State University" by the Ministry of Education and Science of Ukraine (State reg. no. 0121U112684).

References

1. Gupta, B., Hoshi, T., Yoshizawa, H. (2022). High durability variable geometry turbine for commercial vehicle turbochargers. *Journal of Physics: Conference Series*, Vol. 2217(1), 012080. DOI: 10.1088/1742-6596/2217/1/012080
2. Chen, X., Koppe, B., Lange, M., Chu, W., Mailach, R. (2021). Rotating instabilities in a low-speed single compressor rotor row with varying blade tip clearance. *Energies*, Vol. 14(24). DOI: 10.3390/en14248369
3. Lee, T.-W., Hong, D.-K. (2022). Rotor design, analysis and experimental validation of a high-speed permanent magnet synchronous motor for electric turbocharger. *IEEE Access*, Vol. 10, pp. 21955-21969. DOI: 10.1109/ACCESS.2022.3152525
4. Aihara, A., Mendoza, V., Goude, A., Bernhoff, H. (2022). Comparison of three-dimensional numerical methods for modeling of strut effect on the performance of a vertical axis wind turbine. *Energies*, Vol. 15(7). DOI: 10.3390/en15072361
5. Michel, N., Wei, P., Kong, Z., Sinha, A. K., Lin, X. (2022). Modeling and validation of electric multirotor unmanned aerial vehicle system energy dynamics. *ETransportation*, Vol. 12, 100173. DOI: 10.1016/j.etran.2022.100173
6. Jia, Z., Yang, Y., Zheng, Q., Deng, W. (2022). Dynamic analysis of jeffcott rotor under uncertainty based on chebyshev convex method. *Mechanical Systems and Signal Processing*, Vol. 167, 108603. DOI: 10.1016/j.ymssp.2021.108603
7. Li, C., Guo, X., Fu, J., Fu, W., Liu, Y., Chen, H., Wang, R, Li, Z. (2022). Design and analysis of a novel double-stator double-rotor motor drive system for in-wheel direct drive of electric vehicles. *Machines*, Vol. 10(1), 27. DOI: 10.3390/machines10010027
8. Dau, A.-T., Nistor, I., Gavrus, A. (2014). Numerical analysis concerning the harmfulness of crack turbine rotors using a multi-scale approach based on a dynamic finite element method. *Applied Mechanics and Materials*, Vol. 656, pp. 315-324. DOI: 10.4028/www.scientific.net/AMM.656.315
9. Pei, D., Lian, T. (2013). Study on some nonlinear dynamics problems of rotor-sliding bearing system with impact-rubbing. *Information Technology Journal*, Vol. 12(17), pp. 4089-4094. DOI: 10.3923/itj.2013.4089.4094
10. Pavlenko, I., Simonovskyi, V. (2015). Computer program "Critical frequencies of the rotor". Certificate of authorship No. 59855, Ukraine.
11. Pavlenko, I. (2007). *Finite Element Method in Problems of Oscillations of Mechanical Systems*. Sumy State University, Sumy, Ukraine.
12. Champ, C. A., Stefani, F. A., Silvestri, P., Massardo, A. F. (2022). Hysteresis and torsional-lateral vibration coupling in a complex shaft line supported by hydrodyanamic journal bearings. *Mechanical Systems and Signal Processing*, Vol. 181, 109505. DOI: 10.1016/j.ymssp.2022.109505
13. Kumar, A., Kumar, D., Masal, R. (2021). Coupling misalignment detection and condition monitoring of a rotor assembly using FEA-based reduced-order modeling methods. *6th National Symposium on Rotor Dynamics, NSRD 2019. Springer. Lecture Notes in Mechanical Engineering*, pp. 445-458. DOI: 10.1007/978-981-15-5701-9_36
14. Simonovskyi, V. (2012). *Theory of Linear Oscillations*. Sumy State University, Sumy, Ukraine.
15. Phuor, T., Yoon, G. (2022). Model order reduction for Campbell diagram analysis of shaft-disc-blade system in 3D finite elements. *Structural Engineering and Mechanics*, Vol. 81(4), pp. 411-428. DOI: 10.12989/sem.2022.81.4.411

JOURNAL OF ENGINEERING SCIENCES

Volume 9, Issue 2 (2022)

Mbah O. M., Madueke C. I., Umunakwe R., Agba M. N. (2022). Extreme gradient boosting: A machine learning technique for daily global solar radiation forecasting on tilted surfaces. Journal of Engineering Sciences, Vol. 9(2), pp. E1-E6, doi: 10.21272/jes.2022.9(2).e1

Extreme Gradient Boosting: A Machine Learning Technique for Daily Global Solar Radiation Forecasting on Tilted Surfaces

Mbah O. M.[1*], Madueke C. I.[2], Umunakwe R.[2], Agba M. N.[3]

[1] Department of Mechanical Engineering, Federal University Oye-Ekiti, Ikole, City, 370105, Ekiti-State, Nigeria;
[2] Department of Material and Metallurgical Engineering, Federal University Oye-Ekiti, Street, Ikole, 370105, Ekiti -State, Nigeria;
[3] Department of System Engineering, University of Lagos, Street, Akoka, 100213, Lagos State, Nigeria

Article info:
Submitted: August 13, 2022
Accepted for publication: October 27, 2022
Available online: November 2, 2022

***Corresponding email:**
oguejiofor.mbah@fuoye.edu.ng

Abstract. Enhancing solar irradiance and accurate forecasting is required for improved performance of photovoltaic and solar thermal systems. In this study, Extreme Gradient Boosting (XGBoost) model was developed using three input parameters (time, day number, and horizontal solar radiation) and was utilized to forecast daily global solar radiation on tilted surfaces. The proposed model was built using XGBRegressor with five generations, 100 n estimators, and a learning rate of 0.1. Three statistical metrics, such as the coefficient of determination (R^2), root mean square error (RMSE), and mean absolute error (MAE), were used to compare the model's results to observed solar radiation data from the Nation Centre for Energy, Research and Development, University of Nigeria, Nsukka. The results showed improved prediction accuracy and XGBoost capability to estimate daily global solar radiation on tilted surfaces. In the training section, the proposed model had a statistical performance of $R^2 = 0.9977$, RMSE = 1.6988, and MAE = 1.081, and in the testing section, $R^2 = 0.9934$, RMSE = 2.8558, and MAE = 2.033. XGBoost model demonstrated a better performance when compared with other models in the literature. As a result, the proposed model provides an effective approach for estimating solar radiation.

Keywords: machine learning model, extreme gradient boosting, solar radiation prediction.

1 Introduction

Electromagnetic radiation from the sun is referred to as solar radiation. Captured solar radiation can be transformed into electricity or heat energy, which can be utilized to heat thermal systems and power homes. When designing, installing, and forecasting a solar conversion system's energy output, knowing a particular location's solar irradiance is extremely important for maximum performance. Solar systems are installed on tilted surfaces to maximize their exposure to direct sunlight, which increases their efficiency. Most solar radiation measuring instruments take measurements on horizontal surfaces rather than tilted surfaces. As a result, many techniques for estimating global solar radiation on tilted surfaces, such as empirical models [1, 2], satellite-derived models [3] and stochastic models [4] were developed. Empirical models are dependent on sunshine duration, the amount of cloud cover, and the maximum and minimum temperatures [5, 6]. However, problems arise when there is a dearth of or limited sunshine data and maximum and minimum temperatures. Besides that, both the satellite and stochastic models have drawbacks in terms of cost and behavioral characteristics. As a result, these techniques are unstable when used for solar irradiance forecasting and produce approximations. They are also ineffective when the database contains null or missing data. However, the advent of machine learning appears promising in overcoming these obstacles.

2 Literature Review

In Nigeria, empirical models have been used in predicting solar radiation [7, 8]. Chabane et al. [9] developed a model for daily solar radiation estimation in Biskra, Algeria, based on wavelength optical depth. Similarly, a mathematical model was developed by Herath et al. [10] for predicting solar radiation using multiple linear regression analysis. Sunshine hours, humidity, pressure, temperature, radiation, sunset time, date, wind direction, and time served as the model's input parameters. An Artificial Neural Network (ANN) was

used to evaluate the model's performance, and the correlation coefficient was 0.5973. Shourehdeli et al. [11] assessed injector fuel efficiency in basic mode utilizing four conventional models of isentropic coefficients.

Machine learning approaches have been broadly utilized in estimating global solar radiation in many regions. For example, Olatomiwa et al. [12] utilized an adaptive network-based fuzzy inference system (ANFIS) to forecast solar irradiance in Nigeria. The ANFIS model produced a correlation coefficient of 0.6567. Similarly, Hacioğlu and Rifat [13] devised a model for estimating solar radiation based on humidity, pressure, temperature, and wind speed. Both linear and gaussian regression models were used to assess the model's performance. Also, the Support Vector Machine Regression (SVM-R) algorithm has been employed in predicting global solar radiation [14, 15, 16, 17]. Similarly, the ANN technique has been utilized in predicting daily global solar radiation and other observed data [18, 19, 20, 21]. Marzo et al. [22] created an ANN model for estimating daily solar radiation utilizing three input parameters: extraterrestrial radiation, daily maximum, and minimum temperature. Data on solar radiation was used to validate the model. The average relative root mean square derivation (RRMSD) produced by ANN was 0.13, and its correlation coefficient was 0.8.

Furthermore, various researchers have used hybrid machine-learning models to predict global solar radiation. Torabi et al. [23] developed a Cluster-Based Approach that uses support vector machine and artificial neural networks (CBA-SVM-ANN) to estimate the horizontal surface's daily solar radiation. The findings showed that the independent models outperformed the hybrid model (CBA-SVM-ANN) based on the mean absolute percentage inaccuracy. Likewise, three hybrid models (gradient-boosted regression, random forest, and support vector machine) were used by Gala et al. [24] to forecast global solar radiation. The outcomes demonstrate how well the hybrid model works. Achour et al. [25] used the hybrid model to estimate monthly mean global solar radiation in Southern Algeria. Comparative performance of three machine learning models (SVM, ANN, and ANFIS) was done by Quej et al. [26] in estimating daily horizontal surface solar radiation in Mexico. From the results, the support vector machine performed better. A power coefficient equation was proposed by Augbulut et al. [27] in Turkey for predicting system power output and validated the proposed model using four machine learning approaches (Deep Learning, SVM, Kernel and Nearest-Neighbor, and ANN).

Furthermore, four Turkish districts used four machine-learning algorithms to forecast daily solar radiation using six input parameters [28]. The results showed that ANN outperformed the other models. Rabehi et al. [29] created a hybrid model for predicting global solar radiation in Southern Algeria that combines a multilinear-layer perceptron, a boosted decision tree, and linear regression (MLP-BDT-LR). The model's performance was evaluated using the Applied Research Unit for Renewable Energies data. Mbah et al. [30] compared two machine learning techniques (K-nearest neighbor and extreme gradient boosting) to four sky models (Tian, Koronakis, Badescu, Liu, and Jordan) for estimating daily global solar radiation on a tilted surface. According to the results, extreme gradient boosting outperformed other models. Similarly, Feng et al. [31] compared four machine-learning models and four empirical models for predicting daily global solar radiation in China. The MEA-ANN model generally outperformed the other four machine learning models with a correlative coefficient of 0.779, while the fan model outperformed the other four empirical models with a correlative value of 0.733.

This research aims to investigate the applicability of Extreme Gradient Boosting (XGBboost) in forecasting global solar radiation in Nigeria. This inquiry was inspired by the importance of reliable solar radiation data in Engineering, Agriculture, Ecology, and Hydrological investigations.

3 Research Methodology

3.1 Site and measurement

The proposed supervised machine learning model was developed using a daily global solar radiation dataset measured at the Energy Centre from 2016 to 2017, located inside the University of Nigeria, Nsukka. The model's three input parameters were time, day number, and horizontal solar radiation. Solar radiation data was measured using two solarimeters. The first solarimeter measures hourly horizontal solar radiation, while the second measures solar radiation at 15° inclinations toward the south. Time was measured in ten-minute incremental steps using a smartwatch. The proposed model was developed in Python using XGBRegressor with five generations, 100 estimators, and a learning rate of 0.1. The measured solar radiation dataset was split into two sets for training and testing the model. 70% of the dataset was used for sample training, with the remaining 30% used for model testing.

3.2 Machine learning models

Machine learning models are generated by algorithms that try to find the relationship between feature and target variables to detect patterns and make decisions based on previously unseen datasets. The proposed machine learning model is described below.

The Extreme Gradient Boosting algorithm is a supervised machine learning algorithm that forecasts a target output using train data with various features. It applies to both classification and regression problems. The XGBoost model's regularized objective is given by

$$Obj^{(t)} = \sum_{i=1}^{n} l\left(y_i, y_i^{\Lambda(t-1)} + f_t(X_i)\right) + \Omega(f_t) \quad (1)$$

where Ω – a regularized term used to avoid overfitting; l – loss function between the actual and estimated value; f_t – tree output; X_i – training dataset; Y_i – predicted dataset.

The second-order Taylor expansion of the loss function is expressed as follows:

$$Obj^{(t)} = \sum_{i=1}^{n} l\,(y_i, y_i^{\Lambda(t-1)}) + g_i f_t(X_i) + \frac{1}{2} h_i f_t^2(X_i) + \Omega(f_t) \quad (2)$$

where g_i, h_i – the loss function's first and second derivatives, respectively.

3.3 Evaluation of model performance

The XGBoost model's performance was evaluated using the statistical indicators listed below.

The coefficient of determination is a measure that assesses the ability of a model to predict an outcome in linear regression. The coefficient of determination is given as

$$R^2 = \frac{\sum_{i=1}^{n}[(H_{mi}-\overline{H_{mi}}).(H_{pi}-\overline{H_{pi}})]^2}{\sum_{i=1}^{n}(H_{mi}-\overline{H_{mi}})^2 . \sum_{i=1}^{n}(H_{pi}-\overline{H_{pi}})^2}. \quad (3)$$

Also, MAE is determined as:

$$MAE = \frac{1}{n}\sum_{i=1}^{n}\left(\frac{H_{pi}-H_{mi}}{n}\right). \quad (4)$$

The mean absolute error is the sum of all differences between the observed and measured values. It is employed in the evaluation of regression models.

Root mean square error, which is frequently used for regression analysis, informs how concentrated the data points are around the best fit line:

$$RMSE = \sqrt{\frac{1}{n}\sum_{i=1}^{n}(H_{pi} - H_{mi})^2}, \quad (5)$$

where n – sample size; H_{mi} – actual value; H_{pi} – estimated value.

4 Results and Discussion

4.1 Statistical parameters of the dataset

The XGBoost model was developed in this study using three input parameters: time, day number, and horizontal surface hourly solar irradiance. Table 1 lists the statistical parameters for the dataset used in this study.

Table 1 – Statistical parameters of the dataset

Process	R^2	RMSE	MAE
Training	0.9977	1.6988	1.081
Testing	0.9934	2.8558	2.033

4.2 XGboost model analysis

Figure 1 depicts the solar radiation training dataset and predicted values using the XGBoost model, while Figure 2 portrays the testing dataset and the predicted values.

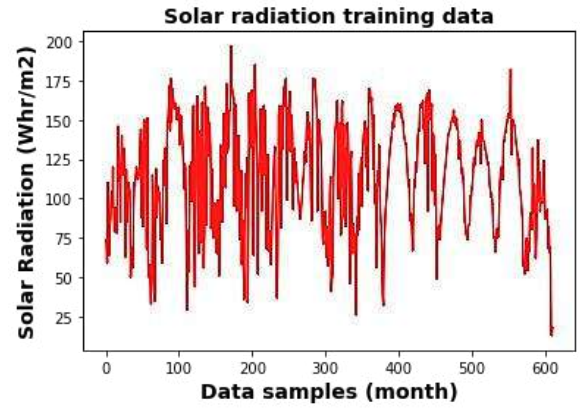

a

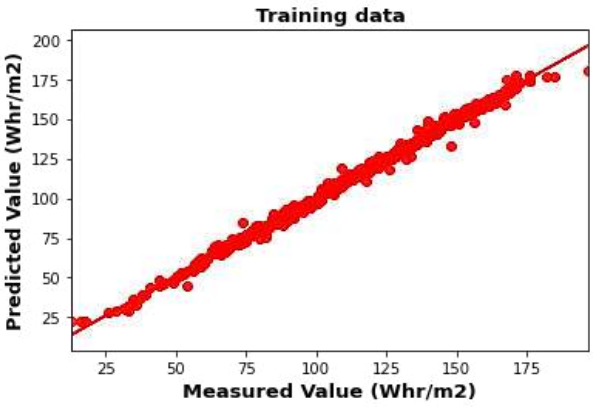

b

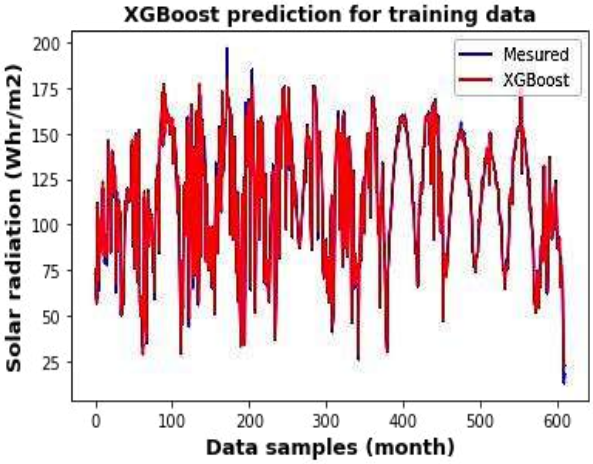

c

Figure 1 –Samples of training data (a), scatter plots of training data and predicted values using XGBoost model (b), and forecasting solar radiation using XGBoost model (c)

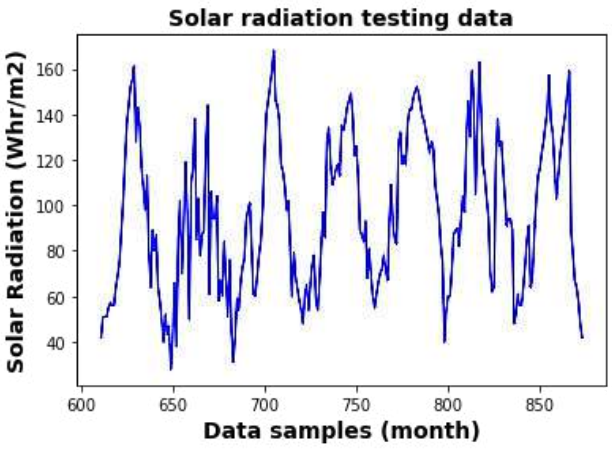

a

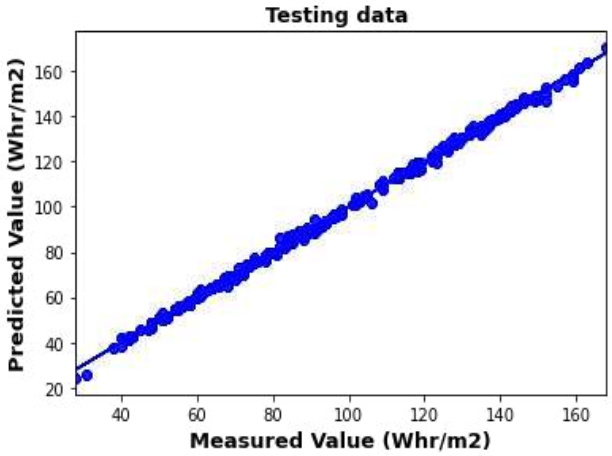

b

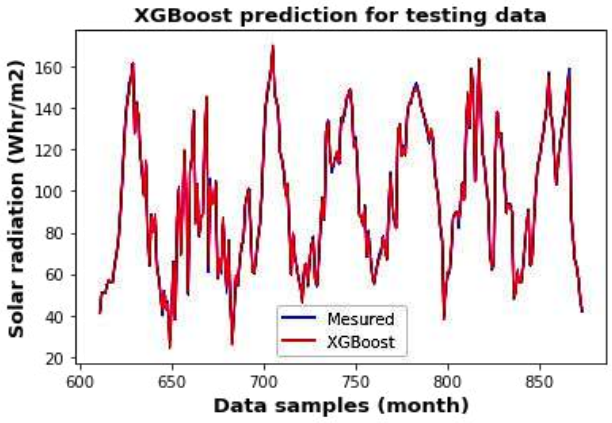

c

Figure 2 – Samples of testing data (a), scatter plots of testing data and predicted values using XGBoost model (b), and forecasting solar radiation using XGBoost model (c)

Figures 1b and 2b depict the relationship between the developed model and observed solar radiation data on the tilted surface during sample training and testing with scattered plots.

While also providing a more tightly compacted set of data points between the proposed model and the observed solar radiation data, both figures demonstrated a very high similar positive linear correlation. As a result, the XGBoost model has a high coefficient of determination for both training and testing data.

The XGBoost model's performance in estimating global solar radiation on a tilted surface was assessed using statistical measures such as coefficient of determination, root mean square error, and mean absolute error.

Table 2 summarizes the XGBoost model's prediction accuracy.

Table 2 – Statistical performance of the XGBoost model

Variable	Min	Max	Mean	Standard deviation
Time	9.16	15.90	12.55	2.01
Day number	20	411	359.14	29.18
Solar radiation on a horizontal surface	12	160	94.80	30.28
Solar radiation on a tilted surface	13	197	108.71	35.43

4.3 Model validation

A correlation between the proposed model and nine other solar radiation prediction models previously proposed by various authors [9, 10, 12, 14, 21, 22, 29, 31] validates XGBoost precision and accuracy in forecasting solar radiation.

As shown in Table 3, a statistical indicator of coefficient of determination was used to compare the proposed model prediction accuracy with other developed models in literature in order to evaluate its performance.

Table 3 – Comparison between the XGBoost model and existing models from the literature

Reference	Model type	Inputs	Country	R^2
Chabane et al. [9]	Empirical	3	Algeria	0.757
Feng et al. [30]	Empirical	1	China	0.733
Herath et al. [10]	Empirical	10	Sri Lanka	0.597
Guermoui et al [14]	SVM-R	1	Algeria	0.974
Olatomiwa et al. [12]	ANFIS	3	Nigeria	0.657
Rahimikhoob [21]	ANN	3	Iran	0.889
Marzo et al. [22]	ANN	3	Chile, Israel, Australia	0.800
Rabehi et al. [29]	Hybrid	4	Algeria	0.977
Feng et al. [30]	Hybrid	1	China	0.779
Present study	XGBoost	3	Nigeria	0.993

Table 3 shows that the XGBoost model has the highest coefficient of determination of the nine models tested. As a result, the proposed model outperforms the benchmark models (empirical, other machine learning, and hybrid models).

5. Conclusion

The importance of accurate solar radiation data in engineering, geography, crop production, and ecological studies cannot be overstated. This study developed an Extreme gradient boosting (XGBoost) model for estimating global solar radiation on tilted surfaces using three input parameters (time, day number, and horizontal solar radiation). The following findings are based on the proposed model's performance evaluation.

The analysis revealed that the XGBoost model predicts global solar radiation on tilted surfaces with high precision and accuracy, as evidenced by the statistical performance metrics obtained during the model testing; R^2, RMSE, and MAE values of 0.9934, 2.8558, and 2.033, respectively.

The proposed model shows significant prediction improvement compared to the literature's reference models (empirical, other machine learning, and hybrid models).

The proposed model can be deployed into a web application browser to predict solar irradiance on tilted surfaces because it is highly efficient and capable of handling various input parameters.

References

1. Halawa, E., Ghaffarian Hoseini, A., Li, D. H. W. (2014). Empirical correlations as a means for estimating monthly average daily global radiation: a critical overview. *Renewable Energy*, Vol. 72, pp. 149-153.
2. Besharat, F., Dehghan, A. A., Faghih, A. R. (2013). Empirical models for estimating global solar radiation: A review and case study. *Renewable and Sustainable Energy Reviews*, Vol. 21, pp. 798-821.
3. Pinker, R. T., Frouin, R., Li, Z. (1995). A review of satellite methods to derive surface shortwave irradiance. *Remote Sensing of Environment*, Vol. 51, pp. 108-124.
4. Hansen, J. W. (1999). Stochastic daily solar irradiance for biological modeling applications. *Agricultural and Forest Meteorology*, Vol. 94, pp. 53-63.
5. Chen, J.-L., Li, G.-S. (2013). Estimation of monthly average daily solar radiation from measured meteorological data in Yangtze River Basin in China. *International Journal of Climatology*, Vol. 33, pp. 487-498.
6. Wu, G., Liu, Y., Wang, T. (2007). Methods and strategy for modeling daily global solar radiation with measured meteorological data – A case study in Nanchang station, China. *Energy Conversion and Management*, Vol. 48, pp. 2447-2452.
7. Mbah, O. M., Mgbemene, C. A., Enibe, S. O., Ozor, P. A., Mbohwa, C. (2018). Comparison of experimental data and isotropic sky models for global solar radiation estimation in Eastern Nigeria. *World Congr. Eng.*, Vol. 2, pp. 4-8.
8. Mbah, O. M., Ozor, P., Mgbemene, C., Enibe, S. O., Mbohwa, C. (2018). Comparative analysis of anisotropic sky models and experimental data in estimating solar radiation on tilted surface in Sub-Saharan African climate. *IEOM Conference. IEOM 2018*, 2018.
9. Chabane, F., Arif, A., Moummi, N., Brima, A. (2020). Prediction of Solar Radiation According to Aerosol Optical Depth. *Iranian (Iranica) Journal of Energy & Environment*, Vol. 11, pp. 271-276.
10. Herath, H., Ariyathunge, S., Karunasena, G. (2021). Development of a Mathematical Model to Forecast Solar Radiation and Validating Results Using Machine Learning Technique. *European PMC, Research Square*, https://doi.org/ 10.21203/rs.3.rs-669429/v1
11. Shourehdeli, S. A., Mobini, K., Asakereh, A. (2022). Modeling of Isentropic Coefficients Used in One Dimensional Model to Predict Ejector Performance at Critical Mode. *Iranian (Iranica) Journal of Energy & Environment*, Vol. 13, pp. 111-123.
12. Olatomiwa, L., Mekhilef, S., Shamshirband, S., Petković, D. (2015). Adaptive neuro-fuzzy approach for solar radiation prediction in Nigeria. *Renewable and Sustainable Energy Reviews*, Vol. 51, pp. 1784-1791.
13. Hacioğlu, R. (2017). Prediction of solar radiation based on machine learning methods. *The Journal of Cognitive Systems*, Vol. 2, pp. 16-20.
14. Guermoui, M., Rabehi, A., Gairaa K., Benkaciali, S. (2018). Support vector regression methodology for estimating global solar radiation in Algeria. *The European Physical Journal Plus*, Vol. 133, pp. 1-9.
15. Chen, J.-L., Li, G.-S. (2014). Evaluation of support vector machine for estimation of solar radiation from measured meteorological variables. *Theoretical and Applied Climatology*, Vol. 115, pp. 627-638.
16. Chen, J.-L., Li, G.-S., Wu, S.-J. (2013). Assessing the potential of support vector machine for estimating daily solar radiation using sunshine duration. *Energy Conversion and Management*, Vol. 75, pp. 311-318, 2013.
17. Chen, J.-L., Liu, H.-B., Wu, W., Xie, D.-T. (2011). Estimation of monthly solar radiation from measured temperatures using support vector machines – A case study. *Renewable Energy*, Vol. 36, pp. 413-420.
18. Benmouiza, K., Cheknane, A. (2013). Forecasting hourly global solar radiation using hybrid k-means and nonlinear autoregressive neural network models. *Energy Conversion and Management*, Vol. 75, pp. 561-569.
19. Motameni, H. (2020). Determining the composition functions of Persian non-standard sentences in terminology using a deep learning fuzzy neural network model. *International Journal of Engineering*, Vol. 33, pp. 2471-2481.

20. Mahdavi Jafari, M., Khayati, G. R., Hosseini, M., Danesh-Manesh, H. (2017). Modeling and optimization of roll-bonding parameters for bond strength of Ti/Cu/Ti clad composites by artificial neural networks and genetic algorithm. *International Journal of Engineering*, Vol. 30, pp. 1885-1893.
21. Rahimikhoob, A. (2010). Estimating global solar radiation using artificial neural network and air temperature data in a semi-arid environment. *Renewable Energy*, Vol. 35, pp. 2131-2135.
22. Marzo, A., Trigo-Gonzalez, M., Alonso-Montesinos, J., Martínez-Durbán, M., López, G., Ferrada, P., Fuentealba, E., Cortés, M., Batlles, F. J. (2017). Daily global solar radiation estimation in desert areas using daily extreme temperatures and extraterrestrial radiation. *Renewable Energy*, Vol. 113, pp. 303-311.
23. Torabi, M., Mosavi, A., Ozturk, P., Varkonyi-Koczy, A., Istvan, V. (2018). A hybrid machine learning approach for daily prediction of solar radiation. *International Conference on Global Research and Education*, 2018.
24. Gala, Y., Fernández, Á., Díaz, J., Dorronsoro, J. R. (2016). Hybrid machine learning forecasting of solar radiation values. *Neurocomputing*, Vol. 176, pp. 48-59.
25. Achour, L., Bouharkat, M., Assas, O., Behar, O. (2017). Hybrid model for estimating monthly global solar radiation for the Southern of Algeria : (Case study: Tamanrasset, Algeria). *Energy*, Vol. 135, pp. 526-539.
26. Quej, V. H., Almorox, J., Arnaldo, J. A., Saito, L. (2017). ANFIS, SVM and ANN soft-computing techniques to estimate daily global solar radiation in a warm sub-humid environment. *Journal of Atmospheric and Solar-Terrestrial Physics*, Vol. 155, pp. 62-70.
27. Ağbulut, Ü., Gürel, A. E., Ergün, A., Ceylan, İ. (2020). Performance assessment of a V-Trough photovoltaic system and prediction of power output with different machine learning algorithms. *Journal of Cleaner Production*, Vol. 268, 122269.
28. Ağbulut, Ü., Gürel, A. E., Biçen, Y. (2021). Prediction of daily global solar radiation using different machine learning algorithms: Evaluation and comparison. *Renewable and Sustainable Energy Reviews*, Vol. 135, 110114.
29. Rabehi, A., Guermoui, M., Lalmi, D. (2020). Hybrid models for global solar radiation prediction: A case study. *International Journal of Ambient Energy*, Vol. 41, pp. 31-40.
30. Mbah, O. M., Madueke, C. I., Umunakwe, R., Okofor, C. O. (2022). Machine learning approach for solar irradiance estimation on tilted surfaces in comparison with sky models prediction. *Journal of Engineering Sciences*, Vol. 9(2), G1-G6, https://doi.org/10.21272/jes.2022.9(2).e1
31. Feng, Y., Gong, D., Zhang, Q., Jiang, S., Zhao, L., Cui, N. (2019). Evaluation of temperature-based machine learning and empirical models for predicting daily global solar radiation. *Energy Conversion and Management*, Vol. 198, 111780.

JOURNAL OF ENGINEERING SCIENCES

Volume 9, Issue 2 (2022)

Javanbakht T., Chakravorty S. (2022). Optimization of machine learning algorithms for proteomic analysis using topsis. Journal of Engineering Sciences, Vol. 9(2), pp. E7-E11, doi: 10.21272/jes.2022.9(2).e2

Optimization of Machine Learning Algorithms for Proteomic Analysis Using TOPSIS

Javanbakht T.[1*], Chakravorty S.[2]

[1] Department of Computer Science, University of Quebec in Montreal,
201, President Kennedy St., Montreal, Quebec H2X 3Y7, Canada;
[2] Biju Patnaik University of Technology, Chhend Colony, Rourkela, Odisha 769004, India

Article info:
Submitted: August 21, 2022
Accepted for publication: November 24, 2022
Available online: November 28, 2022

[*]**Corresponding email:**
javanbakht.taraneh@courrier.uqam.ca

Abstract. The present study focuses on a new application of the TOPSIS method for the optimization of machine learning algorithms, supervised neural networks (SNN), the quick classifier (QC), and genetic algorithm (GA) for proteomic analysis. The main hypotheses are that the change in the weights of alternatives could affect the ranking of algorithms. The obtained data confirmed this hypothesis for their ranking. Moreover, adding labor as a cost criterion to the list of criteria did not affect this ranking. This was because candidate 3 had better fuzzy membership degrees than the two other candidates concerning their criteria. This work showed the importance of the value of the fuzzy membership degrees of the cost criterion of the algorithms in their ranks. The values of the fuzzy membership degrees of the algorithms used for proteomic analysis could determine their priority according to their score differences. One of the advantages of this study was that the studied methods could be compared according to their characteristics. Another advantage was that the obtained results could be related to the new ones after improving these methods. The results of this work could be applied in engineering, where the analysis of proteins would be performed with these methods.

Keywords: multi-criteria decision making, TOPSIS, prediction, proteomic analysis.

1 Introduction

The multi-criteria decision-making (MCDM) techniques are essential tools that have found their applications in diverse fields of science and engineering. Data optimization based on predicting the best alternative and ranking candidates can be carried out using these algorithms. In recent years, some MCDM algorithms have been used to determine the possible optimal alternatives. In these methods, linguistic values are used for the assessment of weights of criteria in order to obtain the ranks of alternatives [1-3].

The technique for order of preference by similarity to ideal solution (TOPSIS) is an MCDM method which is more appropriate than other such techniques in the first technique. Profit and cost criteria are analyzed according to their difference for the candidates [4-6]. The advantages of TOPSIS are important in science and engineering, which are the use of application, universality, consideration of distances to the ideal solutions and simplicity on computation and presentation [7, 8].

Proteomic analysis, which investigates the structure and function of proteins, is an important issue in engineering and its related fields. In the proteomic analysis, the dysregulated proteins in patients are selected, and the protein biomarkers that can influence the metabolisms of organs, such as bone, cartilage, liver, etc., are identified [9-12]. The proteomic pattern identification of diseases, such as different varieties of cancers, for which there are no early specific symptoms, is considered a necessary investigation as no long survival rate is obtained when these diseases are diagnosed in advanced stages [13].

TOPSIS has been used previously to analyze proteomic data and predict disease stages or cell expression profiles [14, 15]. These investigations use this feature ranking approach to select the most discriminative proteins from proteomics data for cancer staging. Moreover, introduced proteins are also investigated, which can potentially be applied in medical practice. Lower computational complexity and more production of general results without overfitting are the advantages of the approach used in these studies.

Although different machine learning algorithms such as neural network (NN), the quick classifier (QC), and genetic algorithm (GA) have been applied for protein analysis [16-21], their optimization in a comparative

study remains a novel topic to be investigated. To our knowledge, algorithms such as supervised neural network (SNN), QC and GA have not yet been optimized with TOPSIS for proteomic analysis. This novel work will provide insight into this method for optimizing these algorithms.

In this work, we investigated the optimization of three algorithms, SNN, QC, and GA, for the proteomic analysis with TOPSIS. The novelty of the current work relies on the feature ranking of the algorithms and their optimization with two series of modifications carried out in our analysis. We modified the weight values and the number of criteria in separate analyses and used TOPSIS as the appropriate optimization method to distinguish the profit and cost criteria. To our knowledge, the optimization of the algorithms used for proteomic analysis has not been investigated with this method.

The rest of the paper includes the following sections. In Section 2, we present the methodology of our paper, including information on the classification algorithms applied for the proteomic analysis and the TOPSIS method. In Section 3, we present our results in three series of analyses. We discuss the results and conclude the paper in Sections 4 and 5, respectively.

2 Research Methodology

This research work focused on optimizing classification algorithms for proteomic analysis with the TOPSIS method. The quantitative approach presented here was based on this method's characteristics, which allowed analyzing these algorithms according to their characteristic differences.

Three machine learning algorithms: SNN (candidate 1), QC (candidate 2), and GA (candidate 3), were analyzed in this work as their characteristics were previously investigated by Swiatly and her colleagues [13].

We used the TOPSIS code in python. The steps of this method were presented in our previous work [22].

We analyzed three algorithms: SNN (candidate 1), QC (candidate 2), and GA (candidate 3). These candidates are indicated as C-1, C-2, and C-3, respectively. The terms considered for the level of the candidates' criteria, such as recognition capability, cross-validation, sensitivity, and specificity, which were all the profit criteria, were as follows: very high, medium, high, and high for C-1, high, high, high and medium for C-2, and very high, medium, very high and medium for C-3, respectively. The terms used in the table were chosen according to the values of the characteristics of these algorithms, as indicated in table 3 of the paper of Swiatly and her colleagues [13].

3 Results

Table 1 shows the triangular fuzzy membership degrees of the candidates' characteristics and their mean values.

The alternative weight value of 0.5 was assigned for all the profit criteria: recognition capability, cross-validation, sensitivity, and specificity. In the criteria matrix, the term "true" was used for the profit criteria.

Table 1 – Triangular fuzzy membership degrees of candidates' characteristics

Candidates/ Criteria	Recognition capability	Cross validation	Sensitivity	Specificity
Triangular fuzzy degrees				
C-1	0.8, 0.9, 1.0	0.4, 0.5, 0.6	0.6, 0.7, 0.8	0.6, 0.7, 0.8
C-2	0.6, 0.7, 0.8	0.6, 0.7, 0.8	0.6, 0.7, 0.8	0.4, 0.5, 0.6
C-3	0.8, 0.9, 1.0	0.4, 0.5, 0.6	0.8, 0.9, 1.0	0.4, 0.5, 0.6
Mean values				
C-1	0.9	0.5	0.7	0.7
C-2	0.7	0.7	0.7	0.5
C-3	0.9	0.5	0.9	0.5

Table 2 shows the values of the candidates' distances from the best and worst alternative of the candidates, their similarity coefficients (CC_i), and rankings.

Table 2 – The distances from the best alternative and the worst alternative, the similarity coefficients, and the rankings

Candidates	d_i^*	d_i^-	CC_i	Ranking
C-1	0.063	0.061	0.493	1
C-2	0.072	0.050	0.413	2
C-3	0.071	0.051	0.417	3

Figure 1 shows the distances from the best and worst alternatives and the similarity coefficients of candidates with the black, red, and green lines, respectively.

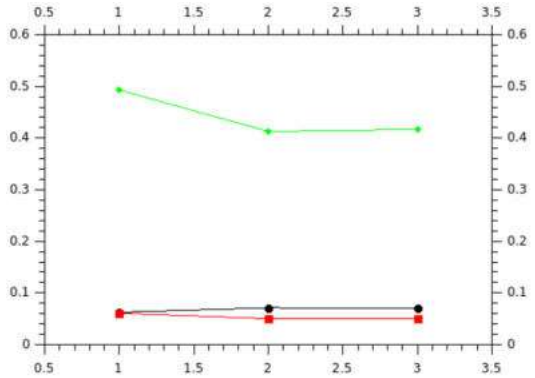

Figure 1 – The distances from the best alternative and the worst alternative and the similarity coefficients of candidates

In the second series of analyses with TOPSIS, we determined how the change in the criteria weights could affect the algorithm's output with the same entry data in the evaluation matrix. The alternative weights for each criterion are shown in Table 2. The recognition capability, cross-validation, sensitivity, and specificity weights for all the candidates were 0.9, 0.9, 0.9, and 0.2, respectively. These characteristics were considered as the profit criteria.

Table 3 shows the values of the candidates' distances from the best and worst alternatives of the candidates, their similarity coefficients (CC_i), and rankings.

Figure 2 shows the distances from the best and worst alternatives and the similarity coefficients of candidates with the black, red, and green lines, respectively.

Table 3 – The distances from the best alternative and the worst alternative, the similarity coefficients, and the rankings

Candidates	d_i*	d_i^-	CC_i	Ranking
C-1	0.078	0.045	0.366	3
C-2	0.065	0.062	0.491	2
C-3	0.064	0.063	0.497	1

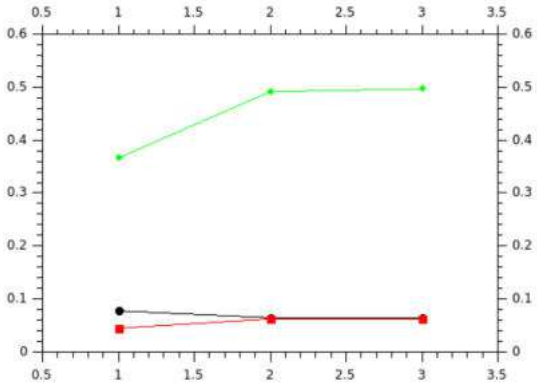

Figure 2 – The distances from the best alternative and the worst alternative and the similarity coefficients of candidates

In the third series of analyses, we added a cost criterion to the entry matrix. Recognition capability, cross-validation, sensitivity, and specificity were the profit criteria.

We considered labor as a cost criterion for the candidates.

The terms considered for the level of the candidates' criteria, such as recognition capability, cross-validation, sensitivity, specificity, and labor, were as follows: very high, medium, high, medium and height for C-1, high, medium, high, medium and very high for C-2, and very high, medium, very high, medium and low for C-3, respectively.

Table 4 shows the triangular fuzzy membership degrees of the candidates' characteristics and their mean values.

The alternative weight values of 0.9, 0.9, 0.9, 0.2, and 0.5 were assigned for recognition capability, cross-validation, sensitivity, specificity, and labor, respectively. In the criteria matrix, the terms "true" and "false" were used for the profit criteria and the cost criterion, respectively.

Table 4 – Triangular fuzzy membership degrees of candidates' characteristics

Candidates/ Criteria	Recognition capability	Cross validation	Sensitivity	Specificity	Labor
Triangular fuzzy degrees					
C-1	0.8, 0.9, 1.0	0.4, 0.5, 0.6	0.6, 0.7, 0.8	0.6, 0.7, 0.8	0.6, 0.7, 0.8
C-2	0.6, 0.7, 0.8	0.6, 0.7, 0.8	0.6, 0.7, 0.8	0.4, 0.5, 0.6	0.8, 0.9, 1.0
C-3	0.8, 0.9, 1.0	0.4, 0.5, 0.6	0.8, 0.9, 1.0	0.4, 0.5, 0.6	0.1, 0.2, 0.3
Mean values					
C-1	0.9	0.5	0.7	0.7	0.7
C-2	0.7	0.7	0.7	0.5	0.9
C-3	0.9	0.5	0.9	0.5	0.2

Table 5 shows the values of the candidates'' distances from the best and worst alternatives of the candidates, their similarity coefficients (CC_i), and rankings.

Table 5 – The distances from the best alternative and the worst alternative, the similarity coefficients, and the rankings

Candidates	d_i*	d_i^-	CC_i	Ranking
C-1	0.092	0.046	0.334	3
C-2	0.104	0.053	0.337	2
C-3	0.055	0.104	0.656	1

Figure 3 shows the distances from the best and worst alternatives and the similarity coefficients of candidates with the black, red, and green lines, respectively.

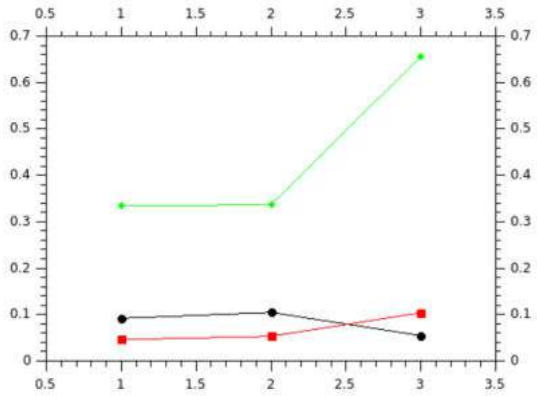

Figure 3 – The distances from the best alternative and the worst alternative and the similarity coefficients of candidates

4 Discussion

The comparison of the obtained data in the tables and figures presented in this paper revealed that the change in the weights of alternatives could affect the ranking of algorithms.

Moreover, the ranking did not change after adding labor as a cost criterion to the list of criteria. This was because the GA, as candidate 3, had better fuzzy membership degrees than the two other candidates concerning their criteria, so the GA could be ranked in first place. In contrast, this algorithm was ranked in the second position before adding labor to the list of criteria. This showed the importance of the values of the fuzzy membership degrees of the cost criterion of algorithms in their ranks.

The obtained results show how the values of the fuzzy membership degrees of the algorithms used for the proteomic analysis could determine their priority according to their score differences. It is worth noting that the improvement of the algorithms SNN (candidate 1) and QC (candidate 2) could change the ranking when labor was considered as a cost criterion. For this purpose, it would be required to increase the recognition capability, cross-validation, sensitivity and specificity of the first and second candidates and reduce their labor. The change in the ranking of these algorithms

could add further information for the proteomic analysis. This issue will be addressed in a further investigation.

The future of proteomic analysis depends on technological developments to resolve current instrument limitations, the integration of biological and protein research approaches to investigate the biological sciences and molecular medicine, and the development of quantitative, tissue-specific proteomes for emphasizing low-abundance metabolic proteins, a direct look at an evolving disease process and extracting the whole factors that are involved in the analysis [23-25].

These developments will help recognize a specific process error before their potentially incorrect diagnosis [26]. The TOPSIS method can be used to predict disease stages in each investigation. The presented approach can also be used to analyze other materials [27-30]. As demonstrated in a series of studies, this approach is applicable to the selection of the analysis methods of biological materials such as DNA, RNA, etc. [31-33]. The same method can be applied to the investigation of the effects of their properties on their ranks [34-37].

Further investigations are required to improve these algorithms for the analysis of proteins, as their sensitivity and specificity could be improved for their applications in science and engineering.

5 Conclusions

This paper investigated the prediction of machine learning algorithms for analyzing proteomic patterns with TOPSIS. The applied method consists of the calculations with the evaluation matrice, including the entry data for which the matrices of weight values and criteria were considered for different analyses. In the presented work, the algorithms previously used for the analysis of proteins were analyzed, and their rankings were compared. We used vector normalization in the TOPSIS method for the data normalization. The results of the two first series of the analysis showed that the third candidate could replace the first one in the rankings when the criteria weights were modified.

In addition, the third candidate could still maintain the first position in the ranking when labor was added as the cost criterion to the list of criteria. The obtained results showed that the optimization of the ranks could be affected by modifying the candidates' weights.

Optimizing the algorithms can lead to a better understanding of proteomic analysis with applications in science and engineering.

References

1. Balioti, V., Tzimopoulos, C., Evangelides, C. (2018). Multi-criteria decision making using TOPSIS method under fuzzy environment. Application in spillway selection. *Proceedings*, 2, 637. https://doi.org/10.3390/proceedings2110637.
2. Tlas, M., Ghani, B. A. (2020). Interactive software for classification and ranking procedures based on multi-criteria decision-making algorithms. *Computational Ecology and Software*, 10(3), 133–150.
3. Rohanah, S. (2018). An evaluation of students performance using TOPSIS and Entropy approaches. *IOSR Journal of Research, Method in Education*, 8(6), 1–6. https://doi.org/10.9790/7388-0806010106.
4. Sałabun, W., Wątróbski, J., Shekhovtsov, A. (2020). Are MCDA methods benchmarkable? A comparative study of TOPSIS, VIKOR, COPRAS, and PROMETHEE II methods. *Symmetry*, 12(9), 1549. https://doi.org/10.3390/sym12091549.
5. Chang, S. - H., Tseng, H.-E. (2008). Fuzzy Topsis decision method for configuration management. *International Journal of Industrial Engineering*, 15(3), 304-313. https://doi.org/10.23055/ijietap.2008.15.3.147.
6. Bulgurcu, B. (2012). Application of TOPSIS technique for financial performance evaluation of technology firms in Istanbul stock exchange market. *Procedia*, 62, 1033-1040. https://doi.org/10.1016/j.sbspro.2012.09.176.
7. Kochkina, M. V., Karamyshev, A. N., Isavnin, A. G. (2017). Modified multi-criteria decision making method development based on "AHP" and "TOPSIS" methods using probabilistic interval estimates. *The Turkish Online Journal of Design, Art and Communication TOJDAC*, 1663-1674. https://doi.org/10.7456/1070DSE/144.
8. Abidin, M. Z., Rusli, R., Shariff, A. M. (2016). Technique for order performance by similarity to ideal solution (TOPSIS)- entropy methodology for inherent safety design decision making tool, *Procedia Engineering*, 148, 1043-1050. https://doi.org/10.1016/j.proeng.2016.06.587.
9. Álvarez, J. V., Bravo, S. B., Chantada-Vázquez, M. P., Barbosa-Gouveia, S., Colón, C., López-Suarez , O., Tomatsu, S., Otero-Espinar, F. J., Couce, M. L. (2021). Plasma proteomic analysis in Morquio A disease. *International Journal of Molecular sciences*, 22, 6165. https://doi.org/10.3390/ijms22116165.
10. Balbao, E., Marín, T., Oyarzún, J. E., Contreras, P. S., Hardt, R., van den Bosch, T., Alvarez, A. R., Rebolledo-Jaramillo, B., Klein, A. D., Winter, D., Zanlungo, S. (2021). Proteomic analysis of Niemann-pick type C hepatocytes reveals potential therapeutic targets for liver damage, *Cells*, 10, 2159. https://doi.org/10.3390/cells10082159.
11. Chen, Y., Yao, H., Zhang, N., Wu, J., Gao, S., Guo, J., Lu, X., Cheng, L., Luo, R., Liang, X., Wong, C. C. L., Zheng, M. (2021). Proteomic analysis identifies prolonged disturbances in pathways related to cholesterol metabolism and myocardium function in the COVID-19 recovery stage. *Journal of Proteome Research*, 20, 7, 3463-3474. https://doi.org/10.1021/acs.jproteome.1c00054.
12. Filbin, M. R., Mehta, A., Schneider, A. M., Kays, K. R., Guess, J. R., Gentili, M., Fenyves, B. G., Charland, N. C., Gonye, A. L. K., Gushterova, I., Khanna, H. K., LaSalle, T. J., Lavin-Parsons, K. M., Lilley, B. M., Lodenstein, C. L., et al. (2021). Longitudinal proteomic analysis of severe COVID-19 reveals survival-associated signatures, tissue-specific cell death, and cell-cell interactions. *Cell Reports Medicine*, 2, 100287. https://doi.org/10.1016/j.xcrm.2021.100287.

13. Swiatly, A., Horala, A., Hajduk, J., Matysiak, J., Nowak-Markwitz, E., Kokot, Z. J. (2017). MALDI-TOF-MS analysis in discovery and identification of serum proteomic patterns of ovarian cancer. *BMC Cancer*, 17, 472, 1–9.
14. Saghapour, E., Kermani, S., Sehhati, M. (2017). A novel feature ranking method for prediction of cancer stages using proteomics data. *Plos One*, 12(9), e0184203. https://doi.org/10.1371/journal.pone.0184203.
15. Mallik, S., Zhao, Z. (2019). Multi-objective optimized fuzzy clustering for detecting cell clusters from single-cell expression profiles. *Genes*, 10(8), 611. https://doi.org/10.3390/genes10080611.
16. Torng, W. Altman, R. B. (2017). 3D deep convolutional neural networks for amino acid environment similarity analysis. *BMC Bioinformatics*, 18, 302. https://doi.org/10.1186/s12859-017-1702-0.
17. Muzio, G., O'Bray, L., Borgwardt, K., Notes, A. (2021). Biological network analysis with deep learning. *Briefings in Bioinformatics*, 22(2), 1515-1530. https://doi.org/10.1093/bib/bbaa257.
18. Chiu, C. -Y., Hsieh, S. -Y., Wong, K. -S., Lai, S. -H., Chen, J. -K., Huang, J. -L. (2015). The value of total protein in guiding management of infectious parapneumonic effusion by using matrix-assisted laser desorption/ionization time-of-flight mass spectrometry. *Journal of Microbiology, Immunology and Infection*, 48(5), 483-489. https://doi.org/10.1016/j.jmii.2013.11.013.
19. Fan, N. -J., Gao, C. -F., Wang, X. -L., Zhao, G., Liu, Q. -Y., Zhang, Y. -Y., Cheng, B. -G. (2012). Serum peptidome patterns of colorectal cancer based on magnetic bead separation and MALDI-TOF mass spectrometry analysis. *J. Biomed. Biotechnol.*, 2012, 985020. https://doi.org/10.1155/2012/985020.
20. Unger, R. (2004). The Genetic Algorithm Approach to Protein Structure Prediction. *Struncture and Bonding*, 110, 2697-2699. https://doi.org/10.1007/b13936.
21. Lv, Y. et al. (2006). Improved Genetic Algorithm for Multiple Sequence Alignment Using Segment Profiles (GASP). International Conference on Advanced Data Mining and Applications, In Lecture notes in computer science, 4093, 388-395. https://doi.org/10.1007/11811305_43.
22. Javanbakht, T., Chakravorty, S. (2022). Prediction of human behavior with TOPSIS. *Fuzzy Extension and Applications*, 3(2), 109-125. https://doi.org/10.22105/jfea.2022.326185.1197.
23. Bark, S. J., Hook, V. (2007). The future of proteomic analysis in biological systems and molecular medicine. *Mol. Biosyst*., 3(1), 14-17. https://doi.org/10.1039/b611446.
24. Dastmalchi, M., Dhaubhadel, S. (2015). Proteomic insights into synthesis of isoflavonoids in soybean seeds. *Proteomics*, 15, 10, 1646-1657. https://doi.org/10.1002/pmic.201400444.
25. Spitzer, A. R., Chace, D. (2008). Proteomics- and metabolomics-based neonatal diagnostics in assessing and managing the critically Ill neonate. *Clinic in Prinatology*, 35(4), 695-716. https://doi.org/10.1016/j.clp.2008.07.019.
26. Conrads, T. P., Fusaro, V. A., Ross, S., Johann, D., Rajapakse, V., Hitt, B. A., Steinberg, S. M., Kohn, E. C., Fishman, D. A., Whitely, G., Barrett, J. C., Liotta, L. A., Petricoin, E. F., Veenstra, T. D. (2204). High-resolution serum proteomic features for ovarian cancer detection, *Endoctrine-Related Cancer*, 11, 163-178. https://doi.org/10.1677/erc.0.0110163.
27. Javanbakht, T., David, E. (2020). Rheological and physical properties of a nanocomposite of graphene oxide nanoribbons with polyvinyl alcohol. *Journal of Thermoplastic Composite Materials*, 0892705720912767. https://doi.org/10.1177/0892705720912767.
28. Javanbakht, T., Laurent, S., Stanicki, D., Frenette, M. (2020). Correlation between physicochemical properties of superparamagnetic iron oxide nanoparticles and their reactivity with hydrogen peroxide. *Canadian Journal of Chemistry*, 98, 601-608. https://doi.org/10.1139/cjc-2020-0087.
29. Javanbakht, T., Sokolowski, W. (2015). Thiol-ene/acrylate systems for biomedical shape-memory polymers. *Shape Memory Polymers for Biomedical Applications*, 157-166. https://doi.org/10.1016/B978-0-85709-698-2.00008-8.
30. Javanbakht, T., Ghane-Motlagh, B., Sawan, M. (2020). Comparative study of antibiofilm activity and physicochemical properties of microelectrode arrays. *Microelectronic Engineering*, 229, 111305. https://doi.org/10.1016/j.mee.2020.111305.
31. Pakpour, S., Olishevska, S., Prasher, S., Milani, A. S., Chénier, M. R. (2013). DNA extraction method selection for agricultural soil using TOPSIS multiple criteria decision-making model. *American Journal of Molecular Biology*, 3, 215-228. https://doi.org/10.4236/ajmb.2013.34028.
32. Tripathy, J., Dash, R., Pattanayak, B. K., Mishra, S. K., Mishra, T. K., Puthal, D. (2022). Combination of reduction detection using TOPSIS for gene expression data analysis, *Big Data and Cognitive Computing*, 6(1), 24. https://doi.org/10.3390/bdcc6010024.
33. Singh, S., Li, H. (2021). Comparative study of bioinformatic tools for the identification of chimeric RNAs from RNA Sequencing, *RNA Biology*, 18, S1, 254-267. https://doi.org/10.1080/15476286.2021.1940047.
34. Djavanbakht, T., Carrier, V., André, J. M., Barchewitz, R., Troussel, P. (2000). Effets d'un chauffage thermique sur les performances de miroirs multicouches Mo/Si, Mo/C et Ni/C pour le rayonnement X mou. *Journal de Physique IV*, France, 10, 281-287. https://doi.org/10.1051/jp4:20001031.
35. Krishnamoorthy, K., Mahalingam, M. (2015). Selection of a suitable method for the preparation of polymeric nanoparticles: Multi-criteria decision making approach. *Advanced Pharmaceutical Bulletin*, 5(1), 57-67. https://doi.org/10.5681/apb.2015.008.
36. Javanbakht, T., Hadian, H., Wilkinson, K. J. (2020). Comparative study of physicochemical properties and antibiofilm activity of graphene oxide nanoribbons. *Journal of Engineering Sciences*, 7(1), C1-C8. https://doi.org/10.21272/jes.2020.7(1).c1.
37. Negi, R. S., Bisht, R. S., Singh, R. K., Prasad, L. (2019). Physico-mechanical and antibacterial properties of pine gum/epoxy composites with/without silver nanoparticles. *Marcomolecular Materials and Engineering*, 304, 7, 1800744. https://doi.org/10.1002/mame.201800744.

JOURNAL OF ENGINEERING SCIENCES

Volume 9, Issue 2 (2022)

Sapozhnykov Y., Zahorulko A., Peczkis G. (2022). Numerical simulation of 2-way FSI problem of face packing seal: Impact of parameters change. Journal of Engineering Sciences, Vol. 9(2), pp. E12-E27, doi: 10.21272/jes.2022.9(2).e3

Numerical Simulation of 2-Way FSI Problem of Face Packing Seal: Impact of Parameters Change

Sapozhnykov Y.[1*[0000-0002-9911-407X]], Zahorulko A.[1[0000-0002-6198-4643]], Peczkis G.[2[0000-0003-1820-3773]]

[1] Sumy State University, 2 Rymskogo-Korsakova St., 40007 Sumy, Ukraine;
[2] Silesian University of Technology, 2A, Academicka St., 44-100 Gliwice, Poland

Article info:
Submitted: September 15, 2022
Accepted for publication: December 8, 2022
Available online: December 12, 2022

***Corresponding email:**
y.sapozhnykov@cm.sumdu.edu.ua

Abstract. The article is devoted to creating a refined computer model of the face packing seal (FPS) based on the solution of the two-way fluid-structure interaction (2-way FSI) problem. An approach to the average gap was proposed based on the micro-space's working medium leakage between the friction pair's roughness elements. Three FPS designs were studied, in which the following operating parameters were alternately changed: inlet pressure, load factor, stuffing box parameters, and friction coefficient. Young's modulus, Poisson's ratio, and the thickness of the annular plate at the bottom of the stuffing box were also changed. The model was created considering the actual geometry of the FPS. The shaft rotation was considered by applying the rotation condition on the wall of the fluid model. The calculation was carried out using the ANSYS Multiphysics software. The results of the calculations were presented in the form of graphic dependences with a comparison of the hydrostatic and contact pressure distributions over the friction pair width. The values of the magnitudes of leakage from the changing parameters were presented. Based on the obtained results, an optimal combination of parameters was evaluated for the most efficient design of the FPS.

Keywords: stuffing-box, ANSYS Multiphysics, hydrostatic pressure, contact pressure, process innovation.

1 Introduction

For modern mechanical engineering, one of the essential criteria, in addition to energy efficiency, in compliance with accepted environmental standards [1, 2]. For pump units, this criterion is related to the leakage of the working medium into the environment. That is why one of the essential tasks today is the improvement of the existing systems of pump seals.

In addition, the need for pumping both liquid and gaseous substances is constantly increasing [3]. The most common type of seal is stuffing box seals, which are used both for sealing shafts of centrifugal pumps and for armature spindles.

Stuffing box seals have become widely used in pumping units that pump neutral media at normal temperatures. Until now, the stuffing-box remains the cheapest and easiest-to-use sealing material. For a long time, the designs of stuffing-box seals and the conformity of the packing to new operating conditions for various types of industries have been improved. Mainly, the seal's service life was increased while maintaining a low leakage rate.

The stuffing box has many options, as it is a central wire with braided fibers. Packings with fluoroplastic fibers (PTFE) have become widespread, as this material is often used as a sealant in fixed joints. In addition, the stuffing can be impregnated with liquid materials based on silicone, which ensures a low friction coefficient and, as a result, a low friction temperature.

Today, end mechanical seals are most often used to seal the shafts of centrifugal machines. Therefore, the most energy-efficient packing seal is the face packing seal of various modifications. Because of this, the improvement of this type of stuffing box seal is considered the most expedient [4]. This work will consider some structural improvements of the FPS.

In today's world, the process of improving any element or system is impossible without the use of computational technology. The existing software complexes are capable of processing huge arrays of data. They allow you to create any computer model with conditions as close as possible to real ones. Some problems, such as problems of hydroaeroelasticity, thermoelasticity, and other interdisciplinary issues, are quite complex to solve

analytically, and it is necessary to resort to numerical modeling of specific processes.

Now there are commercially available software packages ANSYS Multiphysics, STAR-CCM+, Open FOAM, etc., making it possible to create interdisciplinary models.

The fluid-structure interaction problem is the interaction of some solid moving body that deforms with an internal or surrounding fluid flow. This interaction can be stationary or oscillating. In oscillatory interactions, the stress induced in the rigid structure causes the body to move so that the source of deformation is reduced, and the solid body returns to its original state only to repeat the process.

In general, three types of problems of Fluid-structure interaction are considered:

1) the problem for a rigid body (Rigid Body FSI) is a problem of flow around a rigid body. In this case, there are no deformations of the solid body, and only the movement of the body in liquid or gas is considered;

2) the one-way fluid-structure interaction (1-way FSI) involves considering very small deformations of an elastic body under the action of hydrodynamic forces. This algorithm allows you to transfer data from the CFD solver to the Mechanical solver and vice versa;

3) the two-way fluid-structure interaction (2-way FSI) is solved when data is transferred in both directions between the fluid and solid models. This type of coupling is necessary for models with large deformations, such as a heart valve or thermal expansion problems, because the results of one model significantly change the boundary conditions and the result of another [5].

This work aims to create a computer model of the FPS, which is as close as possible to the real sample in terms of leakage indicators and the distribution of hydrostatic pressure in the friction pair. Determining the distribution of contact pressure in the friction pair is also necessary.

2 Literature Review

Until now, any calculations related to compatible problems were performed exclusively analytically based on the results of experiments [6, 7]. The obtained analytical dependences give an idea of the sealing process in the stuffing box seal. However, there was a problem in comparing the distribution of contact pressure in a friction pair, as it was impossible to determine it experimentally.

Later, with the help of the ANSYS software complex, it was possible to create simple models of FPS. The one-way FSI problem is solved in [8]. These models served as the foundation for creating and improving further models of gland seals.

Separately, it is essential to note that in works [9-12], the stuffing box is considered as a porous body with experimentally determined coefficients of porosity and permeability. At the same time, the FSI problem is not solved, and calculations are based on Darcy's law.

3 Research Methodology

The computer model of the FPS represents a sector of 1/6 of the sealing part (Figures 1, 2). Such a simplified model makes it possible to use less machine time for calculation. The model was developed with the help of the ANSYS software complex. This software complex allows you to solve various interdisciplinary problems, including the FSI problem. In this case, the two-way FSI problem is considered. The solution to this problem is based on a distributed approach with a strong coupling between the elements of the solver.

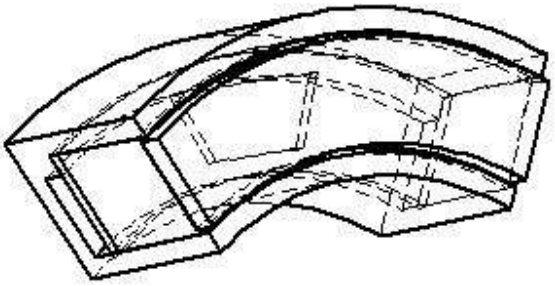

Figure 1 – General view of the FPS model

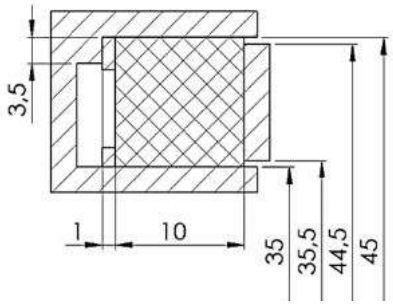

Figure 2 – Section of the FPS model and geometric dimensions

As a solid domain act (Fig. 3), packing chamber 1, packing ring 2, and bushing support disk 3. In the modernized version, the FPS has an annular plate (solid 4 and with grooves in the form of a trapezoid 5). Figure 4 shows two conditional lines, along which the hydrostatic and contact pressure distributions will be determined. The first line passes through the groove and divides the plate segment into two symmetrical parts. Conventional name - groove line. The second line runs along the edge of the plate segment and has the conventional nameplate line. The position of these two lines is chosen so that it is possible to see the difference in pressure distributions for the traditional design (Fig. 3 a) and for designs with an annular plate (Fig. 3 b, c).

The boundary conditions for the solid domain are as follows (Table 1, Figures. 3–5).

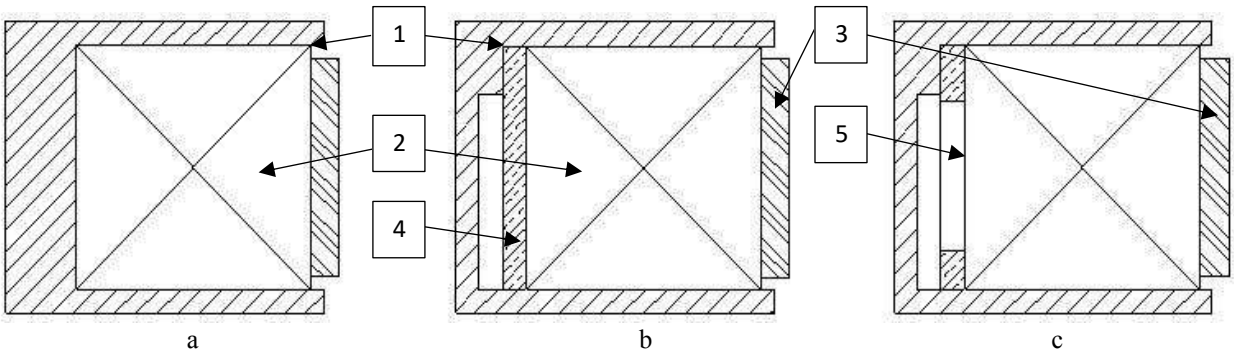

Figure 3 – FPS designs: a – traditional; b – with an annular plate at the bottom of the stuffing box; c – with grooves in the annular plate

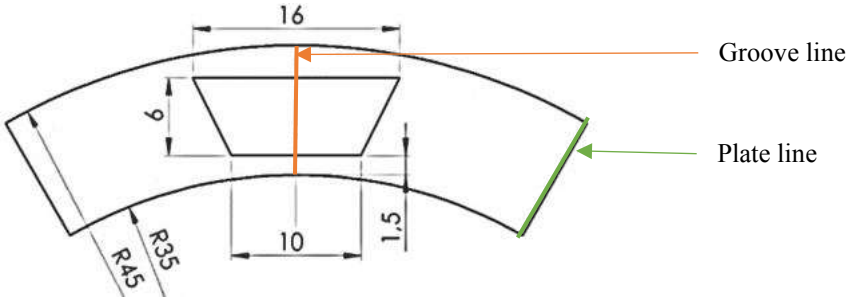

Figure 4 – Sketch and geometric dimensions of the groove in the plate

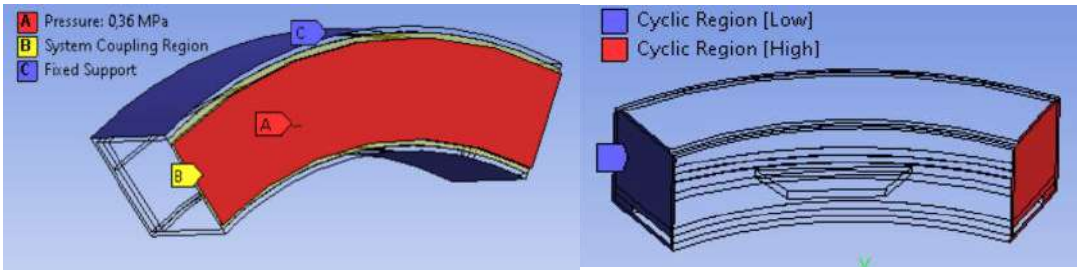

Figure 5 – Boundary conditions of the solid domain

Table 1 – Boundary conditions for the solid domain

No.	Structural element	Boundary condition
1	The walls of the packing chamber 1 (C on Fig. 5)	Fixed support
2	The surface between the annular plate 4/5 and the packing chamber 1	Frictional contact
3	The surface between packing ring 2 and packing chamber 1	Frictional contact
4	The surface between packing ring 2 and annular plate 4/5	Frictional contact
5	The surface between packing ring 2 and bushing support disk 3	Frictional contact
6	The surface of the stuffing box B on Fig.5	System coupling region
7	The surface of sleeve A on Fig.5	Pressure
8	Side surfaces of the model (Low, High in Fig.5)	Cyclic region

The fluid body model is based on the idea that the working medium flows in a friction pair along channels formed by micro-irregularities. In the sealing process, these micro-irregularities acquire an arbitrary shape and size within the main dimensions of roughness (protrusions and depressions) [13]. Thus, it can be concluded that leakage occurs through an averaged gap with a fixed size. Based on such a representation, it is possible to create a fluid domain that will interact with the stuffing box model. A finite-element mesh was created for such a fluid domain, and boundary conditions were determined (Table 2, Fig. 6).

The size of the averaged gap was chosen so that in the created model, the leakage rate coincided with the leakage determined in the experiment [14]. In the experiment, the traditional design of the FPS was studied, the shaft size was 40 mm, and the outer and inner radius of the stuffing box was 45 mm and 35 mm, respectively. Physical and mechanical parameters of the stuffing box: Young's

modulus – 50 MPa, Poisson's ratio – 0.4. For the seal operation mode: inlet pressure – 0.4 MPa, shaft rotation speed – 3000 rpm, the leakage rate is 1.1 l/h. This level of leakage in the computer model is satisfied with an average gap height of about 3 μm.

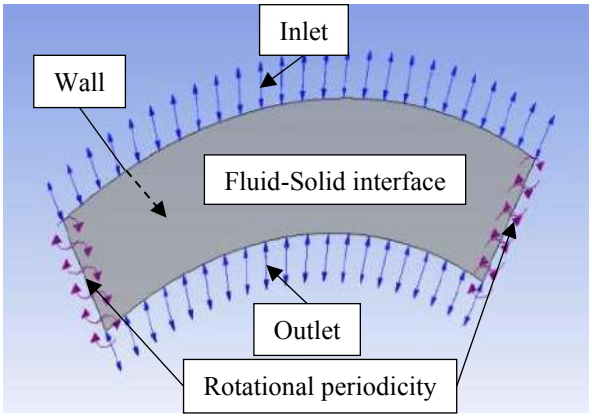

Figure 6 – Boundary conditions for the liquid domain

Table 2 – Boundary conditions of the fluid domain

No.	Surface name	Boundary condition
1	Inlet	Inlet
2	Outlet	Outlet
3	Wall	Wall
4	Fluid-Solid interface	System coupling
5	Symmetry	Rotational periodicity

When creating an FSI model, the first task is to connect two independent mesh domains together while considering the fundamental differences in the mesh formation of each domain. A Lagrangian mesh is used for FEA modeling, where the finite element mesh is fixed to the mass and moves in space as a function of the movement of the mass. In contrast, CFD modeling uses an Eulerian mesh, where a finite element is fixed in time and space with mass passing through the mesh [15].

FSI modeling has three main methods of data transfer between the fluid and solid domains: the Lattice-Boltzmann method, the fictitious domain, and the Arbitrary Lagrange-Euler method. In this work, the arbitrary Lagrange-Euler method is used, in which data transmission is carried out through a seamless interface (Fig. 7).

Processing of finite-element meshes introduces another classification of the analysis of the FSI problem. The two different classifications are conformal and non-conformal meshing methods. For the selected method of data transfer, it is not essential which method of grid creation will be chosen. It does not affect the result of calculations.

In this problem, a non-conformal type of connection between mesh elements of solid and liquid domains is used (Fig. 8)

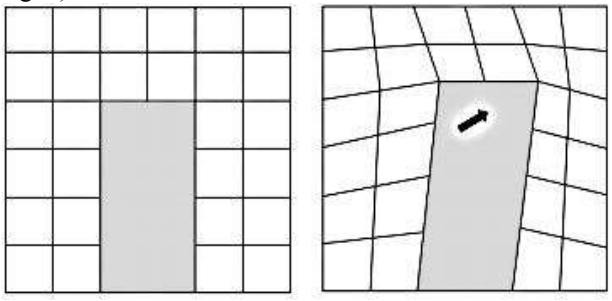

a b

Figure 7 – The black lines represent the fluid domain (Eulerian) mesh, and the gray body represents the solid (Lagrangian) mesh

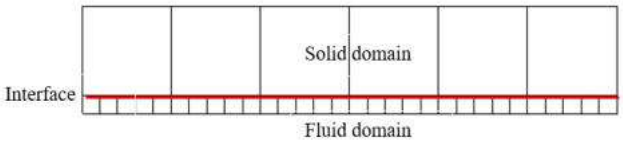

Figure 8 – Non-conformal connection between solid and liquid domain elements

The grid movement created by the arbitrary Lagrange-Euler method is shown from Fig. 7a to Fig. 7b.

The basic model of FPS was studied under the following conditions (Table 3).

Table 3 – Operating parameters and geometric dimensions

	Parameter	Marking	Size
1	Inlet pressure	P	0.4 MPa
2	Shaft rotation frequency	n	3000 rpm
3	The thickness of the annular plate	h	1 mm
4	The thickness of the averaged gap	h_{gap}	3 μm
5	The load factor of the support disk sleeve	K	1

The stuffing box has the following characteristics (Table 4):

Table 4 – Characteristics of the stuffing box

No.	Characteristic	Marking	Size
1	Size (in cross-section)	b	10x10 mm
2	Young`s modulus	E	50 MPa
3	Poisson's ratio	μ	0.4
4	Coefficient of friction	f	0.04

FPS designs with different parameter values were considered. The parameters were alternately changed in the following ranges (tab. 5)

Table 5 – Parameter change ranges

No.	Parameter	Marking	Magnitudes				
1	Load factor of the bushing support disk	*K*	0.85	0.90	0.95	1	1.1
2	Young`s modulus (MPa)	*E*	50	150	250	350	–
3	Poisson's ratio	*μ*	0.40	0.43	0.45	0.47	–
4	Inlet pressure (MPa)	*P*	0.40	0.80	1.20	1.60	–
5	Friction coefficient	*f*	0.04	0.06	0.08	0.10	–
6	Annular plate thickness (mm)	*h*	0.30	0.50	0.80	1	–

4 Results and Discussion

4.1 Parameter *K* influence analysis

As a result, to display the complete picture, a comparison of the graphs of the hydrostatic and contact pressure distribution along the friction pair width is presented (Figures 7–9). Such a comparison makes it possible to conclude the change in the direct contact zone of the stuffing box along the friction pair width.

First, it should be noted that the change in friction coefficients and Poisson's ratios have little effect on the distribution of hydrostatic and contact pressures.

Therefore, in this paper, the graphs of the pressure distribution are indicated for the changes in parameters *K*, *E*, *P*, and *h*.

For the traditional FPS design (Fig. 9, a), the change in the load factor K has little effect on the distribution of hydrostatic pressure (Ph), so it changes according to a linear law, but at the same time, the distribution of contact pressure (Pc) changes. At the load factor K = 0.85, a section with a width of 2.5 mm is observed, on which there is no contact pressure. Accordingly, there is no contact between the friction pairs in this section. That is, in this case, 77.5% of the surface of the friction pair is in contact. As the value of the coefficient K increases, this section decreases, and at a value of $K = 1.1$, full contact is observed along the friction pair width. A sharp jump in contact pressure values is observed in the area of contact from 8.5 to 9 mm, which is caused by a decrease in the hydrostatic pressure indicator to zero. The maximum values of the contact pressure are not displayed on the graph and are presented separately in Table 6. The results obtained for the traditional FPS design are taken as a baseline, and further comparisons are made with respect to them.

For the FPS design with an annular plate, the effect of changing the factor K is the same as for the traditional FPS design (Fig. 9, b). The main difference is that there is a decrease in the contact pressure indicators in the areas close to the exit from the seal. And as a result, there is a decrease in the maximum contact pressure indicators (Table 6). On average, the value of the contact pressure decreased by 3%.

In the case of the FPS model with grooves in the annular plate (Fig. 9, c, d), a change in the distribution of hydrostatic pressure along the width of the friction pair is observed at the load factor $K = 0.9$. When considering the line running along the groove (Fig. 9, c), the contact area is the smallest and is 1.5 mm, which means that only 13.5 % of the friction pair surface is in contact. Along the line passing through the place of the plate (Fig. 9, d), the contact width reaches 5 mm. That is, 45 % of the surface of the friction pair is in contact in this place.

It is worth noting that for all cases, the contact pressure value at the groove level decreases, but at the plate level, it increases and becomes higher than the indicators of the FPS model with an annular plate.

The sealing at $K = 0.85$ becomes impossible since the critical value of the pressure force transmitted from the CFX solver to the solid model solver is reached. At the same time, the contact between the bushing support disk and the packing is completely broken, which makes it impossible to solve the problem further. In practice, this means that the hydrostatic pressure squeezes the packing so much that it ceases to perform the role of a sealant and this causes a high level of leakage through the seal.

When the coefficient K increases ($K = 0.95$, 1.0, and 1.1), the graph of the hydrostatic pressure distribution becomes less complete, but the pressure drop remains different from the linear law. The distribution of contact pressure becomes more like the basic version of the design, but at the same time, most of its values are smaller on average by 27 %. A sharp jump in contact pressure values is observed only in the area from 8 to 9 mm. Therefore, the maximum values of the contact pressure are higher than the indicators of the basic design by 85 % along the line with a groove and by 110 % along the line of a plate (Table 6).

Here figures c and d show the hydrostatic and contact pressure distribution on the groove and plate lines shown in Fig. 3

Table 6 – The value of the maximum contact pressure for the FPS design when the load factor K changes

No.	The value of the load factor *K*	The value of the maximum contact pressure Pc_{max} (MPa) for FPS designs			
		Traditional	With an annular plate at the bottom of the stuffing box	With grooves in the annular plate	
				On groove line	On plate line
1	0.85	0.438	0.424	–	–
2	0.90	0.423	0.454	0.701	0.934
3	0.95	0.495	0.481	0.924	1.000
4	1.00	0.529	0.512	0.973	1.021
5	1.10	0.577	0.560	1.152	1.278

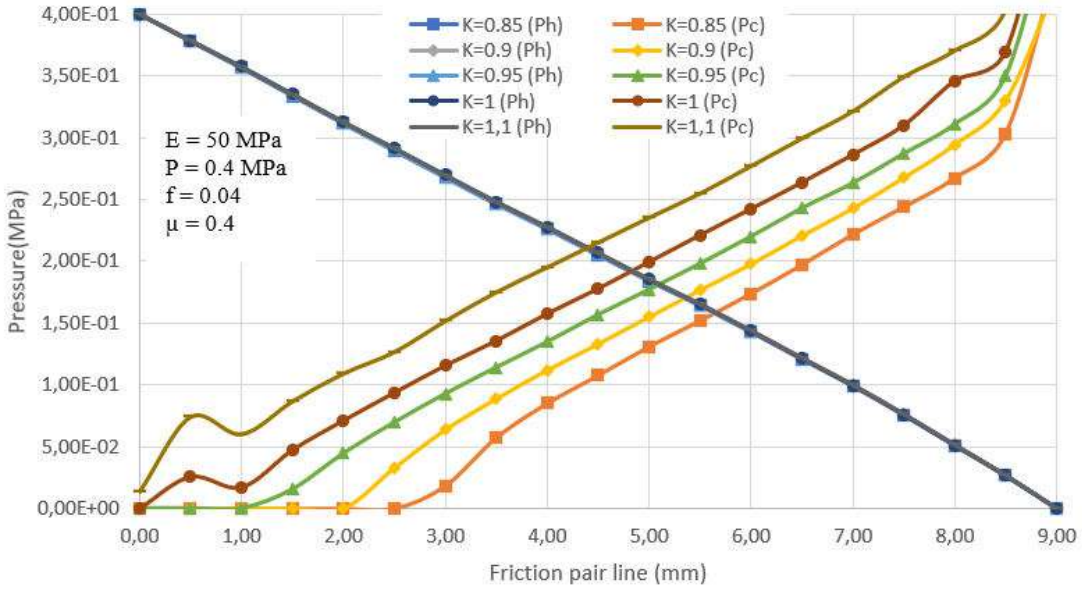

a

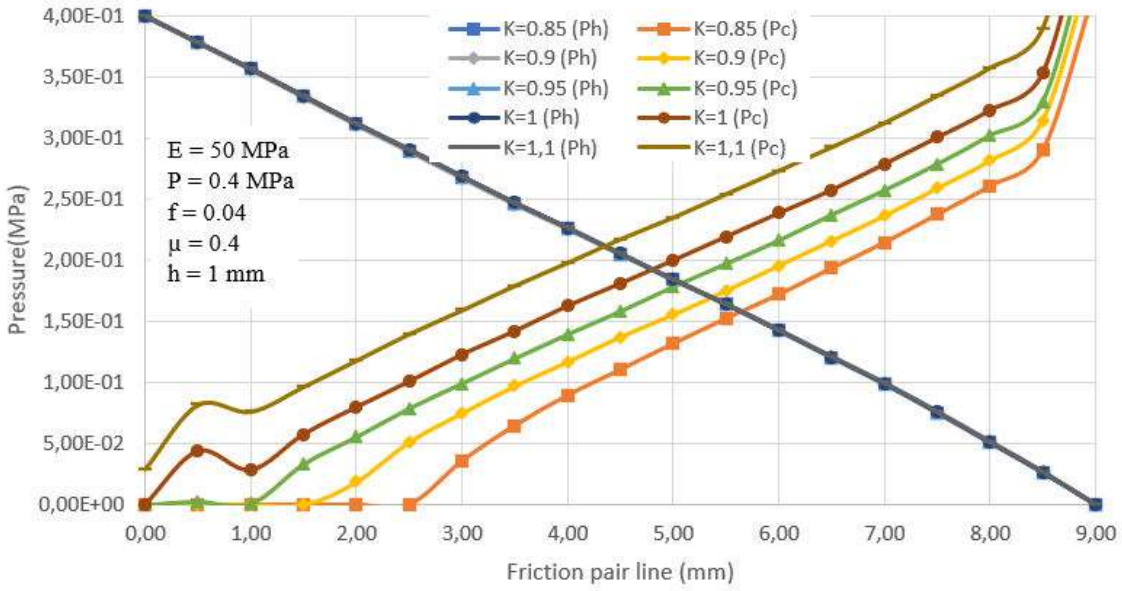

b

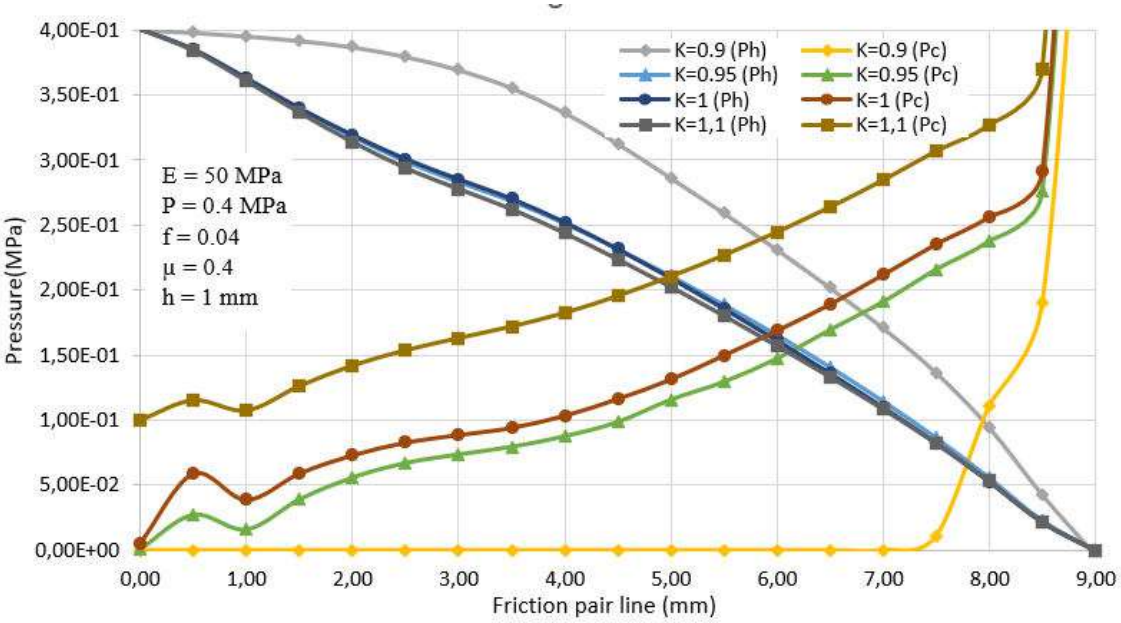

c

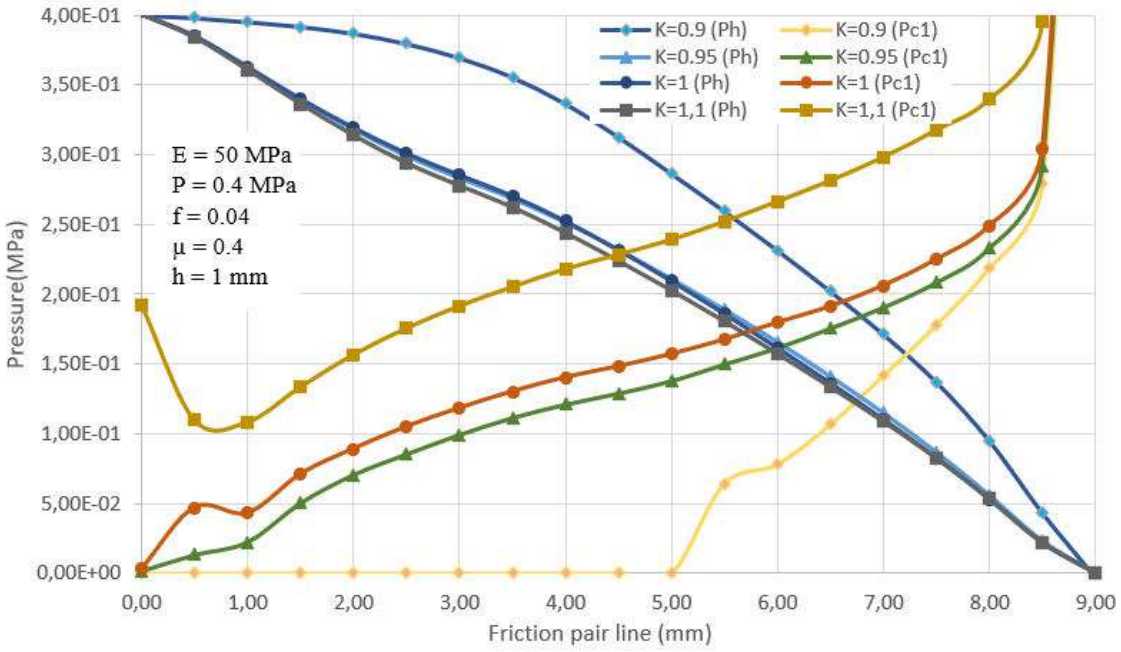

d

Figure 9 – Hydrostatic P_h and contact P_c pressure distribution, which depends on load coefficient K for classic face seal (a), face seal with bottom plate (b), and face seal with grooves in the bottom plate (c, d)

4.2 Parameter *E* influence analysis

For the traditional FPS design (fig. 10, a), the change in Young's modulus does not significantly affect the hydrostatic or contact pressure change. Their distribution remains almost linear. Contact is observed over the entire width of the friction pair.

A change in the shape of the contact pressure distribution with an increase in Young`s modulus value is observed for the FPS design (fig. 10, b) with an annular plate.

In this case, the stiffness of the structural pair of packing + annular plate changes in such a way that the contact pressure tries to equalize. That is, in the area towards the center of the friction pair width (from 0 to 4.75 mm), the contact pressure increases, while in the area after the center (from 4.75 to 9.0 mm), the contact pressure decreases. It will be useful to use this property when designing the FPS design with the best parameter combination.

For the design of the FPS with grooves in the plate (Figures 10c-d), a change in hydrostatic pressure distribution is observed when Young's modulus increases.

The graph of hydrostatic pressure distribution becomes fuller. At the same time, the distribution of contact pressure decreases with an increase in Young's modulus value, but in general, it repeats the picture shown in Fig. 9c-d for the load factor $K = 1$.

Table 7 shows the indicators of the maximum hydrostatic and contact pressures, which are unmarked on the graphs (Fig. 10).

Figures 10c-d show the hydrostatic and contact pressure distribution on the groove line and plate line, shown in Fig. 3.

Table 7 – The value of the maximum contact pressure for the design of the FPS when Young's modulus E changes

No.	Young's modulus (MPa)	The maximum contact pressure Pc_{max} (MPa) for FPS designs			
		Traditional	With an annular plate	With grooves in the annular plate	
				On groove line	On plate line
1	50	0.529	0.512	0.972	1.021
2	150	0.529	0.485	0.804	0.917
3	250	0.527	0.462	0.802	0.881
4	350	0.526	0.444	0.761	0.852

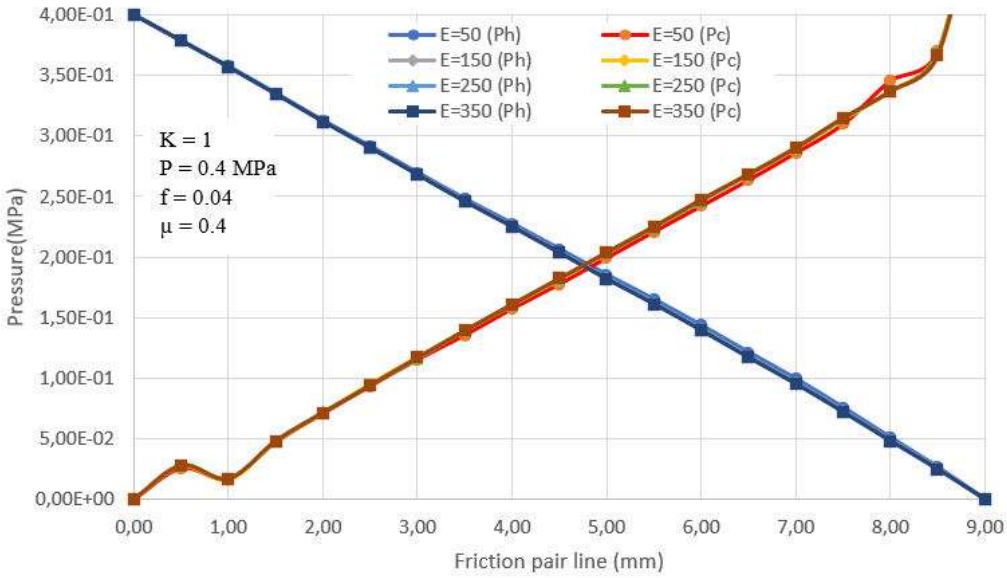

a

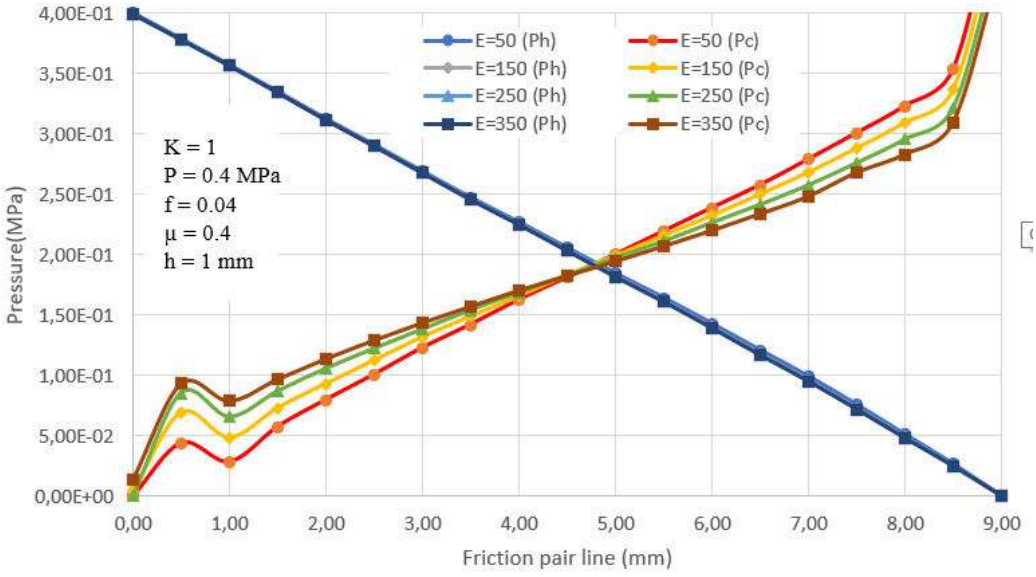

b

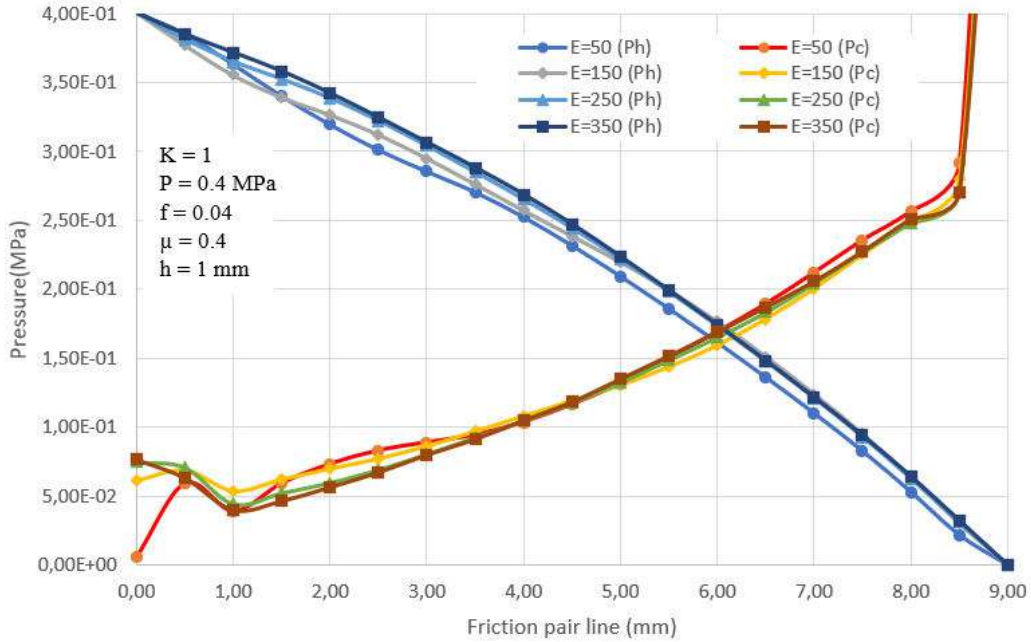

c

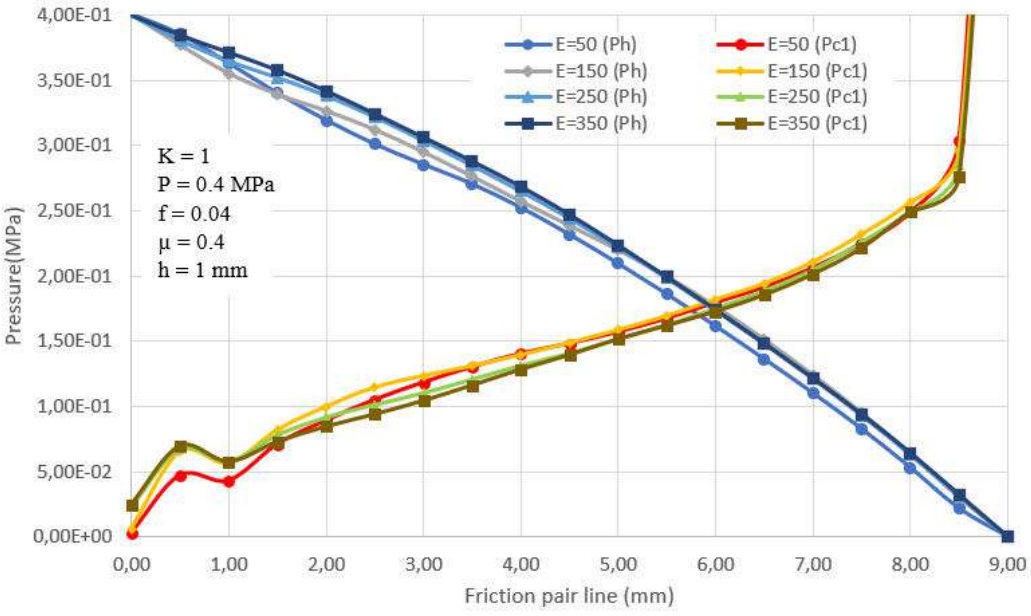

d

Figure 10 – Hydrostatic P_h and contact P_c pressure distribution, which depends on Young's modulus E for classic face seal (a), face seal with bottom plate (b), and face seal with grooves in the bottom plate (c, d)

4.3 Parameter *P* influence analysis

All three designs do not have significant differences depending on the input pressure value (Fig. 11). Pressure distributions change proportionally with increasing inlet pressure. Also, regardless of the value of the input pressure, a contact is present over the entire width of the packing, provided by the load factor K=1.

Separately, Table 8 lists the values of the maximum contact pressure, which are not shown on the graphs (Fig. 11).

Figures 11c-d show the hydrostatic and contact pressure distribution on the groove line and plate shown in Fig. 3.

Table 8 – Values of the maximum contact pressure for the FPS design when the inlet pressure P changes

No.	Inlet pressure, MPa	The value of the maximum contact pressure Pc_{max} (MPa) for FPS structures			
		Traditional	With an annular plate	With grooves in the annular plate	
				On groove line	On plate line
1	0.4	0.529	0.512	0.972	1.021
2	0.8	1.047	1.022	1.916	2.147
3	1.2	1.573	1.522	2.497	3.227
4	1.6	2.037	2.000	3.474	4.513

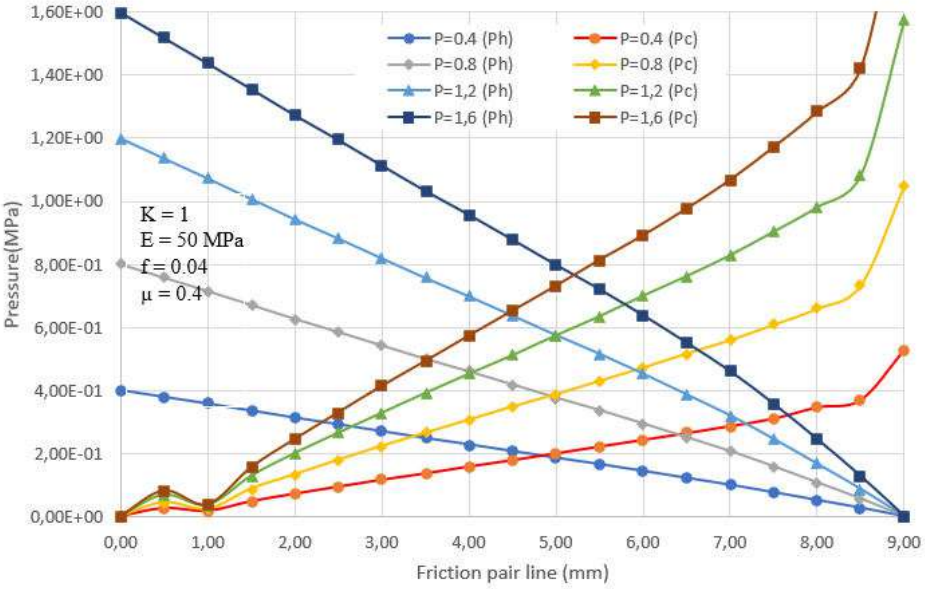

a

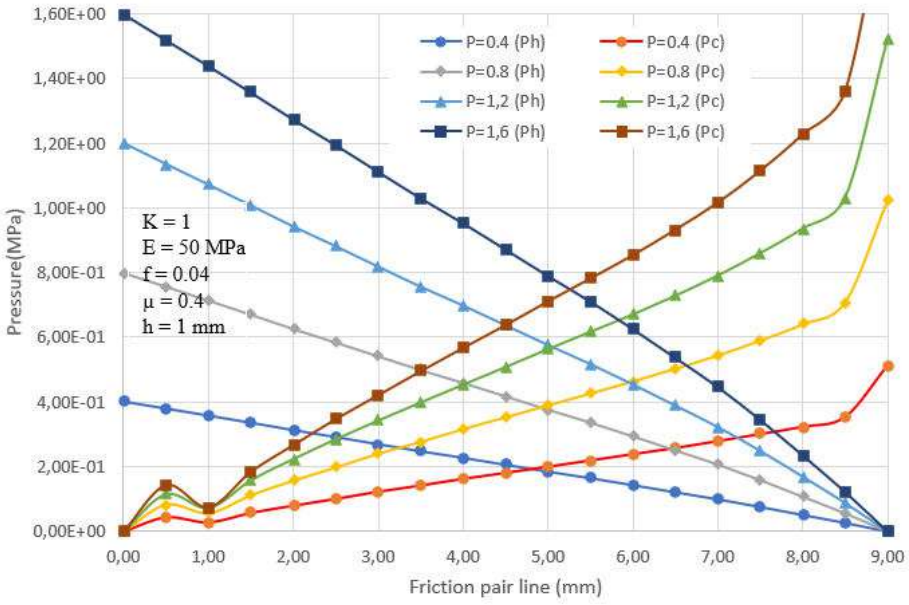

b

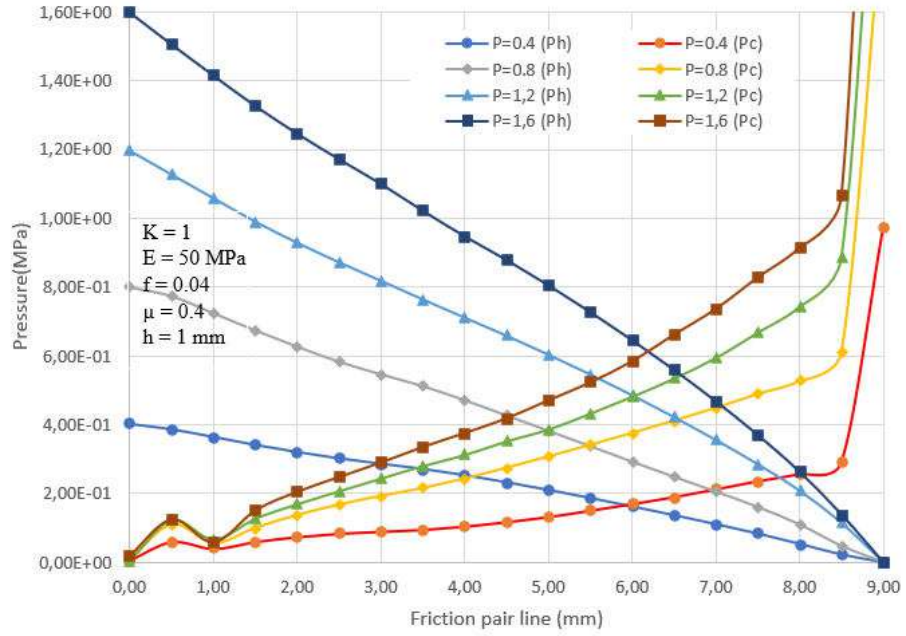

c

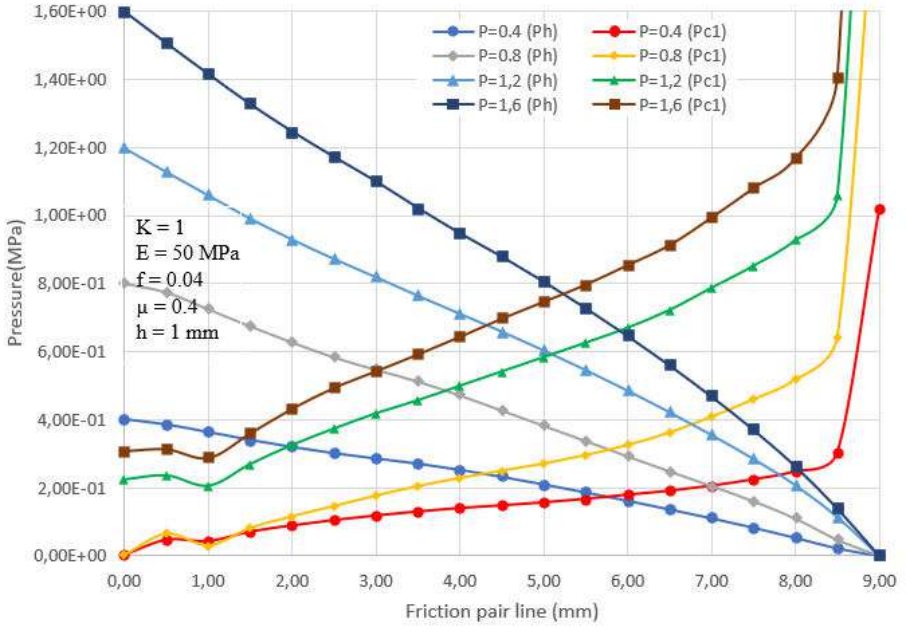

d

Figure 11 – Hydrostatic P_h and contact P_c pressure distribution which depends on inlet pressure P for classic face seal (a), face seal with bottom plate (b), and face seal with grooves in the bottom plate (c, d)

4.4 Parameter *h* influence analysis

A decrease in the thickness of the plate influences the distribution of contact pressure (Fig. 12). A tendency to equalize the contact pressure is observed, similar to the situation with Young's modulus change. But unlike Young's modulus, the limit of reducing the plate thickness is determined by the strength and rigidity of the FPS design. Thus, using a plate with a thickness of less than 0.3 mm leads to a loss of rigidity and eliminates any sense of its use at the bottom of the stuffing box.

It can also be noted that, for a design with a plate, there is no effect on hydrostatic pressure distribution by a change in the plate thickness (Fig. 12a). For the FPS design with a groove in the plate, as the plate thickness decreases, the hydrostatic pressure curve gradually approaches a linear law, i.e., its filling decreases. When the thickness of the plate is less than 0.5 mm, the opposite situation is observed - the distribution becomes less filled and more concave. Thus, a slight increase in contact pressure is observed, and the most significant degree of its alignment is ensured.

Table 9 – The value of the maximum contact pressure for the FPS design when the plate thickness changes *h*

No.	Plate thickness, mm	The value of the maximum contact pressure Pc_{max} (MPa) for FPS designs		
		With an annular plate	With grooves in the annular plate	
			On groove line	On plate line
1	0.3	0.376	0.626	0.852
2	0.5	0.445	0.818	0.989
3	0.8	0.499	0.917	1.007
4	1.0	0.512	0.972	1.021

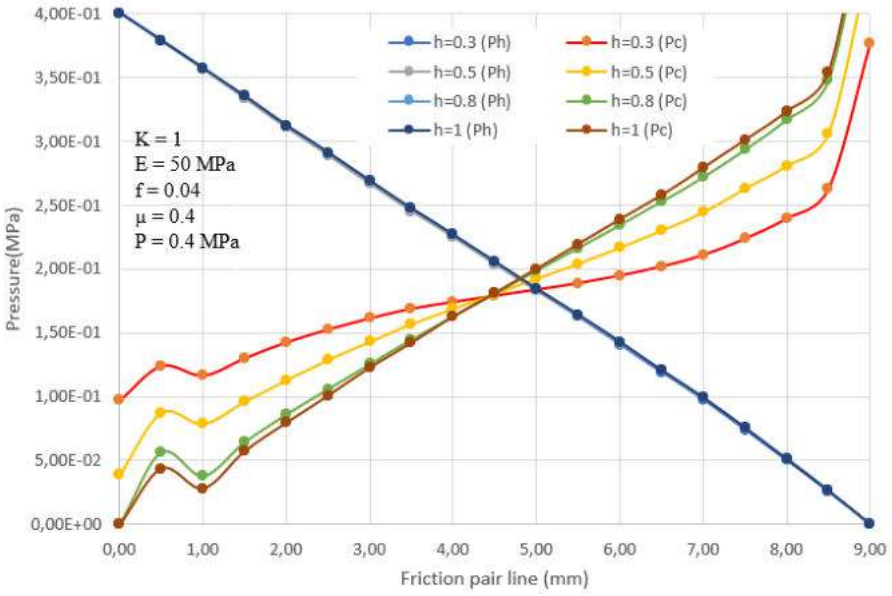

a

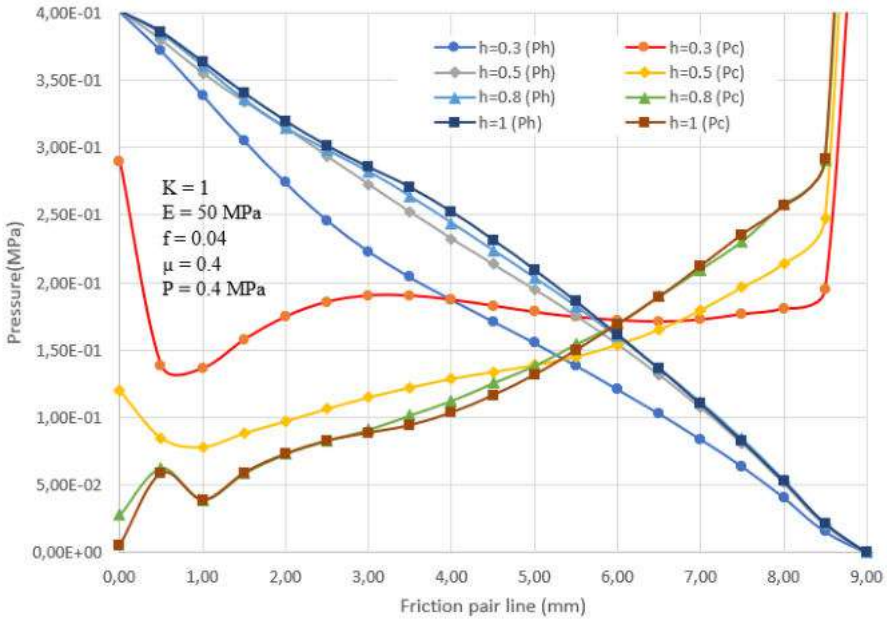

b

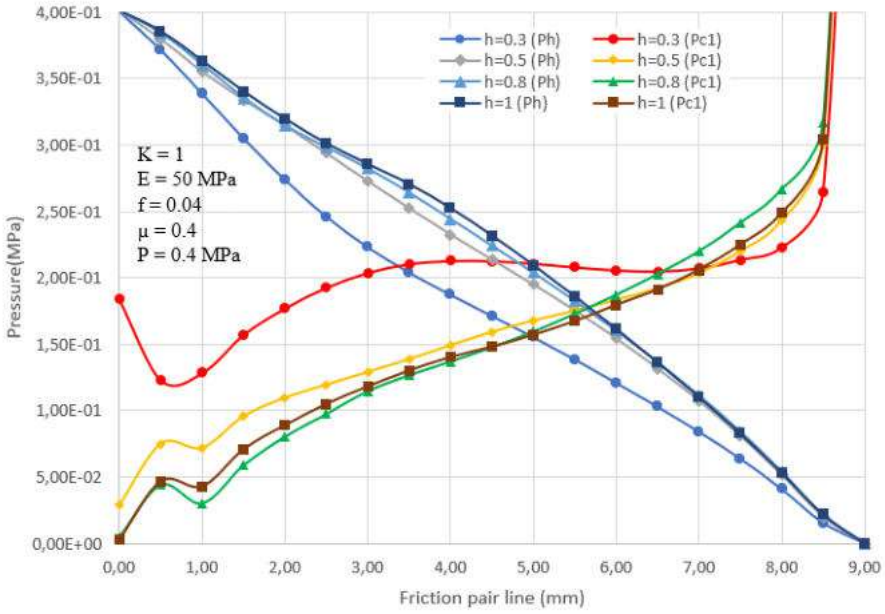

c

Figure 12 – Hydrostatic P_h and contact P_c pressure distribution which depends on plate thickness h for face seal with bottom plate (a) and face seal with grooves in the bottom plate (b, c)

4.5 Analysis of research. Choosing the FSP design with the best parameters combination

Based on the computer simulation results, the following points can be identified that are useful for practical use. Firstly, the design of the FPS with grooves in the annular plate at the bottom of the stuffing box allows you to generally reduce the amount of contact pressure across the width of the friction pair. Secondly, changing parameters E and h create conditions for equalizing the contact pressure on the same contact area. Thus, based on the results described above, it is possible to propose an FPS design with the best parameter combination.

Comparative Table 10 presents combinations of FPS designs and parameters that indicate the impracticality of the combination (red), the possibility of combination, but not a high degree of improvement in indicators (yellow), lack of influence (gray) and the best designs (green).

Thus, the best FPS design is a design with an annular plate and with grooves in the annular plate at $E = 350$ MPa and $h = 0.3$ mm. The simulation was carried out with the following parameters (Table 11). Fig. 13 shows that the combination of parameters E and h ensures equalization of the contact pressure across the friction pair width than the parameters taken separately.

Figures 13, 14 show the distribution of hydrostatic and contact pressures along the friction pair width for FPS designs with the best parameter combination.

After analyzing the given graphs, the following conclusions can be reached. In the design of the FPS with an annular plate, smooth equalization of the contact pressure is performed (without sharp peak values of the contact pressure), which subsequently has a positive effect on the intensity of wear of the entire surface of the packing in the place of contact with the support disk.

At the same time, an insignificant leakage rate is achieved. At the same time, in the FPS design with grooves in the annular plate, the peak value of the contact pressure is preserved closer to the exit from the seal. However, the overall value of the contact pressure distribution is smaller than in the FPS design with an annular plate. At the same time, the leakage rate is also smaller (Table 12).

Table 10 – A comparative analysis

No.	Parameter	The value of the parameter	FPS design		
			Traditional	With annular plate at the bottom of the stuffing box	With a groove in the annular plate
1	Load factor K	0.85		–	–
		0.90			
		0.95			
		1.00			
		1.10			
2	Young's modulus E, MPa	50			
		150			
		250			
		350			
3	Inlet pressure P, MPa	0.4			
		0.8			
		1.2			
		1.6			
4	Plate thickness h, mm	0.3	–		
		0.5	–		
		0.8	–		
		1.0	–		

Table 11 – Modeling the FPS designs with the best parameters combination

	Parameter	Marking	Size
1	Inlet pressure	P	0.4 MPa
2	Shaft rotation frequency	n	3000 rpm
3	The annular plate thickness	h	0.3 mm
4	The height of the average gap	h_{gap}	3 μm
5	Load factor of the support disk	K	1
6	Young's modulus	E	350 MPa
7	Poisson's ratio	μ	0.4
8	Friction coefficient	f	0.04

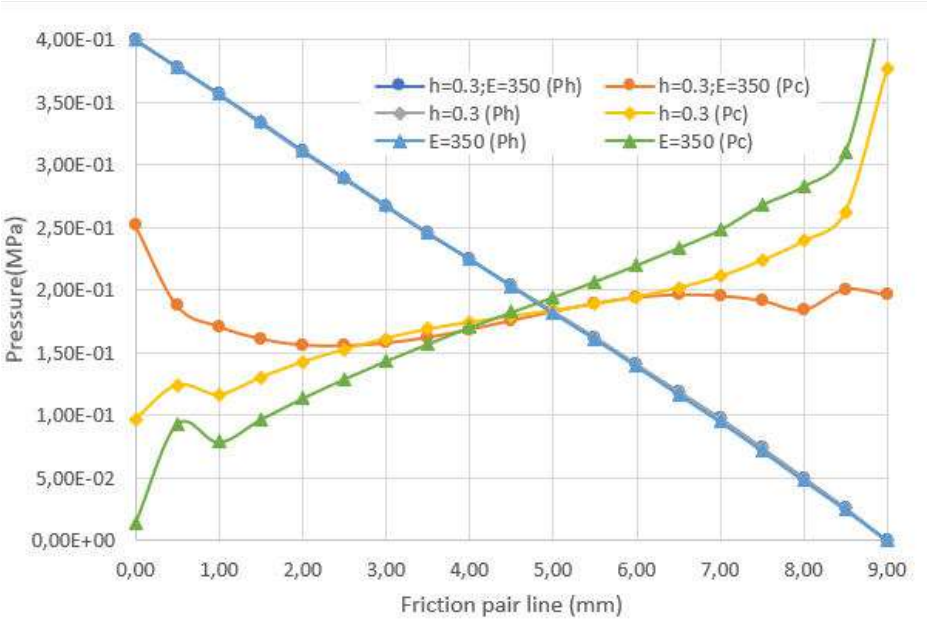

Figure 13 – Hydrostatic P_h and contact P_c pressure distribution for face seal with the annular plate

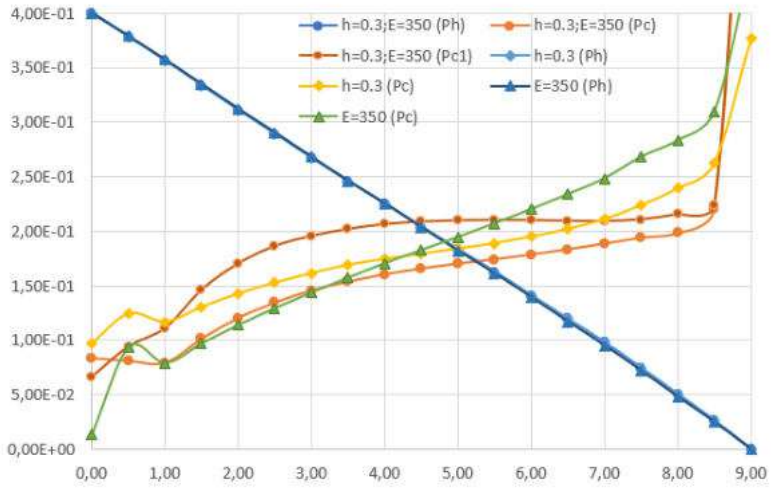

Figure 14 – Hydrostatic P_h and contact P_c pressure distribution for face seal with grooves on the plate

4.6 Leakage rate analysis

In addition to the hydrostatic and contact pressure distributions, the leakage rate is an essential parameter of the seal operation. Table 12 lists the values of leakage for all the above-mentioned FPS designs.

When summarizing the obtained results, it can be noted that the leakage rate decreases when the coefficients K, E, and h increase. In principle, the leakage size differs only in the case of a change in the inlet pressure. For all FPS designs, the maximum amount of leakage is achieved at an inlet pressure of 1.6 MPa.

Separately, it can be noted that for the FPS design with a groove in the annular plate where at the load factor $K = 0.9$ there is a sharp increase in the leakage rate (almost 3 times) compared to other values of the K factors. A similar picture is observed for the parameter $h = 0.3$ mm.

However, in this case, the leakage rate increases by only 18 %.

Comparing different FPS designs, it can be noted that the leakage rate for the annular plate FPS design is, on average 5 % lower compared to the traditional FPS design. And the leakage rate for the FPS design with a groove in the annular plate is, on average, 4.5 % higher than the leakage of the traditional FPS design.

The leakage rate of FPS in terms of contact pressure distribution is 0.0607 l/h for the FPS design with an annular plate, which is 0.2 % lower than the indicators of the traditional FPS design and 0.0614 l/h for the FPS design with a groove in the annular plate - which is higher by 0.9 % for indicators of the conventional FPS design.

Thus, the FPS design quality depends to a greater extent on the contact pressure distribution since the change in the leakage rate for different FPS designs is insignificant.

Table 12 – The leakage rate with different parameters and FPS designs

No.	Parameter	Value	The number of leakage for FPS designs, 1/h		
			Traditional	With an annular plate	With a groove
1	Load factor K	0.85	0.06172	–	–
		0.90	0.06174	0.06270	0.18548
		0.95	0.06160	0.06128	0.06452
		1.00	0.06124	0.06123	0.06417
		1.10	0.06137	0.06127	0.06322
2	Young's modulus E, MPa	50	0.06124	0.06123	0.06417
		150	0.06088	0.06085	0.06261
		250	0.06081	0.06077	0.06221
		350	0.06079	0.06074	0.06233
3	Inlet pressure P, MPa	0.4	0.06124	0.06123	0.06417
		0.8	0.12473	0.12401	0.12255
		1.2	0.18943	0.18770	0.19139
		1.6	0.25856	0.25234	0.25387
4	Plate thickness h, mm	0.3	–	0.06139	0.08336
		0.5	–	0.06199	0.06762
		0.8	–	0.06121	0.06440
		1.0	–	0.06123	0.06417
Optimal FPS designs		With annular plate		With a groove in the annular plate	
		0.06066		0.06139	

5 Conclusions

The developed computer model allows for solving a complex problem that combines the solution of the hydroelasticity problem and the contact problem. This is the first successful attempt to develop a model with two-way coupling for FPS. The obtained results have differences from the results obtained experimentally. In the experiment, the graph of the hydrostatic pressure distribution is more filled and is described by the Poiseuille equation. The pressure distribution in the presented computer model is reduced to Darcy's equation. Except for the case of the FPS design with a groove in the annular plate at the load factor $K = 0.9$. This means that some parameters must be considered when building a model. Finding these parameters is the next goal for improving the model.

When comparing different FPS designs, it is observed that the presence of an annular plate leads to a decrease in contact pressure along the friction pair width. At the same time, the leakage rate increases, which is confirmed experimentally.

Nevertheless, the created model made it possible to determine the parameters that most affect the distribution of contact pressure over the width of the friction pair. This, in turn, made it possible to determine the FPS design with the best parameter combination in which equalization of the contact pressure is achieved. In practice, this means that the stuffing box in this operation mode will have more uniform wear, and therefore the seal's service life will be increased.

6 Acknowledgments

Sumy State University supported this research within the project "Analysis of the Influence of Hydrodynamic Forces Acting in Narrow Clearances of Seals and Bearings on Increasing Energy Efficiency and Reducing the Harmful Emissions and Vibrations of Centrifugal Machines" (No. 0120U102004) funded by the Ministry of Education and Science of Ukraine.

References

1. Kovanova, O. (2018). Climate change modeling in the context of urban decarbonization strategy. *Journal of Engineering Sciences*, Vol. 5(1), pp. H1-H6, https://doi.org/10.21272/jes.2018.5(1).h1
2. Hurets, L.L., Kozii, I.S., Miakaieva, H.M. (2017). Directions of the environmental protection processes optimization at heat power engineering enterprises. *Journal of Engineering Sciences*, Vol. 4(2), pp. G12-G16, https://doi.org/10.21272/jes.2017.4(2).g12
3. Martsynkovskyy, V.A. (2005). Hermomechanics, its role in ensuring the efficiency and environmental friendliness of pumping and compressor equipment. *Bulletin of Sumy State University, Series "Technical Sciences"*, Vol. 1(73), pp. 5-10.
4. Marcinkovsky, V.A., Zagorulko, A.V. (1998). Studies of sealed end seals. *Proceedings of International Science and Technology. Conference "Progressive Engine and Technology of Machine Building, Instrument Building and Welding Production"*, Vol. 3, pp. 322-327.
5. Löhner, R., Cebral, J.R., Yang, C., Baum, J.D., Mestreau, E.L., Soto, O. (2006). Extending the range and applicability of the loose coupling approach for FSI simulations. *Fluid-Structure Interaction*, Vol. 53, pp. 82-100, https://doi.org/10.1007/3-540-34596-5_4
6. Zahorulko, A.V. (1999). Research of the processes of friction and sealing in the front oil seal. *Mashinoznavstvo*, Vol. 8(26), pp. 45-48.
7. Gaft, J., Zahorulko, A., Martsynkovskyy, V., Shevchenko, S. (2000). Face packing seals: new opportunities for pump rotor hermetic sealing. *Proceedings of the XVI International Conference "Fluid Sealing. Successful Sealing", Brugge, Belgium*, pp. 335-349.
8. Zahorulko, A., Gudkov, S. (2010). Solution of problem concerning elastohydrodynamic lubrication for friction pair of face packing seal. *Proceedings of the XIII International Conference on Sealing Technology, Stuttgart, Germany*, pp. 317-326.
9. Bouzid, A.H. (2021). A study on liquid leak rates in packing seals. *Applied Sciences*, Vol. 11(4), 1936, https://doi.org/10.3390/app11041936
10. Macdonald, I., El-Sayed, M., Mow, K., Dullien, F. (1979). Flow through porous media – The Ergun equation revisited. *Ind. Eng. Chem. Fundam.*, Vol. 18, pp. 199-208.
11. Diany, M., Bouzid, A.H. (2009). Analytical evaluation of stresses and displacements of stuffing-box packing based on a flexibility analysis. *Tribology International*, Vol. 42(6), pp. 980-986, https://doi.org/10.1016/j.triboint.2009.02.002
12. Diany, M., Bouzid, A.H. (2009). Short term relaxation modeling of valve stem packings. *Journal of Tribology*, Vol. 131(3), 032201, https://doi.org/10.1115/1.3118787
13. Greenwood, J.A., Williamson, J.B.P. (1966). Contact of nominally flat surfaces. *Proceedings of the Royal Society of London. Series A, Mathematical and Physical Sciences*, Vol. 295(1442), pp. 300-319.
14. Zahorulko, A.V. (2001). *Research on the Mechanism of Sealing and Development of Methods of Calculation and Design of End Packings of Sealed Rotors of Pumps*. Ph.D. Thesis, Sumy State University, Sumy, Ukraine.
15. Cook, R., Malkus, D., Plesha, M., Witt, R. (2002). *Concepts and Applications of Finite Element Analysis*. John Wiley & Sons, Inc.

JOURNAL OF ENGINEERING SCIENCES

Volume 9, Issue 2 (2022)

Suprunenko M. K., Zborshchyk O. P., Sokolov O. (2022). Information-extreme machine learning of wrist prosthesis control system based on the sparse training matrix. Journal of Engineering Sciences, Vol. 9(2), pp. E28-E35, doi: 10.21272/jes.2022.9(2).e4

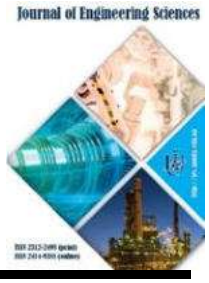

Information-Extreme Machine Learning of Wrist Prosthesis Control System Based on the Sparse Training Matrix

Suprunenko M. K.[1*], Zborshchyk O. P.[1], Sokolov O.[2]

[1] Sumy State University, 2, Rymskogo-Korsakova St., 40007 Sumy, Ukraine;
[2] Nicolaus Copernicus University in Torun, 5, Grudziadzka St., 87-100 Torun, Poland

Article info:
Submitted: October 3, 2022
Accepted for publication: December 11, 2022
Available online: December 14, 2022

[*]**Corresponding Author's Address:**
suproger0nikita@gmail.com

Abstract. The article considers the problem of machine learning of a wrist prosthesis control system with a non-invasive biosignal reading system. The task is solved within the framework of information-extreme intelligent data analysis technology, which is based on maximizing the system's information productivity in machine learning. The idea of information-extreme machine learning of the control system for recognition of electromyographic biosignals, as in artificial neural networks, consists in adapting the input information description to the maximum total probability of making correct classification decisions. However, unlike neuro-like structures, the proposed method was developed within a functional approach to modeling the cognitive processes of the natural intelligence of forming and making classification decisions. As a result, the proposed method acquires the properties of adaptability to the intersection of classes in the space of recognition features and flexibility when retraining the system due to the recognition class alphabet expansion. In addition, the decision rules constructed within the framework of the geometric approach are practically invariant to the multidimensionality of the space of recognition features. The difference between the developed method and the well-known methods of information-extreme machine learning is the use of a sparse training matrix, which allows for reducing the degree of intersection of recognition classes significantly. The optimization parameter of the input information description, the training dataset, is the quantization level of electromyographic biosignals. As an optimization criterion is considered the modified Kullback information measure. The proposed machine learning algorithm results are shown in the example of recognition of six finger movements and wrist.

Keywords: information-extreme intelligent technology, machine learning, process innovation, sparse training matrix, prosthesis control system, information criterion, electromyographic sensor, biosignal.

1 Introduction

Despite a significant number of studies on improving the interaction of a person with a disability with a limb prosthesis, the convenience, functionality, and prevalence of active prostheses in everyday life remain low. For the user, the accuracy of movement selection, the intuitiveness of control, and the system's reaction time are essential properties of prosthesis control. The main direction of the development of hand prostheses is provided based on electromyography as a method of analyzing the natural control impulses of the nervous system. The most advanced are limb prostheses with an invasive biosignal reading system. But their main drawback is a very high cost on the world market. In addition, the use of invasive biosignal reading systems requires prior surgical intervention. This makes it possible to increase the "biosignal/interference" ratio, which significantly affects the accuracy of performing cognitive commands but creates additional inconveniences for people with disabilities. Non-invasive bionic prostheses controlled by signals from passive electromyographic sensors, as a rule, have a limited set of commands, and the corresponding cognitive commands are provided with insufficient accuracy. The reasons for this unsatisfactory state are the high noise of biosignals, mainly due to the unstable contact of the electromyographic sensor.

The primary trend of increasing the functional efficiency of non-invasive hand prostheses is the application of intelligent information technologies of data analysis based on machine learning and pattern recognition. The complexity of the information synthesis of the intelligent prosthesis control system lies in need to

solve scientific and methodological problems caused by the arbitrary initial conditions of the operation of the prosthesis control system and the intersection in the space of features of recognition classes that characterize the possible permissible movements of the prosthesis.

The article deals with the issue of increasing the functional efficiency of the machine learning system for controlling a wrist prosthesis with a non-invasive electromyographic system for reading biosignals by using the so-called sparse training matrix.

2 Literature Review

Papers [1, 2] consider hand prostheses with an invasive system for reading biosignals, which require surgical intervention and have a high cost, being considered. Works [3, 4] describe prostheses endowed with a tactile function capable of recognizing and feeling the surface of an object. In addition, work [5] proposed to increase the accuracy of cognitive command execution using an additional eye movement optical tracking system. Still, this approach significantly increases the prosthesis's cost and complicates its use conditions. As for existing non-invasive prostheses controlled by signals from passive electromyographic sensors, achieving high accuracy depends on the reliability of recognizing electromyographic biosignals by the prosthesis control system. This is especially relevant when recognizing electromyographic biosignals of cognitive commands for the movement of individual fingers, even with undamaged muscle tissue. The unsatisfactory state of recognition of biosignals of the relevant cognitive commands is due to the shortcomings of modern intelligent information technologies of data analysis. There are well-known machine learning algorithms for establishing correspondence between biosignals and cognitive commands based on neural networks [6–8] and the method of support vectors [9, 10]. But the main disadvantages of these methods are sensitivity to the multidimensionality of the dictionary of recognition features and the alphabet of recognition classes, which occurs when recognizing biosignals of cognitive commands. In works [11, 12], it is proposed to use input data extractors built on artificial neural networks, which do not exclude the loss of information. The paper [13] considers the possibility of using fuzzy neural networks for signal recognition, but at the same time, there is also a problem of multidimensionality.

The use of ideas and methods of the so-called information-extreme intelligent technology (IEIT) of data analysis, which is based on maximizing the system's information capacity in the process of machine learning [14, 15], should be considered as a perspective direction. The central paradigm of information-extreme machine learning, as well as in neuro-like structures, is adapting the system's input information description to the maximum reliability of pattern recognition. But in contrast to neuro-like structures, the decision-making rules constructed within the framework of the geometric approach are practically invariant to the multidimensionality of the space of recognition features. The paper [16] considered the information-extreme machine learning system for controlling a wrist prosthesis for three gestures.

This article aims to increase the functional efficiency of the information-extreme machine learning of the hand bone prosthesis control system by optimizing the quantization of biosignals at the output of the electromyographic sensor. This approach makes it possible to form the so-called sparse training matrix, which reduces the influence of the power of the alphabet of recognition classes on the probability of making the correct classification decisions.

3 Research Methodology

3.1 Statement of the research task

Let the alphabet of recognition classes $\{X_m^o \mid m=\overline{1,M}\}$ and proper training matrix of the "object-property" type be formed $\| y_{m,i}^{(j)} \mid i=\overline{1,N}; j=\overline{1,J_{\max}} \|$, where *N, J_{max}* – the number of signs of recognition features and pattern realizations, respectively.

According to the concept of IEIT a structured vector of functioning parameters of the system, trained to reconise class X_m^o realisations, is given in the binary space of Hamming recognition features:

$$g_m =< x_m, d_m, \delta, h. >, \quad (1)$$

where x_m – averaged binary feature vector of the recognition class X_m^o; d_m – the radius of the hyperspherical container of the recognition class X_m^o, which in the process of machine learning is restored in the radial basis of the space of recognition features; δ – parameter of the field of control tolerances on recognition features;

h – quantization step by electromyographic biosignal level.

The parameter δ is equal to half of the symmetrical field of control tolerances on recognition features as shown in Figure 1.

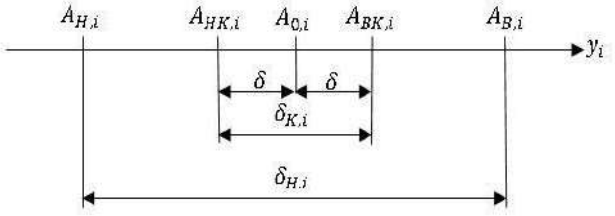

Figure 1 – Tolerance fields for the recognition feature

The following notations are used in Figure 1: $A_{0,i}$ – the nominal value of the feature y_i; $A_{H,i}$ – lower normalized (operational) tolerance; $A_{B,i}$ – upper

normalized tolerance; $A_{HK,i}$ – lower control tolerance; $A_{BK,i}$ – upper control tolerance; $\delta_{K,i}$ – field of control tolerances; $\delta_{H,i}$ – field of normalized tolerances.

The parameters of the system functioning, which will be called parameters of machine learning, are imposed by the following restrictions:

- the value range of recognition features is set by the maximum battery current of 100 mA
- the inequality gives the range of values of the radius of the recognition class container

$$d_m < d(x_m \oplus x_c),$$

where $d(x_m \oplus x_c)$ – intercenter distance between the averaged feature vector x_m and analogous vector x_c nearest neighbor class X_c^o;

- the parameter δ value range is given by inequality

$$\delta < \delta_H / 2,$$

where δ_H – the normalized field of tolerances for recognition features, which defines the range of values of control tolerances;

- the value of the parameter h is determined by the number of biosignal quantization steps in the range [0...100 mA].

It is necessary for the process of information-extreme machine learning of the hand prosthesis management system to:

1) optimize the parameters of machine learning (1), which provide the maximum value of the information optimization criterion in the working (acceptable) area of defining its function:

$$\overline{E}^* = \frac{1}{M}\sum_{m=1}^{M} \max_{G_E \cap \{k\}} E_m^{(k)}, \qquad (2)$$

where $E_m^{(k)}$– the value of the information criterion calculated at the k-th step of machine learning; G_E – the working area of defining the information criterion; $\{k\}$– is an ordered set of machine learning steps.

2) decide whether the recognized realization belongs to one of the classes of the given alphabet at the exam stage to check the functional effectiveness of machine learning.

Thus, the task of information synthesis of an intelligent wrist prosthesis control system consists of optimizing machine learning parameters (1) by approximating the global maximum of the information criterion (2) to its maximum limit value.

3.2 Functional categorical model of machine learning

The categorical model of information-extreme learning of the prosthesis control system is considered in the form of an oriented graph, the edges of which are characterized by set mapping operators. At the same time, the input mathematical description has the following structure

$$I = < G, T, \Sigma, Z, Y, X;\ f_1,\ f_2 >,$$

where G – a set of biosignals registered by the system; T – a set of data registration time moments; Σ – a dictionary of recognition features; Z – the space of possible functional states of the controlled process; Y – set of vectors of realizations of recognition classes, which forms an input training matrix; X – binary training matrix; f_1 – the operator of the input training matrix Y formation; f_2 - binary training matrix formation operator X.

Figure 2 shows the functional categorical model of information-extreme machine learning of the prosthesis control system with optimization of control tolerances on recognition features and quantization levels of biosignals at the output of the electromyographic sensor.

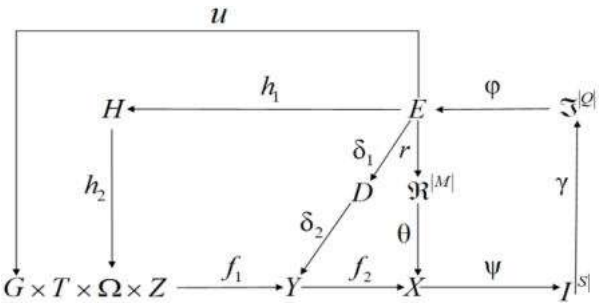

Figure 2 – Functional categorical model of information-extreme machine learning of the prosthesis control system

In Figure 2, the term set E, the elements calculated at each step of machine learning according to formula (2), is common to all optimization contours of vector parameters (1). The operator $r: E \to \widetilde{\Re}^{|M|}$, in the process of machine learning, restores the containers of recognition classes in the radial basis of the binary feature space, which generally forms a fuzzy partition $\widetilde{\Re}^{|M|}$. The operator θ reflects the partitioning $\widetilde{\Re}^{|M|}$ into a fuzzy distribution of a priori classified binary feature vectors of recognition classes. The next operator is $\psi: X \to I^{|S|}$, where $I^{|S|}$ – the set of hypotheses that checks the main statistical hypothesis $\gamma_1: x_m^{(j)} \in X_m^o$. The operator γ defines a set of accuracy characteristics $\Im^{|Q|}$, where $Q = S^2$, and operator φ calculates a set of values of information optimization criterion E that is a function of accuracy characteristics.

The categorical model contains the contour of optimization of control tolerances on recognition features, which is closed through the term set D of permissible values of control tolerances. At the same time, the operator δ_1 changes the control field at each step of machine learning, and the operator δ_2 evaluates the dependence of recognition features on the given control field of tolerances. In addition, the categorical model contains a circuit for optimizing the quantization levels of electromyographic biosignals, which includes the term set H of admissible values of quantization levels. In this circuit, at each step of machine learning, the operator h_1 changes the quantization level, and the operator h_2 changes the dictionary of recognition features Σ. The operator u regulates the process of machine learning.

3.3 Description of the machine learning algorithm

According to the categorical model (Fig. 2), the information-extreme machine learning algorithm of the prosthesis control system is presented in the form of a three-cycle iterative procedure for finding the global maximum of the information optimization criterion (2) in the working area of determining its function:

$$h^* = \arg\max_{G_h}\{\max_{G_\delta}\{\max_{G_E \cap \{k\}} \overline{E}^{(k)}_{\delta,h}\}\}, \qquad (3)$$

where $\overline{E}^{(k)}_{\delta,h}$ – the average value of the information criterion, calculated according to formula (2) at the k-th step of machine learning; G_h – the range of permissible values of quantization levels of biosignals; G_δ – the area of permissible values of control tolerances on recognition features.

The implementation of the machine learning algorithm of the prosthesis control system according to procedure (3) was carried out with the parallel optimization of control tolerances on recognition features, in which all tolerances for recognition features change simultaneously by a given value.

The input information for the machine learning algorithm is the array of the training matrix $\{y^{(j)}_{m,i}\}$ and the system of fields of normalized tolerances $\{\delta_{H,i}\}$ for recognition features, which sets the range of values of the corresponding control tolerances.

Let's consider the main stages of information-extreme machine learning:

1) Definition for a given alphabet of the basic class of recognition, in relation to which the control tolerances on the features of the averaged vector are determined. For this purpose, the internal cycle of procedure (3) is implemented, the main functions of which are the calculation of the information optimization criterion (2) at each machine learning step and the search for its global maximum, which determines the optimal radii of hyperspherical containers of recognition classes. At the same time, this procedure is carried out for all classes of recognition, which are considered consistently basic. The scheme of the algorithm, for example, in the case of the base class, X^o_m looks like this:

a) the averaged feature vector $y_m \in X^o_m$ is determined;

b) the input training matrix is transformed into a working binary training matrix, the elements of which are determined by the rule

$$x^{(j)}_{m,i} = \begin{cases} 1, & \text{if } y_{m,i} - \delta \le y^{(j)}_{1,i} \le y_{m,i} + \delta; \\ 0, & \text{if else;} \end{cases}$$

c) an array of averaged binary realization vectors is formed $\{x_{m,i} | m = \overline{1,M}, i = \overline{1,N}\}$, it's elements are formed by the rule

$$x_{m,i} = \begin{cases} 1, & if \ \ \frac{1}{n}\sum_{j=1}^{n} x^{(j)}_{m,i} > \rho_m; \\ 0, & ifelse, \end{cases}$$

where ρ_m – the selection level of binary vector coordinates $x_m \in X^o_m$, which is set by default ρ_m=0,5;

d) division of the set of averaged feature vectors $\{x_m\}$ into pairs of nearest "neighbors": $\Re^{|2|}_m = \langle x_m, x_l \rangle$, where x_l – the averaged feature vector of the neighboring class X^o_l;

e) optimization of the code distance d_m according to the iterative procedure of finding the global maximum of the information criterion for machine learning parameters optimization in the working area of its function determining:

$$d^*_m = \arg\max_{G_E \cap \{k\}} E^{(k)}_m$$

when fulfilling the restriction on the value of the radius d_m of the container of the recognition class X^o_m, it gain the form

$$d_m < d(x_m \oplus x_l).$$

As a result of sorting through all the recognition classes, the class with the maximum value of the optimization criterion (2) is taken as the basic. Then, for a given alphabet with a defined basic recognition class, procedure (3) is implemented in full, and optimal lower $A^*_{H,i}$ and upper $A^*_{B,i}$ control tolerances on recognition features are determined, respectively, according to the rules

$$A^*_{H,i} = y_{m,i} - \delta^*; \quad A^*_{B,i} = y_{m,i} + \delta^*;$$

Thus, for hyperspherical containers of recognition classes, the optimal parameters of information-extreme machine learning are the averaged vectors of recognition features $\{x^*_m\}$ for a given alphabet $\{X^o_m\}$, the radii of containers $\{d^*_m\}$ of recognition classes and the system of

control tolerances $\{A^*_{H,i}\}$ and $\{A^*_{B,i}\}$ on recognition features.

As a criterion for the optimization of machine learning parameters, we will use the modified information criterion of Kullbak, the working formula of which in case of equally probable two alternative hypotheses has the form

$$E_m^{(k)} = \frac{\left[n - (K_{1,m}^{(k)} + K_{2,m}^{(k)})\right]}{n} * \log_2 \left\{ \frac{2n + 10^{-p} - \left[K_{1,m}^{(k)} + K_{2,m}^{(k)}\right]}{\left[K_{1,m}^{(k)} + K_{2,m}^{(k)}\right] + 10^{-p}} \right\}, \quad (4)$$

where $K_{1,m}^{(k)}$ – the amount of events that mean the non-belonging of "own" feature vectors to the recognition class X_m^o; $K_{2,m}^{(k)}$ – the number of events that mean belonging to "foreign" feature vectors of the recognition class X_m^o; 10^{-p} – is a sufficiently small number that is entered to avoid division by zero; p – a number that is recommended in practice to choose from the interval $1 < p \le 3$.

The normalized modification of criterion (5) is given in the form [2]

$$E = \frac{E_m^{(k)}}{E_{\max}}, \quad (5)$$

where $E_{\max}$ – the value of the information criterion at the maximum values of the first and second reliabilities and zero errors of the first and second kind.

Decision rules were formed according to the optimal geometric parameters of the recognition class containers obtained in the process of machine learning. These rules may be presented in production form

$$(\forall X_m^o \in \widetilde{\Re}^{|M|}) \Big(if\ [(\mu_m > 0)\ \&\ (\mu_m = \max_{\{m\}} \{\mu_m\})]$$
$$then\ x^{(j)} \in X_m^o \quad else\ x^{(j)} \notin X_m^o \Big), \quad (6)$$

where $x^{(j)}$ – is a vector to recognizd; μ_m – is the function of the vector $x^{(j)}$ belonging to the container of the recognition class X_m^o.

In expression (6), the membership function for the hyperspherical container of the recognition class X_m^o is determined by the formula

$$\mu_m = 1 - \frac{d(x_m^* \oplus x^{(j)})}{d_m^*}, \quad (7)$$

where $d(x_m^* \oplus x^{(j)})$ – code distance between the vector x_m^* and the vector $x^{(j)}$ to be recognized.

Since the decision rules (7) are built within the framework of a geometric approach, they are practically invariant to the multidimensionality of the dictionary of recognition features and are characterized by high efficiency, which is an important indicator of the functional efficiency of the prosthesis control system in the working mode.

4 Results

The implementation of the machine learning algorithm considered above was carried out according to a fuzzy classified three-dimensional input learning matrix, obtained by processing electromyographic biosignals for seven movements of the wrist and fingers:

a) squeezing the thumb and middle fingers into a ring (class X_1^o);

b) pinch little finger and thumb (class X_2^o);

c) squeezing the thumb and forefinger into a ring (class X_3^o);

d) palm flexion (class X_4^o);

e) clenching the palm into a fist (class X_5^o);

f) palm extension (class X_6^o);

i) pinching the thumb and ring finger into a ring (class X_7^o).

Based on the electromyographic biosignals given in [17], an input training matrix was formed for each of the specified recognition classes. The formation of structured vectors of features of the corresponding classes of recognition was carried out by time quantization of a biosignal with a period of 10 ms at a given time interval of 2 s. That is, each vector consisted of 200 recognition features, and the number of vectors for each recognition class was equal to $n = 40$. At the same time, in order to filter the noise, the quantization of the biosignal began when its amplitude reached the threshold value of 30 mV.

The recognition class X_4^o (palm flexion) was chosen as the basic one, for which the maximum average value of the normalized criterion (5) was obtained. Then, machine learning of the prosthesis control system was implemented according to the procedure (3). At the same time, the quantization level was changed by 20 mV at each step of machine learning. Figure 3 shows graphs of the dependence of criterion (5) on the radii of the recognition class containers at the initial quantization level $h = 30mV$.

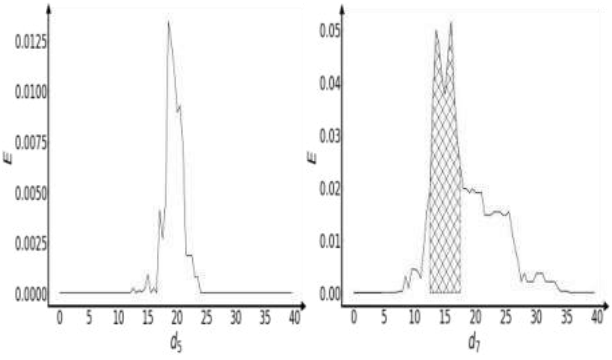

a b

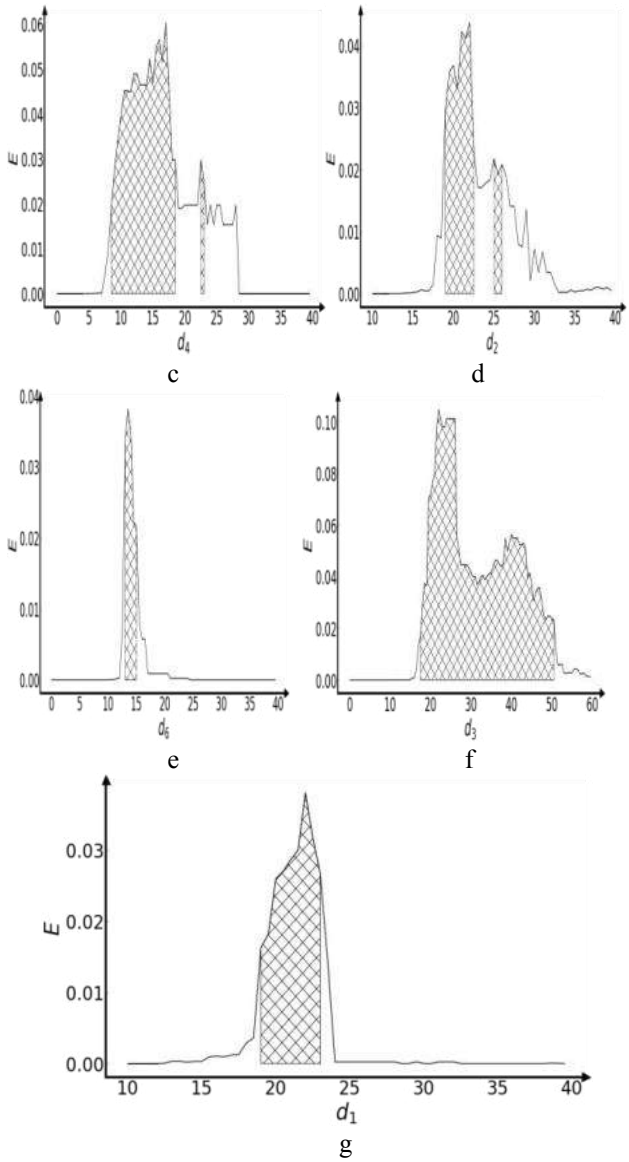

Figure 3 – Graphs of the dependence of the optimization criterion (5) on the radii of the recognition class containers: a – class X_1^o ; b – class X_2^o ; c – class X_3^o ; d – class X_4^o ; e – class X_5^o ; f – class X_6^o ; g – class X_7^o

In Figure 3, the working (allowable) area of the definition of the function of the information criterion (4) is indicated by double hatching, in which, with two alternative solutions, the first and second reliability is more, respectively, errors of the first and second kind.

The analysis of this figure shows that at the initial quantization level of biosignals ($h = 30mV$), the average value of the normalized information optimization criterion (5) is equal to $\overline{E} = 0{,}04$. At the same time, the recognition class X_1^o was not classified since there is no working area of the defining function of the information criterion. In the process of machine learning, the level of quantization of biosignals $h^* = 70mV$ is considered optimal, because the average value of criterion (5) is equal to $\overline{E} = 0{,}18$, i.e. increased more than four times.

Figure 4 shows graphs of the dependence of the normalized information criterion (5) on the radii of the recognition class containers at the optimal quantization level.

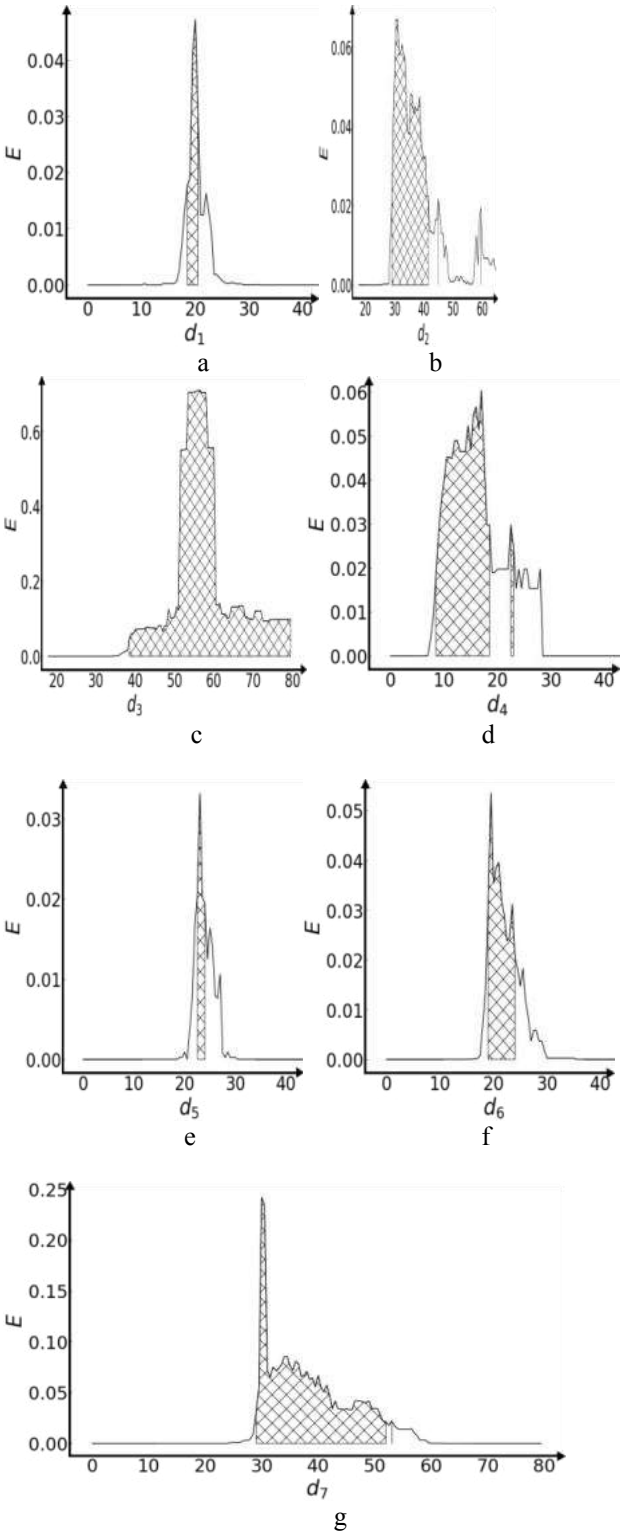

Figure 4 – Graphs of the dependence of the optimization criterion (5) on the radii of the recognition class containers at optimal level of quantization of biosignals: a – class X_1^o ; b – class X_2^o ; c – class X_3^o ; d – class X_4^o ; e – class X_5^o ; f – class X_6^o ; g – class X_7^o

In Figure 4, all recognition classes have working areas for determining the function of the optimization criterion, which means they are all informationally separated. To construct the decision rules (6), knowledge of the optimal geometric parameters of the recognition class containers obtained in machine learning is required. The analysis of Figure 4 shows that the optimal radii of the containers of the recognition classes are equal to: $d_1^* = 20$ (the Hamming distance in code units is still used here) for the class X_1^o, $d_2^* = 31$ for the class X_2^o, $d_3^* = 59$ for the class X_3^o, $d_4^* = 19$ for the class X_4^o, $d_5^* = 23$ for the class X_5^o, $d_6^* = 19$ for the class X_6^o і $d_7^* = 29$ for the class X_7^o.

The relatively low value of the criterion for optimizing machine learning parameters indicates the existence of a significant intersection of recognition classes in the space of Hamming features.

Conclusions

The information-extreme machine learning algorithm of the prosthesis control system is proposed for the recognition of electromyographic biosignals of cognitive commands for seven wrist and finger movements. The depth of machine learning was equal to the third level, at which the geometric parameters of the recognition class containers, the system of control tolerances for recognition features, and the levels of quantization of biosignals from the output of the electromyographic sensor were optimized.

This level of depth of information-extreme machine learning made it possible to obtain the information separability of all classes of recognition from the given alphabet. In addition, optimizing the quantization level of biosignals made it possible to significantly increase the functional efficiency of machine learning due to the formation of a sparse learning matrix. The use of a sparse matrix reduces the degree of intersection of recognition classes in the feature space, which makes it possible to increase the reliability of classification cracks. Based on the optimal geometric parameters of the recognition class containers obtained in machine learning, decisive rules are built that are characterized by high efficiency.

A promising direction for increasing the functional efficiency of the proposed method of information-extreme machine learning is to increase its level of depth by optimizing additional parameters, including input data processing parameters. In addition, when increasing the power of the alphabet of recognition classes, it is advisable to use hierarchical information-extreme machine learning.

Acknowledgment

The research was partially carried out within the project “Fulfillment of tasks of the perspective plan of development of a scientific direction “Technical sciences” Sumy State University” funded by the Ministry of Education and Science of Ukraine (State reg. no. 0121U112684).

References

1. Svensson, P., Wijk, U., Björkman, A., Antfolk, C. (2017). A review of invasive and non-invasive sensory feedback in upper limb prostheses. *Expert Review of Medical Devices*, Vol. 14(6), pp. 439–447, doi: 10.1080/17434440.2017.1332989.
2. Roche, A. D., Rehbaum, H., Farina, D., Aszmann, O. C. (2014). Prosthetic myoelectric control strategies: a clinical perspective. *Curr. Surg. Reports*, Vol. 2(3), doi: 10.1007/s40137-013-0044-8.
3. Zhang, T., Jiang, L., Liu, H. (2018). Design and functional evaluation of a dexterous myoelectric hand prosthesis with biomimetic tactile sensor. *IEEE Trans. Neural Syst. Rehabil. Eng.*, Vol. 26(7), pp. 1391–1399, doi: 10.1109/TNSRE.2018.2844807.
4. Liang, G., Wang, Y., Mei, D., Xi, K., Chen, Z. (2015). Flexible capacitive tactile sensor array with truncated pyramids as dielectric layer for three-axis force measurement. *J. Microelectromechanical Syst.*, Vol. 24(5), pp. 1510–1519, doi: 10.1109/JMEMS.2015.2418095.
5. Markovic, M., Dosen, S., Popovic, D., Graimann, B., Farina, D. (2015). Sensor fusion and computer vision for context-aware control of a multi degree-of-freedom prosthesis. *J. Neural Eng.*, Vol. 12(6), doi: 10.1088/1741-2560/12/6/066022.
6. Basturk, A., Yuksel, M. E., Caliskan, A., Badem, H. (2017). Deep Neural Network Classifier for Hand Movement Prediction. *Proceedings of the 25th Signal Processing and Communications Applications Conference, SIU 2017, June 2017*, doi: 10.1109/SIU.2017.7960566.
7. Stango, A., Negro, F., Farina, D. (2015). Spatial correlation of high density EMG signals provides features robust to electrode number and shift in pattern recognition for myocontrol. *IEEE Trans. Neural Syst. Rehabil. Eng.*, Vol. 23(2), pp. 189–198, doi: 10.1109/TNSRE.2014.2366752.
8. Atzori, M., Cognolato, M., Müller, H. (2016). Deep learning with convolutional neural networks applied to electromyography data: A resource for the classification of movements for prosthetic hands. *Front. Neurorobot.*, Vol. 10(SEP), 9, doi: 10.3389/fnbot.2016.00009.
9. Gheorghe, M. (2015). A support vector machine approach for developing telemedicine solutions: medical diagnosis. *Network Intelligence Studies*, Vol. 3(1(5)), pp. 43-48.
10. Rossi, M., Benatti, S., Farella, E., Benini, L. (2015). Hybrid EMG classifier based on HMM and SVM for hand gesture recognition in prosthetics. *Proceedings of the IEEE International Conference on Industrial Technology, June 2015*, pp. 1700–1705, doi: 10.1109/ICIT.2015.7125342.

11. Olsson, A. E., Sager, P., Andersson, E., Björkman, A., Malešević, N., Antfolk, C. (2019). Extraction of multi-labelled movement information from the raw HD-sEMG image with time-domain depth. *Sci. Rep.*, Vol. 9(1), doi: 10.1038/s41598-019-43676-8.
12. Moskalenko, V. V., Korobov, A. G. (2017). Information-extreme algorithm of the system for recognition of objects on the terrain with optimization parameter feature extractor. *Radio Electronics, Computer Science, Control*, Vol. 2, pp. 61–69, doi: 10.15588/1607-3274-2017-2-7
13. Subbotin, S. (2013). The neuro-fuzzy network synthesis and simplification on precedents in problems of diagnosis and pattern recognition. *Optical Memory and Neural Networks*, Vol. 22(2), .pp. 97–103, doi: 10.3103/s1060992x13020082.
14. Dovbysh, A. S., Budnyk, M. M., Piatachenko, V. Yu., Myronenko, M. I. (2020). Information-extreme machine learning of on-board vehicle recognition system. *Cybernetics and Systems Analysis*, Vol. 56(4), pp 534–543, doi: 10.1007/s10559-020-00269-y.
15. Dovbysh, A. S., Shelehov, I. V., Prylepa, D. V., Golub, I. (2016). Information synthesis of adaptive system for visual diagnostics of motional and mental state of a person. *Eastern-European Journal of Enterprise Technologies*, Vol. 4/9(82), pp. 11–17, doi: 10.15587/1729-4061.2016.75683.
16. Dovbysh, A. S., Piatachenko, V. Y., Simonovskiy, J. V., Shkuropat, O. A. (2020). Iinformation-extreme hierarchical machine learning of the hand brush prosthesis control system with a non-invasive bio signal reading system. *Radio Electron. Comput. Sci. Control*, Vol. 4, pp. 178–187, doi: 10.15588/1607-3274-2020-4-17.
17. Kaczmarek, P., Mańkowski, T., Tomczyński, J. (2019). PutEMG – A surface electromyography hand gesture recognition dataset. *Sensors*, Vol. 19(16), 3548, doi: 10.3390/s1916354.

JOURNAL OF ENGINEERING SCIENCES

Volume 9, Issue 2 (2022)

5-th Grabchenko's International Conference on Advanced Manufacturing Processes (InterPartner-2023)

Dear Colleagues!

We would like to invite you to submit original and unpublished research papers to the **5-th Grabchenko's International Conference on Advanced Manufacturing Processes (InterPartner-2023)**, organized by Odessa Polytechnic National University, National Technical University «Kharkiv Polytechnic Institute», Sumy State University and International Association for Technological Development and Innovations, which will be held on September 05–08, 2023 in Odessa, Ukraine. The official website is http://interpartner.odessa.ua

InterPartner-2023 focuses on promoting research and developmental activities, intensification of scientific information interchange between researchers, developers, and engineers. The conference is an ideal platform for people to share views and experiences in fields of **Manufacturing Engineering**, **Mechanical Engineering**, **Materials Science**, and **Quality Assurance**.

Authors should submit their papers online using the EasyChair Conference Management System. The submission page for InterPartner-2023 is https://easychair.org/conferences/?conf=interpartner2023

The deadline for paper submission is **February 15, 2023**. After the careful reviewing process, all accepted papers will be published and submitted to the database Scopus, Web of Science, and |other indexing services. Accepted papers must be presented at the conference by one of their authors, who commit to register and attend the conference. The Steering Committee reserves the right to exclude papers that have not been presented from the proceedings.

Looking forward to your submissions!

Best regards,

Prof. Volodymyr Tonkonogyi,
Conference Chair

JOURNAL OF ENGINEERING SCIENCES

Volume 9, Issue 2 (2022)

Salahudeen N., Abubakar M. (2022). Isotherm study of crystal violet on activated carbon synthesized from millet stover. Journal of Engineering Sciences, Vol. 9(2), pp. F1-F5, doi: 10.21272/jes.2022.9(2).f1

Isotherm Study of Crystal Violet on Activated Carbon Synthesized from Millet Stover

Salahudeen N.*, Abubakar M.

Department of Chemical and Petroleum Engineering, Bayero University, Kano 700281, Nigeria

Article info:
Submitted: March 20, 2022
Accepted for publication: July 22, 2022
Available online: September 5, 2022

***Corresponding email:**
nsalahudeen.cpe@buk.edu.ng

Abstract. Continuous release of synthetic dyes from industrial effluent into surface water poses a huge environmental threat and health hazard to humans and aquatic life. The need to right the wrong occasioned by the inimical industrial practice of uncontrolled release of carcinogenic dyes into the surface water calls for research into effective treatment technologies for the treatment of dye-contaminated industrial effluent. The isotherm of Crystal Violet (CV) solution on activated carbon (AC) synthesized from millet stover was investigated and presented herein. Samples of AC were synthesized from millet stover at 120ºC using phosphoric acid as the activating agent. Employing varying mix ratios of stover-to-phosphoric acid (1:0, 1:1, 1:2, 1:3, and 1:4), respective samples of AC were synthesized. The batch adsorption process of the various samples of the AC in 15 mg/l initial concentration of an aqueous solution of CV was carried out at varying times. The CV's change in the sorbate's concentration was monitored using a UV spectrophotometer. The optimum adsorption time was 240 min. The optimally synthesized activated carbon was the 1:2 sample having an equilibrium sorbent concentration of 0.74 mg/L and sorbate uptake of 95.1%. Langmuir, Freundlich and Temkin isotherm models were employed for the isotherm analysis. The R^2 values of the Langmuir, Freundlich and Temkin models were 0.99, 0.90, and 0.94, respectively. The isotherm constants for the Langmuir, Freundlich and Temkin models were –1.52 l/mg, –4.08, and 0.005 l/min, respectively. The Langmuir isotherm model best fitted the adsorption mechanism with a maximum equilibrium adsorption capacity of 14.0 mg/g.

Keywords: millet stover, activated carbon, crystal violet, isotherm model.

1 Introduction

Activated carbon is a porous adsorbent with a highly developed internal pore structure and large surface area prepared from the activation of biomass. Activated carbon possesses active sites and is applied for the adsorption of sorbate molecules. They are usually applied in wastewater and municipal water treatments and in air purification [1].

Globally, the annual production of activated carbon was estimated to be about 100,000 tonnes [2]. The feedstock used for activated carbon production is agricultural materials which normally are disposed of as wastes [3, 4]. Examples of the agricultural wastes used in the synthesis of activated carbon include coconut shell [5], rice husk, sugarcane bagasse, sawdust [6], yam peels, potatoes peels, cassava peels, durian peel [7, 8], and watermelon. The carbon content of these materials ranges from 40 to 90% wt. [9, 10]. Activated carbon is produced by the activation process involving the thermal activation of a biomass feedstock in the presence of a chemical activating agent in an inert atmosphere. The most used activating agent for the synthesis of activated carbon is potassium hydroxide (KOH), sodium hydroxide (NaOH), zinc chloride (ZnCl), phosphoric acid (H_3PO_4) and potassium carbonate (K_2CO_3).

Recent studies on the statistics of activating agents employed for the synthesis of the activating agent over the last two decades have shown that used KOH, NaOH, ZnCl, H_3PO4, K_2CO_3, and new activating agents were 22.0, 11.0, 18.5, 21.0, 14.0, and 13.5%, respectively.

The active sites of activated carbon contain functional groups such as carboxyl, carbonyl, phenol, lactone, and quinone responsible for adsorbing contaminants. The functional group in a particular activated carbon is a function of the biomass feedstock used for the synthesis and the synthesis condition. The mechanism and extent of adsorption of sorbate molecules on activated carbon is a function of the functional group present on the active site and their chemical affinity with the sorbate molecules [2].

This work aimed to study the isotherm of adsorption of crystal violet contaminated water over a low temperature synthesized activated carbon using millet stover biomass feedstock.

2 Research Methodology

Materials used include; raw millet stover collected from a farm in Janguza, Ungogo Local Government Area of Kano State – Nigeria, Phosphoric acid, crystal violet powder, and distilled water. Equipment includes weighing balance (Model; PE-160), shaker (KJ-201 BS OSCILLATOR), UV-Vis spectrophotometer (Model; Zuzi-4201/20), milling machine, and laboratory oven. Apparatus used include measuring cylinder, conical flask, crucibles, beakers, and spatula.

Synthesis of activated carbon was synthesized at low temperatures using phosphoric acid as the activating agent. Different samples of the AC were prepared to measure a constant weight of millet stover in each case and to add a varying dosage of phosphoric acid to make 1:0, 1:1, 1:2, 1:3, and 1:4. The mixture was thoroughly mixed and then heated in the oven at 120 °C for 1 h. After activation, the activated carbon was washed with distilled water until the pH was 7.0. The washed AC samples were dried in the oven at 110 °C for 1 h to remove the moisture content.

Adsorption study of aqueous CV solution (sorbate) on varying samples of synthesized AC (sorbent) was carried out using 50 ml of CV sorbate at the constant initial concentration of 15 mg/l. The adsorption process was carried out by continuous mechanical shaking action of a laboratory shaker. The percentage sorbate uptake (%A) and the equilibrium adsorption capacity of the sorbent, q_e (mg/g) were determined by the following equations:

$$\%\mathrm{A} = \frac{C_o - C_e}{C_o} \times 100; \quad (1)$$

$$q_e = \frac{C_o - C_e}{m} v, \quad (2)$$

where C_O – the initial concentration of the sorbate; C_e – equilibrium concentration of the sorbate; m – the weight of adsorbent, g; v – the volume of the sorbate, l.

An isotherm study of the adsorption of CV sorbate on the synthesized AC was carried out using Langmuir, Freundlich, and Temkin models. Graphical analysis of the linearized form of the various isotherm models was carried out using experimental laboratory data to establish the various model parameters.

The Langmuir isotherm mechanism is based on the monolayer adsorption model and depicts homogeneity in the adsorbent surface [17]. The Langmuir isotherm model is as follows:

$$q_e = \frac{q_\infty \mathrm{b} C_e}{1 + \mathrm{b} C_e}, \quad (3)$$

where q_∞ – the monolayer theoretical capacity of the adsorbent or the maximum achievable adsorption density (mg of adsorbate per 1 g of adsorbent); b – the Langmuir equilibrium constant, l/mg.

The linearized Langmuir isotherm model is as follows:

$$\frac{C_e}{q_e} = \frac{C_e}{q_\infty} + \frac{1}{q_\infty \mathrm{b}}. \quad (4)$$

The Freundlich isotherm mechanism is based on a multilayer adsorption model, and depicts heterogeneity in the adsorbent surface [11]. The Freundlich isotherm mechanism is based on the multilayer heterogeneous adsorption model. The isotherm model is as follows:

$$q_e = K_f C_e^{1/n}, \quad (5)$$

where K_f – the Freundlich multilayer adsorption constant, related to bond strength and the dimensionless heterogeneity factor, l/g; n – adsorption intensity.

The linearized form of the Freundlich isotherm model is as follows [12]:

$$\log q_e = \log K_f + 1/\mathrm{n} \log C_e. \quad (6)$$

The Temkin isotherm mechanism is based on the interaction between the adsorbent surface and the sorbate molecules/ions. The isotherm is developed on the assumption that the free energy of sorption is a function of the surface coverage [13, 14]. The Temkin isotherm model is as follows:

$$A_t C_e = e^{\frac{q_e b_t}{RT}}, \quad (7)$$

where C_e – concentration of the adsorbate at equilibrium, mg/l; q_e – the amount of adsorbate adsorbed at equilibrium, mg/g; T – the absolute temperature, K; R – the ideal gas constant, J/(mol·K); $\frac{RT}{b_t}$ – a measurement of heat of adsorption; $\frac{1}{b_t}$ – the adsorption potential of the adsorbent, mol/kJ.

A_t – Temkin constant as the equilibrium binding constant (l/min), corresponding to the maximum binding energy. Linearized Freundlich isotherm model is as follows:

$$q_e = \left(\frac{RT}{b_t}\right) \ln A_t + \left(\frac{RT}{b_t}\right) \ln C_e. \quad (8)$$

3 Results and Discussion

Table 1 presents the adsorption results using varying samples of the synthesized AC.

Table 1 – Percentage uptake of CV on the various samples of the synthesized AC

AC Sample	C_e, mg/l	%A
1:0	2.1942	85.37
1:1	0.9427	93.72
1:2	0.74089	95.06
1:3	0.9546	93.64
1:4	0.9974	93.35

It could be observed that the inactivated sample of the millet stover (1:0) had a sorbate uptake of 85.4%. However, the 1:1 AC sample gave 8.3% higher sorbate uptake, while a further increase of 1.3% was observed for the 1:2 AC sample. The sorbent uptake declined for the AC samples having a higher dosage of an activating agent. Therefore, the 1:2 AC sample was considered the optimum synthesized AC sample with an equilibrium sorbent concentration of 0.74 mg/l and sorbate uptake of 95.1%.

For the adsorption carried out using the 1:2 sample, Table 2 presents the equilibrium sorbate concentration at varying adsorption times.

Table 2 – Equilibrium sorbate concentration and adsorption capacity at varying adsorption time

Time, min	C_e, mg/l	q_e, mg/g
30	6.01	15.00
60	3.50	19.20
90	2.86	20.20
120	2.51	20.82
150	1.68	22.20
180	1.94	21.76
240	1.77	22.06
270	1.62	22.30

Starting with the initial sorbate concentration of 15 mg/l, the equilibrium sorbate concentration dropped by 60% after 30 min to attain a value of 6.01 mg/l.

Using equation (1), the equilibrium adsorption capacity after 30 min was 15.0 ml/l. With a further increase in the adsorption time, the equilibrium sorbate concentration dropped until no substantial decrease was observed after 240 min.

Figure 1 shows the Freundlich isotherm graph for the adsorption of CV sorbate on the sorbent synthesized from millet stover.

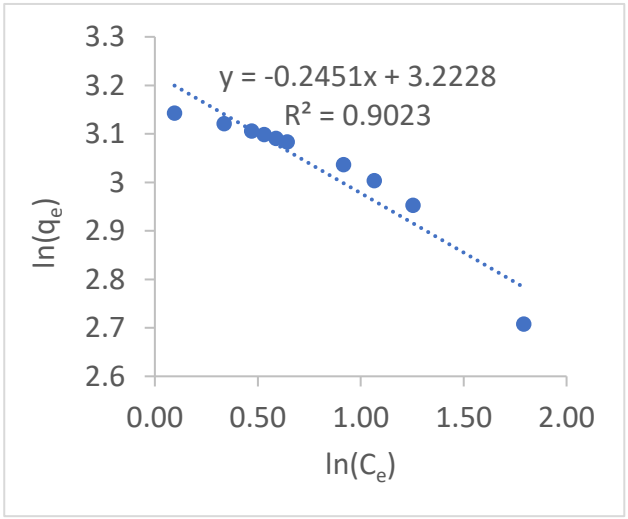

Figure 1 – Freundlich isotherm graph of the adsorption process

The Freundlich model properly fits the adsorption mechanism with an R^2 of 0.90. The graph had a negative slope of –0.2451 and a positive intercept of 3.2. Therefore, the Freundlich multilayer adsorption constant, K_f was 1,584.9 l/g, and the dimensionless heterogeneity factor, n was –4.08.

Figure 2 shows the Langmuir isotherm chart of the adsorption of the sorbate on the sorbent.

The high coefficient of determination, R^2 of 0.99 showed that the Langmuir model fitted the adsorption mechanism perfectly. The graph's slope was 0.0715 g/mg, and the intercept was –0.0471. Therefore, the maximum adsorption capacity of the sorbent was 14.0 mg/g. Langmuir constant, b was determined as –1.52 l/mg.

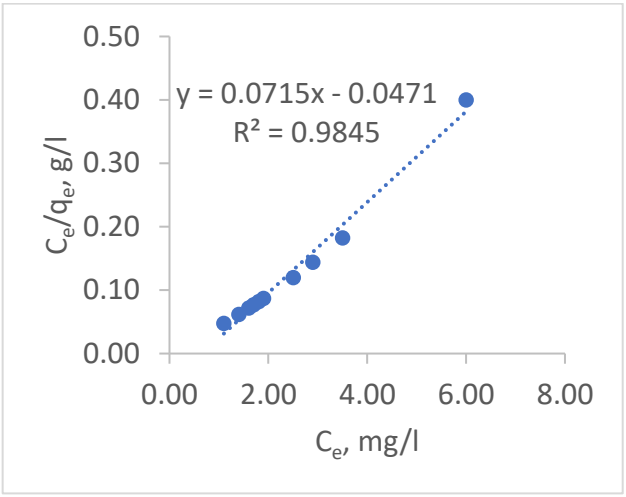

Figure 2 – Langmuir isotherm graph of the adsorption process

Figure 3 shows the Temkin graph for the adsorption of CV sorbate on the synthesized sorbent.

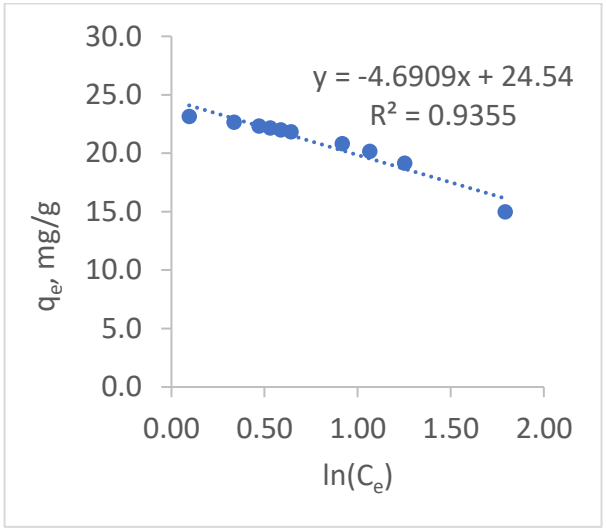

Figure 3 – Temkin isotherm graph of the adsorption process

The Temkin model also gave a good fit of the adsorption mechanism with a fairly R^2 of 0.94. The graph had a negative slope of –4.69 and a positive intercept of 24.54. The adsorption process was conducted at 298 K, using the gas constant of 8.314 J/(mol·K), the adsorption potential of the adsorbent $\frac{1}{b_t}$ was –0.002 mol/kJ, and the maximum binding energy A_t was 0.005 l/min.

Table 3 presents a summary of the various adsorption parameters determined for the adsorption of CV on the AC synthesized from millet stover.

Table 3 – Summary of the various isotherm parameters

Langmuir		Freundlich		Temkin	
R^2	0.99	R^2	0.90	R^2	0.94
q_e, mg/g	14.0	K_f, l/g	1,584.9	$\frac{1}{b_t}$, mol/kJ	–0.002
b, l/mg	–1.52	n	–4.08	A_t, l/min	0.005

It could be observed that Langmuir was the best fit based on the R^2 value.

The Langmuir isotherm had the highest R^2 value of 0.99. This implied that the adsorption process was homogeneous monolayer adsorption [15, 16].

The equilibrium adsorption capacity was 14.0 mg/g, and the Langmuir constant was negative, having a value of –1.52 l/mg. This further implied that the sorbate molecules had a negative binding affinity to the site of the sorbent [17].

Although the Freundlich isotherm gave a reasonably high R^2 value of 0.90, the isotherm model was unsuitable for the adsorption mechanism as the Freundlich constant, n representing the multilayer adsorption intensity, was negative [18].

The Temkin isotherm model also gave a reasonably high R^2 value of 0.94. It had a negative adsorption potential, implying that the Temkin model was not a good fit for the adsorption mechanism.

4 Conclusions

Adsorption isotherm study of crystal violet solution over activated carbon synthesized from millet stover at low temperature was carried out.

Activation of the stover millet was carried out at 120 °C using phosphoric acid as the activating agent. Varying sorbent samples based on the activating agent's dosage were prepared. They were 1:0, 1:1, 1:2, 1:3, and 1:4 samples.

The Adsorption study showed that the 1:2 sample was the optimum, with an equilibrium sorbent concentration of 0.74 mg/l and sorbate uptake of 95.1 %. The adsorption isotherm study using Langmuir, Freundlich, and Temkin isotherm models showed Langmuir's coefficient of determination (R2), Freundlich, and Temkin models were 0.99, 0.90, and 0.94, respectively. The adsorption process was homogeneous monolayer adsorption as the Langmuir isotherm model gave the best fit for the adsorption mechanism having a maximum equilibrium adsorption capacity of 14.0 mg/g and the Langmuir constant of –1.52 l/mg. The sorbate molecules had a negative binding affinity to the site of the sorbent, as suggested by the negative value of the Langmuir adsorption constant.

References

1. Samsuri, A., Sadegh-Zadeh, F., Seh-Bardan, B. (2014). Characterization of biochars produced from oil palm and rice husks and their adsorption capacities for heavy metals. Int J Environ Sci Technol, Vol. 11, pp. 967-976.
2. Yousefi, M., Arami, S., Takallo, M. (2019). Modification of pumice with HCl and NaOH enhancing its fluoride adsorption capacity: kinetic and isotherm studies. Hum Ecol Risk Assess, Vol. 25, pp. 1508-1520.
3. Rahman, M. M., Bari, Q. H., Mohammad, N., Ahsan, A., Sobuz, H. R., Uddin, M. A. (2013). Characterization of rice husk carbon produced through simple technology. Adv. Mater. Sci. Appl., Vol. 2 (1), pp. 25-30.
4. Alvarez, J., Lopez, G., Amutio, M., Bilbao, J., Olazar, M. (2014). Upgrading the rice husk char obtained by flash pyrolysis for the production of amorphous silica and high quality activated carbon. Bioresour. Technol., Vol. 170, pp. 132–137.
5. Boopathy, R., Karthikeyan, S. (2013). Adsorption of ammonium ion by coconut shell-activated carbon from aqueous solution: kinetic, isotherm, and thermodynamic studies. Env. Sci Pollut Res., Vol. 20, pp. 533-542.
6. Kini, S. M., Saidutta, M. B., Murty, R. V., Kadoli, S. V. (2015). Adsorption of basic dye from aqueous solution using HCl treated saw dust (Lagerstroemia microcarpa): kinetic, modeling of equilibrium, thermodynamic. International Research Journal of Environment Sciences, Vol. 2 (8), pp. 6-16.
7. Saueprasearsit, P. (2011). Adsorption of chromium (Cr+6) using durian peel. Intl Conf on Biotechnology and Environment Management, Singapore, Vol. 18, pp. 33-38.
8. Srikun, S., Hirunpraditkoon, S., Nuithitikul, K. (2011). Lead adsorption of activated carbon synthesized from durian peel. Adv. Fluid Mechnics Heat. Mass Transf., Vol. 2011, pp. 66-71.
9. Cui, X., Jia, F., Chen, Y., Gan, J. (2011). Influence of single-walled carbon nanotubes on microbial availability of phenanthrene in sediment. Ecotoxicology, Vol. 20, pp. 1277-1285.
10. Khadhri, N., Saad, M. E. K., Mosbah, M., Moussaoui, Y. (2019). Batch and continuous column adsorption of indigo carmine onto activated carbon derived from date palm petiole. J Environ Chem Eng., Vol. 7, 102775.
11. Alwi, R. S., Gopinathan, R., Bhowal, A., Garlapati, C. (2020). Adsorption characteristics of activated carbon for the reclamation of eosin Y and indigo carmine colored effluents and new isotherm model. Molecules, Vol. 25(24), 6014.
12. Bedia, J., Peñas-Garzón, M., Gómez-Avilés, A., Rodriguez, J. J., Belver, C. (2020). Review on activated carbons by chemical activation with FeCl3. Journal of Carbon Research, Vol. 6(2), 21.

13. Huang, Y., Zhao, G. (2016). Preparation and characterization of activated carbon fibers from liquefied wood by KOH activation. Holzforschung, Vol. 70, pp. 195-202.
14. Heidarinejad, Z., Dehghani, M. H., Heidar, M., Javedan, G., Sillanpaa, I. A. M. (2020). Methods for preparation and activation of activated carbon: A review. Environmental Chemistry Letters, Vol. 18, pp. 393-415.
15. Somsesta, N., Sricharoenchaikul, V., Aht-Ong, D. (2020). Adsorption removal of methylene blue onto activated carbon/cellulose biocomposite films: Equilibrium and kinetic studies. Mater. Chem. Phys., Vol. 240, 122221.
16. Zakaria, R., Jamalluddin, N. A., Bakar, Z. M. A. (2021). Effect of impregnation ratio and activation temperature on the yield and adsorption performance of mangrove based activated carbon for methylene blue removal. Results in Materials, Vol. 10, 100183.
17. Islam, M. A., Chowdhury, M. A., Mozumder, M. S. I., Uddin, M. T. (2021). Langmuir adsorption kinetics in liquid media: Interface Reaction Model. ACS Omega, Vol. 6, pp. 14481-14492.
18. Das, B., Mondal, N. K., Bhaumik, R., Roy, P. (2014). Insight into adsorption equilibrium, kinetics and thermodynamics of lead onto alluvial soil. Int. J. Environ. Sci. Technol., Vol. 11, pp. 1101-1114.

JOURNAL OF ENGINEERING SCIENCES

Volume 9, Issue 1 (2022)

Huliienko S. V., Korniyenko Y. M., Muzyka S. M., Holubka K. (2022). Simulation of reverse osmosis process: Novel approaches and development trends. Journal of Engineering Sciences, Vol. 9(2), pp. F6-F36, doi: 10.21272/jes.2022.9(2).f2

Simulation of Reverse Osmosis Process: Novel Approaches and Development Trends

Huliienko S. V.[1*[0000-0002-9042-870X]], Korniyenko Y. M.[1[0000-0002-3031-6212]], Muzyka S. M.[1], Holubka K.[2]

[1] National Technical University of Ukraine "Igor Sikorsky Kyiv Polytechnic Institute", 37, Peremohy Ave., 03056, Kyiv, Ukraine;
[2] University of Montpellier, 163, Auguste Broussonnet St., 34090, Montpellier, France

Article info:
Submitted: May 8, 2022
Accepted for publication: September 9, 2022
Available online: September 12, 2022

***Corresponding email:**
sergii.guliienko@gmail.com

Abstract. Reverse osmosis is an essential technological separation process that has a large number of practical applications. The mathematical simulation is significant for designing and determining the most effective modes of membrane equipment operation and for a deep understanding of the processes in membrane units. This paper is an attempt at systematization and generalizing the results of the investigations dedicated to reverse osmosis simulation, which was published from 2011 to 2020. The main approaches to simulation were analyzed, and the scope of use of each of them was delineated. It was defined that computational fluid dynamics was the most used technique for reverse osmosis simulation; the intensive increase in using of molecular dynamics methods was pointed out. Since these two approaches provide the deepest insight into processes, it is likely that they will further be widely used for reverse osmosis simulations. At the same time, for the simulation of the membrane plant, it is reasonable to use the models that required the simplest solutions methods. The solution-diffusion model appears to be the most effective and flexible for these purposes. Therefore, this model was widely used in considering the period. The practical problems solved using each of the considered approaches were reviewed. Moreover, the software used for the solution of the mathematical models was regarded.

Keywords: reverse osmosis, membrane, simulation, optimization, software.

1 Introduction

The pressure-driven membrane processes are widely used in many industries, including chemical, food, pharmaceutical, biotechnologies, water treatment, and environmental protection. The mathematical simulation of the process plays an essential role in designing and exploring such equipment since this technique defines the most rational design of apparatus and operation modes with a lower number of experimental investigations. However, there exists quite a significant number of approaches to the simulation. Therefore, the systematized information about types of mathematical models of pressure-driven membrane processes would help choose the simulation method for the particular process. In previous work [1], the attempt was to systematize the theoretical investigation of pressure driven membrane processes from 2000 to 2010. This work is an extension of the previous one, and the works published between 2011 and 2020 are considered there.

First of all, it should be noted that in work [1], in the waste majority of cases, it was considered the articles published in the leading thematic journal, namely Journal of Membrane Science and Desalination by Elsevier. In contrast, the attention to the other publication was insufficient. Also, during the considered period, new thematic journals began to be issued, particularly Membranes by MDPI. Therefore, the current work analyzed the bigger number of journals and more than 1000 publications dedicated to pressure driven membrane processes simulation. The publication distribution by years is shown in Figure 1, and the distribution among the main processes is shown in Figure 2.

It can be seen from Figure 1 that despite the drop in 2017 and 2018, the number of publications stable increased, which is evident that the actuality of such kind of investigation is increased. Moreover, the trend of the increase is more clearly seen than it was in work [1]. Figure 2, in turn, shows that the most significant number of research is dedicated to the question of simulation of reverse osmosis, which is the most widely applicated industrial pressure-driven membrane process. Also, a significant number of publications are dedicated to the simulation of nanofiltration (NF) and forward osmosis

(FO), which in work [1] was not considered. A lesser number of works are dedicated simulation of ultrafiltration (UF), microfiltration (MF), and also membrane bioreactors. The last ones were not considered in work [1] as a separate kind of process.

Taking into account a large number of publications in the considered period it was decided to make a review for each process separately. Correspondingly, the purpose of the current work is the analysis and generalization of the investigations dedicated to the simulation of reverse osmosis in the period from 2011 to 2020. The objectives of the research include: (1) the review and evaluation of areas for applications of the different approaches to RO simulations; (2) the comparison of the trends in developments of methods of RO simulation in the first two decades of the XXI century; (3) the analysis perspectives of the development of the RO simulation.

The distribution of the published works dedicated to RO simulation is shown in Figure 3. The represented data demonstrate that the research interest in this direction was steadily increasing.

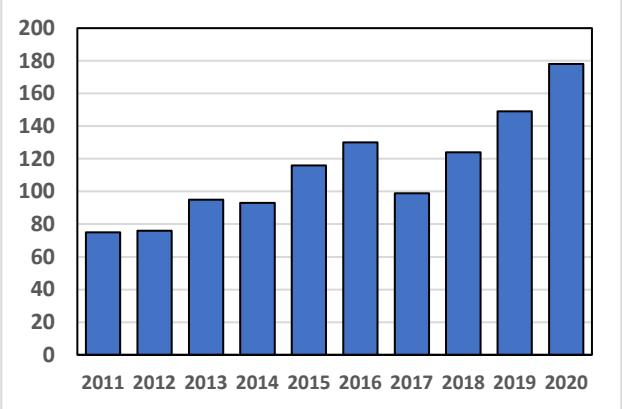

Figure 1 – The distribution of the publications selected for review by the years

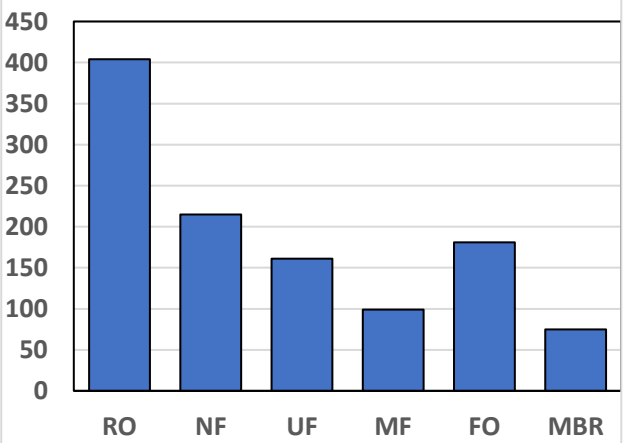

Figure 2 – The distribution the publication selected for review by the processes

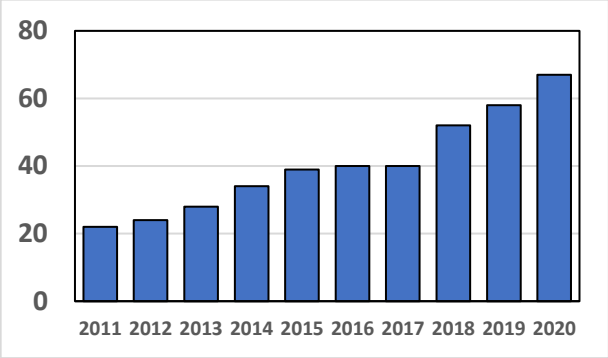

Figure 3 – The distribution of publications dedicated to the simulation of reverse osmosis by the years

As in work [1], the review does not claim comprehensiveness, however, it allows to sufficiently evaluate the main trends in the mathematical simulation of RO and the areas of application of the main approaches to the simulation.

It should be noticed that in 2011-2020 several substantial review articles were published in which the question of reverse osmosis simulation was considered. These works will be discussed below.

2 Research Methodology

In work [1] it was noticed that the traditional models include the following groups: irreversible thermodynamics-based models, diffusion-based models, and pore-flow-based models. The investigations with the application of computational fluid dynamics, artificial neuron networks, optimization, and economic analysis were identified as individual groups. The others approaches to the reverse osmosis simulation including semi-empirical models were also considered separately.

During 2011-2020 several reviews were published which prove the acceptability of such classifications with some corrections. In particular, in work [1] the models based on Kedem–Katchalsky equation (irreversible thermodynamics) were considered, and in work [3] detailed analysis of the irreversible thermodynamics and solution-diffusion models was made. The traditional models were also considered in the general review of RO desalination [4] and the review of the desalination processes simulation [5]. The reviewed works dedicated to the simulation with using of the computation fluids dynamics (CFD) [6-8] and molecular dynamics [9-11] were also published. Moreover, in works [12-13] it was considered both the traditional models and the molecular dynamics methods, in addition, in work [13] it was noticed that in researches until 2000 the application of the preferential sorption-capillary flow model was predominated while after 2001 the biggest progress was achieved with using of the molecular dynamic methods. The question of the RO optimization was considered in reviewed works [5, 14], and in work [15] the studies of the energy analysis of RO were revied.

In this review works the authors considered mainly modern researches, and the fraction of the works published

in the 1960s-1980s is relatively low. They significantly provide an indication of the state of art in the reverse osmosis mathematical simulation according to the individual approaches, however, no one of them did not consider all main approaches together. For example, in generalized works [12-13] the simulation using the CFD methods was not considered, and the attention to the artificial neuron networks in the reviews is almost absent. Therefore, such a review like the current work would be useful for the generalized understanding of the RO simulation and the trends of the mathematical modeling of RO.

Taking into account the works [9-11] and work [15], it was decided that except the class of models distinguished in the previous work [1] to consider individually the molecular dynamics method and energy analysis. With this, the distribution of the approaches in chosen for the review publication is shown in Figure 4.

As in the previous period, the most number of works are dedicated to the simulation with an application of CFD and optimization methods, while the number of irreversible thermodynamics-based models and pore flow-based models is still low. It was unexpected to define the relatively high number of models based on the solution-diffusion concept.

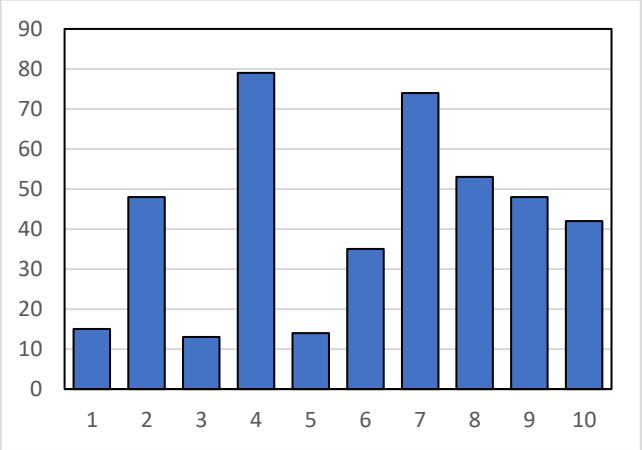

Figure 4 – The distribution of the RO models in chosen publication by classes: 1 – irreversible thermodynamics; 2 – diffusion; 3 – pore flow; 4 – computational fluid dynamics; 5 – artificial neuron networks; 6 – molecular dynamics; 7 –optimization; 8 – energy analysis; 9 – economic analysis; 10 – others models

3 Results

3.1 Irreversible thermodynamics models

The main models of this class include the Kedem–Katchalsky and the Spiegler–Kedem model, which was used in the limited extend during 2011-2020 (Figure 5). In particular. The Kedem–Katchalsky model was considered in works [2, 16-19], the works [20-27] were dedicated to the Spiegler–Kedem model, and in works [3, 28], both models were used.

The Kedem–Katchalsky model is based on the assumption of a linear relationship between flux and potential gradient. The membrane performance, in this case, can be determined by using phenomenological coefficients [9].

The transport through the membrane of non-electrolyte binary solutions, caused by the pressure difference and also by the osmotic pressure difference, according to the Kedem–Katchalsky model can be described by the following equations [2]:

$$J_w = L_p\left(\Delta p - \sigma\cdot\Delta\pi\right) \quad (1)$$

$$J_s = \omega\cdot\Delta\pi + \left(1-\sigma\right)\cdot\overline{c}\cdot J_w \quad (2)$$

where Δp is the applied pressure difference; $\Delta\pi$ is the osmotic pressure difference; $\overline{c}$ is the mean concentration of salt in the membrane which can be determined as mean arithmetic [2] or mean logarithm [9] value. The values L_p, σ and ω are the phenomenological constants that are concentration depended.

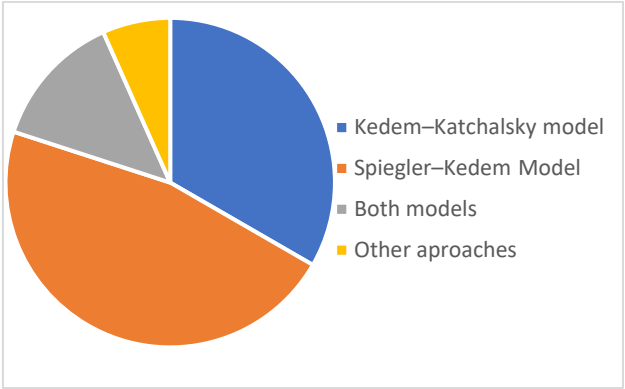

Figure 5 – The distribution of the irreversible thermodynamic based models in chosen publications

The selectivity of process can be evaluated be using of the rejection coefficient [9]:

$$R = 1-\frac{c_3}{c_1} = 1-\frac{J_s}{J_w c_1} \quad (3)$$

where c_1 is the solute concentration in feed solution; c_2 is the solute concentration in permeate.

The osmotic pressure value can be defined by the van't Hoff equation [2, 9]:

$$\Delta\pi = RT\Delta c = RT\left(c_2 - c_3\right) \quad (4)$$

where R is the universal gas constant; T is the absolute temperature; c_1 is the solute concentration near the membrane surface.

$$\pi(i) = 1.19\left(T+273\right)\sum_1^i m(i) \quad (5)$$

where T is the solution temperature; $m(i)$ – is molar concentration of ions.

On the other hand, in work [19] the osmotic pressure of glucose solution was determinated as the function of concentration:

$$\pi(c) = -RT \ln\left\{\frac{\left[\left(100 - c/M_w\right) - \left(2c/M_g\right)\right]}{\left[\left(100 - c/M_w\right) - \left(c/M_g\right)\right]}\right\} \quad (6)$$

where R is the gas constant; T is the solutions temperatures; M_g is the glucose molar weight; M_w is the water molar weight.

Also, the set of the temperature and concentration dependences of osmotic pressure is represented in the work [27].

The dependences of phenomenological constants in equations (1) and (2) from the operation condition are discussed in detail in the review work [2].

The use of the Kedem–Katchalsky model in the considered period was limited and related to the simulation of the hydrogen peroxide [16, 17], the rejection of N-nitrosamines [18] and boron [28], and also for the glucose solution concentration.

The more recent Spiegler–Kedem model describe the process of the substance transport through the membrane using the differential equations in a form [24]:

$$J_w = -A\left(\frac{dp}{dx} - \sigma\frac{d\pi}{dx}\right) \quad (7)$$

$$J_s = -B\frac{dc}{dx} + (1-\sigma)J_w\bar{c} \quad (8)$$

The rejection coefficient can be represented in a form [24]:

$$R = 1 - \frac{\left(K_{ic} - \left(D_{ip}/RT\right)V_{is}\left(8\eta/r_p^2\right)\phi\right)}{1 - \exp(-\mathrm{Pe}')\left[1 - \phi\left(K_{ic} - \left(D_{ip}/RT\right)V_{is}\left(8\eta/r_p^2\right)\right)\right]} \quad (9)$$

where K_{ic} is the factor of the resistance to diffusion; D_i is the diffusivity of the component i in the pores; R is the universal gas constant; T is the absolute temperature; V_{is} is the solute partial molar volume; η is the solution dynamic viscosity; r_p is pore radius; ϕ is the volumetric factor; Pe' is modified Peclet number.

In work [3] the other relationship was proposed for the rejection coefficient calculation:

$$R_s = 1 - \frac{1-\sigma}{1 - \sigma\exp\left[\frac{(\sigma-1)J_w}{\omega^-}\Delta x\right]} \quad (10)$$

where σ is reflection coefficient; ω^- is the local permeation coefficient.

The osmotic pressure value is determinated in the same as in the previous case. The phenomenological coefficients (7) and (8) in contrast with the Kedem–Katchalsky model do not depend on the solvent concentration [3].

The application of the Spiegler–Kedem model also was not wide. But this model was used for the analysis of phenol rejection [22], brackish [20] and seawater [25] desalination, N-nitrosamines rejection [21, 27], boron rejection [24, 28], water purification from organic contaminant [23], and glucose concentration [24]. In works [22-23], it also noticed that the description of processes is carried out for spiral wound modules.

It also should be noticed, that the thermodynamical approach and the phenomenological equation were used in work [29]. However, the thermodynamic method were also applied for energy analysis, which will be discussed below.

However, in general, the application of the irreversible thermodynamics models, despite their relative simplicity, in considered period were limited, and the relative number substantially decreased compared with previous period, considered in work [1].

3.2 Diffusion based models

From Figure 4 it can be seen that in the period 2011-2020 diffusion based models were used in a quite wide range, which was unexpected, taking into account the relatively low number of publications with using this approach in the previous decade [1].

In the vast majority of cases, the solution-diffusion model was used. Its main assumption is that the skin layer is non-porous. In this case the transport of solvent and solute can be recognized as diffusion and it can be described by the equations in a form [3, 28, 30-55]:

$$J_w = A_w\left(\Delta p - \Delta\pi\right) \quad (11)$$

$$J_s = B\left(C_f - C_p\right) \quad (12)$$

where A_w is the solvent penetration constant; B is the solute penetration constant; Δp is the applied pressure difference; $\Delta\pi$ is the osmotic pressure difference; C_f is the solute concentration in the feed solution; C_p is the solvent concentration in the permeate.

$$J_s = -D_m\frac{dC_m}{dx} = \frac{D_m}{l}\left(D_{m0} - D_{ml}\right) =$$

$$= \frac{D_m K_m}{l}\left(C_f - C_p\right) = B\left(C_f - C_p\right) \quad (13)$$

where D_m is the solute diffusivity in membrane; l is the active layer thickness; C_{m0} is the solute concentration in membrane on the feed side; C_{ml} is the solute concentration in the membrane on the permeate side; K_m is the partition coefficient.

In general, in several works the relationships for determination of the constants in equation (11) and (12) are represented.

For example, in work [46] the solvent penetration constant was represented in a form:

$$A = \frac{D_i \cdot K_i \cdot c_{i0} \cdot V_i}{l \cdot R \cdot T} \quad (14)$$

where D_i is the solvent diffusivity; K_i is the solvent sorption coefficient; c_{i0} is the solvent concentration in the feed solution; V_i is the solvent molar volume; l is the

membrane thickness; T is the solvent temperature; R is gas constant. The similar relationship was used in work [54].

The penetration constant also can be expressed by using the membrane resistance concept [30]:

$$A = \frac{1}{R_m \cdot \mu} \tag{15}$$

where R_m is the membrane resistance; μ is the solvent dynamic viscosity coefficient.

Although, equation (14) directly includes the temperature, in several works for taking into account this parameter influence in the RO process the others relationships were applied. For example, in work [31] for this purpose, the change in the viscosity with temperature was used. In this case, the equations for the penetration coefficients became:

$$A(T) = \frac{A_0 \cdot \mu(T_0)}{\mu(T)} \tag{16}$$

$$B(T) = \frac{B_0 (T + 273{,}15) \cdot \mu(T_0)}{T_0 \cdot \mu(T)} \tag{17}$$

where A_0, B_0 are the coefficient values under base temperature.

In others works, the more complex relationships were used. Thus, in work [28] following equations were proposed:

$$A_w = A_0 e^{\left(-\frac{E_A}{R}\left(\frac{1}{T}-\frac{1}{298{,}15}\right)\right)} \left(\frac{10^{-3}}{24 \cdot 60 \cdot 60}\right) \tag{18}$$

$$B_s = B_0 e^{\left(-\frac{E_{Bst}}{R}\left(\frac{1}{T}-\frac{1}{298{,}15}\right)\right)} \left(\frac{10^{-3}}{24 \cdot 60 \cdot 60}\right) \tag{19}$$

where E_A, E_{Bst} are the activation energies of the solvent and solute molecules transport through the membrane; R is gas constant.

At the same time, in work [35] for water solution it was used equations in a form:

$$A_{w,T} = 9.059 \cdot 10^{-7} \left(\frac{T}{25}\right)^{0{,}62} \left(\frac{36.0 \cdot 10^5 Q_f}{400}\right)^{-0.1447} \tag{20}$$

$$B_{s,i} = B_{s.i.\mathrm{Ref}} \exp\left(0.098\left(T - T_{\mathrm{Ref}}\right)\right) \tag{21}$$

The equation (20) was also used in work [37].

In work [57] the influence of the temperature was taken into account with following relationships:

$$A_{w(T)} = A_{w(25°\mathrm{C})} \exp\left[0.0343\left(T - 25\right)\right] \text{ at } T < 25°\mathrm{C} \tag{22}$$

$$A_{w(T)} = A_{w(25°\mathrm{C})} \exp\left[0.0307\left(T - 25\right)\right] \text{ at } T > 25°\mathrm{C} \tag{23}$$

$$B_{s(T)} = B_{s(25°\mathrm{C})} \left(1 + 0.08\left(T - 25\right)\right) \text{ at } T < 25°\mathrm{C} \tag{24}$$

$$B_{s(T)} = B_{s(25°\mathrm{C})} \left(1 + 0.05\left(T - 25\right)\right) \text{ at } T > 25°\mathrm{C} \tag{25}$$

The influence of the temperature was taken into account with using of the temperature correction factor. Thus, in work [58] the following equation was used:

$$A_{w(T)} = A_{w(25°\mathrm{C})} \cdot TFC \cdot F_f \tag{26}$$

where $A_{w(T)}$ is the penetration coefficient under base temperature (25°C); TFC is the temperature correction factor; F_f is the fouling factor.

The analogical relationships were used in works [59-60], and in work [43] the more detailed form was applied:

$$J_w = A \cdot TFC \cdot FF \cdot \left[\left(P_F - P_P - \frac{\Delta P_f}{2}\right) - \left(\pi_w - \pi_p\right)\right] \cdot E + 6 \tag{27}$$

Also, in work [43] the relationships for the temperature correction factor were proposed:

$$TFC_P = \exp\left[0.0343\left(T - 25\right)\right] < 25°\mathrm{C} \tag{28}$$

$$TFC_P = \exp\left[0.0307\left(T - 25\right)\right] < 25°\mathrm{C} \tag{29}$$

In work [20] the long-term performance of RO plant and for the changes of the penetration coefficient in time the following relationship was proposed:

$$A_n = \delta_1 \cdot e^{-\frac{t}{\tau_1} \cdot k_{fp}} + \delta_2 \cdot e^{-\frac{t}{\tau_2} \cdot k_{fp}} \tag{30}$$

Also, in work [49] except the temperature impact the influence of pressure were taken into account with following equations:

$$A_w = A_{w_0} \exp\left(\alpha_1 \frac{T_1 - 273}{273} - \alpha_2 \left(P_f - P_d\right)\right) \tag{31}$$

$$B_S = S_{S_0} \exp\left(\beta_1 \frac{T - 273}{273}\right) \tag{32}$$

Obviously, all represented relationships have a limited range of applicability, and the condition of the validity of the equations should be checked in the corresponding publications.

The osmotic pressure values can be calculated in the same way as in the case of irreversible thermodynamics (equations (4) through (6)), and also in some works, the other methods of this parameter calculation were considered.

For example, in work [61] the van't Hoff equation were written in a form:

$$\pi = \frac{i \cdot \Re}{M \cdot 10^5} \cdot T \cdot C \tag{33}$$

At the same time, in work [48] the following relationship was proposed:

$$\Delta\pi = RT\left(\frac{J_s}{B_s}\right) \tag{34}$$

Also, the empirical temperature and concentration dependences for several substances are represented in works [35, 38, 55, 59].

For the evaluation of the selectivity both the rejection coefficient (equation (4)) and the solvent concentration in permeate were used.

For the rejection calculation were proposed following relationships:

in work [38]:

$$R_i = \left[1 + \frac{AC_{wp}}{B\left(\Delta p - \Delta\pi\right)}\right]^{-1} \tag{35}$$

where is the water concentration in permeate.

in work [47]:

$$R = \frac{A\left(\Delta p - \Delta\pi\right)}{A\left(\Delta p - \Delta\pi\right) + B} \tag{36}$$

Also, the relationship between the rejection coefficient and other parameters can be represented in a form [41]:

$$B = \frac{\left(1 - R\right)\cdot J_w}{R} \tag{37}$$

or [54]:

$$\frac{1}{R} = B\frac{1}{J_w} + 1 \tag{38}$$

Also, the relationships for the solute concentration in permeate were proposed. In work [38] the following equation was used:

$$C_P = \frac{C_f B}{B + \dfrac{J_w}{\exp\left(J_w / k\right)}} \tag{39}$$

where k is the mass transfer coefficient.

A similar form of equation was applied in works [40], [48], and [53]. At the same time, in work [59], the temperature correction factor and fouling factor and with the accounting of them, the equation for the solvent concertation in permeate calculations became:

$$C_P = B\cdot FF\cdot TCF\cdot\frac{1}{J_w}\cdot\left(\frac{C_f\cdot\left(1 + CF\right)}{2}\right) \tag{40}$$

where CF is the concentration factor.

For more accurate analysis of the process the solution-diffusion model was complemented. In particular, in works [33-35, 49, 53, 56] during the RO process simulation the concertation polarization was taken into account (mainly by application of the film model). Moreover, the model was complemented by the material balance [49, 53, 55, 62], the optimization methods [35, 45, 61, 63], unsteady-state conditions [32], and by the fouling impact [39]. Also, in work [64] for the description of the processes in spiral wound membrane module the cylindrical coordinate system was used.

The solution-diffusion model was primarily used for the description of the water purification [30, 33, 36, 38, 47, 50, 64, 65], including sea water [25, 40, 41, 43, 49, 52, 55, 57, 61, 66] and brackish water [20, 31, 42, 45, 58, 59, 60, 65] desalination, and also the wastewater treatment [30, 48, 51, 53-54, 56, 67]. Also, with using of this model it was described the processes of the removal of zinc [32], boron [28, 52], chlorophenol [36, 38], N-nitrosodimethylamine [38, 63], weak acids [25], and ammonia compounds [51, 54], apple juice concentration [35, 37], and also for the membrane characterization [46]. The solution-diffusion model was also widely used for the analysis of the hybrid membrane systems performance [31, 41, 42-43, 48, 55, 57, 61, 65, 69-70]. In most cases, the processes were analyzed in the spiral wound membrane modules [33, 34-35, 37, 39, 58-60, 64, 68], the hollow fiber modules [62] and laboratory cells were also considered.

For the mathematical models' solutions, the most often used software includes MATLAB [32, 36, 52, 60], ROSA [39], and the programing language C++ [36].

The other models of this class were used much less often. Thus, the solution-diffusion-imperfection model was considered in works [71, 72], and the extended solution diffusion model was applied in work [72].

The solution-diffusion-imperfection model takes into account the possibility of the convective transport of substances through possible pores (imperfections) in the membrane active layer. In this case, the equations for the calculation of the solvent and solute fluxes will be written in a form [71]:

$$J_w = A\cdot\left(\Delta p - \Delta\pi\right) + L\cdot\Delta p \tag{41}$$

$$J_S = B\cdot\left(C_f - C_P\right) + L\cdot\Delta p\cdot C_f \tag{42}$$

where L is the leakage factor.

The rejection coefficient can be calculated by the equation [72]:

$$R = \left[1 + \left(\frac{B}{A}\right)\left(\frac{1}{\Delta p - \Delta\pi}\right) + \left(\frac{L}{A}\right)\left(\frac{\Delta p}{\Delta p - \Delta\pi}\right)\right] \tag{43}$$

The extended solution-diffusion model takes into account the influence of the applied pressure on the solute transport, which was not considered in the classical solution-diffusion model. In this case, the equations become [72]:

$$J_w = A\left(\Delta p - \Delta\pi\right) \tag{44}$$

$$J_s = B\left(C_f - C_p\right) + L_{sp}\Delta p \tag{45}$$

here L_{sp} is the phenomenological coefficient.

The rejection coefficient can be calculated by the equation [72]:

$$\frac{1}{R}\left[1 - \frac{L_{sp}}{C_f A}\left(1 - \frac{\Delta\pi}{\Delta p}\right)\right] = 1 + \frac{K_s D_s}{A\left(\Delta p - \Delta\pi\right)} \tag{46}$$

The unexpected wide range of the solution diffusion models applications in the considered period is probably related to its relative simplicity, because of what there is no necessity for the application of the complex computational techniques, and also the convenience of the model for the hybrid system analysis and the model-based optimization. It should be noticed that the significant contribution in this field was done by one research group [3, 34-38, 57-58, 63]. At the same time, the solution-diffusion-imperfection model and the extended solution diffusion model do not have these advantages, therefore, as in the previous period, they were applied in a limited range.

3.3 Pore flow based models

As in the previous period [1], the models of this class were used rarely, yielding to the computational fluid dynamics methods. Thus, among the large number of publications dedicated to the RO simulation the models which directly considered the pore flow are mentioned in less than 5% of cases. In most cases, the preferentially sorption pore flow model (also known as Kimura–Sourirajan model) was considered. Also, the surface force-pore flow model and some other approaches were applied (Figure 6).

Unlike the solution diffusion model, the models of this class consider the active layer as porous, and the transport is carried out by both diffusion and convection [1].

The preferentially sorption pore flow model describes the solute and solvent fluxes by the equations in a form [73]:

$$J_w = A_w\left(\Delta p - \Delta\pi\right) \tag{47}$$

$$J_s = B_s\left(C_m - C_p\right) \tag{48}$$

Such equations have a similar form to solution-diffusion models, which also can be seen in works [46, 74-75]. However, as mentioned in the previous review [1], the principal difference is in the nature of the transport coefficients, which are determined by the different conceptions of the active layer structure. Unfortunately, due to the low number of publications in the considered period, the making of a detailed review of the parameters of the preferentially sorption pore flow model does not seem possible.

For the evaluation of the selectivity the concertation in permeate may be used. It can be calculated by the equation [73-75]:

$$J_s = B_s\left(C_m - C_p\right) \tag{49}$$

Also, in work [73], the recovery ratio, which was determined as the permeate and feed ratio, was calculated:

$$R = \frac{Q_P}{Q_f}\cdot 100\% \tag{49}$$

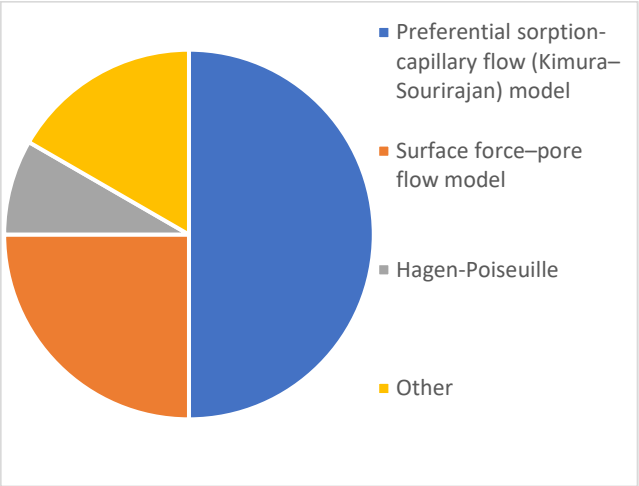

Figure 6 – The distribution of the pore flow based model in chosen publications

This model was complemented by the balance equations [73] and the optimization methods [74-75]. It was primarily used for the description of seawater desalination [74-76] and industrial effluent purification [73, 77], and also for the determinations of the characteristics and internal structure of the membrane [46]. This model was also used for the analysis of the hybrid system [76].

Also, in a few works, the surface force-pore flow model was found. This model considers the separate pore, which dimensions are characterized by the dimensionless coordinates [78-79]:

$$\rho = \frac{r}{R_w} \tag{51}$$

$$\zeta = \frac{z}{\tau} \tag{52}$$

where r is the cylindrical coordinate perpendicular to the pore wall; R_w is the pore radius; z is the cylindrical coordinate parallel to the pore axis; τ is the average pore length.

Taking this into account, the differential equation describing the velocity profile in pores can be written in a form [78-79]:

$$\left[\frac{d^2\alpha(\rho)}{d\rho^2} + \frac{1}{\rho}\frac{d\alpha(\rho)}{d\rho}\right] + \frac{1}{\beta_1}\left[\frac{\Delta P}{\pi_2} - \frac{\pi_2\sigma_2(\rho) - \pi_3\sigma_3(\rho)}{\pi_2}\right] - \frac{1}{\beta_1}\left(1 - \frac{1}{b(\rho)}\right)\left[\alpha(\rho) + \omega(\rho)\right]\times \left[1 + \frac{1 - \left(\frac{\pi_3}{\pi_2}\right)k\cdot\rho}{\exp\left[\alpha(\rho) - \omega(\rho)\right] - 1}\right]\exp\left(-\Phi(\rho,0)\right) = 0 \tag{53}$$

The physical meaning of the parameters in the equation (51) is described in detail in works [78-79].

The boundary conditions herewith are following [78-79]:

$$\alpha(\rho)=0 \quad \text{at} \quad \rho=1 \tag{54}$$

$$\frac{d\alpha(\rho)}{d\rho}=0 \ \text{ at } \ \rho=0 \tag{55}$$

The solution of the equation (51) allows to represent the solvent and solute fluxes in a form [78-79]:

$$N_A=\frac{2}{X_{AB}}\left(\frac{\varepsilon}{\tau}\right)\times$$

$$\times\int_0^{1-\lambda}\frac{\left[\alpha(\rho)+\omega(\rho)\right]}{b(\rho)}\left(\pi_2+\frac{\pi_2-k\cdot\rho\cdot\pi_3}{\exp\left[\alpha(\rho)-\omega(\rho)\right]-1}\right)\times$$

$$\times\exp\left(-\Phi(\rho,0)\right)\rho d\rho \tag{56}$$

$$N_B=\frac{2}{X_{AB}}\left(\frac{\varepsilon}{\tau}\right)CRT\int_0^1\alpha(\rho)\rho d\rho \tag{57}$$

The solute concentration in permeate can be calculated by the equation [78-79]:

$$C_{A3}=C\left[1+CRT\frac{l_1}{l_3}\right]^{-1} \tag{58}$$

Moreover, in work [80] the following equation for the rejection coefficient calculation was proposed:

$$R=1-\frac{\Phi K_c}{1-(1-\Phi K_c)\exp(-\mathrm{Pe})} \tag{59}$$

where Pe is the Peclet number.

In contrast with previous models, the surface force-pore flow model is complex and requires complex solution methods without visualization, the distinctive for the CFD methods. This determined the narrow range of this model application which was only used for the description of the ground waters purification from pesticides [80].

Also, in work [81] for the description of the pressure driven membrane processes including RO the Hagen-Poiseuille equation was considered:

$$u(r)=-\frac{1}{4\mu}\frac{dp}{dx}\left(R^2-r^2\right) \tag{60}$$

However, this approach is more suitable for the simulation of the ultrafiltration and microfiltration.

Despite that, the models of this class take into account both diffusive and convective transport through the membrane, in work [82], the analytical solution-diffusion pore-flow model was presented. Also, in work [83] the similarity of the processes in the membrane with convective heat transfer was considered. However, that approaches were used rarely.

3.4 Computational fluid dynamics based models

As mentioned in work [1], the flow conditions have a significant influent on the operation of the processes during membrane separation, including mass transfer, concentration polarization, and fouling layers formation, the pressure drop in the membrane channels. Taking into account the critical importance of the hydrodynamic conditions not only for the membrane processes but for engineering in general, the development of the method for the mathematical description and analysis of the flow named computational fluid dynamics (CFD) is natural. The method itself is based on the mathematical description of the fluid flow, which includes the Navier-Stokes equation, the continuity equation, and the mass and energy conversation equation [84].

For the steady state laminar flow of the Newtonian fluid these equations can be written in a form:

- the continuity equation [84]:

$$\frac{\partial u}{\partial x}+\frac{\partial v}{\partial y}+\frac{\partial w}{\partial z}=0 \tag{61}$$

- the Navier-Stokes equation [84]:

$$u\frac{\partial u}{\partial x}+v\frac{\partial u}{\partial x}+w\frac{\partial u}{\partial z}=-\frac{1}{\rho}\frac{\partial P}{\partial x}+\frac{\mu}{\rho}\left[\frac{\partial^2 u}{\partial x^2}+\frac{\partial^2 u}{\partial y^2}+\frac{\partial^2 u}{\partial z}\right] \tag{62}$$

$$u\frac{\partial v}{\partial x}+v\frac{\partial v}{\partial x}+w\frac{\partial v}{\partial z}=-\frac{1}{\rho}\frac{\partial P}{\partial x}+\frac{\mu}{\rho}\left[\frac{\partial^2 v}{\partial x^2}+\frac{\partial^2 v}{\partial y^2}+\frac{\partial^2 v}{\partial z}\right] \tag{63}$$

$$u\frac{\partial w}{\partial x}+v\frac{\partial w}{\partial x}+w\frac{\partial w}{\partial z}=-\frac{1}{\rho}\frac{\partial P}{\partial x}+\frac{\mu}{\rho}\left[\frac{\partial^2 w}{\partial x^2}+\frac{\partial^2 w}{\partial y^2}+\frac{\partial^2 w}{\partial z}\right] \tag{64}$$

- mass conversation equation [84]:

$$u\frac{\partial C}{\partial x}+v\frac{\partial C}{\partial y}+w\frac{\partial C}{\partial z}=D\left[\frac{\partial^2 C}{\partial x^2}+\frac{\partial^2 C}{\partial y^2}+\frac{\partial^2 C}{\partial z^2}\right] \tag{65}$$

In these equations: u, v, w are the velocity projections on the coordinate axes; P is the pressure; C is the solute concentration; ρ is the feed solution density; μ is the feed solution viscosity; D is the diffusivity.

The equations are also represented in a similar way in works [85-97], including written for the two-dimension simplification [89, 91, 96], in the cylindrical coordinates [90], and matrix form [93]. Moreover, in works [93-94], the unsteady-state conditions were taken into account.

However, the equations (61) – (65) due to their awkwardness are often written in an operator form with using of the differential operators, including the full derivative operator, the Hamilton operator, the Laplace operator etc., and also the rules of the vector and tensor analysis. In this case, the equations of the mathematical model of the fluid flow can be written in a form:

- the Navier-Stokes equation [98]:

$$\rho(\bar{u}\cdot\nabla)\bar{u}+\nabla P-\mu\nabla^2\bar{u}=0 \tag{66}$$

- the continuity equation [98]:

$$\nabla \cdot \bar{u} = 0 \tag{67}$$

- mass conversation equation [98]:

$$D\nabla^2 C = \bar{u} \cdot \nabla C \tag{68}$$

The equations are written in a similar way, for example, in works [6, 99–126].

For accounting of the unsteady-state conditions these equations can be rewritten in a following way [127]:

$$\frac{\partial \rho}{\partial t} + \nabla \cdot (\rho u) = 0 \tag{69}$$

$$\frac{\partial (\rho u)}{\partial t} + (u \cdot \nabla) \rho u = -\nabla p + \nabla \cdot (\mu \nabla u) \tag{70}$$

$$\frac{\partial C}{\partial t} + (u \cdot \nabla) C = \nabla \cdot (D \nabla C) \tag{71}$$

The similar equations are in works [128-129].

Also, the equations are represented in the reviews [6-8].

As it was mentioned above, equations (60)-(64) are suitable for the laminar flow. However, in the channels of the membrane apparatuses, there exist favorable conditions for turbulence development. Therefore, the models of flow are often supplemented by turbulence models. The k-ω and k-ε models are most widely used. The distribution between them is represented in Figure 7.

The k-ε turbulence model operate by the terms of the specific turbulent kinetic energy k and the dissipation rate ε. The equations of this model are following [138]:

$$\frac{\partial (\rho k)}{\partial t} + \nabla \rho \bar{u} k = \nabla \left[\left(\mu_k + \frac{\mu_{eff}}{\sigma_k} \right) \nabla k \right] + \mu_{eff} S^2 - \rho \varepsilon \tag{72}$$

$$\frac{\partial (\rho \varepsilon)}{\partial t} + \nabla \rho \bar{u} \varepsilon = \nabla \left[\left(\mu_k + \frac{\mu_{eff}}{\sigma_k} \right) \nabla \varepsilon \right] + $$

$$+ C_1 S \rho \varepsilon - C_2 \frac{\rho \varepsilon^2}{k + \sqrt{\nu \varepsilon}} \tag{73}$$

The physical meanings of the parameters in equations (72) and (73) are described in work [138].

This model was also used, for example, in works [91, 137, 139].

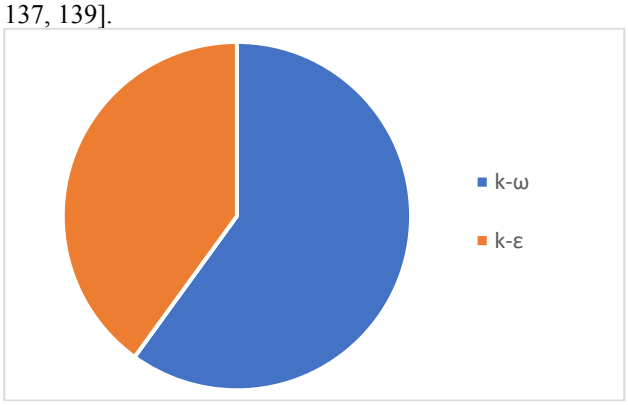

Figure 7 – The distributions of the main turbulence models in the chosen articles

In contrast, the other model uses the value of the specific dissipation rate ω instead of ε. This model can be represented in a form [97]:

$$u_j \frac{\partial u_i}{\partial x_j} = -\frac{1}{\rho} \frac{\partial P}{\partial x_i} + \frac{1}{\rho} \frac{\partial}{\partial x_j} \left((\mu + \mu_t) \frac{\partial u_i}{\partial x_j} \right) \tag{74}$$

where the turbulent viscosity can be calculated by following equation [97]:

$$\mu_t = \rho \frac{a_1 k}{\max (a_1 \omega; \Omega F_2)} \tag{75}$$

The equations for calculations of the k and ω values according this model are following [97]:

$$u_j \frac{\partial (\rho k)}{\partial x_j} = \tau_{ij} - \beta^* \rho \omega k + \frac{\partial}{\partial x_j} \left[(\mu + \sigma_{k1} \mu_t) \frac{\partial k}{\partial x_j} \right] \tag{76}$$

$$u_j \frac{\partial (\rho k)}{\partial x_j} = \frac{\gamma}{\nu_t} \tau_{ij} \frac{\partial u_i}{\partial x_j} - \beta \rho \omega^2 + \frac{\partial}{\partial x_j} \left[\left(\mu + \sigma_\omega \mu_t \frac{\partial \omega}{\partial x_j} \right) \right] +$$

$$+ 2\rho (1 - F_1) \sigma_{\omega 2} \frac{1}{\omega} \frac{\partial k}{\partial x_j} \frac{\partial \omega}{\partial x_j} \tag{77}$$

This model was also used, for example, in works [85-88, 97, 126].

Since the equations of models are differential, the starting and boundary conditions are needed for the obtain the result. These conditions strongly depend from the geometrical and physical conditions of the considered process, for example, for the equations (61) – (65) for the case of the fluid flow in the spiral wound membrane channel with the spacer in work [84] the following boundary conditions were applied:

- inlet boundary conditions:

$$C = C_0; u = \frac{m}{\rho A_i}; v = w = 0 \tag{78}$$

- membrane boundary conditions:

$$C = C_m; u = v = w = 0 \tag{79}$$

- filament boundary conditions:

$$\frac{\partial C}{\partial n} = 0; u = v = w = 0 \tag{80}$$

- symmetry face boundary conditions:

$$\frac{\partial C}{\partial z} = 0; \frac{\partial u}{\partial z} = \frac{\partial v}{\partial z} = \frac{\partial w}{\partial z} = 0 \tag{81}$$

- outlet boundary condition:

$$P = P_0 \tag{82}$$

Also, the boundary conditions are described in details, for example, in works 89-90, 92, 109, 117, 127-132, 134, 140], and also in the review work [8].

Due to the complexity of the equations described above, the mathematical models should be solved by numerical methods, mainly by using specialized software. In work [1], it was noticed, that for the case of RO, the most widely used commercial software included ANSYS FLUENT and ANSYS CFX, however, in the considered period, the range of applied software was wider. The distribution of them in chosen publications is shown in figure 8. Since the ANSYS software is still the most widely used, it is reasonable to consider the ratio between the main algorithms (FLUENT and CFX) that are shown in figure 9. Thus, the ANSYS FLUENT was most widely used, in particular, in works [90-91, 95-96, 107, 110, 116, 118, 124, 126-127. 133, 137-139, 141-145]. The ANSYS CFX was applied to a lesser extent, for example in works [85-88, 93, 113, 128-131, 134, 146-147, 121]. Moreover, the ANSYS was used without pointing out the algorithm in works [84, 99, 121, 123]. Among the other software un should be noticed the wide range of applications of COMSOL Multiphysics, for example, in works [98-99, 101-106, 111-112, 119, 122-123, 148], and open-source product OpenFOAM [92, 94, 114, 132, 135, 137].

The other software, including MATLAB [102, 104, 117], ROSA [149-151], NUMECA [152], MUSUBI [153], was used rarely. Also, in work [154], it was carried out the analysis of the possibility of applying the RO seawater desalination by the commercial systems CORMIX, VISUAL PLUMES, and VISJET. Meanwhile, the popular engineering system SolidWorks was not used almost. Only in work [121], the geometry was created in this system, whereas the calculations were carried out in ANSYS.

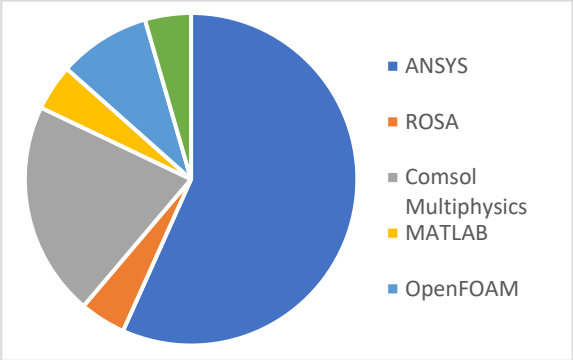

Figure 8 – The application of the software for the RO simulations

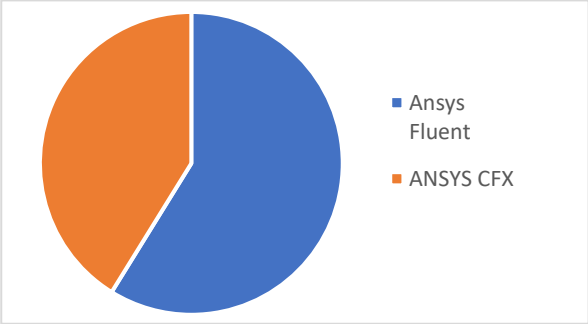

Figure 9 – The application of the algorithms of the ANSYS software for RO simulation

In some works, namely [23, 89, 97, 100, 108-109, 140, 155-157], it was not pointed out the applied software or mentioned that the algorithm of the mathematical model solution was designed independently.

Taking into account the importance of the geometry of the channels for the simulation by the CFD method, great attention was dedicated to the module design. As in others approaches, the greatest number of researches were carried out for the spiral wound membrane modules, in particular in works [6, 23, 84, 88, 98, 101, 104, 106, 110, 112-114, 117, 121, 141, 149, 151, 155-157]. In this case, it should be noticed, that in work [149] it was declared that the influence of the channel curvature is significant and the neglect of this factor can lead to a significant mistake. At the same time, the channels of the spiral wound membrane modules were conditionally rolled out into the plane, in particular in works [6, 88-89, 104]. Also, in a significant number of works the hollow fiber modules were considered [86, 106, 116, 121, 125-126, 137, 139], whereas the plate and frame modules were considered in a lesser number of the researches [91, 108-109]. The same situation is observed for the tubular modules [127, 137], and also for the multichannel ceramic modules [124] and similar designs [152]. Also, in some works the original designs were considered including rotating [90, 142] and test and lab cells [98, 135, 143]. The works, in which the patterned [111] and corrugated [97] membrane surface, should be noticed individually.

Taking into account the importance of the spiral wound modules and the correspondingly large number of studies, it was expected, that a large number of the investigations by CFD methods were dedicated to the influence of spacers on the process performance. Thus, in work [147], the important parameters, which impact the process, were pointed out. They include the angle between the spacer filament, the spacer thickness, and the filament placement in the channel. In some works, for example [92, 141, 144, 155] the commercial spacers designs were considered. Also, it should be noticed, that in works [87, 92, 95] the spacer filament was considered cylindrical, and in work [144] it was considered with the elliptical cross-section. Therefore, along with this, it should be pointed out the works [104[and [105], in which the real geometry of the spacer was determined by the microscope measurements and X-ray computer tomography and reproduced in the CFD programs. Moreover, in the result of the comparison with the ideal geometry, in work [104] it was mentioned, that the cylindrical form of the spacer filament is a good approximation, whereas in work [105] it was pointed out the possible inaccuracies (in particular the overestimation of the pressure drop), which can be obtained without taking into account the real geometry of spacer filament. The comparison of the wound and non-wound spacers was another direction of the investigations, as was shown in works [84, 103, 153]. In this case, in work [103], it was pointed out, that the wound geometry has advantages, while in work [153] it was shown the bigger pressure drop in the channel with the wound spacers. Great attention was dedicated to the spacer filament placement by the channel width, in particular in works [96, 100, 114, 119, 129, 134].

At that, in most cases, it was pointed out, that the pest results were obtained for the zigzag placement of the filament. The influence of the angle between spacers was investigated in works [87-88, 106, 145, 155-157]. In work [1] it was pointed out, that the determination of the optimal angles is still debatable. The result of the consideration of the mentioned publication confirms this statement. In contrast with the previous period, in 2011-2020, it was proposed a large number of novel spacer designs, in particular in many studies the design with the different thicknesses of the filament between the spacer nodes, in particular in works [99, 101, 102, 112, 113, 118]. Also, it was proposed the sinusoidal spacer design [123] and the design with the screw thread on the filament [107]. Despite the benefits of the proposed designs, there are some doubts about the possibility of realizing these geometrical forms for the manufacturing of the real spacers taking into account their real thickness. The same doubts are also related to the original design of the hollow fibers with the specific cross-section, with was described in the work [116]. These doubts are appearing from the accounting of the results of the comparison of the real and ideal geometry, carried out in works [104-105]. Moreover, in work [148] it was also pointed out the significant influence of the deviations from ideal geometry for the multibore polymer membrane modules. It also should be noticed the application of the multilayer spacers [121, 130]. The novel designs of the spacers were also considered in the review [8].

In works using the CFD method, the separation process for which the simulation is carried out is not often pointed out, however, in most cases, this is about the desalination processes [85-87, 101, 108-109, 152].

In general, the mathematical simulation of the RO using CFD methods, as was predicted in work [1], is intensively developing and, likely, in the near future, will remain the most effective and widely used.

3.5 Artificial neural networks based models

In work [1], among the novel approaches except the CFD methods, the artificial neuron networks (ANN) were considered. Such systems are built by analogy with the architecture of the biological nervous systems, which mainly consist of simple nerve cells or neurons, which work in parallel for the simplification of quick decisions. Similarly, the neuron networks are made from a large number of primitive processing elements, which are organized in a massive parallel set. Then, in the neuron networks the artificial connections (synapses), connect these elements. They are characterized by the set of the weight coefficients, which could be updated in the learning proves [79, 158-160]. Thus, the artificial neuron networks are the computational method for comparing the input and output data from the process be the nonlinear regression model. The ANN method has the ability to analyze the relationship between input and output data based on the functions of the biological neuron networks, as mentioned above. The simple architecture of the ANN includes three-layer namely, input, hidden, and output. The input signal received from an external source is multiplied by the mentioned above weight coefficients. When the result of the multiplication exceeds the threshold, the signal would be released and sent to the output depending on the ANN activation function. In this respect, three stages, namely training, testing, and validating, with several computational operations are applied to achieve the desired goal through ANN [161].

The advantages of the simulations using the ANN include [160]: (1) the ability of the simulation of complex relationships, which is impossible for the models based on conventional mathematical methods; (2) in many cases the ANN has higher accuracy than conventional mathematical models; (3) the ANN can be adapted with new data and modernized with them; (4) the best combination of the design parameters in the ANN can be obtained by the trial and error method.

In each stage of the ANN, the main computational operation has the following form [161]:

The equations of the output signal for any hidden or output layer are determinated by the following equations [161]:

$$a_1 = \sum_{i=1}^{i=n} \left(W_i X_i + b1 \right) \tag{83}$$

$$a_2 = \sum_{j=1}^{j=k} \left(W_j a_1 + b2 \right) \tag{84}$$

where a_1, a_2 are the output signals of the first and second layer correspondingly; X is input parameter; W and b are the weight coefficients and bias, correspondingly [161].

The activation function is used for the data normalization in range [0 -1] and [-1 1], which is discrete or continuous in a form of sigmoid [161]:

$$f\left(s\right) = \frac{1}{1+e^{-s}} \tag{85}$$

or in a form of the hyperbolic tangent:

$$f\left(s\right) = \left(e^{s} - e^{-s}\right) / \left(e^{s} + e^{-s}\right) \tag{86}$$

s is the value of the input parameter. The network may ne linear on nonlinear in the activation function [161]:

$$f = \begin{cases} 1 \text{ if } s > 0 \\ -1 \text{ otherwise} \end{cases} \tag{87}$$

The normalization equation has following form [161]:

$$s_i = \frac{0.8}{d_{\max} - d_{\min}} \left(d_i - d_{\min} \right) + 0.1 \tag{88}$$

$d_{\min}$, $d_{\max}$ and d_i are minimum, maximum and i value of the input/output data correspondingly. The predicted or target equation can be represented in a form [161]:

$$Y = \sum_{j=1}^{j=k} f_2 \left(W_j f_1 \left(\sum_{i=1}^{i=n} W_i X_i \right) \right) \tag{89}$$

Y is predicted output value. The weight matrices are calculated by applying an error back-propagation method.

The accuracy of the weight coefficient depends on the minimal error (E) of the output $\{z(k);\ 1 \le k \le K\}$ on the learning stage and calculated using the sum of the square error [161]:

$$E = \sum_{k=1}^{K}\left[e(k)\right]^2 = \sum_{k=1}^{K}\left[d(k) - z(k)\right]^2 = \\ = \sum_{k=1}^{K}\left[d(k) - f\left(W_x(k)\right)\right]^2 \quad (90)$$

where $[W_x]$ is the weight matrices; $[x]$ is input vector; and d is desired target value.

In general, there are three criteria used for the evaluation of the ANN performance, namely coefficient of correlation (r), mean square error, and mean absolute error [162].

The ANN are especially effective when it is difficult to develop mechanistic models [161].

In some works, the ANN were used together with other methods, in particular with the solution-diffusion model [158, 163], the surface force-pore flow model [79], the CFD methods [164], and also with the surface response methodology [166]. Moreover, in work [79], it was noticed, that the ANN predictions were more accurate than the surface force-pore flow model ones. Also. The ANN were applied for consideration of the systems with a high level of fouling [167-168], moreover, in work [168], it was mentioned that mechanistic models oversimplify the fouling phenomena.

In most cases, the ANN methods of simulation were used for the analysis of the desalination processes [158, 160, 162, 166, 168-169] and the water and wastewater treatment [161, 163, 165, 167].

In general, during 2011-2020, ANN were used for the RO process simulation in a limited range. The likely reason for this is the high enough level of the development of mechanistic models, in particular, the suitability of the CFD methods for these purposes. The ANN and be used the most effectively in systems with a high level of fouling [167-168] or systems with nonconventional energy sources [163, 169].

3.6 Molecular dynamics based models

In addition to the CFD and ANN methods, the molecular dynamics (MD) methods are a relatively new approach to the RO process. As in the case of CFD, this method is based on the numerical solution of the Newton equations of motion, but on the molecular level [10].

The concept of classical molecular dynamics is based on Newtonian mechanics. According to the second Newton law, the relationship among the mass, acceleration, and force excreted to the particle i is described by the equations [10]:

$$F_i = m_i a_i = m_i \frac{d^2 r_i}{dt^2} \quad (91)$$

where m_i is the particle mass; a_i is the acceleration; F_i is the force excreted to the particle; r_i is the distance between particles; t is the time.

The Newtonian force also can be expressed in a form of the gradient of the potential energy [10]:

$$F_i = -\nabla_i U\left(r_i\right) = -\frac{\partial U\left(r^N\right)}{\partial r_i} \quad (92)$$

Using the relationships, represented by equations (90) and (91), it is possible to obtain the trajectories for all atoms, which are described by the successive positions, velocities, and momenta. These trajectories become the initial data for the prediction of the bulk properties of the systems, with further conations to the physical phenomena [10].

Insight the determined system, the pair of atoms are in interaction, irrespective of that they are bounded or separated by the distance. These interactions formed the basis of the simulation by the MD method. From this force, the equation for the potential energy can be obtained for the description of the stretching, vibrations, and rotation of the particles around the bounds as a result of the intermolecular force. This equation can be represented in the following way [10]:

$$U_{total} = U_{bond} + U_{angle} + U_{dihedral} + \\ + U_{VdW} + U_{Coulomb} + U_{external} \quad (93)$$

The values U_{bond}, U_{angle} and $U_{dihedral}$ take into account the stretching, bending, and torsion, which take place in atoms, correspondingly. On the other hand, the values U_{VdW} and $U_{Coulomb}$ describe the non-bounded interactions. Moreover, the van der Waal's forces have origin in the weak force existing for the non-bounded atoms, whereas the $U_{Coulomb}$ is used for the description of the electrostatic interactions, which are caused by electrostatic interactions. The last term of the total potential energy $U_{external}$ takes into account the external forces, applied to the system. In the investigation of the RO process, the main external force is the applied pressure [10].

The protentional energy of the intermolecular interaction also can be described by the following equation [171, 172]:

$$U_{(r_{ij})} = 4\varepsilon_{ij}\left[\left(\frac{\sigma_{ij}}{r_{ij}}\right)^{12} - \left(\frac{\sigma_{ij}}{r_{ij}}\right)^{6}\right] + \frac{q_i \cdot q_j}{4\pi\varepsilon_0 r_{ij}} \quad (94)$$

where r_{ij} is the distance between particles i and j; q_i and q_j are the patiale charges of the i and j; ε_{ij} and σ_{ij} are empirical Lennard-Jones parameters.

The MD method has an advantage, which consists of the ability to achieve the temporal and spatial solutions which are difficultly available by experimental investigations. For example, the solutions are possible for the dimension less than Angstrom and the periods of time less than a femtosecond [173].

Taking into account that the considered approach requires large volumes of calculations, the necessity of the

special software application is evident. For the MD methods realization of the many software packages, algorithms, and codes. In particular, for the RO simulations the following software was used: Visual Molecular Dynamics (VMD) [171-172, 174-178], Nanoscale Molecular Dynamics (NAMD) [171-172, 174-175, 179-180], Groningen Molecular Simulation package (GROMACS) [176-178, 181-183], Chemistry at Harvard Molecular Mechanics (CHARMM) [172, 175-176, 184], Large-scale Atomic/Molecular Massively Parallel Simulator (LAMMPS) [185-187], Materials Studio [181, 188-191], especially Amorphous Cell package of Material Studio software [192-193], Assisted Model Building and Energy Refinement (AMBER) [180, 192-195], Optimized Potential for Liquid Simulations (OPLS-AA) [181-182], Condensed-phased-optimized Molecular Potential for Atomistic Simulation Studies (COMPASS) [188, 190], DL_POLY [194-195]. The data about such software developers and more detailed pieces of information about its application are represented in the review work [11].

During the simulation by MD methods, statistical techniques were used, including the Monte-Carlo method [174, 192-194] and surface response methodology [189]. A more detailed description of the MD methods is represented in the review work [10].

Taking into account the features of the method, during its application special attention was dedicated to the membrane material. In many works, conventional materials, such as polyamides [11, 175, 179, 184, 187, 190, 192-195], sulfonated diamine [189], and polyether sulphones [181], were considered. At the same time, a significant number of publications were dedicated to the use of membrane manufacturing such novel materials as graphene [9, 182, 187, 196] and graphene oxide [178, 197]. Also, the considered method was used for the analysis of the performance of the membrane made using the carbon [172, 176, 196, 198] and aluminosilicate [185], nanoporous carbon [199], boron nitride [171, 200], fullerite [188], and MoSe2 [177]. It should be noticed that in work [188] it was claimed that the fullerite membranes have the higher flux than the graphene and conventional membranes, and in work [177], it was declared that the flux of the productivity of the proposed membranes is who orders of magnitude higher than the commercially available membrane one.

In most cases, the investigation was dedicated the water treatment [175-176, 180, 190-191, 194-195, 199, 201], including desalination [11, 177, 182-185, 187-188, 192-193, 196-197, 200] and the heavy metal ions removal [171-172, 178].

3.7 Optimization and process control

In work [1], it was noticed that the determination of the optimal condition and processes control are the important practical application of the mathematical simulation of the pressure driven membrane processes, including RO. The large number of publications dedicated to these questions in the period from 2011 to 2020 completely confirm this statement.

Also, in work [1] it was noticed, that the optimization problem consists in finding the most beneficial values of the operation parameters. The important factor of the successive optimization procedure includes the choice of the target function and the optimization criterion. As in 20200-2010, in the considered period in most works authors used the economical optimization criteria, primarily the minimization of costs [49, 61, 74-75, 202-217], and also the minimization of the energy consumption, which is the significant part of the operational cost [27, 38, 49, 66, 73, 204-205, 219-228]. Also, the economic criteria included the profit maximization [229-230], and the minimization of the cost factor, which in work [231] was determined as the ratio of the water price and energy price in a hybrid system with reverse osmosis and pressure retarded osmosis. The main technological parameters for optimization included maximization of the removal of the component from solution 27, 36, 38, 63, 200, 221, 232-233], minimization of the concertation [234], maximizing of the permeate concertation [35], maximizing of the recovery ratio [235], maximizing of the productivity [236-237], and minimization of the applied pressure [36]. The other direction of the optimization involved the minimization of the fouling level [238] and the minimization of the environmental impact [230]. In the set of works, multiobjective optimization was applied [239-240].

In many works, the optimization was carried out based on the conventional mathematical models described in previous chapters. In particular, the solution-diffusion model was the most widely used [35-36, 38, 61, 66, 75, 204, 209, 214, 218, 221, 241]. Also, it was applied the Kedem-Katchalsky model [205, 219], Spiegler-Kedem model [27], Kimura-Surirajan [73], the surface force-pore flow model [78], and also the molecular dynamics models [200]. Moreover, the factor experiment method and other regression and statistical methods were applied [212, 228, 232, 235, 243-244]. The questions of the optimal control and processes control were considered in the works [220, 236-237, 245-248].

For the optimization problem solution, a large number of methods and algorithms can be used. In the considered researches the most widely used methods included the nonlinear programming [35, 49, 61, 74-75, 204-211, 218, 222, 229-230], the generic algorithm [28, 38, 237, 241-242], the particle swarm method [202, 247, 250], the sequential quadratic programming [219, 233], the surface response methodology [232], the pattern search algorithm [251], the harmony search algorithm [66], and the bees algorithm [213]. The work [216] should be pointed out, since in it the nineteen optimization algorithms were considered and compared.

For the solution of the considered optimization problems the wide range of the software and programing languages was applied including Matlab [73, 203, 250, 252], gPROMS [63, 218, 235], GAMS [49, 209, 211, 246, 254], Design–Expert [232], ASPEN [214], ChemCAD [215], ROSA [206-207], Modelica [219], C++ [36, 38], R [244].

As in the most considered RO simulation methods, the optimization was applied mainly for the analysis of the water treatment processes, primarily the seawater and brackish water desalination [49, 61, 66, 73-75, 200, 202-203, 206-210, 212-217, 219-227, 229, 234-235, 237-240, 242, 244-246, 248-250, 251-255], the potable water production from ground waters [256-257], the wastewater treatment [230-231, 238, 258], and recycling [211], and also the ultrapure water production [259]. In some works, it was considered the special pollutant removal including chlorophenol [36, 204, 233, 243], N-nitrosamine [27, 63], arsenic [205], boron [218] and bentazon [232]. Except for the water treatment, the concentration of the apple juice [35] and the maple syrup [228] was also considered.

The optimization methods appear to be effective for the analysis of the hybrid systems performance, in which the RO was combined with thermal distillation [214-215, 241], forward osmosis [238], pressure retarded osmosis [219, 229, 231], and forward osmosis and electrodialysis [224]. The other important direction was the optimization of the system with renewable energy sources [216, 260], including solar [202, 216, 253] and wind [216] energy.

It should be noticed, that the application of the optimization methods can give a significant economic effect, for example, it was noticed the achievement of decreasing of energy consumption by 16% in work [227], the decreasing operational cost by 26% in work [209], and the economy of the 27 % of the annual costs of the obtained product in work [211].

3.8 Energy analysis

It was mentioned above that energy consumption is a significant part of the operative costs during RO exploration. In the period from 2010 to 2020, a large number of articles dedicated to calculations and analysis of the energy parameters of RO were published, therefore, it is reasonable to consider this direction in general terms.

Mainly, the energy analysis of the RO systems was based on the mass and energy balances [43, 228, 261-266], theoretical calculations of the specific energy consumption [43, 228, 261-266], the exergy analysis [15, 43, 241-242, 263, 265, 275, 286-290], the pinch-analysis [292], and the calculations of the thermodynamical effectivity [293-294].

It should be noticed that, in many cases, the energy and exergy balances were written for the full set-up rather than RO apparatuses. At that the RO can be combined with energy recovery systems (including pressure exchangers and turbines) [276, 288-289, 290], Rankin cycle [296], internal combustion engine [269], electrodialysis [268, 270], distillation [262-263, 282, 290-291], humidification-dehumidification [43], membrane distillation [278, 298], forward and pressure retarded osmosis [278, 299], photovoltage system [264], and capacitive deionization [284].

As in the case of the optimization, the grate attention was dedicated to renewable energy sources including solar energy [262-264, 272-273, 275, 289, 293, 297, 301-303], wind energy [267, 287, 262-263, 301-302, 304], and also tidal energy [266, 272].

As in all previous cases, the high effectiveness of the analysis was achieved via the application of specialized software and programming languages. For the energy analysis such means as ROSA [150, 265, 272, 295, 300], Matlab [261, 295], ASPEN [205], Visual Design Software [288], WAWE [305], EES [289], and R [244] were widely used.

In most cases, the desalination processes were considered. Also, in many works, the significant economical effect was pointed out. For example, in work [287] on the results of the exergo-economic analysis, the authors managed to find a way of decreasing energy consumption by 24%. In works [288] a similar analysis shows that the application of the turbine allows to decrease the energy consumption by 49%, and the application of the pressure exchanger – by 77. In work [289]. It was shown that application of the Pelton turbine allows for recovery of 24% of the consumed energy.

3.9 Economic analysis

During consideration of most approaches, especially optimization and energy analysis, it was pointed out that the economic parameters have significant importance for the performance analysis of the RO systems. Therefore, it is reasonable also to consider in general terms the economic methods of the analysis of the considered process.

Except optimization [202, 204-205, 231, 241] and energoeconomic analysis [205, 230, 241, 266-270, 280, 285-287, 306], the economical models included the determination of the relationship for calculation of the capital cost (CAPEX) [55, 204-205, 234, 230, 266, 268, 270, 280, 286, 297, 300, 307-317], operating costs (OPEX) [55, 204-205, 209, 230, 234, 266, 280, 300, 307, 309-318], and product price [268, 274, 280, 297-298, 302, 306-307, 314, 319-324]. Among other parameters the profit [325], cost saving coefficient [319], cost factor [231], and water price index [326] can be pointed out. In certain works, the simplified economic balance [327] and socio-economic evaluation [328] were considered.

The other joint characteristic of the investigation based on economic analysis with ones based on optimization and energy analysis is the significant number of works dedicated to hybrid systems and systems with renewable energy sources. In particular, the hybrid systems RO-distillation were considered in works [55, 230, 241, 307-308, 314-315], and the works [321, 241, 300, 309, 311] were dedicated to the systems RO-FO and RO-PRO. The other hybrid systems including electrodialysis [270, 310], crystallization [268, 270], and power plant [55, 274]. Among the alternative energy sources, the most attention was dedicated to solar energy [202, 297, 302, 308, 320-321, 328]. Wind energy [302, 306], tidal energy [266], and geothermal energy [314] were also considered.

Among the software, in works dedicated to the economic analysis of the RO systems, it was mentioned ROSA [231, 266, 324], COMFAR III [323], and ESS [324].

As in all other approaches to the RO simulation, in most cases, the application of RO for the seawater and brackish

waters desalination [55, 202, 209, 234, 241, 266-270, 274, 280, 287, 297, 302, 306-309, 311-312, 314, 317-324] was considered. In addition, the questions about wastewater treatment [298, 300, 310, 315-316, 327], including the removal of certain pollutants such as chlorophenol [204] and arsenic [205], were regarded.

4 Discussion

In certain works, the other approaches, which cannot be related to the described above groups, were applied. Those models can be based on the empirical data (both with and without combination with conventional models) [329-336], the mass and energy balances [337-341], the Monte-Carlo method [342-344], the concentration polarization models [345-347] and osmotic pressure [348], the boundary layer theory [349], the dynamic modeling [350], the materials flow analysis [351], the risk and fault analysis [352-353], the numerical methods [354], the chemical kinetics and equilibrium [355], or its combinations [356]. However, such investigations were low numerous and it does not seem possible to define some of them as perspectives.

It should also be noted, that in some works for the RO description the extended Nernst-Plank equation [358-359] and the Donnan equilibrium [359] were used, however, such approaches are conventionally used for the NF, as was shown in work [1], Moreover, the special software (such as ROSA or Q+), which was widely used for the analysis of the economical and energy paraments of RO systems, can be also used for the simulation of the technological parameters and system design, as it was realized, for example, in works [340, 360-365].

5 Conclusions

The technological, energetic, and economic advantages of the reverse osmosis process in conjunction with the benefits of the mathematical simulation determined the considerable spread of this type of investigation. Therefore, it is natural, that the stable trend increasing in the number of publications dedicated to the reverse osmosis simulation is observed. The analysis of publications about this question in the period from 2011 to 2020 allows also traces the main direction and the advantages and disadvantages of the main approaches to the RO simulations.

Thus, the number of publications dedicated to the application of the CFD methods for the mathematical simulation of RO appears to be the largest. The increasing computational power of computer equipment and the development of specialized software, including the appearance the open-source programs, are the evident reasons for this. It is logical to assume, that the same factors promoted the significant increase in the application of the molecular dynamics methods in comparison with the previous decade. Such a trend allows us to conclude, that these two approaches will remain the most widely used in the near future. The main advantages of this method consist in the possibility to obtain a deep understanding of the processes which take place in the membrane apparatus (CFD) or in the membrane itself and on its surface (MD). They also allow us to determine the influence of the large number of factors affecting the process and, therefore, the productivity and effectiveness of separation. However, the simulation using these methods requires the application of more complex and cumbersome calculation methods, and also a high level of skills of operation in corresponding software.

On the other hand, the published results indicate that the interest of the researchers and engineers in hybrid systems, in which the RO is combined with other processes, mostly with distillation, forward osmosis, and renewable energy sources increased significantly. For the simulations of such systems, it is reasonable to apply the simulation techniques which require simpler calculation methods. It was quite unexpected that, for these purposes, the solution-diffusion model was used in the widest range. In the considered period it was used both for the direct RO simulation and for the optimization, energy and economic analysis, and even as boundary conditions in CFD investigation.

At the same time, the application of the irreversible thermodynamics methods, pore flow based models, and other diffusion based models was limited and, likely, further these models will be used mainly for the specific processes analysis. Also, the application of artificial neuron networks was limited, which probably is due to the fact that the possibility of the mechanistic model construction is relatively high for the case of RO. In these conditions, the ANN will be the most effective in systems that are significantly complicated by concentration polarization and fouling.

Therefore, based on the current review it is possible to choose the strategy for the simulation of the RO system. It also should be noticed that represented in the current review the analysis of the software applied for the reverse osmosis simulation, would be useful for educational purposes.

6 Acknowledgments

Authors would like to thank the Armed Forces of Ukraine, National Guard, Territorial Defense, Volunteers for providing security to perform this work. This work has become possible only because resilience and courage of the Ukrainian Army.

References

1. Huliienko S. V. Korniienko Y. M., Gatilov K. O. (2020). Modern trends in the mathematical simulation of pressure-driven membrane processes. *Journal of Engineering Sciences*, Vol. 7(1), pp. F1–F21, doi: https://doi.org/10.21272/jes.2020.7(1).f1
2. Jarzyńska M., Pietruszka M. (2011). The application of the Kedem–Katchalsky equations to membrane transport of ethyl alcohol and glucose. *Desalination*. Vol. 280, Issues 1–3, pp. 14-19, doi: https://doi.org/10.1016/j.desal.2011.07.034
3. Al-Obaidi M.A., Kara-Zaitri C., Mujtaba M. (2017). Scope and limitations of the irreversible thermodynamics and the solution diffusion models for the separation of binary and multi-component systems in reverse osmosis process. *Computers & Chemical Engineering*. Vol. 100, pp. 48-79, doi: https://doi.org/10.1016/j.compchemeng.2017.02.001
4. Qasim M., Badrelzaman M., Darwish N.N., Darwish N. A., Hilal N. (2019). Reverse osmosis desalination: A state-of-the-art review. *Desalination*. Volume 459, pp. 59-104, doi: https://doi.org/10.1016/j.desal.2019.02.008
5. Ahmed F. E., Hashaikeh R., Diabat A., Hilal N. (2019). Mathematical and optimization modelling in desalination: State-of-the-art and future direction. *Desalination*. Vol. 469, 114092, doi: https://doi.org/10.1016/j.desal.2019.114092
6. Karabelas A.J., Kostoglou M., Koutsou C.P. (2015). Modeling of spiral wound membrane desalination modules and plants – review and research priorities. *Desalination*. Vol. 356, pp. 165-186, doi: https://doi.org/10.1016/j.desal.2014.10.002
7. Keir, G., Jegatheesan, V. (2014). A review of computational fluid dynamics applications in pressure-driven membrane filtration. *Reviews in Environmental Science and Bio/Technology*. Vol. 13, pp. 183–201, doi: https://doi.org/10.1007/s11157-013-9327-x
8. Toh K. Y., Liang Y. Y., Lau W. J., Fimbres Weihs G. A. (2020). A Review of CFD Modelling and Performance Metrics for Osmotic Membrane Processes. *Membranes*. Vol. 10, Is. 10, 285, doi: https://doi.org/10.3390/membranes10100285
9. Cohen-Tanugi D., Grossman J. C. (2015). Nanoporous graphene as a reverse osmosis membrane: Recent insights from theory and simulation. *Desalination*. Vol. 366, pp. 59-70, doi: https://doi.org/10.1016/j.desal.2014.12.046
10. Ebro H., Kim Y. M., Kim J. H. (2013). Molecular dynamics simulations in membrane-based water treatment processes: A systematic overview. *Journal of Membrane Science*. Vol. 438, pp. 112-125, doi: https://doi.org/10.1016/j.memsci.2013.03.027
11. Ridgway H. F., Orbell J., Gray S. (2017). Molecular simulations of polyamide membrane materials used in desalination and water reuse applications: Recent developments and future prospects. *Journal of Membrane Science*. Vol. 524, pp. 436-448, doi: https://doi.org/10.1016/j.memsci.2016.11.061
12. Wang J., Dlamini D. S., Mishra A. K., Pendergast M. T. M., Wong M. C.Y., Mamba B. B., Freger V., Verliefde A. R.D., Hoek E. M.V. (2014). A critical review of transport through osmotic membranes. *Journal of Membrane Science*. Vol. 454, pp. 516-537, doi: https://doi.org/10.1016/j.memsci.2013.12.034
13. Ismail A. F., Matsuura T. (2018). Progress in transport theory and characterization method of Reverse Osmosis (RO) membrane in past fifty years. *Desalination*. Vol. 434, pp. 2-11, doi: https://doi.org/10.1016/j.desal.2017.09.028
14. Alsarayreh A. A., Al-Obaidi M. A., Patel R., Mujtaba I. M. (2020). Scope and Limitations of Modelling, Simulation, and Optimisation of a Spiral Wound Reverse Osmosis Process-Based Water Desalination. *Processes*. Vol. 8, Is. 5, 573, doi: https://doi.org/10.3390/pr8050573
15. Park K. Kim J., Yang D. R., Hong S. (2020). Towards a low-energy seawater reverse osmosis desalination plant: A review and theoretical analysis for future directions. *Journal of Membrane Science*. Vol. 595, 117607, doi: https://doi.org/10.1016/j.memsci.2019.117607
16. Abejón R., Garea A., Irabien A. (2012). Analysis, modelling and simulation of hydrogen peroxide ultrapurification by multistage reverse osmosis. *Chemical Engineering Research and Design*. Vol. 90, Is.3, pp. 442-452, doi: https://doi.org/10.1016/j.cherd.2011.07.025
17. Abejón R., Garea A., Irabien A. (2012). Integrated countercurrent reverse osmosis cascades for hydrogen peroxide ultrapurification, *Computers & Chemical Engineering*, Vol. 41, pp. 67-76, doi: https://doi.org/10.1016/j.compchemeng.2012.02.017
18. Fujioka T., Khan S. J., McDonald J. A., Roux A., Poussade Y., Drewes J. E., Nghiem L. D. (2014). Modelling the rejection of N-nitrosamines by a spiral-wound reverse osmosis system: Mathematical model development and validation, *Journal of Membrane Science*, Vol. 454, pp. 212-219, doi: https://doi.org/10.1016/j.memsci.2013.12.008
19. Zaghbani N., Nakajima M., Nabetani Hiroshi, Hafiane A. (2017). Modeling of reverse osmosis flux of aqueous solution containing glucose, *Korean Journal of Chemical Engineering*, Vol. 34, pp. 407–412, doi: https://doi.org/10.1007/s11814-016-0298-9
20. Ruiz-García A., Nuez I. (2016). Long-term performance decline in a brackish water reverse osmosis desalination plant. Predictive model for the water permeability coefficient, *Desalination*, Vol. 397, pp. 101-107, doi: https://doi.org/10.1016/j.desal.2016.06.027
21. Al-Obaidi M. A., Kara-Zaïtri C., Mujtaba I. M. (2016). Development and Validation of N-nitrosamine Rejection Mathematical Model Using a Spiral-wound Reverse Osmosis Process, *Chemical engineering transactions*, Vol. 52, pp. 1129-1134, doi: https://doi.org/10.3303/CET1652189
22. Al-Obaidi M.A., Kara-Zaïtri C., Mujtaba I.M. (2017). Removal of phenol from wastewater using spiral-wound reverse osmosis process: Model development based on experiment and simulation, *Journal of Water Process Engineering*, Vol. 18, pp. 20-28, doi: https://doi.org/10.1016/j.jwpe.2017.05.005
23. Karabelas A. J., Kostoglou M., Koutsou C. P. (2019). Advanced Dynamic Simulation of Membrane Desalination Modules Accounting for Organic Fouling, *Journal of Membrane Science & Research*, Vol. 5, Is. 2, pp. 178-186, doi: https://doi.org/10.22079/JMSR.2019.94172.1216

24. Kezia K., Lee J., Hill A. J., Kentish S. E. (2013). Convective transport of boron through a brackish water reverse osmosis membrane, *Journal of Membrane Science*, Vol. 445, pp. 160-169, doi: https://doi.org/10.1016/j.memsci.2013.05.041
25. Nir O., Lahav O. (2014). Modeling weak acids' reactive transport in reverse osmosis processes: A general framework and case studies for SWRO, *Desalination*, Vol. 343, pp. 147-153, doi: https://doi.org/10.1016/j.desal.2013.11.009
26. Chen C., Qin H. (2019). A Mathematical Modeling of the Reverse Osmosis Concentration Process of a Glucose Solution, *Processes*, Vol. 7(5), 271, doi: https://doi.org/10.3390/pr7050271
27. Al-Obaidi M.A., Kara-Zaïtri C., Mujtaba I.M. (2018). Simulation and optimisation of spiral-wound reverse osmosis process for the removal of N-nitrosamine from wastewater. *Chemical Engineering Research and Design*. Vol. 133, pp. 168-182, https://doi.org/10.1016/j.cherd.2018.03.012
28. Patroklou G., Sassi K. M., Mujtaba I. M. (2013). Simulation of Boron Rejection by Seawater Reverse Osmosis Desalination, *Chemical engineering transactions*, Vol. 32, pp. 1873-1878, doi: https://doi.org/10.3303/CET1332313
29. Arjmandia M., Chenar M. P., Altaee A., Arjmandi A., Peyravi M., Jahanshahi M., Binaeian E. (2020). Caspian seawater desalination and whey concentration through forward osmosis (FO)-reverse osmosis (RO) and FO-FO-RO hybrid systems: Experimental and theoretical study. *Journal of Water Process Engineering*. Vol. 37, 101492, doi: https://doi.org/10.1016/j.jwpe.2020.101492
30. Gaublomme D., Strubbe L., Vanoppen M., Torfs E., Mortier S., Cornelissen E., De Gusseme B., Verliefde A. Nopens I. (2020). A generic reverse osmosis model for full-scale operation. *Desalination*. Vol. 490, 114509, doi: https://doi.org/10.1016/j.desal.2020.114509
31. Ennasri H., Drighil A., Adhiri R., Fahli A., Moussetad M. (2019). Design and Simulation of a Solar Energy System for Desalination of Brackish Water. *Environmental and Climate Technologies*. Vol. 23, Is. 1, pp. 257–276, doi: https://doi.org/10.2478/rtuect-2019-0017
32. Al-Alawy A. F., Salih M. H. (2016). Experimental Study and Mathematical Modelling of Zinc Removal by Reverse Osmosis Membranes. *Iraqi Journal of Chemical and Petroleum Engineering*. Vol.17 No.3, pp. 57- 73.
33. Sachit D. E. (2017). Effect of Several Parameters on Membrane Fouling by Using Mathematical Models of Reverse Osmosis Membrane System. *Al-Nahrain Journal for Engineering Sciences*. Vol.20 No.4, pp.864-870.
34. Al-Obaidi M.A., Mujtaba I.M. (2016). Steady state and dynamic modeling of spiral wound wastewater reverse osmosis process. *Computers & Chemical Engineering*. Vol. 90, pp. 278-299, doi: https://doi.org/10.1016/j.compchemeng.2016.04.001
35. Al-Obaidi M.A., Kara- Zaïtri C., Mujtaba I.M. (2017). Optimum design of a multi-stage reverse osmosis process for the production of highly concentrated apple juice. *Journal of Food Engineering*. Vol. 214, pp. 47-59. doi: https://doi.org/10.1016/j.jfoodeng.2017.06.020
36. Al-Obaidi M.A., Li J-P., Kara-Zaïtri C., Mujtaba I.M. (2017). Optimisation of reverse osmosis based wastewater treatment system for the removal of chlorophenol using genetic algorithms. *Chemical Engineering Journal*. Vol. 316, pp. 91-100. doi: https://doi.org/10.1016/j.cej.2016.12.096
37. Al-Obaidi M.A., Kara-Zaïtri C., Mujtaba I.M. (2017). Development of a mathematical model for apple juice compounds rejection in a spiral-wound reverse osmosis process. *Journal of Food Engineering*. Vol. 192, pp.111-121, doi: https://doi.org/10.1016/j.jfoodeng.2016.08.005
38. Al-Obaidi M.A., Li J-P., Alsadaie S., Kara-Zaïtri C., Mujtaba I.M. (2018). Modelling and optimisation of a multistage Reverse Osmosis processes with permeate reprocessing and recycling for the removal of N-nitrosodimethylamine from wastewater using Species Conserving Genetic Algorithms. *Chemical Engineering Journal*. Vol. 350, pp. 824-834, doi: https://doi.org/10.1016/j.cej.2018.06.022
39. Altaee A. (2012). Computational model for estimating reverse osmosis system design and performance: Part-one binary feed solution. *Desalination*. Vol. 291, pp. 101-105, doi: https://doi.org/10.1016/j.desal.2012.01.028
40. Altaee A., Zaragoza G., van Tonningen H. R. (2014). Comparison between Forward Osmosis-Reverse Osmosis and Reverse Osmosis processes for seawater desalination. *Desalination*. Vol. 336, pp. 50-57, doi: https://doi.org/10.1016/j.desal.2014.01.002
41. Altaee A., Sharif A., Zaragoza G., Ismail A. F. (2015). Evaluation of FO-RO and PRO-RO designs for power generation and seawater desalination using impaired water feeds. *Desalination*. Vol. pp. 27-35, doi: https://doi.org/10.1016/j.desal.2014.06.022
42. Altaee A., Hilal N. (2015). High recovery rate NF–FO–RO hybrid system for inland brackish water treatment. *Desalination*. Vol. 363, pp. 19-25, doi: https://doi.org/10.1016/j.desal.2014.12.017
43. Ameri M., Eshaghi M. S. (2016). A novel configuration of reverse osmosis, humidification–dehumidification and flat plate collector: Modeling and exergy analysis. *Applied Thermal Engineering*. Vol. 103, pp. 855-873, doi: https://doi.org/10.1016/j.applthermaleng.2016.04.047
44. Barello M., Manca D., Patel R., Mujtaba I.M. (2015). Operation and modeling of RO desalination process in batch mode. *Computers & Chemical Engineering*. Vol. 83, pp. 139-156. doi: https://doi.org/10.1016/j.compchemeng.2015.05.022
45. Choi J.-S., Kim J.-T. (2015). Modeling of full-scale reverse osmosis desalination system: Influence of operational parameters. *Journal of Industrial and Engineering Chemistry*. Vol. 21, pp. 261-268, doi: https://doi.org/10.1016/j.jiec.2014.02.033
46. Fujioka T., Oshima N., Suzuki R., Price W. E., Nghiem L. D. (2015). Probing the internal structure of reverse osmosis membranes by positron annihilation spectroscopy: Gaining more insight into the transport of water and small solutes. *Journal of Membrane Science*. Vol. 486, pp. 106-118, doi: https://doi.org/10.1016/j.memsci.2015.02.007
47. Hung L.-Y., Lue S. J., You J.-H. (2011). Mass-transfer modeling of reverse-osmosis performance on 0.5–2% salty water. *Desalination*. Vol. 265, pp 67-73, doi: https://doi.org/10.1016/j.desal.2010.07.033

48. Jbari Y., Abderaf S. (2020). Parametric study to enhance performance of wastewater treatment process, by reverse osmosis-photovoltaic system. *Applied Water Science*. Vol. 10, 217, doi: https://doi.org/10.1007/s13201-020-01301-4
49. Jiang A., Biegler L. T., Wang J., Cheng W., Ding Q., Jiangzhou S. (2015). Optimal operations for large-scale seawater reverse osmosis networks. *Journal of Membrane Science*. Vol. 476, pp. 508-524, doi: https://doi.org/10.1016/j.memsci.2014.12.005
50. Kim J., Park M., Shon H. K., Kim J. H. (2016). Performance analysis of reverse osmosis, membrane distillation, and pressure-retarded osmosis hybrid processes. *Desalination*. Vol. 380, pp. 85-92, doi: https://doi.org/10.1016/j.desal.2015.11.019
51. Álvarez J. R., Antón F. E., Álvarez-García S., Luque S. (2020). Treatment of Aqueous Effluents from Steel Manufacturing with High Thiocyanate Concentration by Reverse Osmosis. *Membranes*. Vol. 10, Is. 12, 437, doi: https://doi.org/10.3390/membranes10120437
52. Nir O., Lahav O. (2013). Coupling mass transport and chemical equilibrium models for improving the prediction of SWRO permeate boron concentrations. *Desalination*. Vol. 310, pp. 87-92, doi: https://doi.org/10.1016/j.desal.2012.09.001
53. Sundaramoorthy S., Srinivasan G., Murthy D.V.R. (2011). An analytical model for spiral wound reverse osmosis membrane modules: Part I — Model development and parameter estimation. *Desalination*. Vol. 280, Is. 1–3, pp. 403-411, doi: https://doi.org/10.1016/j.desal.2011.03.047
54. Gui S., Mai Z., Fu J., Wei Y., Wan J. (2020). Transport Models of Ammonium Nitrogen in Wastewater from Rare Earth Smelteries by Reverse Osmosis Membranes. *Sustainability*. Vol. 12, Is. 15, 6230, doi: https://doi.org/10.3390/su12156230
55. Wu X., Hu Y., Wu L., Li H. (2014). Model and Design of Cogeneration System for Different Demands of Desalination Water, Heat and Power Production. *Chinese Journal of Chemical Engineering*. Vol. 22, Is. 3, pp. 330-338, doi: https://doi.org/10.1016/S1004-9541(14)60036-7
56. Mai Z., Gui S., Fu J., Jiang C., Ortega E., Zhao Y., Tu W., Mickols W., Van der Bruggen B. (2019). Activity-derived model for water and salt transport in reverse osmosis membranes: A combination of film theory and electrolyte theory. *Desalination*, Vol. 469, 114094. doi: https://doi.org/10.1016/j.desal.2019.114094
57. Filippini G., Al-Obaidi M.A., Manenti F., Mujtaba I.M. (2018). Performance analysis of hybrid system of multi effect distillation and reverse osmosis for seawater desalination via modelling and simulation. *Desalination*, Vol. 448, pp. 21-35, doi: https://doi.org/10.1016/j.desal.2018.09.010
58. Al-Obaidi M.A., Alsarayreh A.A., Al-Hroub A.M., Alsadaie S., Mujtaba I.M. (2018). Performance analysis of a medium-sized industrial reverse osmosis brackish water desalination plant. *Desalination*. Vol. 443, pp. 272-284. doi: https://doi.org/10.1016/j.desal.2018.06.010
59. Ruiz-García A., de la Nuez Pestana I. (2019). Feed spacer geometries and permeability coefficients. Effect on the performance in BWRO spiral-wound membrane modules. *Water*. Vol. 11, 152. doi: https://doi.org/10.3390/w11010152
60. Ruiz-García A., de la Nuez Pestana I. (2018). A computational tool for designing BWRO systems with spiral wound modules. *Desalination*. Vol. 426, pp. 69-77. doi: http://dx.doi.org/10.1016/j.desal.2017.10.040
61. Skiborowski M. Mhamdi A., Kraemer K., Marquardt W. (2012). Model-based structural optimization of seawater desalination plants. *Desalination*. Vol. 292, pp. 30-44. doi: http://dx.doi.org/10.1016/j.desal.2012.02.007
62. Gautam D. K., Teklu H., Subbiah S. (2020). Analysis of reverse osmosis process in hollow fiber module with and without secondary permeate outlet. *Journal of Water Process Engineering*. Vol. 36, 101336. doi: https://doi.org/10.1016/j.jwpe.2020.101336
63. Al-Obaidi M.A., Kara-Zaitri C., Mujtaba I.M. (2018). Performance evaluation of multi-stage and multi-pass reverse osmosis networks for the removal of N-nitrosodimethylamine -D6 (NDMA) from wastewater using model-based techniques. *Journal of Environmental Chemical Engineering*. Vol. 6, Is. 4, pp. 4797-4808. doi: https://doi.org/10.1016/j.jece.2018.06.014
64. Gu B. Xu X. Y., Adjiman C. S. (2017). A predictive model for spiral wound reverse osmosis membrane modules: The effect of winding geometry and accurate geometric details. *Computers & Chemical Engineering*. Vol. 96, pp. 248-265. doi: https://doi.org/10.1016/j.compchemeng.2016.07.029
65. Efraty A. (2016). CCD series no-22: Recent advances in RO, FO and PRO and their hybrid applications for high recovery desalination of treated sewage effluents. *Desalination*. Vol. 389, pp. 18-38. doi: http://dx.doi.org/10.1016/j.desal.2016.01.009
66. Kim J., Park K., Hong S. (2020). Optimization of two-stage seawater reverse osmosis membrane processes with practical design aspects for improving energy efficiency. *Journal of Membrane Science*. Vol. 601, 117889. doi: https://doi.org/10.1016/j.memsci.2020.117889
67. Fraidenraich N., de Castro Vilela O., dos Santos Viana M., Gordon J. M. (2016). Improved analytic modeling and experimental validation for brackish-water reverse-osmosis desalination. *Desalination*. Vol. 380, pp.60-65. doi: http://dx.doi.org/10.1016/j.desal.2015.11.014
68. M.A., Kara-Zaitri C., Mujtaba I.M. (2019). Performance evaluation of multi-stage reverse osmosis process with permeate and retentate recycling strategy for the removal of chlorophenol from wastewater. *Computers & Chemical Engineering*. Vol. 121, pp. 12-26. doi: https://doi.org/10.1016/j.compchemeng.2018.08.035
69. Wang Q., Zhou Z., Li J., Tang Q., Hu Y. (2019). Investigation of the reduced specific energy consumption of the RO-PRO hybrid system based on temperature-enhanced pressure retarded osmosis. *Journal of Membrane Science*. Vol. 581, pp. 439-452. doi: https://doi.org/10.1016/j.memsci.2019.03.079
70. Kim J., Park M., Snyder Sh. A., Kim J. H. (2013). Reverse osmosis (RO) and pressure retarded osmosis (PRO) hybrid processes: Model-based scenario study. *Desalination*. Vol. pp. 121-130. doi: http://dx.doi.org/10.1016/j.desal.2013.05.010

71. Niewersch C., Rieth C., Hailemariam L., Oriol G. G., Warczok J. (2020). Reverse osmosis membrane element integrity evaluation using imperfection model. *Desalination*. Vol. 476, 114175. doi: https://doi.org/10.1016/j.desal.2019.114175
72. Zaidi S.M. J., Fadhillah F., Khan Z., Ismail A.F. (2015). Salt and water transport in reverse osmosis thin film composite seawater desalination membranes. *Desalination*. Vol. 368, pp. 202-213. doi: http://dx.doi.org/10.1016/j.desal.2015.02.026
73. Yao S., Ji M. (2020). A small RO and MCDI coupled seawater desalination plant and its performance simulation analysis and optimization. *Processes*. 2020, Vol. 8(8), 944. doi: https://doi.org/10.3390/pr8080944
74. Sassi K., Mujtaba I. (2011). Optimal design of reverse osmosis based desalination process with seasonal variation of feed temperature. *Chemical Engineering Transactions*. Vol. 25, pp. 1055-1060. doi: https://doi.org/10.3303/CET1125176
75. Sassi K., Mujtaba I. (2011). Optimal design and operation of reverse osmosis desalination process with membrane fouling. *Chemical Engineering Journal*. Vol. 171, Is. 2, pp. 582-593. doi: https://doi.org/10.1016/j.cej.2011.04.034
76. Park K., Heo H., Kim D. Y., Yang D. R. (2018). Feasibility study of a forward osmosis/crystallization/reverse osmosis hybrid process with high-temperature operation: Modeling, experiments, and energy consumption. *Journal of Membrane Science*. Vol. 555, pp. 206-219. doi: https://doi.org/10.1016/j.memsci.2018.03.031
77. Venkata Swamy B., Madhumala M., Prakasham R.S., Sridhar S. (2013). Nanofiltration of bulk drug industrial effluent using indigenously developed functionalized polyamide membrane. *Chemical Engineering Journal*. Vol. 233, pp. 193-200. doi: https://doi.org/10.1016/j.cej.2013.08.045
78. Golnari A., Moradi A., Soltani A. (2013). Effects of different potential functions on modeling of RO membrane performance by use of an advanced model. *Research on Chemical Intermediates*. Vol. 39, pp. 2603–2619. doi: https://doi.org/10.1007/s11164-012-0784-6
79. Moradi A., Mojarradi V., Sarcheshmehpour M. (2013). Prediction of RO membrane performances by use of artificial neural network and using the parameters of a complex mathematical model. *Research on Chemical Intermediates*. Vol. 39, pp. 3235–3249. doi: https://doi.org/10.1007/s11164-012-0835-z
80. Madsen H. T., Søgaard E. G. (2014). Applicability and modelling of nanofiltration and reverse osmosis for remediation of groundwater polluted. with pesticides and pesticide transformation products. *Separation and Purification Technology*. Vol. 125, pp. 111-119. doi: http://dx.doi.org/10.1016/j.seppur.2014.01.038
81. Takeuchi Sh., Tazaki A., Miyauchi S., Kajishim T. (2019). A relation between membrane permeability and flow rate at low Reynolds number in circular pipe. *Journal of Membrane Science*. Vol. 582, pp. 91-102. doi: https://doi.org/10.1016/j.memsci.2019.03.018
82. Merdaw A.A., Sharif A.O., Derwish G.A.W. (2011). Mass transfer in pressure-driven membrane separation processes, Part I. *Chemical Engineering Journal*. Vol. 168, pp. 215-228. doi: https://doi.org/10.1016/j.cej.2010.12.071
83. Rohlfs W., Thiel G. P., Lienhard V J. H. (2016). Modeling reverse osmosis element design using superposition and an analogy to convective heat transfer. *Journal of Membrane Science*. Vol. 512, pp. 38-49. doi: http://dx.doi.org/10.1016/j.memsci.2016.03.049
84. Kavianipour O., Ingram G. D., Vuthaluru H. B. (2017). Investigation into the effectiveness of feed spacer configurations for reverse osmosis membrane modules using Computational Fluid Dynamics. *Journal of Membrane Science*. Vol. 526, pp. 156-171. doi: http://dx.doi.org/10.1016/j.memsci.2016.12.034
85. Anqi A. E., Alkhamis N., Oztekin A. (2015). Numerical simulation of brackish water desalination by a reverse osmosis membrane. *Desalination*. Vol. 369, pp. 156-164. doi: http://dx.doi.org/10.1016/j.desal.2015.05.007
86. Anqi A. E., Alrehili M., Usta M., Oztekin A. (2016). Numerical analysis of hollow fiber membranes for desalination. *Desalination*. Vol. 398, pp. 39-51. doi: http://dx.doi.org/10.1016/j.desal.2016.07.019
87. Anqi A. E., Alkhamis N., Oztekin A. (2016). Steady three dimensional flow and mass transfer analyses for brackish water desalination by reverse osmosis membranes. *International Journal of Heat and Mass Transfer*. Vol. 101, pp. 399-411. doi: http://dx.doi.org/10.1016/j.ijheatmasstransfer.2016.05.102
88. Anqi A. E., Alkhamis N., Oztekin A. (2016). Computational study of desalination by reverse osmosis – Three-dimensional analyses. *Desalination*. Vol. 388, pp. 38-49. doi: http://dx.doi.org/10.1016/j.desal.2016.03.017
89. Hamdache A., Belkacem M. (2018). Efects of a zero normal-concentration-gradient outfow boundary condition on concentration polarization in a CFD study of a reverse osmosis process. *Journal of the Brazilian Society of Mechanical Sciences and Engineering*. Vol. 40, 507. doi: https://doi.org/10.1007/s40430-018-1430-z
90. Jogdand A., Chaudhuri A. (2015). Modeling of concentration polarization and permeate flux variation in a roto-dynamic reverse osmosis filtration system. *Desalination*. Vol. 375, pp. 54-70. doi: http://dx.doi.org/10.1016/j.desal.2015.07.011
91. Min J., Zhang B. (2014). Numerical Studies of Convective Mass Transfer Enhancement in a Membrane Channel by Rectangular Winglets. *Chinese Journal of Chemical Engineering*. Vol. 22, pp. 1061-1071. doi: http://dx.doi.org/10.1016/j.cjche.2014.09.004
92. Mojab S. M., Pollard A., Pharoah J. G., Beale S. B., Hanff E. S. (2014). Unsteady Laminar to Turbulent Flow in a Spacer-Filled Channel. *Flow, Turbulence and Combustion*. Vol. 92, pp. 563–577. doi: http://dx.doi.org/10.1007/s10494-013-9514-4
93. Ratnayake P., Setiawan R., Bao J., Fimbres-Weihs G., Wiley D. E. (2016). Spatio-temporal frequency response analysis of forced slip velocity effect on solute concentration oscillations in a reverse osmosis membrane channel. *Computers & Chemical Engineering*. Vol. 84, pp. 151-161. doi: http://dx.doi.org/10.1016/j.compchemeng.2015.08.016
94. Rohlfs W., Lienhard V J. H. (2016). Entrance length effects on Graetz number scaling in laminar duct flows with periodic obstructions: Transport number correlations for spacer-filled membrane channel flows. *International Journal of Heat and Mass Transfer*. Vol. 97, pp. 842-852. doi: http://dx.doi.org/10.1016/j.ijheatmasstransfer.2016.02.078

95. Saeed A., Vuthaluru R., Vuthaluru H. B. (2015). Investigations into the effects of mass transport and flow dynamics of spacer filled membrane modules using CFD. *Chemical Engineering Research and Design*. Vol. 93, pp. 79-99. doi: http://dx.doi.org/10.1016/j.cherd.2014.07.002
96. Sousa P., Soares A., Monteiro E., Rouboa A. (2014). A CFD study of the hydrodynamics in a desalination membrane filled with spacers. *Desalination*. Vol. 349, pp. 22-30. doi: http://dx.doi.org/10.1016/j.desal.2014.06.019
97. Usta M., Anqi A. E., Oztekin A. (2017). Reverse osmosis desalination modules containing corrugated membranes – Computational study. *Desalination*. Vol. 416, pp. 129-139. doi: http://dx.doi.org/10.1016/j.desal.2017.05.005
98. Kaufman Y., Kasher R., Lammertink R. G.H., Freger V. (2012). Microfluidic NF/RO separation: Cell design, performance and application. *Journal of Membrane Science*. Vol. 396, pp. 67-73. doi: http://doi.org/10.1016/j.memsci.2011.12.052
99. Abdelbaky M. M. A., El-Refaee M. M. (2019). A 3D CFD comparative study between torsioned and non-torsioned net-type feed spacer in reverse osmosis. *SN Applied Sciences*. Vol. 1, 1059. doi: https://doi.org/10.1007/s42452-019-1098-8
100. Jeong K., Park M., Ohd S., Kim J. H. (2020). Impacts of flow channel geometry, hydrodynamic and membrane properties on osmotic backwash of RO membranes—CFD modeling and simulation. *Desalination*. Vol. 476, 114229. doi: https://doi.org/10.1016/j.desal.2019.114229
101. Luo J., Lie M., Heng Y. (2020). A hybrid modeling approach for optimal design of non-woven membrane channels in brackish water reverse osmosis process with high-throughput computation. *Desalination*. Vol. 489, 114463. doi: https://doi.org/10.1016/j.desal.2020.114463
102. Bucs Sz.S., Radu A.I., Lavric V., Vrouwenvelder J.S., Picioreanu C. (2014). Effect of different commercial feed spacers on biofouling of reverse osmosis membrane systems: A numerical study. *Desalination*. Vol. 343, pp. 26-37. doi: http://dx.doi.org/10.1016/j.desal.2013.11.007
103. Gu B., Adjiman C. S., Xu X. Y. (2017). The effect of feed spacer geometry on membrane performance and concentration polarisation based on 3D CFD simulations. *Journal of Membrane Science*. Vol. 527, pp. 78-91. doi: http://dx.doi.org/10.1016/j.memsci.2016.12.058
104. Haaksman V. A., Siddiqui A., Schellenberg C., Kidwell J., Vrouwenvelder J. S., Picioreanu C. (2017). Characterization of feed channel spacer performance using geometries obtained by X-ray computed tomography. *Journal of Membrane Science*. Vol. 522, pp. 124-139. doi: http://dx.doi.org/10.1016/j.memsci.2016.09.005
105. Horstmeyer N., Lippert T., Schön D., Schlederer F., Picioreanu C., Achterhold K., Pfeiffer F., Drewes J. E. (2018). CT scanning of membrane feed spacers – Impact of spacer model accuracy on hydrodynamic and solute transport modeling in membrane feed channels. *Journal of Membrane Science*. Vol. 564, pp 133-145. doi: https://doi.org/10.1016/j.memsci.2018.07.006
106. Gogar R., Vaseghi G., Lipscomb G. (2019). Comparisons of Experimental and Simulated Velocity Fields in Membrane Module Spacers. *Journal of Membrane Science & Research*. Vol. 5, Is. 4, pp. 283-294. doi: https://doi.org/10.22079/JMSR.2019.101683.1242
107. Kerdi S., Qamar A., Alpatova A., Vrouwenvelder J. S., Ghaffour N. (2020). Membrane filtration performance enhancement and biofouling mitigation using symmetric spacers with helical filaments. *Desalination*. Vol. 484, pp. 114454. doi: https://doi.org/10.1016/j.desal.2020.114454
108. Kostoglou M., Karabelas A. J. (2013). Comprehensive simulation of flat-sheet membrane element performance in steady state desalination. *Desalination*. Vol. 316, pp. 91-102. doi: http://dx.doi.org/10.1016/j.desal.2013.01.033
109. Kostoglou M., Karabelas A.J. (2016). Dynamic operation of flat sheet desalination-membrane elements: A comprehensive model accounting for organic fouling. *Computers & Chemical Engineering*. Vol. 93, pp. 1-12. doi: http://dx.doi.org/10.1016/j.compchemeng.2016.06.001
110. Koutsou C. P., Karabelas A. J. (2015). A novel retentate spacer geometry for improved spiral wound membrane (SWM) module performance. *Journal of Membrane Science*. Vol. 488, pp. 129-142. doi: http://dx.doi.org/10.1016/j.memsci.2015.03.064
111. Lee Y. K., Won Y.-J., Yoo J. H., Ahn K. H., Lee C.-H. (2013). Flow analysis and fouling on the patterned membrane surface. *Journal of Membrane Science*. Vol. 427, pp. 320-325. doi: http://dx.doi.org/10.1016/j.memsci.2012.10.010
112. Li M., Bui T., Chao S. (2016). Three-dimensional CFD analysis of hydrodynamics and concentration polarization in an industrial RO feed channel. *Desalination*. Vol. 397, pp. 194-204. doi: http://dx.doi.org/10.1016/j.desal.2016.07.005
113. Mansouri N., Moghimi M., Taherinejad M. (2019). Investigation on hydrodynamics and mass transfer in a feed channel of a spiral-wound membrane element using response surface methodology. *Chemical Engineering Research and Design*. Vol. 149, pp. 147-157. doi: https://doi.org/10.1016/j.cherd.2019.07.006
114. Shoukat G., Ellahi F., Sajid M., Uddin E. (2020). Computational Study of Zigzag Spacer Design with Elliptical Cross-Section Filaments. *MATEC Web of Conferences*. Vol. 307, 01047. doi: https://doi.org/10.1051/matecconf/202030701047
115. Minelli M., Baschetti M. G., Doghieri F. (2011). A comprehensive model for mass transport properties in nanocomposites. *Journal of Membrane Science*. Vol. 381, Is. 1–2, pp. 10-20. doi: https://doi.org/doi:10.1016/j.memsci.2011.06.036
116. Motevalian S. P., Borhan A., Zhou H., Zydney A. (2016). Twisted hollow fiber membranes for enhanced mass transfer. *Journal of Membrane Science*. Vol. 514, pp. 586-594. doi: http://dx.doi.org/10.1016/j.memsci.2016.05.027
117. Park J., Lee K. S. (2017). A two-dimensional model for the spiral wound reverse osmosis membrane module. *Desalination*. Vol. 416, pp. 157-165. doi: http://dx.doi.org/10.1016/j.desal.2017.05.006
118. Qamar A., Bucs S., Picioreanu C., Vrouwenvelder J., Ghaffour N. (2019). Hydrodynamic flow transition dynamics in a spacer filled filtration channel using direct numerical simulation. *Journal of Membrane Science*. Vol. 590, 117264. doi: https://doi.org/10.1016/j.memsci.2019.117264

119. Ronen A., Lerman S., Ramon G. Z., Dosoretz C. G. (2015). Experimental characterization and numerical simulation of the anti-biofuling activity of nanosilver-modified feed spacers in membrane filtration. *Journal of Membrane Science*. Vol. 475, pp. 320-329. doi: http://dx.doi.org/10.1016/j.memsci.2014.10.042
120. Toh K.Y., Liang Y.Y., Lau W.J., Fimbres Weihs G.A. (2020). 3D CFD study on hydrodynamics and mass transfer phenomena for SWM feed spacer with different floating characteristics. *Chemical Engineering Research and Design*. Vol. 159, pp. 36-46. doi: https://doi.org/10.1016/j.cherd.2020.04.010
121. Usta M., Morabito M., Anqi A., Alrehili M., Hakim A., Oztekin A. (2018). Twisted hollow fiber membrane modules for reverse osmosis-driven desalination. *Desalination*. Vol. 441, pp. 21-34. doi: https://doi.org/10.1016/j.desal.2018.04.027
122. Qi J., Lv J., Li Z., Bian W., Li J., Liu S. (2020). A Numerical Simulation of Membrane Distillation Treatment of Mine Drainage by Computational Fluid Dynamics. *Water*. Vol. 12, Is. 12., 3403. doi: https://doi.org/10.3390/w12123403
123. Xie P., Murdoch L. C., Ladner D. A. (2014). Hydrodynamics of sinusoidal spacers for improved reverse osmosis performance. *Journal of Membrane Science*. Vol. 453, pp. 92-99. doi: http://dx.doi.org/10.1016/j.memsci.2013.10.068
124. Yang Zh., Cheng J., Yang C., Liang B. (2016). CFD-based optimization and design of multi-channel inorganic membrane tubes. *Chinese Journal of Chemical Engineering*. Vol. 24, Is. 10, pp. 1375-1385. doi: http://dx.doi.org/10.1016/j.cjche.2016.05.044
125. Zhuang L., Guo H., Wang P., Dai G. (2015). Study on the flux distribution in a dead-end outside-in hollow fiber membrane module. *Journal of Membrane Science*. Vol. 495, pp. 372-383. doi: http://dx.doi.org/10.1016/j.memsci.2015.07.060
126. Zhuang L., Guo H., Dai G., Xu Z. (2017). Effect of the inlet manifold on the performance of a hollow fiber membrane module-A CFD study. *Journal of Membrane Science*. Vol. 526, pp. 73-93. doi: http://dx.doi.org/10.1016/j.memsci.2016.12.018
127. Uppu A., Chaudhuri A., Das Sh. P., Prakash N. (2020). CFD modeling of gypsum scaling in cross-flow RO filters using moments of particle population balance. *Journal of Environmental Chemical Engineering*. Vol. 8, Is. 5, 104151. doi: https://doi.org/10.1016/j.jece.2020.104151
128. Liang Y.Y., Fimbres Weihs G.A., Fletcher D.F. (2018). CFD study of the effect of unsteady slip velocity waveform on shear stress in membrane systems. *Chemical Engineering Science*. Vol. 192, pp. 16-24. doi: https://doi.org/10.1016/j.ces.2018.07.009
129. Liang Y.Y., Fimbres Weihs G.A., Wiley D.E. (2020). Comparison of oscillating flow and slip velocity mass transfer enhancement in spacer-filled membrane channels: CFD analysis and validation. *Journal of Membrane Science*. Vol. 593, 117433. doi: https://doi.org/10.1016/j.memsci.2019.117433
130. Liang Y.Y., Toh K.Y., Fimbres Weihs G.A. (2019). 3D CFD study of the effect of multi-layer spacers on membrane performance under steady flow. *Journal of Membrane Science*. Vol. 580, pp. 256-267. doi: https://doi.org/10.1016/j.memsci.2019.02.015
131. Lim S.Y., Liang Y.Y., Fimbres Weihs G.A., Wiley D.E., Fletcher D.F. (2018). A CFD study on the effect of membrane permeance on permeate flux enhancement generated by unsteady slip velocity. *Journal of Membrane Science*. Vol. 556, pp. 138-145. doi: https://doi.org/10.1016/j.memsci.2018.03.070
132. Onorato C., Gaedtke M., Kespe M., Nirschl H., Schäfer A. I. (2019). Renewable energy powered membrane technology: Computational fluid dynamics evaluation of system performance with variable module size and fluctuating energy. *Separation and Purification Technology*. Vol. 220, pp. 206-216. doi: https://doi.org/10.1016/j.seppur.2019.02.041
133. Qi B., Wang Y., Wang Z., Zhang Y., Xu Sh., Wang Sh. (2013). Theoretical Investigation on Internal Leakage and Its Effect on the Efficiency of Fluid Switcher-Energy Recovery Device for Reverse Osmosis Desalting Plant. *Chinese Journal of Chemical Engineering*. Vol. 21, Is. 11, pp. 1216-1223. doi: https://doi.org/10.1016/S1004-9541(13)60625-4
134. Foo K., Liang Y.Y., Fimbres Weihs G.A. (2020). CFD study of the effect of SWM feed spacer geometry on mass transfer enhancement driven by forced transient slip velocity. *Journal of Membrane Science*. Vol. 597, 117643. doi: https://doi.org/10.1016/j.memsci.2019.117643
135. Gruber M. F., Aslak U., Hélix-Nielsen C. (2016). Open-source CFD model for optimization of forward osmosis and reverse osmosis membrane modules. *Separation and Purification Technology*. Vol. 158, pp. 183-192. doi: http://dx.doi.org/10.1016/j.seppur.2015.12.017
136. Ahmed S., Taif Seraji M., Jahedi J., Hashi M.A. (2012). Application of CFD for simulation of a baffled tubular membrane. *Chemical Engineering Research and Design*. Vol. 90, Is. 5, pp. 600-608. doi: http://dx.doi.org/doi:10.1016/j.cherd.2011.08.024
137. Haddadi B., Jordan C., Miltner M., Harasek M. (2018). Membrane modeling using CFD: Combined evaluation of mass transfer and geometrical influences in 1D and 3D. *Journal of Membrane Science*. Vol. 563, pp. 199-209. doi: https://doi.org/10.1016/j.memsci.2018.05.040
138. Kaya R., Deveci G., Turken T., Sengur R., Guclu S., Koseoglu-Imer D.Y., Koyuncu I. (2014). Analysis of wall shear stress on the outside-in type hollow fiber membrane modules by CFD simulation. *Desalination*. Vol. 351, pp. 109-119. doi: http://dx.doi.org/10.1016/j.desal.2014.07.033
139. Wu S.-E., Lin Y.-Ch., Hwang K.-J., Cheng T.-W., Tung K.-L. (2018). High-efficiency hollow fiber arrangement design to enhance filtration performance by CFD simulation. *Chemical Engineering and Processing - Process Intensification*. Vol. 125, pp. 87-96. doi: https://doi.org/10.1016/j.cep.2018.01.003
140. Li W., Su X., Palazzolo A., Ahmed Sh., Thomas E. (2017). Reverse osmosis membrane, seawater desalination with vibration assisted reduced inorganic fouling. *Desalination*. Vol. 417, pp. 102-114. doi: http://dx.doi.org/10.1016/j.desal.2017.05.016
141. Kavianipour O., Ingram G. D., Vuthaluru H. B. (2019). Studies into the mass transfer and energy consumption of commercial feed spacers for RO membrane modules using CFD: Effectiveness of performance measures. *Chemical Engineering Research and Design*. Vol. 141, pp. 328-338. doi: https://doi.org/10.1016/j.cherd.2018.10.041

142. Naskar M., Rana K., Chatterjee D., Dhara T., Sultana R., Sarkar D. (2019). Design, performance characterization and hydrodynamic modeling of intermeshed spinning basket membrane (ISBM) module. *Chemical Engineering Science*. Vol. 206, pp. 446-462. doi: https://doi.org/10.1016/j.ces.2019.05.049
143. Ahmed I., Hussain A., Hasani S.M.F., Shakaib M., Yunus R. M. (2012). Computational modeling for visualization of flow patterns in a membrane testing device. *Separation and Purification Technology*. Vol. 90, pp. 1-9. doi: https://doi.org/doi:10.1016/j.seppur.2012.02.004
144. Chaumeil F., Crapper M. (2013). DEM simulations of initial deposition of colloidal particles around non-woven membrane spacers. *Journal of Membrane Science*. Vol. 442, pp. 254-263. doi: http://dx.doi.org/10.1016/j.memsci.2013.04.031
145. Saeed A., Vuthaluru R., Yang Y., Vuthaluru H. B. (2012). Effect of feed spacer arrangement on flow dynamics through spacer filled membranes. *Desalination*. Vol. 285, pp. 163-169. doi: https://doi.org/10.1016/j.desal.2011.09.050
146. Fimbres Weihs G.A., Wiley D.E. (2014). CFD analysis of tracer response technique under cake-enhanced osmotic pressure. *Journal of Membrane Science*. Vol. 449, pp. 38-49. doi: http://dx.doi.org/10.1016/j.memsci.2013.08.015
147. Srivathsan G., Sparrow E. M., Gorman J. M. (2014). Reverse osmosis issues relating to pressure drop, mass transfer, turbulence, and unsteadiness. *Desalination*. Vol. 341, pp. 83-86. doi: https://doi.org/10.1016/j.desal.2014.02.021
148. Wypysek D., Rall D., Wiese M., Neef T., Koops G.-H., Wessling M. (2019). Shell and lumen side flow and pressure communication during permeation and filtration in a multibore polymer membrane module. *Journal of Membrane Science*. Vol. 584, pp. 254-267. doi: https://doi.org/10.1016/j.memsci.2019.04.070
149. Taherinejad M., Moghimi M., Derakhshan Sh. (2019). Hydrodynamic modeling of the spiral-wound membrane module including the membrane curvature: reverse osmosis case study. *Korean Journal of Chemical Engineering*. Vol. 36, pp. 2074–2084. doi: https://doi.org/10.1007/s11814-019-0372-1
150. Ligaray M., Kim N.-H., Park S., Park J.-S., Park J. Kim Y., Cho K. H. (2020). Energy projection of the seawater battery desalination system using the reverse osmosis system analysis model. *Chemical Engineering Journal*. Vol. 395, pp. 125082. doi: https://doi.org/10.1016/j.cej.2020.125082
151. Taherinejad M., Derakhshan Sh., Yavarinasab A. (2017). Hydrodynamic analysis of spiral wound reverse osmosis membrane recovery fraction and permeate water flow rate. *Desalination*. Vol. 411, pp. 59-68. doi: http://dx.doi.org/10.1016/j.desal.2017.02.009
152. Nejati S., Mirbagheri S. A., Warsinger D. M., Fazeli M. (2019). Biofouling in seawater reverse osmosis (SWRO): Impact of module geometry and mitigation with ultrafiltration. *Journal of Water Process Engineering*. Vol. 29, 100782. doi: https://doi.org/10.1016/j.jwpe.2019.100782
153. Johannink M., Masilamani K., Mhamdi A., Roller S., Marquardt W. (2015). Predictive pressure drop models for membrane channels with non-woven and woven spacers. *Desalination*. Vol. 376, pp. 41-54. doi: http://dx.doi.org/10.1016/j.desal.2015.07.024
154. Palomar P., Lara J.L., Losada I.J., Rodrigo M., Alvárez A. (2012). Near field brine discharge modelling part 1: Analysis of commercial tools. *Desalination*. Vol. 290, pp. 14-27. doi: https://doi.org/10.1016/j.desal.2011.11.037
155. Haidaria A.H., Heijman S.G.J., van der Meer W.G.J. (2018). Optimal design of spacers in reverse osmosis. *Separation and Purification Technology*. Vol. 192, pp. 441-456. doi: https://doi.org/10.1016/j.seppur.2017.10.042
156. Karabelas A.J., Koutsou C.P., Kostoglou M. (2014). The effect of spiral wound membrane element design characteristics on its performance in steady state desalination — A parametric study. *Desalination*. Vol. 332, Is. 1, 2 pp. 76-90. doi: http://dx.doi.org/10.1016/j.desal.2013.10.027
157. Koutsou C.P., Karabelas A.J., Kostoglou M. (2014). Membrane desalination under constant water recovery – The effect of module design parameters on system performance. *Separation and Purification Technology*. Vol. 147, pp. 90-113. doi: http://dx.doi.org/10.1016/j.seppur.2015.04.012
158. Barello M., Manca D., Patel R., Mujtaba I.M. (2014). Neural network based correlation for estimating water permeability constant in RO desalination process under fouling. *Desalination*. Vol. 345, pp. 101-111. doi: http://dx.doi.org/10.1016/j.desal.2014.04.016
159. Farahbakhsh J., Delnavaz M., Vatanpour V. (2019). Simulation and characterization of novel reverse osmosis membrane prepared by blending polypyrrole coated multiwalled carbon nanotubes for brackish water desalination and antifouling properties using artificial neural networks. *Journal of Membrane Science*. Vol. 581, pp. 123-138. doi: https://doi.org/10.1016/j.memsci.2019.03.050
160. Salami E. S., Ehetshami M., Karimi-Jashni A., Salari M., Nikbakht Sheibani S., Ehteshami A. (2016). A mathematical method and artificial neural network modeling to simulate osmosis membrane's performance. *Modeling Earth Systems and Environment*. Vol. 2, pp. 1–11. doi: https://doi.org/10.1007/s40808-016-0261-0
161. Mohammad A. Th., Al-Obaidi, M. A., Hameed E. M., Basheer B. N., Mujtab I. M. (2020). Modelling the chlorophenol removal from wastewater via reverse osmosis process using a multilayer artificial neural network with genetic algorithm. *Journal of Water Process Engineering*. Vol. 33, 100993. doi: https://doi.org/10.1016/j.jwpe.2019.100993
162. Aish A. M., Zaqoot H. A., Abdeljawad S. M. (2015). Artificial neural network approach for predicting reverse osmosis desalination plants performance in the Gaza Strip. *Desalination*. Vol. 367, pp. 240-247. doi: http://dx.doi.org/10.1016/j.desal.2015.04.008
163. Jbari Y., Abderaf S. (2020). Parametric study to enhance performance of wastewater treatment process, by reverse osmosis-photovoltaic system. *Applied Water Science*. Vol. 10, 217. doi: https://doi.org/10.1007/s13201-020-01301-4

164. Gu J., Luo J., Lif M., Huang C., Heng Y. (2020). Modeling of pressure drop in reverse osmosis feed channels using multilayer artificial neural networks. *Chemical Engineering Research and Design*. Vol. 159, pp. 146-156. doi: https://doi.org/10.1016/j.cherd.2020.04.019
165. Rall D., Schweidtmann A. M., Kruse M., Evdochenko E., Mitsos A., Wessling M. (2020). Multi-scale membrane process optimization with high-fidelity ion transport models through machine learning. *Journal of Membrane Science*. Vol. 608, 118208. doi: https://doi.org/10.1016/j.memsci.2020.118208
166. Khayet M., Cojocaru C., Essalhi M. (2011). Artificial neural network modeling and response surface methodology of desalination by reverse osmosis. *Journal of Membrane Science*. Vol. 368, Is. 1–2, pp. 202-214. doi: https://doi.org/10.1016/j.memsci.2010.11.030
167. Park S., Baek S.-S., Pyo J. C. Pachepsky Y., Park J., Cho K. H. (2019). Deep neural networks for modeling fouling growth and flux decline during NF/RO membrane filtration. *Journal of Membrane Science*. Vol. 587, 117164. doi: https://doi.org/10.1016/j.memsci.2019.06.004
168. Roehl E. A., Ladner D. A., Daamen R. C., Cook J. B., Safarik J., Phipps D. W., Xie P. (2018). Modeling fouling in a large RO system with artificial neural networks. *Journal of Membrane Science*. Vol. 552, pp. 95-106. doi: https://doi.org/10.1016/j.memsci.2018.01.064
169. Cabrera P., Carta J. A., González J., Melián G. (2018). Wind-driven SWRO desalination prototype with and without batteries: A performance simulation using machine learning models. *Desalination*. Vol. 435, pp. 77-96. doi: https://doi.org/10.1016/j.desal.2017.11.044
170. Sargolzaei J., Haghighi Asl M., Hedayati Moghaddam A. (2012). Membrane permeate flux and rejection factor prediction using intelligent systems. *Desalination*. Vol. 284, pp. 92-99. doi: https://doi.org/10.1016/j.desal.2011.08.041
171. Azamat, J., Khataee, A. Joo, S.W. (2014) Separation of a heavy metal from water through a membrane containing boron nitride nanotubes: molecular dynamics simulations. *Journal of Molecular Modeling*. Vol. 20, 2468. doi: https://doi.org/10.1007/s00894-014-2468-1
172. Talati S., Mohebbi A., Dorrani H. (2019). Investigation of the Capability of Carbon Nanotube Membranes in Separating the Heavy Metal Ions from Aqueous Solutions by Molecular Dynamics Simulation. *Journal of Engineering Thermophysics* Vol. 28, pp. 123–137. doi: https://doi.org/10.1134/S1810232819010107
173. Hinkle K. R., Wang X., Gu X., Jameson C. J., Murad S. (2018). Computational Molecular Modeling of Transport Processes in Nanoporous Membranes. *Processes*. Vol. 6. Is. 8. 124. doi: https://doi.org/10.3390/pr6080124
174. Boateng L. K., Madarshahian R., Yoon Y. Caicedo J. M., Flora J. R. V. (2016). A probabilistic approach for estimating water permeability in pressure-driven membranes. *Journal of Molecular Modeling*. Vol. 22, 185. doi: https://doi.org/10.1007/s00894-016-3049-2
175. Gao W., She F., Zhang J., Dumée L. F., He L., Hodgson P. D., Kong L. (2015). Understanding water and ion transport behaviour and permeability through poly(amide) thin film composite membrane. *Journal of Membrane Science*. Vol. 487, pp. 32-39. doi: https://doi.org/10.1016/j.memsci.2015.03.052
176. Li J., Kong X., Lu D., Liu Zh. (2015). Italicized carbon nanotube facilitating water transport: a molecular dynamics simulation. *Science Bulletin*. Vol. 60, Is.18, pp. 1580-1586. doi: https://doi.org/10.1007/s11434-015-0888-7
177. Shen J.-W., Li J., Liu F., Zhang L., Liang L., Wang H., Wu J.-Y. (2020). A molecular dynamics study on water desalination using single-layer MoSe2 nanopore. *Journal of Membrane Science*. Vol. 595, 117611. doi: https://doi.org/10.1016/j.memsci.2019.117611
178. Zheng B., Tian Y., Jia Sh., Zhao X., Li H. (2020). Molecular dynamics study on applying layered graphene oxide membranes for separating cadmium ions from water. *Journal of Membrane Science*. Vol. 603, 117996. doi: https://doi.org/10.1016/j.memsci.2020.117996
179. Shen M., Keten S., Lueptow R. M. (2016). Rejection mechanisms for contaminants in polyamide reverse osmosis membranes. *Journal of Membrane Science*. Vol. 509, pp. 36-47. doi: https://doi.org/10.1016/j.memsci.2016.02.043
180. Shen M., Keten S., Lueptow R. M. (2016). Dynamics of water and solute transport in polymeric reverse osmosis membranes via molecular dynamics simulations. *Journal of Membrane Science*. Vol. 506, pp. 95-108. doi: https://doi.org/10.1016/j.memsci.2016.01.051
181. Kiat Ng C., Domilongo Bope C., Nalaparaju A., Cheng Y., Lu L., Wang R., Cao B. (2016). Concentrating synthetic estrogen 17α-ethinyl estradiol using microporous polyethersulfone hollow fiber membranes: Experimental exploration and molecular simulation. *Chemical Engineering Journal*. Vol. 314, pp. 80-87. doi: https://doi.org/10.1016/j.cej.2016.12.109
182. Li T., Tu Q., Li Sh. (2019). Molecular dynamics modeling of nano-porous centrifuge for reverse osmosis desalination. *Desalination*. Vol. 451, pp. 182-191. doi: https://doi.org/10.1016/j.desal.2017.09.015
183. Zhao Z., Jiang J. (2020). POC/PIM-1 mixed-matrix membranes for water desalination: A molecular simulation study. *Journal of Membrane Science*. Vol. 608, 118173. doi: https://doi.org/10.1016/j.memsci.2020.118173
184. Luo Y., Harder E., Faibish R. S., Roux B. (2011). Computer simulations of water flux and salt permeability of the reverse osmosis FT-30 aromatic polyamide membrane. *Journal of Membrane Science*. Vol. 384, Is. 1–2, pp. 1-9. doi: https://doi.org/10.1016/j.memsci.2011.08.057
185. Lyu Q., Kang D.-Y., Hu S., Lin L.-Ch. (2020). Exploiting interior surface functionalization in reverse osmosis desalination membranes to mitigate permeability–selectivity trade-off: Molecular simulations of nanotube-based membranes. *Desalination*. Vol. 491, 114537. doi: https://doi.org/10.1016/j.desal.2020.114537

186. Chen Q., Yang X. (2015). Pyridinic nitrogen doped nanoporous graphene as desalination membrane: Molecular simulation study. *Journal of Membrane Science*. Vol. 496, pp. 108-117. doi: https://doi.org/10.1016/j.memsci.2015.08.052
187. Surblys D., Yamada T., Thomsen B., Kawakami T., Shigemoto I., Okabe J., Ogawa T., Kimura M., Sugita Y., Yagi K. (2020). Amide A band is a fingerprint for water dynamics in reverse osmosis polyamide membranes. *Journal of Membrane Science*. Vol. 596, 117705. doi: https://doi.org/10.1016/j.memsci.2019.117705
188. Ji W.M., Zhang L.W. (2019). Molecular dynamics simulations of water desalination through polymerized fullerite membrane. *Journal of Membrane Science*. Vol. 576, pp. 108-115. doi: https://doi.org/10.1016/j.memsci.2019.01.028
189. Yao Y., Li M., Cao X., Zhang P., Zhang W., Zheng J., Zhang X., Wang L. (2018). A novel sulfonated reverse osmosis membrane for seawater desalination: Experimental and molecular dynamics studies. *Journal of Membrane Science*. Vol. 550, pp. 470-479. doi: https://doi.org/10.1016/j.memsci.2018.01.023
190. Tomohisa Y., Kotaka K., Nakagawa K., Shintani T., Wu H.-Ch., Matsuyama H., Fujimura Y., Kawakatsu T. (2018). Molecular dynamics simulation study of polyamide membrane structures and RO/FO water permeation properties. *Membranes*. Vol. 8, Is. 4, 127. doi: https://doi.org/10.3390/membranes8040127
191. Rizzuto C., Pugliese G., Bahattab M. A., Aljlil S. A., Drioli E., Tocci E. (2018). Multiwalled carbon nanotube membranes for water purification. *Separation and Purification Technology*. Vol. 193, pp. 378-385. doi: https://doi.org/10.1016/j.seppur.2017.10.025
192. Ding M., Szymczyk A., Goujon F., Soldera A., Ghouf A. (2014). Structure and dynamics of water confined in a polyamide reverse-osmosis membrane: A molecular-simulation study. *Journal of Membrane Science*. Vol. 458, pp. 236-244. doi: http://dx.doi.org/10.1016/j.memsci.2014.01.054
193. Ding M., Ghoufi A., Anthony S. (2014). Molecular simulations of polyamide reverse osmosis membranes. *Desalination*. Vol. 343, pp. 48-53. doi: https://doi.org/10.1016/j.desal.2013.09.024
194. Ding M., Szymczyk A., Ghouf A. (2015). On the structure and rejection of ions by a polyamide membrane in pressure-driven molecular dynamics simulations. *Desalination*. Vol. 368, pp. 76-80. doi: http://dx.doi.org/10.1016/j.desal.2015.01.003
195. Ding M., Szymczyk A., Ghouf A. (2016). Hydration of a polyamide reverse-osmosis membrane. *Journal of Membrane Science*. Vol. 501, pp. 248-253. doi: http://dx.doi.org/10.1016/j.memsci.2015.12.036
196. Azamat J., Baghbani N. B., Erfan-Niya H. (2020). Atomistic understanding of functionalized γ-graphyne-1 nanosheet membranes for water desalination. *Journal of Membrane Science*. Vol. 604, 118079. doi: https://doi.org/10.1016/j.memsci.2020.118079
197. Yang H., Baek J., Park H. G. (2020). Architecture and mass transport properties of graphene-based membranes. *JMST Advances*. Vol. 2, pp. 77–88. doi: https://doi.org/10.1007/s42791-020-00032-6
198. Zhu Y., Zhou J., Lu X., Guo X., Lu L. (2013). Molecular simulations on nanoconfined water molecule behaviors for nanoporous material applications. *Microfluidics and Nanofluidics*. Vol. 15, pp. 191–205. doi: https://doi.org/10.1007/s10404-013-1143-7
199. Müller E. A. (2013). Purification of water through nanoporous carbon membranes: a molecular simulation viewpoint. *Current Opinion in Chemical Engineering*. Vol. 2, Is. 2, pp. 223-228. doi: http://dx.doi.org/10.1016/j.coche.2013.02.004
200. Nguyen Ch. Th., Beskok A. (2020). Water desalination performance of h-BN and optimized charged graphene membranes. *Microfluidics and Nanofluidics*. Vol. 24, 39. doi: https://doi.org/10.1007/s10404-020-02340-8
201. Song Y., Wei M., Xu F., Wang Y. (2020). Molecular simulations of water transport resistance in polyamide RO membranes: interfacial and interior contributions. *Engineering*. Vol. 6, Is. 5, pp. 577-584. doi: https://doi.org/10.1016/j.eng.2020.03.008
202. Karavas Ch.-S., Arvanitis K. G., Papadakis G. (2019). Optimal technical and economic configuration of photovoltaic powered reverse osmosis desalination systems operating in autonomous mode. *Desalination*. Vol. 466, pp. 97-106. doi: https://doi.org/10.1016/j.desal.2019.05.007
203. Atia A. A., Fthenakis V. (2019). Active-salinity-control reverse osmosis desalination as a flexible load resource. *Desalination*. Vol. 468, 114062. doi: https://doi.org/10.1016/j.desal.2019.07.002
204. Al-Obaidi M.A., Kara-Zaïtri C., Mujtaba I.M. (2019). Economic removal of chlorophenol from wastewater using multi-stage spiral-wound reverse osmosis process: Simulation and optimisation. *Journal of Water Process Engineering*. Vol. 31, 100829. doi: https://doi.org/10.1016/j.jwpe.2019.100829
205. Abejón A., Garea A., Irabien A. (2015). Arsenic removal from drinking water by reverse osmosis: Minimization of costs and energy consumption. *Separation and Purification Technology*. Vol. 144, pp. 46-53. doi: https://doi.org/10.1016/j.seppur.2015.02.017
206. Alnouri S., Linke P. (2013). Optimal SWRO network synthesis and design assessment with water quality insights. *Chemical Engineering Transactions*. Vol. 35, pp. 1225-1230. doi: https://doi.org/10.3303/CET1335204
207. Alnouri S. Y., Linke P. (2013). Optimal SWRO desalination network synthesis using multiple water quality parameters. *Journal of Membrane Science*. Vol. 444, pp. 493-512. doi: https://doi.org/10.1016/j.memsci.2013.04.066
208. Alnouri S. Y., Linke P. (2014). Optimal seawater reverse osmosis network design considering product water boron specifications. *Desalination*. Vol. 345, pp. 112-127. doi: https://doi.org/10.1016/j.desal.2014.04.030
209. Jiang A., Wang J., Biegler L. T., Cheng W., Xing Ch., Jiang Zh. (2015). Operational cost optimization of a full-scale SWRO system under multi-parameter variable conditions. *Desalination*. Vol. 355, pp. 124-140. doi: https://doi.org/10.1016/j.desal.2014.10.016
210. Xu D., Acker T., Zhang X. (2019). Size optimization of a hybrid PV/wind/diesel/battery power system for reverse osmosis desalination. *Journal of Water Reuse and Desalination*. Vol. 9, Is. 4, pp. 405–422. doi: https://doi.org/10.2166/wrd.2019.019

211. Khor Ch. S., Chachuat B., Shah N. (2012). A superstructure optimization approach for water network synthesis with membrane separation-based regenerators. *Computers & Chemical Engineering*. Vol. 42, pp. 48-63. doi: https://doi.org/10.1016/j.compchemeng.2012.02.020
212. Maalouf S., Rosso D., Yeh W. W.-G. (2014). Optimal planning and design of seawater RO brine outfalls under environmental uncertainty. *Desalination*. Vol. 333, Is. 1, pp. 134-145. doi: https://doi.org/10.1016/j.desal.2013.11.015
213. Maleki A. (2018). Design and optimization of autonomous solar-wind-reverse osmosis desalination systems coupling battery and hydrogen energy storage by an improved bee algorithm. *Desalination*. Vol. 435, pp. 221-234. doi: https://doi.org/10.1016/j.desal.2017.05.034
214. Malik S. N., Bahri P. A., Vu L. T.T. (2016). Steady state optimization of design and operation of desalination systems using Aspen Custom Modeler. *Computers & Chemical Engineering*. Vol. 91, pp. 247-256. doi: https://doi.org/10.1016/j.compchemeng.2016.04.024
215. Toth A. J. (2020). Modelling and optimisation of multi-stage flash distillation and reverse osmosis for desalination of saline process wastewater sources. *Membranes*. Vol. 10, Is. 10, 265. doi: https://doi.org/10.3390/membranes10100265
216. Peng W., Maleki A., Rosend M. A., Azarikhah P. (2018). Optimization of a hybrid system for solar-wind-based water desalination by reverse osmosis: Comparison of approaches. *Desalination*. Vol. 442, pp. 16-31. doi: https://doi.org/10.1016/j.desal.2018.03.021
217. Prathapaneni D. R., Detroja K. (2020). Optimal design of energy sources and reverse osmosis desalination plant with demand side management for cost-effective freshwater production. *Desalination*. Vol. 496, 114741. doi: https://doi.org/10.1016/j.desal.2020.114741
218. Sassi K. M., Mujtaba I. M. (2013). MINLP based superstructure optimization for boron removal during desalination by reverse osmosis. *Journal of Membrane Science*. Vol. 440, pp. 29-39. doi: https://doi.org/10.1016/j.memsci.2013.03.012
219. Senthil S., Senthilmurugan S. (2016). Reverse Osmosis–Pressure Retarded Osmosis hybrid system: Modelling, simulation and optimization. *Desalination*. Vol. 389, pp. 78-97. doi: https://doi.org/10.1016/j.desal.2016.01.027
220. Zebbar M., Messlem Y., Gouichiche A., Tadjine M. (2019). Super-twisting sliding mode control and robust loop shaping design of RO desalination process powered by PV generator. *Desalination*. Vol. 458, pp. 122-135. doi: https://doi.org/10.1016/j.desal.2019.02.011
221. Ruiz-García A., Nuez I., Carrascosa-Chisvert M.D., Santana J.J. (2020). Simulations of BWRO systems under different feedwater characteristics. Analysis of operation windows and optimal operating points. *Desalination*. Vol. 491, 114582. doi: https://doi.org/10.1016/j.desal.2020.114582
222. Jiang A., Wang J., Cheng W., Xing Ch., Jiangzhou Sh. (2014). A Dynamic Optimization Strategy for the Operation of Large Scale Seawater Reverses Osmosis System. *Mathematical Problems in Engineering*. Volume 2014, ID 635434. doi: https://doi.org/10.1155/2014/635434
223. Bdour M., Dalala Z., Al-Addous M., Kharabsheh A., Khzouz H. (2020). Mapping RO-Water Desalination System Powered by Standalone PV System for the Optimum Pressure and Energy Saving. *Applied Sciences*. Vol. 10, Is. 6, 2161. doi: https://doi.org/10.3390/app10062161
224. Bitaw T. N., Park K., Yang D. R. (2016). Optimization on a new hybrid Forward osmosis-Electrodialysis-Reverse osmosis seawater desalination process. *Desalination*. Vol. 398, pp. 265-281. doi: https://doi.org/10.1016/j.desal.2016.07.032
225. Dimitriou E., Boutikos P., Mohamed E. Sh., Koziel S., Papadakis G. (2017). Theoretical performance prediction of a reverse osmosis desalination membrane element under variable operating conditions. *Desalination*. Vol. 419, pp. 70-78. doi: https://doi.org/10.1016/j.desal.2017.06.001
226. Kim J., Hong S. (2018). Optimizing seawater reverse osmosis with internally staged design to improve product water quality and energy efficiency. Journal of Membrane Science. Vol. 568, pp. 76-86. doi: https://doi.org/10.1016/j.memsci.2018.09.046
227. Li M. (2012). Optimal plant operation of brackish water reverse osmosis (BWRO) desalination. *Desalination*. Vol. 293, pp. 61-68. doi: https://doi.org/10.1016/j.desal.2012.02.024
228. Weaver N. J., Wilkin G. S., Morison K. R., Watson M. J. (2020). Minimizing the energy requirements for the production of maple syrup. *Journal of Food Engineering*. Vol. 273, 109823. doi: https://doi.org/10.1016/j.jfoodeng.2019.109823
229. Almansoori A., Saif Y. (2014). Structural optimization of osmosis processes for water and power production in desalination applications. *Desalination*. Vol. 344, pp. 12-27. doi: https://doi.org/10.1016/j.desal.2014.03.002
230. Al-Aboosi F. Y., El-Halwagi M. M. (2019). A Stochastic Optimization Approach to the Design of Shale Gas/Oil Wastewater Treatment Systems with Multiple Energy Sources under Uncertainty. *Sustainability*. Vol. 11, Is. 18, 4865. doi: https://doi.org/10.3390/su11184865
231. Blankert B., Kim Y., Vrouwenvelder H., Ghaffour N. (2020). Facultative hybrid RO-PRO concept to improve economic performance of PRO: Feasibility and maximizing efficiency. *Desalination*. Vol. 478, 114268. doi: https://doi.org/10.1016/j.desal.2019.114268
232. Nematzadeh, M., Samimi, A., Shokrollahzadeh, S., Mohebbi-Kalhori, D. (2019). Bentazon removal from aqueous solution by reverse osmosis; optimization of effective parameters using response surface methodology. *Advances in Environmental Technology*. Vol. 5, Is. 4, pp. 193-201. doi: https://doi.org/10.22104/aet.2020.4228.1209
233. Al-Obaidi M.A., Kara-Zaïtri C., Mujtaba I.M. (2018). Simulation and optimisation of a two-stage/two-pass reverse osmosis system for improved removal of chlorophenol from wastewater. *Journal of Water Process Engineering*. Vol. 22, pp. 131-137. doi: https://doi.org/10.1016/j.jwpe.2018.01.012

234. Emamjome A., Zahedi M. M., Ziyaadini M. (2019). Economic analysis for process optimization of Chabahar Maritime University reverse osmosis desalination plant: a case study. *Applied Water Science*. Vol. 9, 114. doi: https://doi.org/10.1007/s13201-019-0995-8
235. Mirghaderi F., Rahmanian N., Patel R., Manca D., Mujtaba I. M. (2017). Simulation and Optimization of a Continuous Reverse Osmosis Desalination Process for Making Fresh Water. *Chemical Engineering Transactions*. Vol. 61, pp. 1783-1788. doi: https://doi.org/10.3303/CET1761295
236. Emad A., Ajbar A., Almutaz I. (2012). Periodic control of a reverse osmosis desalination process. *Journal of Process Control*. Vol. 22, Is. 1, pp. 218-227. doi: https://doi.org/10.1016/j.jprocont.2011.09.001
237. Kelley L. C., Dubowsky S. (2013). Thermal control to maximize photovoltaic powered reverse osmosis desalination systems productivity. *Desalination*. Vol. 314, pp. 10-19. doi: https://doi.org/10.1016/j.desal.2012.11.036
238. Volpin F., Fons E., Chekli L., Kim J. E., Jang A., Shon H. K. (2018). Hybrid forward osmosis-reverse osmosis for wastewater reuse and seawater desalination: Understanding the optimal feed solution to minimise fouling. *Process Safety and Environmental Protection*. Vol. 117, pp. 523-532. doi: https://doi.org/10.1016/j.psep.2018.05.006
239. Peters Ch. D., Hankins N. P. (2019). Osmotically assisted reverse osmosis (OARO): Five approaches to dewatering saline brines using pressure-driven membrane processes. *Desalination*. Vol. 458, pp. 1-13. doi: https://doi.org/10.1016/j.desal.2019.01.025
240. Antipova E., Pozo C., Guillén-Gosálbez G., Boer D., Cabeza L.F., Jiménez L. (2015). On the use of filters to facilitate the post-optimal analysis of the Pareto solutions in multi-objective optimization. *Computers & Chemical Engineering*. Vol. 74, pp. 48-58. doi: https://doi.org/10.1016/j.compchemeng.2014.12.012
241. Khoshgoftar Manesh M.H., Ghalami H., Amidpour M., Hamedi M.H. (2013). Optimal coupling of site utility steam network with MED-RO desalination through total site analysis and exergoeconomic optimization. *Desalination*. Vol. 316, pp. 42-52. doi: https://doi.org/10.1016/j.desal.2013.01.022
242. Sadri S., Khoshkhoo R.H., Ameri M. (2016). Multi objective optimization of reverse osmosis desalination plant with exergy approach. *Journal of Mechanical Science and Technology*. Vol. 30, pp. 4807–4814. doi: https://doi.org/10.1007/s12206-016-0953-4
243. Al-Obaidi M. A., Kara-Zaïtri C., Mujtaba I. M. (2018). Statistical-Based Modeling and Optimization of Chlorophenol Removal from Wastewater Using Reverse Osmosis Process. *Chemical Engineering Transactions*. Vol. 70, pp. 2023-2028. doi: https://doi.org/10.3303/CET1870338
244. Stillwell A. S., Webber M. E. (2016). Predicting the Specific Energy Consumption of Reverse Osmosis Desalination. *Water*. Vol. 8, Is. 12, 601. doi: https://doi.org/10.3390/w8120601
245. Manenti F., Nadezhdin I. S., Goryunov A. G., Kozin K. A., Baydali S. A., Papasidero D., Rossi F., Potemin R. V. (2015). Operational Optimization of Reverse Osmosis Plant Using MPC. *Chemical Engineering Transactions*. Vol. 45. pp. 247-252. doi: https://doi.org/10.3303/CET1545042
246. Gong M., Jiang A., Zhang Q., Wang H., Hu J., Lin Y. (2017). An Improved Finite Element Meshing Strategy for Dynamic Optimization Problems. *Mathematical Problems in Engineering*. Vol. 2017, 4829195. doi: https://doi.org/10.1155/2017/4829195
247. Patnana N., Pattnaik S., Varshney T., Singh V. P. (2020). Self-Learning Salp Swarm Optimization Based PID Design of Doha RO Plant. *Algorithms*. Vol. 13, Is. 11, 287. doi: https://doi.org/10.3390/a13110287
248. Li D., Yang N., Niu R., Qiu H., Xi Y. (2012). FPGA based QDMC control for reverse-osmosis water desalination system. *Desalination*. Vol. 285, pp. 83-90. doi: https://doi.org/10.1016/j.desal.2011.09.037
249. Sobana S., Panda R. C. (2014). Modeling and control of reverse osmosis desalination process using centralized and decentralized techniques. *Desalination*. Vol. 344, pp, 243-251. doi: https://doi.org/10.1016/j.desal.2014.03.014
250. Ehteram M., Salih S.Q., Yaseen, Z.M. (2020). Efficiency evaluation of reverse osmosis desalination plant using hybridized multilayer perceptron with particle swarm optimization. *Environmental Science and Pollution Research*. Vol. 27, pp. 15278–15291. doi: https://doi.org/10.1007/s11356-020-08023-9
251. Jeong K., Park M., Ki S. J., Kim J. H. (2017). A systematic optimization of Internally Staged Design (ISD) for a full-scale reverse osmosis process. *Journal of Membrane Science*. Vol. 540, pp. 285-296. doi: https://doi.org/10.1016/j.memsci.2017.06.066
252. Jeong K., Park M., Chong T. H. (2019). Numerical model-based analysis of energy-efficient reverse osmosis (EERO) process: Performance simulation and optimization. *Desalination*. Vol. 453, pp. 10-21. doi: https://doi.org/10.1016/j.desal.2018.11.021
253. Fellah B., Benyoucef B., Chermiti A., Belarbi M., Amara S. (2018). Optimal sizing of a hybrid photovoltaic/wind system supplying a desalination unit. *Journal of Engineering Science and Technology*. Vol. 13, No. 6, pp. 1816-1833
254. Ghobeity A., Mitsos A. (2014). Optimal design and operation of desalination systems: new challenges and recent advances. *Current Opinion in Chemical Engineering*. Vol. 6, pp. 61-68. doi: https://doi.org/10.1016/j.coche.2014.09.008
255. Sano Y., Mahidul I. (2018) Optimum operating condition of a hollow fiber reverse osmosis desalination system. *Cogent Engineering*. Vol. 5, Is. 1, 1463898. doi: https://doi.org/10.1080/23311916.2018.1463898
256. Davies P.A. (2011). A solar-powered reverse osmosis system for high recovery of freshwater from saline groundwater. *Desalination*. Vol. 271, Is. 1–3, pp. 72-79. doi: https://doi.org/10.1016/j.desal.2010.12.010
257. Jabari F., Mohammadi-ivatloo B., Mohammadpourfard M. (2019). Robust optimal self-scheduling of potable water and power producers under uncertain electricity prices. *Applied Thermal Engineering*. Vol. 162, 114258. doi: https://doi.org/10.1016/j.applthermaleng.2019.114258

258. Sannino D., Sacco O., Chianese A. (2013). Determination of Optimal Operating Condition in Nanofiltration (NF) and Reverse Osmosis (RO) During the Treatment of a Tannery Wastewater Stream. *Chemical Engineering Transactions*. Vol. 32, pp. 1993-1998. doi: https://doi.org/10.3303/CET1332333
259. Zhao P., Bai Y., Liu B., Chang H., Cao Y., Fang J. (2019). Process optimization for producing ultrapure water with high resistivity and low total organic carbon. *Process Safety and Environmental Protection*. Vol. 126, pp. 232-241. doi: https://doi.org/10.1016/j.psep.2019.04.017
260. Namany S., Al-Ansari T., Govindan R. (2019). Optimisation of the energy, water, and food nexus for food security scenarios. *Computers & Chemical Engineering*. Vol. 129, 106513. doi: https://doi.org/10.1016/j.compchemeng.2019.106513
261. Cao Zh., Deng J., Ye F., Garris Ch. A. (2017). Performance Analysis of Thermal Vapor Compression Integrated with Reverse Osmosis Desalination System. *Chemical Engineering Transactions*. Vol. 61, pp. 919-924. doi: https://doi.org/10.3303/CET1761151
262. Heidary B., Tavakoli Hashjin T., Ghobadian B., Roshande R. (2019). Performance analysis of hybrid solar-wind RO-MSF desalination system. *Resource-Efficient Technologies*. Vol. 2, pp. 1-16. doi: https://doi.org/10.18799/24056537/2019/2/184
263. Heidary B., Tavakoli Hashjin T., Ghobadian B., Roshandel R. (2019). Exergy of a hybrid solar-wind reverse osmosis-MSF desalination system. *Resource-Efficient Technologies*. Vol. 1, pp. 8-19. doi: https://doi.org/10.18799/24056537/2019/1/227
264. Lacroix C., Perier-Muzet M., Stitou D. (2019). Dynamic Modeling and Preliminary Performance Analysis of a New Solar Thermal Reverse Osmosis Desalination Process. *Energies*. Vol. 12, Is. 20, 4015. doi: https://doi.org/10.3390/en12204015
265. Haryati S., Hamzah A. B., Goh P. S., Abdullah M. S., Ismail A. F., Bustan M. D. (2017). Process intensification of seawater reverse osmosis through enhanced train capacity and module size – Simulation on Lanzarote IV SWRO plant. *Desalination*. Vol. 408, pp. 92-101. doi: https://doi.org/10.1016/j.desal.2017.01.011
266. Ling Ch., Wang Y., Min Ch., Zhang Y. (2018). Economic evaluation of reverse osmosis desalination system coupled with tidal energy. *Frontiers in Energy*. Vol. 12, pp. 297–304. doi: https://doi.org/10.1007/s11708-017-0478-2
267. García Latorre F. J., Pérez Báez S. O., Gómez Gotor A. (2015). Energy performance of a reverse osmosis desalination plant operating with variable pressure and flow. *Desalination*. Vol. 366, pp. 146-153. doi: https://doi.org/10.1016/j.desal.2015.02.039
268. Nayar K. G., Fernandes J., McGovern R. K., Dominguez K. P., McCance A., Al-Anzi B. S., Lienhard V J. H. (2019). Cost and energy requirements of hybrid RO and ED brine concentration systems for salt production. *Desalination*. Vol. 456, pp. 97-120. doi: https://doi.org/10.1016/j.desal.2018.11.018
269. Qin M., Deshmukh A., Epsztein R., Patel S. K., Owoseni O. M., Walker W. Sh., Elimelech M. (2019). Comparison of energy consumption in desalination by capacitive deionization and reverse osmosis. *Desalination*. Vol. 455, pp. 100-114. doi: https://doi.org/10.1016/j.desal.2019.01.003
270. . Nayar K. G., Fernandes J., McGovern R. K., Al-Anzi B. S., Lienhard V J. H. (2019). Cost and energy needs of RO-ED-crystallizer systems for zero brine discharge seawater desalination. *Desalination*. Vol. 457, pp. 115-132. doi: https://doi.org/10.1016/j.desal.2019.01.015
271. Koutsou C.P., Kritikos E., Karabelas A.J., Kostoglou M. (2020). Analysis of temperature effects on the specific energy consumption in reverse osmosis desalination processes. *Desalination*. Vol. 476, 114213. doi: https://doi.org/10.1016/j.desal.2019.114213
272. Delgado-Torres A. M., García-Rodríguez L., del Moral M. J. (2020). Preliminary assessment of innovative seawater reverse osmosis (SWRO) desalination powered by a hybrid solar photovoltaic (PV) - Tidal range energy system. *Desalination*. Vol. 477, 114247. doi: https://doi.org/10.1016/j.desal.2019.114247
273. . Arsović M. R., Topić R. M., Komatina M. S., Gojak M. (2015). Thermodynamical research of using solar energy for desalination of seawater. *Thermal Science*. Vol. 19, No. 5, pp. 1709-1721. doi: https://doi.org/10.2298/TSCI141220074A
274. Reimers A. S., Webber M. E. (2018). Systems-level thermodynamic and economic analysis of a seawater reverse osmosis desalination plant integrated with a combined cycle power plant. *Texas Water Journal*. Vol. 9, No 1, pp. 82-95. doi: https://doi.org/10.21423/twj.v9i1.7065
275. Akhatov J. S. (2016). Energy and Exergy Analysis of Solar PV Powered Reverse Osmosis Desalination. *Applied Solar Energy*. Vol. 52, pp. 265–270. doi: https://doi.org/10.3103/S0003701X16040034
276. Alanezi A. A., Altaee A., Sharif A. O. (2020). The effect of energy recovery device and feed flow rate on the energy efficiency of reverse osmosis process. *Chemical Engineering Research and Design*. Vol. 158, pp. 12-23. doi: https://doi.org/10.1016/j.cherd.2020.03.018
277. Bartholomew T. V., Mey L., Arena J. T., Siefert N. S., Mauter M. S. (2017). Osmotically assisted reverse osmosis for high salinity brine treatment. *Desalination*. Vol. 421, pp. 3-11. doi: https://doi.org/10.1016/j.desal.2017.04.012
278. Chae S. H., Seo J., Kim J., Kim Y. M., Kim J. H. (2018). A simulation study with a new performance index for pressure-retarded osmosis processes hybridized with seawater reverse osmosis and membrane distillation. *Desalination*. Vol. 444, pp. 118-128. doi: https://doi.org/10.1016/j.desal.2018.07.019
279. El-Sayed T. A., Abdel Fatah A. A. (2016). Performance of hydraulic turbocharger integrated with hydraulic energy management in SWRO desalination plants. *Desalination*. Vol. 379, pp. 85-92. doi: https://doi.org/10.1016/j.desal.2015.10.013
280. Jia X., Klemeš J. J., Varbanov P. S., Alwi Sh. R. W. (2019). Analyzing the Energy Consumption, GHG Emission, and Cost of Seawater Desalination in China. *Energies*. Vol. 12, Is. 3, 463. doi: https://doi.org/10.3390/en12030463
281. Castro M., Alcanzare M., Esparcia Jr. E., Oco J. (2020). A Comparative Techno-Economic Analysis of Different Desalination Technologies in Off-Grid Islands. *Energies*. Vol. 13, Is. 9., 2261. doi: https://doi.org/10.3390/en13092261

282. Karabelas A.J., Koutsou C.P., Kostoglou M., Sioutopoulos D.C. (2018). Analysis of specific energy consumption in reverse osmosis desalination processes. *Desalination*. Vol. 431, pp. 15-21. doi: https://doi.org/10.1016/j.desal.2017.04.006
283. Mazlan N. M., Peshev D., Livingston A. G. (2016). Energy consumption for desalination — A comparison of forward osmosis with reverse osmosis, and the potential for perfect membranes. *Desalination*. Vol. 377, pp. 138-151. doi: https://doi.org/10.1016/j.desal.2015.08.011
284. Minhas M.B., Jande Y.A.C., Kim W.S. (2014). Combined reverse osmosis and constant-current operated capacitive deionization system for seawater desalination. *Desalination*. Vol. 344, pp. 299-305. doi: https://doi.org/10.1016/j.desal.2014.03.043
285. Segal H., Birnhack L., Nir O., Lahav O. (2018). Intensification and energy minimization of seawater reverse osmosis desalination through high-pH operation: Temperature dependency and second pass implications. *Chemical Engineering and Processing - Process Intensification*. Vol. 131, pp. 84-91. doi: https://doi.org/10.1016/j.cep.2018.07.009
286. Lourenço A. B., Carvalho M. (2020). Exergoeconomic and exergoenvironmental analyses of an off-grid reverse osmosis system with internal combustion engine and waste heat recovery. *Chemical Engineering Journal Advances*. Vol. 4, 100056. doi: https://doi.org/10.1016/j.ceja.2020.100056
287. Muhammad A. J., Qureshi B. A., Zubair S. M. (2017). Exergo-economic analysis of a seawater reverse osmosis desalination plant with various retrofit options. *Desalination*. Vol. 401, pp. 88-98. doi: https://doi.org/10.1016/j.desal.2016.09.032
288. Eshoul N. M., Agnew B., Al-Weshahi M. A., Atab M. S. (2015). Exergy Analysis of a Two-Pass Reverse Osmosis (RO) Desalination Unit with and without an Energy Recovery Turbine (ERT) and Pressure Exchanger (PX). *Energies*. Vol. 8, Is. 7, pp. 6910-6925. doi: https://doi.org/10.3390/en8076910
289. Islam Sh., Dincer I., Yilbas B. S. (2018). Development of a novel solar-based integrated system for desalination with heat recovery. *Applied Thermal Engineering*. Vol. 129, pp. 1618-1633. doi: https://doi.org/10.1016/j.applthermaleng.2017.09.02 8
290. Mokhtari H., Sepahvand M., Fasihfar A. (2016). Thermoeconomic and exergy analysis in using hybrid systems (GT + MED + RO) for desalination of brackish water in Persian Gulf. *Desalination*. Vol. 399, pp. 1-15. doi: https://doi.org/10.1016/j.desal.2016.07.044
291. Sadri S., Ameri M., Khoshkhoo R. H. (2017). Multi-objective optimization of MED-TVC-RO hybrid desalination system based on the irreversibility concept. *Desalination*. Vol. 402, pp. 97-108. doi: https://doi.org/10.1016/j.desal.2016.09.029
292. Li Q., Moya W., Esfahani I. J., Rashidi J., Yoo Ch. K. (2017). Integration of reverse osmosis desalination with hybrid renewable energy sources and battery storage using electricity supply and demand-driven power pinch analysis. *Process Safety and Environmental Protection*. Vol. 111, pp. 795-809. doi: https://doi.org/10.1016/j.psep.2017.09.009
293. Palenzuela P., Zaragoza G., Alarcón D., Blanco J. (2011). Simulation and evaluation of the coupling of desalination units to parabolic-trough solar power plants in the Mediterranean region. *Desalination*. Vol. 281, pp. 379-387. doi: https://doi.org/10.1016/j.desal.2011.08.014
294. Shrivastava A., Rosenberg S., Peery M. (2015). Energy efficiency breakdown of reverse osmosis and its implications on future innovation roadmap for desalination. *Desalination*. Vol. 368, pp. 181-192. doi: https://doi.org/10.1016/j.desal.2015.01.005
295. Mansour T. M., Ismail T. M., Ramzy Kh., El-Salam M. A. (2020). Energy recovery system in small reverse osmosis desalination plant: Experimental and theoretical investigations. *Alexandria Engineering Journal*. Vol. 59, Is. 5, pp. 3741-3753. doi: https://doi.org/10.1016/j.aej.2020.06.030
296. Mansouri M. T., Amidpour M., Ponce-Ortega J. M. (2019). Optimal integration of organic Rankine cycle and desalination systems with industrial processes: Energy-water-environment nexus. *Applied Thermal Engineering*. Vol. 158, 113740. doi: https://doi.org/10.1016/j.applthermaleng.2019.113740
297. Kaya A., Evren Tok M., Koc M. (2019). A Levelized Cost Analysis for Solar-Energy-Powered Sea Water Desalination in The Emirate of Abu Dhabi. *Sustainability*. Vol. 11, Is 6, 1691. doi: https://doi.org/10.3390/su11061691
298. Aydiner C., Sen U., Topcu S., Ekinci D., Altinay A. D., Koseoglu-Imer D. Y., Keskinler B. (2014). Techno-economic viability of innovative membrane systems in water and mass recovery from dairy wastewater. *Journal of Membrane Science*. Vol. 458, pp. 66-75. doi: https://doi.org/10.1016/j.memsci.2014.01.058
299. He W., Wang Y., Sharif A., Shaheed M. H. (2014). Thermodynamic analysis of a stand-alone reverse osmosis desalination system powered by pressure retarded osmosis. *Desalination*. Vol. 352, pp. 27-37. doi: https://doi.org/10.1016/j.desal.2014.08.006
300. Kim J. E., Phuntsho Sh., Chekli L., Choi J. Y., Shon H. K. (2018). Environmental and economic assessment of hybrid FO-RO/NF system with selected inorganic draw solutes for the treatment of mine impaired water. *Desalination*. Vol. 429, pp. 96-104. doi: https://doi.org/10.1016/j.desal.2017.12.016
301. Gökçek M. (2018). Integration of hybrid power (wind-photovoltaic-diesel-battery) and seawater reverse osmosis systems for small-scale desalination applications. *Desalination*. Vol. 435, pp. 210-220. doi: https://doi.org/10.1016/j.desal.2017.07.006
302. Caldera U., Bogdanov D., Breyer Ch. (2016). Local cost of seawater RO desalination based on solar PV and wind energy: A global estimate. *Desalination*. Vol. 385, pp. 207-216. doi: https://doi.org/10.1016/j.desal.2016.02.004
303. Clarke D. P., Al-Abdeli Y. M., Kothapalli G. (2013). The effects of including intricacies in the modelling of a small-scale solar-PV reverse osmosis desalination system. *Desalination*. Vol. 311, pp.127-136. doi: https://doi.org/10.1016/j.desal.2012.11.006
304. Ma Q., Lu H. (2011). Wind energy technologies integrated with desalination systems: Review and state-of-the-art. *Desalination*. Vol. 277, Is. 1–3, pp. 274-280. doi: https://doi.org/10.1016/j.desal.2011.04.041
305. Hirsimaki C., Outram J. G., Millar G. J., Altaee A. (2020). Process simulation of high pH reverse osmosis systems to facilitate reuse of coal seam gas associated water. *Journal of Environmental Chemical Engineering*. Vol. 8, Is. 5, 104122. doi: https://doi.org/10.1016/j.jece.2020.104122

306. Gökçek M., Gökçek Ö. B. (2016). Technical and economic evaluation of freshwater production from a wind-powered small-scale seawater reverse osmosis system (WP-SWRO). *Desalination*. Vol. 381, pp. 47-57. doi: https://doi.org/10.1016/j.desal.2015.12.004
307. Al-Obaidi M.A., Filippini G., Manenti F., Mujtaba I.M. (2019). Cost evaluation and optimisation of hybrid multi effect distillation and reverse osmosis system for seawater desalination. *Desalination*. Vol. 456, pp. 136-149. doi: https://doi.org/10.1016/j.desal.2019.01.019
308. Filippini G., Al-Obaidi M.A., Manenti F., Mujtaba I.M. (2019). Design and economic evaluation of solar-powered hybrid multi effect and reverse osmosis system for seawater desalination. *Desalination*. Vol. 465, pp.114-125. doi: https://doi.org/10.1016/j.desal.2019.04.016
309. Im S. J., Jeong S., Jeong S., Jang A. (2020). Techno-economic evaluation of an element-scale forward osmosis-reverse osmosis hybrid process for seawater desalination. *Desalination*. Vol. 476, 114240. doi: https://doi.org/10.1016/j.desal.2019.114240
310. Tobin T., Gustafson R., Bura R., Gough H. L. (2020). Integration of wastewater treatment into process design of lignocellulosic biorefineries for improved economic viability. *Biotechnology for Biofuels*. Vol. 13, 24. doi: https://doi.org/10.1186/s13068-020-1657-7
311. Blandin G., Verliefde A. R.D., Tang Ch. Y., Le-Clech P. (2015). Opportunities to reach economic sustainability in forward osmosis–reverse osmosis hybrids for seawater desalination. *Desalination*. Vol. 363, pp. 26-36. doi: https://doi.org/10.1016/j.desal.2014.12.011
312. Castel Ch., Favre E. (2018). Membrane separations and energy efficiency. *Journal of Membrane Science*. Vol. 548, pp. 345-357. doi: https://doi.org/10.1016/j.memsci.2017.11.035
313. Kook S., Lee Ch., Nguyen Th. T., Lee J., Shon H. K., Kim I. S. (2018). Serially connected forward osmosis membrane elements of pressure-assisted forward osmosis-reverse osmosis hybrid system: Process performance and economic analysis. *Desalination*. Vol. 448, pp. 1-12. doi: https://doi.org/10.1016/j.desal.2018.09.019
314. Loutatidou S., Arafat H. A. (2015). Techno-economic analysis of MED and RO desalination powered by low-enthalpy geothermal energy. *Desalination*. Vol. 365, pp. 277-292. doi: https://doi.org/10.1016/j.desal.2015.03.010
315. Valizadeh B., Ashtiani F. Z., Fouladitajar A., Dabir B., Baraghani S. S. M.ϭ Armand S. B., Salari B., Kouchakiniya N. (2015). Scale-up economic assessment and experimental analysis of MF–RO integrated membrane systems in oily wastewater treatment plants for reuse application. *Desalination*. Vol. 374, pp. 31-37. doi: https://doi.org/10.1016/j.desal.2015.07.017
316. Bick A., Gillerman L., Manor Y., Oron G. (2012). Economic Assessment of an Integrated Membrane System for Secondary Effluent Polishing for Unrestricted Reuse. *Water*. Vol. 4, Is. 1, pp. 219-236. doi: https://doi.org/10.3390/w4010219
317. Edalat A., Hoek E. M. V. (2020). Techno-Economic Analysis of RO Desalination of Produced Water for Beneficial Reuse in California. *Water*. Vol. 12, Is. 7, 1850. doi: https://doi.org/10.3390/w12071850
318. Toh K.Y., Liang Y.Y., Lau W.J., Fimbres Weihs G.A. (2020). The techno-economic case for coupling advanced spacers to high-permeance RO membranes for desalination. *Desalination*. Vol. 491, 114534. doi: https://doi.org/10.1016/j.desal.2020.114534
319. La Cerva M., Gurreri L., Cipollina A., Tamburini A., Ciofalo M., Micale G. (2019). Modelling and cost analysis of hybrid systems for seawater desalination: Electromembrane pre-treatments for Reverse Osmosis. *Desalination*. Vol. 467, pp. 175-195. doi: https://doi.org/10.1016/j.desal.2019.06.010
320. Ghafoor A., Ahmed T., Munir A., Arslan Ch., Ahmad S.A. (2020). Techno-economic feasibility of solar based desalination through reverse osmosis. *Desalination*. Vol. 485, 114464. doi: https://doi.org/10.1016/j.desal.2020.114464
321. Castro M. T., Esparcia Jr. E. A., Odulio C. M. F., Ocon J. D. (2019). Technoeconomics of Reverse Osmosis as Demand-Side Management for Philippine Off-Grid Islands. *Chemical Engineering Transactions*. Vol. 76, pp. 1129-1134. doi: https://doi.org/10.3303/CET1976189
322. Widiasa I.N., Yoshi L.A. (2016). Techno-Economy Analysis A Small Scale Reverse Osmosis System for Brackish Water Desalination. *International Journal of Science and Engineering*. Vol. 10, Is. 2, pp. 51-57. doi: https://doi.org/10.12777/ijse.10.2.51-57
323. Hoveidi H., Vahidi H., CheraghAli S. M. T., Aslemanda A. (2017). Economic Evaluation of RO and MEH *Desalination Units in Iranian South-Eastern Villages*. Vol. 1, Is. 1., pp. 99-112. doi: https://doi.org/10.22097/EEER.2017.46460
324. Laissaoui M., Palenzuela P., Sharaf Eldean M. A., Nehari D., Alarcón-Padilla D.-C. (2018). Techno-economic analysis of a stand-alone solar desalination plant at variable load conditions. *Applied Thermal Engineering*. Vol. 133, pp. 659-670. doi: https://doi.org/10.1016/j.applthermaleng.2018.01.074
325. Abejon R., Abejon A., Puthai W., Ibrahim S.B., Nagasawa H., Tsuru T., Garea A. (2017). Preliminary techno-economic analysis of non-commercial ceramic and organosilica membranes for hydrogen peroxide ultrapurification. *Chemical Engineering Research and Design*. Vol. 125, pp. 385-397. doi: https://doi.org/10.1016/j.cherd.2017.07.018
326. Kumar Sh., Groth A., Vlacic L. (2014). An analytical index for evaluating manufacturing cost and performance of low-pressure hollow fibre membrane systems. *Desalination*. Vol. 332, Is. 1, pp. 44-51. doi: https://doi.org/10.1016/j.desal.2013.10.013
327. Ochando-Pulido J. M., Hodaifa G., Victor-Ortega M. D., Martinez-Ferez A. (2013). Performance Modeling and Cost Analysis of a Pilot-Scale Reverse Osmosis Process for the Final Purification of Olive Mill Wastewater. *Membranes*. Vol. 3, Is. 4, pp. 285-297. doi: https://doi.org/10.3390/membranes3040285
328. Abraham T., Luthra A. (2011). Socio-economic & technical assessment of photovoltaic powered membrane desalination processes for India. *Desalination*. Vol. 268, Is. 1–3, pp. 238-248. doi: https://doi.org/10.1016/j.desal.2010.10.035

329. Idrees M. F. (2020). Performance Analysis and Treatment Technologies of Reverse Osmosis Plant – A case study. *Case Studies in Chemical and Environmental Engineering*. Vol. 2, 100007. doi: https://doi.org/10.1016/j.cscee.2020.100007
330. Al-Obaidi M.A., Jarullah A.T., Kara-Zaïtri C., Mujtaba I.M. (2018). Simulation of hybrid trickle bed reactor–reverse osmosis process for the removal of phenol from wastewater. *Computers & Chemical Engineering*. Vol. 113, pp. 264-273. doi: https://doi.org/10.1016/j.compchemeng.2018.03.016
331. Al-Obaidi M.A., Kara-Zaïtri C., Mujtaba I.M. (2019). Evaluation of chlorophenol removal from wastewater using multi-stage spiral-wound reverse osmosis process via simulation. *Computers & Chemical Engineering*. Vol. 130, 106522. doi: https://doi.org/10.1016/j.compchemeng.2019.106522
332. Alsarayreh A. A., Al-Obaidi M.A., Al-Hroub A.M., Patel R., Mujtaba I.M. (2020). Performance evaluation of reverse osmosis brackish water desalination plant with different recycled ratios of retentate. *Computers & Chemical Engineering*. Vol. 135, 106729. doi: https://doi.org/10.1016/j.compchemeng.2020.106729
333. Riverol C., Pilipovik M.V. (2011). Prediction of the behaviour of the Silt Density Index (SDI) in the Caribbean Seawater and its impact on RO desalination plants. Desalination. Vol. 268, Is. 1–3, pp. 262-265. doi: https://doi.org/10.1016/j.desal.2010.09.049
334. Venkatesan A. K., Ahmad S., Johnson W., Batista J. R. (2011). Salinity reduction and energy conservation in direct and indirect potable water reuse. *Desalination*. Vol. 272, Is. 1–3, pp. 120-127. doi: *https://doi.org/10.1016/j.desal.2011.01.007*
335. Zhou J., Chang V. W.-C., Fane A. G. (2011). Environmental life cycle assessment of reverse osmosis desalination: The influence of different life cycle impact assessment methods on the characterization results. *Desalination*. Vol. 283, pp. 227-236. doi: https://doi.org/10.1016/j.desal.2011.04.066
336. Pascual X., Gu H., Bartman A. R., Zhu A., Rahardianto A., Giralt J., Rallo R., Christofides P. D., Cohen Y. (2013). Data-driven models of steady state and transient operations of spiral-wound RO plant. *Desalination*. Vol. 316, pp. 154-161. doi: https://doi.org/10.1016/j.desal.2013.02.006
337. Qian Z., Miedema H., de Smet L.C.P.M., Sudholter E.J.R. (2018). Modelling the selective removal of sodium ions from greenhouse irrigation water using membrane technology. *Chemical Engineering Research and Design*. Vol. 134, pp. 154-161, doi: https://doi.org/10.1016/j.cherd.2018.03.040
338. Phuc B. D. H., You S.-S., Lim T.-W., Kim H.-S. (2017). Dynamical analysis and control synthesis of RO desalination process against water hammering. *Desalination*. Vol. 402, pp. 133-142. doi: https://doi.org/10.1016/j.desal.2016.09.023
339. Cao Zh., Deng J., Ye F., Garris Jr. Ch. A. (2018). Analysis of a hybrid Thermal Vapor Compression and Reverse Osmosis desalination system at variable design conditions. *Desalination*. Vol. 438, pp. 54-62, doi: https://doi.org/10.1016/j.desal.2018.03.019
340. Lu Y., Liao A., Hu Y. (2013) Design of reverse osmosis networks for multiple freshwater production. *Korean Journal of Chemical Engineering*. Vol, 30, pp. 988–996. doi: https://doi.org/10.1007/s11814-013-0009-8
341. Qian Zh, Liu X., Yu Zh., Zhang H., Jü Y. (2012). A Pilot-scale Demonstration of Reverse Osmosis Unit for Treatment of Coal-bed Methane Co-produced Water and Its Modeling. *Chinese Journal of Chemical Engineering*. Vol. 20, Is. 2, pp. 302-311. doi: https://doi.org/10.1016/S1004-9541(12)60392-9
342. Salo, A. (2017). Simulation of water purification machine for vending cyber physical systems. *Technology Audit and Production Reserves*, Vol. 2, No. (2(40), pp. 16–21. doi: https://doi.org/10.15587/2312-8372.2018.128543
343. Lucay F., Cisternas L.A., Gálvez E.D. (2015). Global sensitivity analysis for identifying critical process design decisions. *Chemical Engineering Research and Design*. Vol. 103, pp. 74-83. doi: https://doi.org/10.1016/j.cherd.2015.06.015
344. Singh S., Henderson R. K., Baker A., Stuetz R. M., Khan S. J. (2012). Characterisation of reverse osmosis permeates from municipal recycled water systems using fluorescence spectroscopy: Implications for integrity monitoring. *Journal of Membrane Science*. Vol. 421–422, pp. 180-189. doi: https://doi.org/10.1016/j.memsci.2012.07.008
345. Kim Y. Ch., Min T. (2020). Influence of osmotic mediation on permeation of water in reverse osmosis: Experimental and numerical analysis. *Journal of Membrane Science*. Vol. 595, 117574. doi: https://doi.org/10.1016/j.memsci.2019.117574
346. Huang Q., Ma W. (2012). A model of estimating scaling potential in reverse osmosis and nanofiltration systems. *Desalination*. Vol. 288, pp. 40-46. doi: https://doi.org/10.1016/j.desal.2011.12.007
347. Kim D.Y., Gu B., Yang D.R. (2013). An explicit solution of the mathematical model for osmotic desalination process. *Korean Journal of Chemical Engineering*. Vol. 30, pp. 1691–1699. doi: https://doi.org/10.1007/s11814-013-0123-7
348. Raim V., Srebnik S. (2018). Simulation of osmotic pressure across an amorphous semipermeable membrane. *Journal of Membrane Science*. Vol. 563, pp. 183-190. doi: https://doi.org/10.1016/j.memsci.2018.05.058
349. Ochando-Pulido J. M., Martínez-Férez A., Stoller M. (2019). Analysis of the Flux Performance of Different RO/NF Membranes in the Treatment of Agroindustrial Wastewater by Means of the Boundary Flux Theory. *Membranes*. Vol. 9, Is. 1, 2. doi: https://doi.org/10.3390/membranes9010002
350. Rivas-Perez R., Sotomayor-Moriano J., Pérez-Zuñiga G., Soto-Angles M. E. (2019). Real-Time Implementation of an Expert Model Predictive Controller in a Pilot-Scale Reverse Osmosis Plant for Brackish and Seawater Desalination. *Applied Sciences*. Vol. 9, Is. 14, 2932. doi: https://doi.org/10.3390/app9142932
351. Manheim D. C., Jiang S. C. (2017). Investigation of Algal Biotoxin Removal during SWRO Desalination through a Materials *Flow Analysis. Water*. Vol. 9, Is. 10, 730. doi: https://doi.org/10.3390/w9100730
352. Zafra-Cabeza A., Ridao M. A., Camacho E. F. (2011). A mixed integer quadratic programming formulation of risk management for reverse osmosis plants. *Desalination*. Vol. 268, Is. 1–3, pp. 46-54. doi: https://doi.org/10.1016/j.desal.2010.09.048

353. Bourouni K. (2013). Availability assessment of a reverse osmosis plant: Comparison between Reliability Block Diagram and Fault Tree Analysis Methods. *Desalination*. Vol. 313, pp. 66-76. doi: https://doi.org/10.1016/j.desal.2012.11.025
354. Ramon G. Z., Hoek E. M.V. (2013). Transport through composite membranes, part 2: Impacts of roughness on permeability and fouling. *Journal of Membrane Science*. Vol. 425–426, pp. 141-148. doi: https://doi.org/10.1016/j.memsci.2012.08.004
355. Waly T., Kennedy M. D., Witkamp G.-J., Amy G., Schippers J. C. (2011). Predicting and measurement of pH of seawater reverse osmosis concentrates. *Desalination*. Vol. 280, Is. 1–3, pp.27-32. doi: https://doi.org/10.1016/j.desal.2011.06.057
356. Alhseinat E., Sheikholeslami R. (2012). A completely theoretical approach for assessing fouling propensity along a full-scale reverse osmosis process. *Desalination*. Vol. 301, pp. 1-9. doi: https://doi.org/10.1016/j.desal.2011.12.014
357. Lee B.-S. (2015). Nuclide separation modeling through reverse osmosis membranes in radioactive liquid waste. *Nuclear Engineering and Technology*. Vol. 47, Is. 7, pp. 859-866. doi: https://doi.org/10.1016/j.net.2015.08.001
358. Kezia K., Lee J., Ogieglo W., Hill A., Benes N. E., Kentish S. E. (2014). The transport of hydronium and hydroxide ions through reverse osmosis membranes. *Journal of Membrane Science*. Vol. 459, pp. 197-206. doi: https://doi.org/10.1016/j.memsci.2014.02.018
359. Karakhim S. O., Zhuk P. F., Kosterin S. O. (2020). Kinetics simulation of transmembrane transport of ions and molecules through a semipermeable membrane. *Journal of Bioenergetics and Biomembranes*. Vol. 52, pp. 47–60. doi: https://doi.org/10.1007/s10863-019-09821-8
360. Peñate B., García-Rodríguez L. (2012). Seawater reverse osmosis desalination driven by a solar Organic Rankine Cycle: Design and technology assessment for medium capacity range. *Desalination*. Vol. 284, pp. 86-91. doi: https://doi.org/10.1016/j.desal.2011.08.040
361. Aghababaei N. (2017). Reverse osmosis design with IMS design software to produce drinking water in Bandar Abbas, Iran. *Journal of Applied Research in Water and Wastewater*. Vol. 7, Is. 1, pp. 314-318. doi: https://doi.org/10.22126/ARWW.2017.776
362. Park K., Burlace L., Dhakal N., Mudgal A., Stewartd N. A., Davies P. A. (2020). Design, modelling and optimisation of a batch reverse osmosis (RO) desalination system using a free piston for brackish water treatment. *Desalination*. Vol. 494, 114625. doi: https://doi.org/10.1016/j.desal.2020.114625
363. Al-hotmani O. M. A., Al-Obaidi M. A. A., John Y. M., Patel R., Mujtaba I. M. (2020). An Innovative Design of an Integrated MED-TVC and Reverse Osmosis System for Seawater Desalination: Process Explanation and Performance Evaluation. *Processes*. Vol. 8, Is. 5, 607. doi: https://doi.org/10.3390/pr8050607
364. Srivastava S., Vaddadi S., Kumar P., Sadistap Sh. (2018). Design and development of reverse osmosis (RO) plant status monitoring system for early fault prediction and predictive maintenance. *Applied Water Science*. Vol. 8, 159. doi: https://doi.org/10.1007/s13201-018-0821-8
365. Husnil Y. A., Harvianto G. R., Andika R., Chaniago Y. D., Lee M. (2017). Conceptual designs of integrated process for simultaneous production of potable water, electricity, and salt. *Desalination*. Vol. 409, pp. 96-107. doi: https://doi.org/10.1016/j.desal.2017.01.024

JOURNAL OF ENGINEERING SCIENCES

Volume 9, Issue 1 (2022)

Serdiuk V., Sklabinskyi V., Bolshanina S., Ochowiak M., Radchenko A., Babenko O., Kharchenko Y. (2022). Regeneration of chromate galvanic solutions in membrane electrochemical devices. Journal of Engineering Sciences, Vol. 9(2), pp. F37-F42, doi: 10.21272/jes.2022.9(2).f3

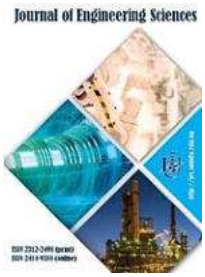

Regeneration of Chromate Galvanic Solutions in Membrane Electrochemical Devices

Serdiuk V.[1,2*[0000-0001-9388-5861]], Sklabinskyi V.[1[0000-0001-9388-5861]], Bolshanina S.[1[0000-0002-9482-8620]], Ochowiak M.[3[0000-0003-1543-9967]], Radchenko A.[1], Babenko O.[2[0000-0002-1416-2700]], Kharchenko Y.[2[0000-0002-8960-2440]]

[1] Sumy State University, 2, Rymskogo-Korsakova St., 40007 Sumy, Ukraine;
[2] Sumy State Pedagogical University named after A. S. Makarenko, 87, Romenska St., 40002 Sumy, Ukraine;
[3] Poznan University of Technology, 5, M. Skłodowskiej-Curie Sq., 60-965 Poznan, Poland

Article info:
Submitted: October 27, 2022
Accepted for publication: December 4, 2022
Available online: December 7, 2022

***Corresponding email:**
mikishasumy@gmail.com

Abstract. The regeneration processes of industry technological passivating baths of electrochemical cadmium lines and electrochemical galvanizing lines as an applied result of two-chamber membrane cation-exchange electrochemical devices researched. Actual industrial passivation baths of cadmium and zinc galvanic coatings applied as anode chambers. The cathode chamber contained sulfuric acid 1 % solution and a titanium cathode (BT-0). A window was cut in one of the walls with a RALEX®CM-PES 11-66 cation exchange membrane placed in it. The lead (C-0) was used as the anode. A comparative analysis of the performance of these technological baths before and after the using cation exchange membrane electrochemical devices was carried out. As a result of long-term experimental studies, the ecological and economic feasibility of their use was proven.

Keywords: electrolysis, environmental hazard, reagent, energy efficiency, pollutant tax.

1 Introduction

Passivation baths are used in the electrochemical cadmium coating processes and electrochemical galvanization at the galvanic production of JSC Sumy Plant Nasosenergomash. These baths are technologically necessary thanks to their protective aid conversion films created on the corresponding galvanic coatings [1, 2]. The conversion film is formed from cadmium and zinc chromates, respectively, and serves as additional protection for this type of coating against corrosion. The thickness of the conversion film is several tens of nanometers. The protective properties of the created conversion films are controlled by a lead (II) acetate solution following the requirements of the product control rules for nuclear power plants.

The passivating solutions, accordingly, to the galvanic works technological process of JSC "Nasosenergomash" (Sumy, Ukraine), are an aqueous solution containing: $Na_2Cr_2O_7$ – 150–200 g/l, H_2SO_4 – 10–12 g/l.

As a result of these baths operation, the sodium dichromate and sulfuric acid concentrations gradually decrease, and polluting ions Cr^{3+}, Cd^{2+}, and Zn^{2+} accumulate as a result of the corresponding reactions: of the corresponding reactions:

$$3Zn + 2CrO_4^{2-} + 16H^+ \rightarrow 3Zn^{2+} + 2Cr^{3+} + 8H_2O; \quad (1)$$

$$3Cd + 2CrO_4^{2-} + 16H^+ \rightarrow 3Cd^{2+} + 2Cr^{3+} + 8H_2O; \quad (2)$$

$$Zn + 2H^+ \rightarrow Zn^{2+} + H_2\uparrow; \quad (3)$$

$$Cd + 2H^+ \rightarrow Cd^{2+} + H_2\uparrow. \quad (4)$$

As a result of the passivation of parts with a considerable surface area in these technological baths, the concentration of the reagents decreases, and the impurity ions concentration increases to a critical level because the bath function is lost: the creation of a high-quality protective conversion film on the surface of the coating. To restore their properties, it is necessary to increase the $Na_2Cr_2O_7$ and H_2SO_4 concentration by adding a certain amount of them to the bath solution or dilute the bath solution if possible to reduce the contaminating metal ions critical concentrations or combine these methods of adjusting the contents of the bath.

When correcting the passivation baths by adding new portions of sodium dichromate and sulfuric acid, the baths restore their efficiency only for a short time. Adjustments occur with a certain periodicity. As a result of such adjustments to the bath content, the concentration of both reagents and reactions 1–4 products gradually increases.

Such actions are a consequence to an increase in the amount of reagent removal and reaction products in the washing water. It is common knowledge that the average removal of chromate solutions is 0.2-0.4l/m^2 of the total parts area [3]. Consequently, the amount of reagents and products increases significantly in the wastewater of galvanic production, as a consequence, the costs of reagents for neutralization as dichromate anions increase, as well as for the precipitation of heavy metal ions.

As a result of such work, chromating baths are an irrational use of resources: reactive substances and water. Due to the electrolysis laws, the ion-exchange membranes properties, and their application in world practice for electrodialysis, membrane filtration, and membrane electrolysis, a scheme of membrane electrolysis is introduced for cleaning and regeneration of passivation baths.

2 Research Methodology

To regenerate and rationally use resources and reduce the burden on wastewater treatment, an industrial electrochemical membrane device similar to a laboratory device, which is used to study the patterns of metals electrodeposition, was created [4, 5].

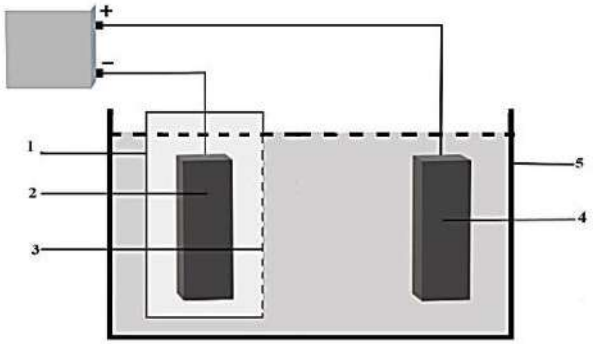

Figure 1 – The design scheme of an industrial membrane cation exchange electrochemical device: 1 – cathode chamber, 2 – cathode; 3 – cation exchange membrane with a filter cloth; 4 – anode; 5 – anode chamber – industrial passivation bath.

Unlike the laboratory membrane electrochemical device, the industrial sample differs in size. Since industrial passivation baths have a volume of approximately 150 l, the industrial electrochemical device must have significantly larger dimensions of the membrane, cathode, anode, and cathode chamber, but at the same time be compact - not take up a large volume in the working process bath. For the manufacture of an industrial electrochemical cell, considering account compactness, the dimensions of the membrane, anode, and cathode chamber were increased several times compared to the laboratory model. The cathode chamber case 1 (Fig. 1) was made of chemically resistant polypropylene of the PPH brand with a catholyte volume of 3.7l, a height of 400mm, a width of 190mm, and a thickness of 55mm. A window was cut in one of the chamber walls for fixing the RALEX®CM-PES 11-66 membrane with a height of 300mm and a width of 60mm, while the area of membrane 3 (Fig. 1) was 1.8 dm^2. A BT0 titanium plate with working dimensions of 350x20x1 mm was used as cathode 2 (Fig. 1) the cathode working area was 1.05 dm^2. As anode 4 (Fig. 1) lead C0 was used with working dimensions of 320x60x3mm, the working area of the anode was 2.88 dm^2. The ratio of the cathode area to the anode area was 1:2.74. The anode was located in the working chamber of the passivation bath 5 (Fig. 1) at a distance of 8-10mm from the membrane.The cathode chamber of the industrial membrane device contained a 1% solution of sulfuric acid as a catholyte. The electrolysis was conducted with the help of a direct current source VU12/6 at a voltage of 9 V and a current of 5 A. Thus, the cathodic current density was 4.76 A/dm^2. At the same time, the anode current density was 1.736 A/dm^2, and the membrane current density was 2.77 A/dm^2.

The passivation solutions are anodic chambers 5 (Fig. 1) and contain anodes made of lead (C0) on which the head electrochemical reaction is the water oxidation reaction with the oxygen release and acidification of the solution:

$$2H_2O - 4\bar{e} \rightarrow O_2\uparrow + 4H^+. \quad (5)$$

A feature of lead anodes is the ability to oxidize Cr^{3+} ions into CrO_4^{2-} ions [6-8]. Cr^{3+} ions are formed in passivation baths due to the interaction of cadmium or zinc coating in the formation processes of protective conversion films on them. Thus, these ions are always present in working technological baths and constantly accumulate and consequently of constant work pollute them (reactions 1, 2). But the Cr^{3+} oxidation reaction ions with accompanying acidification of the solution take place at the lead anode:

$$Cr^{3+} + 4H_2O - 3\bar{e} \rightarrow CrO_4^{2-} + 8H^+. \quad (6)$$

The rate of Cr^{3+} ions oxidation to CrO_4^{2-} ions at the anode depends on the concentration of Cr^{3+} ions in the solution, temperature, and current density at the anode [9]. Thus, to maintain the concentration at approximately 1 % in electrochemical chromium plating electrolytes, it is necessary to have a ratio between the cathode areas and anodes in the bath of 1:2 [8]. The lack of proportionality between the reaction rate and the anode current density indicates that the Cr^{3+} ion's oxidation to CrO_4^{2-} ions at the anode is not a purely electrochemical reaction [9, 10].

Therefore, consequently of the electro-membrane device operation, the hexavalent chromium compounds regeneration [11, 12] of the passivation solutions and the harmful impurities removal of heavy metal ions in the cathode chamber, which accumulate as a result of these technological baths operations, happens. Thus, with the constant electric current help, a cation exchange membrane that separates the cathode chamber from the main composition of the bath, regeneration of the head components of the capacity, and removal of polluting impurities takes place.

Research on the restoration of chromate concentrations in passivation solutions of cadmium and zinc galvanic coatings happened in the applying membrane electrolysis procedure with the industrial membrane electrochemical devices help. These studies were carried out in working

technological baths. To find out the content of Cr^{+6} ions and Cr^{3+} ions in the passivation baths, titrimetric and photocolorimetric methods of analysis were used. Detection of the content of Cr^{+6} ions and Cr^{3+} ions determined after certain intervals of operation in technological baths of electrochemical membrane devices, are shown in Table 1.

From the obtained results of analyzes of the chromium ions concentrations, it was established that the Cr^{+6} ions concentration in the passivation baths of galvanic coatings increases, and the Cr^{3+} ions concentration decreases due to the operation of membrane electrochemical devices. This change in the Cr^{+6} ions concentrations and Cr^{3+} ions is caused by reaction 6 occurring at the lead anode. During the operation of the baths, the total chromium concentration in them gradually decreases due to the deposition of the formed metal chromates on the parts in the form of conversion films and the electrolyte removal to the portions into the washing water.

Table 1 – Dynamics of changes in the Cr^{+6} ions and Cr^{3+} ions concentrations in the passivation baths of cadmium and zinc coatings during the operation of membrane electrochemical devices

Pollutant ion	Concentrations of ions, g/l			Tempera-ture, °C	Time, h	Growth of Cr^{+6} ions, g/l	The total increase of Cr^{+6} ions, g	The rate of Cr^{+6} ions regeneration	
	Cr^{+6}	Cr^{3+}	Gen. Cr					g/hour	mole/h
Cd^{2+}	44.01	39.25	83.26	18	0	–	–	–	–
	45.10	37.80	82.90	18	24	1.09	163.5	6.8125	0.1310
	46.53	35.19	81.72	18	24	1.43	214.5	8.9375	0.1718
	46.99	33.92	80.91	17	24	0.46	69.0	2.8750	0.0553
	47.59	32.64	80.23	18	24	0.60	90.0	3.7500	0.0721
	48.66	31.08	79.74	18	24	1.07	160.5	6.6875	0.1286
Zn^{2+}	59.14	28.27	87.41	18	0	–	–	–	–
	60.17	26.94	87.11	18	24	1.03	154.5	0.6042	0.0116
	61.07	25.18	86.25	17	24	0.90	135.0	5.6250	0.1082
	61.68	24.22	85.9	18	24	0.61	91.5	3.8125	0.0733
	62.83	22.34	85.17	18	24	1.15	172.5	7.1875	0.1382
	64.42	20.45	84.87	18	24	1.59	238.5	13.6875	0.2632

As shown in Table 1, the magnification of the Cr^{+6} ions concentration in the baths occurs unevenly. Such results are explained by uneven loading of the baths, resulting which reactions 1 and 2 happening at different speeds. The dynamics of changes in the Cr^{+6} ions concentrations and Cr^{3+} ions are the differences between the rates of reactions 1 and 2 and anodic reaction 6. Therefore, thanks to the constant formation of Cr^{+6} ions at the anode, the technological solution is constantly enriched with the main component - CrO_4^{2-} ions, which does not require the addition of sodium dichromate additional portions due to its regeneration. Thus, from the data in Table 1, it can be concluded that, on average, at an anodic current density of 1.736A/dm^2 on a lead anode with an area of 2.88 dm^2, thanks to a side reaction, about 6 g/h of hexavalent chromium ions are recovered in the chromating bath.

Therefore, during the operation of industrial electrochemical devices in the cadmium or zinc coating passivation bath, the bath solution is cleaned of polluting ions Cd^{2+} and Zn^{2+} and enriched with chromates.

3 Results and Discussion

As a result of the conducted experimental studies, the amounts of cathode-formed metals per unit of time were also found experimentally. The obtained results are shown in Table 2.

Thus, with the help of the operation of these membrane electrochemical devices, at a maximum current density of 2.77 A/dm^2, 0.74 g/h of cadmium and 0.27 g/h of zinc are formed on the cathodes.

Table 2 – Dynamics of the cathodic release of metal Cd and Zn in the membrane electrolysis process in passivation baths

No.	Electrolysis time, h	Cadmium release, g		Zinc release, g	
		$m_{general}$	m_{hour}	$m_{general}$	m_{hour}
1	7.5	5.5461	0.7395	2.0754	0.2767
2	16.5	12.3523	0.7486	4.4927	0.2723
3	8.0	5.9621	0.7453	2.2079	0.2760
4	16.0	11.6894	0.7306	4.4123	0.2758
5	8.0	5.8936	0.7367	2.1823	0.2728
6	16.0	11.2578	0.7036	4.3568	0.2723
7	7.0	5.4676	0.7811	1.9482	0.2783
8	17.0	12.2339	0.7196	4.4937	0.2643
9	8.5	6.2825	0.7391	2.3354	0.2748
10	15.5	11.4176	0.7366	4.2568	0.2746
11	8.0	5.9482	0.7435	2.2243	0.2780
12	16.0	11.5893	0.7243	4.3612	0.2726
13	7.5	5.5424	0.7390	2.0747	0.2766
14	16.5	11.9651	0.7252	4.3674	0.2647
15	8.0	5.8264	0.7284	2.1758	0.2720
16	15.5	11.3739	0.7338	4.2165	0.2720
17	7.0	5.2376	0.7482	1.9548	0.2793
18	16.5	12.0742	0.7318	4.5337	0.2748
19	8.5	6.2488	0.7351	2.3285	0.2739
20	15.5	11.5686	0.7464	4.2374	0.2734
Σ	–	175.4774	–	65.2358	–
μ	–	–	0.7373	–	0.2741

Therefore, during the operation day of these membrane electrochemical devices, Cd^{2+} and Zn^{2+} ions are extracted from the passivation baths into the cathode chamber and deposited on the cathode in the form of simple metal

substances masses that are about 17.70 g and 6.58 g, respectively.

Analyzing the data in Table 1, it is obviously that the chromate anions concentration increases during the operation day of the membrane device due to the anodic reaction 6 by 0.60–1.59 g/l. At the same time, the total mass of chromate anions recovered at the anodes ranges from 90.0 g to 238.5 g per day. And the content of total chromium gradually decreases by 0.30–1.18 g/l, which is 0.6 g/l on average. The changing dynamics of the increase in the chromates concentration and the unstable decrease in the concentration of total chromium were reasoned by the uneven removal of the electrolyte from the surface of the parts immersed for processing.

Before the industrial membrane electrochemical devices introduction in the passivation baths of cadmium and zinc galvanic coatings in the electroplating section of workshop No. 3 of JSC "Nasosenergomash" (Sumy, Ukraine), the baths lost their functions 1–2 times a month.

It was necessary to periodically restore the functionality of passivating baths by adjusting their composition - by adding reagents to 1/3. Thanks to such actions, 5 kg of sodium dichromate and 0.3 kg of sulfuric acid were added to the baths. If the addition of new portions of reagents did not restore the functions of the bath, then the contents of the baths were partially or fully poured into the neutralization station, and new solutions had prepared accordingly. The solutions replacement by ½ part or the total replacement took place 1–2 times a year.

After the industrial membrane electrochemical devices' commissioning, the passivation baths of galvanic coatings began to work stably and efficiently, and there was no deterioration of their functions. As a result of the constant anodic renewal of chromate anions(reaction 6), the need to frequently add new sodium dichromate and sulfuric acid portions disappeared. Thus, the need to add new reagents portions arose only after six months of these electrochemical devices operations due to a decrease in the hexavalent chromium ions concentration to 20-25g/l as a result of removal from the surface of the parts to the washing baths and the neutralization station. Thus, owing to the operation of industrial membrane electrochemical devices, the chromates load to the neutralization station was reduced by six times. Before these membrane electrochemical devices use, the need for sodium dichromate was at least 5kg/month for each passivation bath, and as a result of their working, it was 0.833 kg/month.

The technological solution ecological hazard (EH) is the ratio of the pollutant concentration in the solution (C0) to the maximum permissible concentration (MPC) [10]. Thus, before working industrial membrane electrochemical devices in cadmium and zinc passivation baths, the Cr^{+6} ions concentration fluctuated between 100-200 g/l, which averaged about 150 g/l. As a result of the operation of these electrochemical devices, the Cr^{+6} ions working concentration decreased to 30–50 g/l, which is also an average of about 40 g/l.

According to the order of the Ministry of Regional Development, Construction and Housing and Communal Services of Ukraine dated 01.12.2017 No. 316, Appendix 5 to the rules for accepting wastewater into centralized drainage systems MPC (Cr^{+6} ions) = 0.1 g/m^3, in accordance:

$$EH = C^0/MPC; \quad (7)$$
$$EH_{before} = (150g/l)/(0,1g/l) = 1500;$$
$$EH_{after} = (40g/l)/(0,1g/l) = 400.$$

In this way, the environmental hazard of technological passivation solutions of cadmium and zinc galvanic coatings decreased by an average of 3.75 times.

The difference in the use of sodium dichromate before the electrochemical membrane devices operation and when they are exploited in one bath is:

$\Delta m(Na_2Cr_2O_7)$ = 5kg/month - 0,833kg/month = 4,167kg/month;

This difference shows the effectiveness of the use of reagents for technological purposes and the costs for the neutralization of wastewater. Thus, in the electroplating section of workshop No. 3 of JSC "Nasosenergomash" (Sumy, Ukraine), a reagent wastewater treatment method of electroplating production is used. Neutralization takes place in two stages. In the first stage, sodium metabisulfite is the application, and in the second stage - sodium carbonate:

$$2Na_2Cr_2O_7 + 3Na_2S_2O_5 + 5H_2SO_4 \rightarrow$$
$$\rightarrow 2Cr_2(SO_4)_3 + 5Na_2SO_4 + 5H_2O; \quad (8)$$

$$Cr(SO_4)_3 + 3Na_2CO_3 + 3H_2O \rightarrow$$
$$\rightarrow 2Cr(OH)_3\downarrow + 2Na_2SO_4 + 3CO_2\uparrow. \quad (9)$$

After carrying out calculations according to reaction equation 8, it had defined that for the transformation of sodium dichromate weighing 4.167 kg into Cr^{3+} ions, it is necessary to spend theoretically sodium pyrosulfite $Na_2S_2O_5$ weighing 4.533 kg and sulfuric acid weighing 3.897 kg. To transform the received $Cr_2(SO_4)_3$ weighing 6.235 kg into insoluble chromium(III) hydroxide (reaction 9), it is necessary to spend theoretically 5.058 kg of soda ash.

According to data for January 2021, the prices (P), excluding VAT, for the listed substances were, in UAH/kg: $P(Na_2Cr_2O_7)$ = 120.00, $P(Na_2S_2O_5)$ = 24.75, $P(H_2SO_4)$ = 35.18, and $P(Na_2CO_3)$ = 11.67.

The total cost of reagents Creag., participating in the reactions, is found by the ratio:

$$C_{reag.} = (P(Na_2Cr_2O_7)\cdot m(Na_2Cr_2O_7) +$$
$$P(Na_2S_2O_5)\cdot m(Na_2S_2O_5) +$$
$$+ P(H_2SO_4)\cdot m(H_2SO_4) +$$
$$+ P(Na_2CO_3)\cdot m(Na_2CO_3))\cdot 1.2, \quad (10)$$

where 1.2 is the coefficient for taking into account 20 % VAT, then C_{reag} = 970 UAH.

As calculated above, as a result of using an industrial membrane electrochemical device in one technological passivation bath per month, the savings on unspent reagents working in this bath and their neutralization is theoretically 970 UAH.

During the operation of the membrane electrochemical device, electricity had consumed. The direct current source used for membrane electrolysis had powered by alternating current from a 220V power grid. The AC power used to power this DC source was measured with a DT-399B clamp-on multimeter. The alternating current power was 1.3 A, so the power consumption according to ratio 11 is equal to:

$$P_{cons.} = I \cdot U; \quad (11)$$
$$P_{cons.} = 1.3 \text{ A} \cdot 220 \text{ V} = 286 \text{ W/h}.$$

For a day of work and for 30 days, which is conventionally one month, this electrochemical device consumes, respectively, $P_{cons.day}$ = 6.864 kW and $P_{cons.month}$ = 205.92 kW/month.

As of January 2021, the total price of electricity 1 kW for JSC "Nasosenergomash" (Sumy, Uraine) amounted to Sel. = 2.54 UAH/kW. Thus, the electricity consumption S for the electro-membrane device operation per month was:

$$S = P_{cons.month.} \cdot Sel. = 523.04 \text{ UAH/month}. \quad (12)$$

The operation efficiency E of an industrial membrane electrochemical device is the difference between the reagents cost Creag. it was saved per month and the electricity cost S for the device operation:

$$E = C_{reag.} - S = 446.95 \text{ UAH/month}. \quad (13)$$

But the efficiency of this device is not fully calculated. For its calculation, the polluting substances tax for the discharge had not been considered. According to Article 249.5 of the Ukraine Tax Code: the tax amount paid for discharges of polluting substances into water bodies (Ps) is calculated by the payers independently every quarter based on the actual discharges volumes, tax rates, and adjustment factors according to the formula:

$$\Pi c = \sum(M_i \cdot H_i \cdot K), \quad (14)$$

where M_i is the volume of discharge of that pollutant per year, in tons (t); H_i – tax rates in the current year for a ton of the i-th type of polluting substance, in UAH; K – a multiplier equals to 1.5 and is used in the incident of pollutants discharge into ponds and lakes (in other cases, the coefficient is equal to 1).

Based on equation (14), we calculate the difference in the amount of the monthly tax by which the payments decrease as a result of the operation of a definite membrane electrochemical device $\Delta\Pi c$:

$$\Delta\Pi c(Cd) = \Delta M(Cr^{+6}) \cdot H(Cr^{+6}) \cdot K + \\ + \Delta M(Cd^{2+}) \cdot H(Cd^{2+}) \cdot K; \quad (15)$$

$$\Delta\Pi(Zn) = \Delta M(Cr^{+6}) \cdot H(Cr^{+6}) \cdot K + \\ \Delta M(Zn^{2+}) \cdot H(Zn^{2+}) \cdot K. \quad (16)$$

The $\Delta M(Cr^{+6})$ is the difference in the amount of sodium dichromate used per month before the use of membrane electrochemical devices and, because of their application, as mentioned above, is 4.167 kg or 0.004 tons. The tax rate of $H(Cr^{+6})$, which includes highly toxic Cr^{+6} ions, for the discharge of 1 ton of substances with a concentration of 0.001–0.100 mg/l is 122,347.23 UAH. Cd^{2+} ions are also highly toxic, so $H(Cd^{2+})$ = 122347.23 UAH. The $H(Zn^{2+})$ tax rate is 21,092.69 UAH/t for dumping 1 t of substances with a concentration of 0.1–1.0 mg/l.

The differences in the discharges volumes $\Delta M(Cd^{2+})$ and $\Delta M(Zn^{2+})$ are the masses of cadmium and zinc released on the cathodes of the cathode chambers during one month of its operation.

In January 2021, the masses of cadmium and zinc released on the cathodes in the cathode chambers of these electrochemical devices were 457.8 g and 178.1 g, respectively. The K_{oc} coefficient is equal to 1 since harmful substances are not discharged into ponds and lakes. Therefore, $\Delta\Pi(Cd)$ = 565.83 UAH, and $\Delta\Pi(Zn)$ = 513.58 UAH.

Thus, the average monthly tax on polluting substances due to the saving of sodium dichromate and cathodic deposition of metals is decreasing by the amounts calculated above. Therefore, the work total performance $E_{sum.}$ of industrial membrane electrochemical devices in passivation baths of cadmium and zinc galvanic coatings, respectively, are:

$$E_{sum.} = E + \Delta\Pi c. \quad (17)$$

Therefore, $E_{sum.}(Cd)$ = 1012.78 UAH, and $E_{sum.}(Zn)$ = 960.53 UAH.

As well known, passivation reactions of cadmium or zinc galvanic coatings occur directly on the coating surface. Therefore, it is advisable to calculate the membrane electrochemical devices' performance per unit surface area of the corresponding galvanic coating, i.e., 1m2. Thus, according to the work data of 2019 and 2020, the total area of $S_{gen.}$ parts covered with cadmium and zinc in the electroplating section of workshop No. 3 of JSC "Nasosenergomash" (Sumy, Ukraine) is 1287.74 m^2 and 604.35 m^2, respectively. We use these data to find the average monthly areas of parts covered with cadmium and zinc $S_{month.}$:

$$S_{month..Me} = S_{gen.Me}/24; \quad (18)$$

So, $S_{month..}Cd$ = 53.66 m^2, and $S_{month..}Zn$ = 25.18 m^2.

Knowing the total effectiveness of industrial membrane electrochemical devices $E_{sum.}$, and the general area of cadmium- and zinc-coated parts during one month $S_{month.}$ we find the benefit E_s of these devices per 1 m2 of the corresponding galvanic coating:

$$E_s = E_{sum.}/S_{month.} \quad (19)$$

So, E_s.Cd = 18.74 UAH/m^2; E_s.Zn = 38.15 UAH/m^2.

Therefore, the above practical calculations show that the working membrane electrochemical devices in galvanic coatings passivation baths is economically beneficial. So, it is understandable that the efficiency of these industrial electrochemical devices is within 1000 UAH/month. And it should be noted that owing to the use of industrial membrane electrochemical devices, the price of cadmium and zinc galvanic coatings is decreasing by 18.74 UAH/m^2 and 38.15 UAH/m^2, respectively.

4 Conclusions

As a result of the conducted experimental studies, it had established. Firstly, the effectiveness of the anodic regeneration process of hexavalent chromium ions in passivation baths under realistic production conditions is established. Secondly, a decrease in the working concentrations of chromate anions in the passivation baths was ascertained owing to the constant cleaning of the solution from polluting metal cations and the permanent anodic synthesis of hexavalent chromium ions.

Also, calculations of the ecological and economic efficiency of industrial electrochemical modules had done because of their operation for six months.

A significant reduction in the environmental hazard of passivation solutions had established as a result of a reduction in the working concentrations of chromates into them from 100–200 g/l to 30–50 g/l.

References

1. Bohm, L., Jankhah, S., Tihon, J., Berruber, P., Kraumel, M. (2014). Application of the electrodiffusion method to measure wall shear stress: Integrating theory and practice. *Chemical Engineering and Technology*, Vol. 37(6), pp. 938–950.
2. Hasnat, M., Alam, M., Karim, M., Rashed, M., Machida, M. (2011). Divergent catalytic behaviors of Pt and Pd films in the cathode of a sandwiched type membrane reactor. *Applied Catalysis B: Environmental*, Vol. 107(3-4), pp. 294-301.
3. Jegadeesan, G., Mondal, K., Lalvani, S. (2005). Iron removal and simultaneous regeneration of hexavalent chromium in spent plating solutions. *Journal of the Electrochemical Society*, Vol. 152(2), pp. D26-D33.
4. Kruglikov, S. (2009). Removal of metal cations from chromate-based solutions by membrane electrolysis. *Metal Finishing*, Vol. 107(11), pp. 13-15.
5. Nebavskaya, K. A., Sarapulova, V. V., Sabbatovskiy, K. G., Sobolev, V. D., Pismenskaya, N. D., Nekrasova, N. E., Nevmyatullina, Kh. A., Kharin, P. A., Kruglikova, E. S. (2016). Application of a two-chamber immersion electrochemical module for increasing the stability of a lead anode in aggressive media. *Electroplating and Surface Treatment*, Vol. 24(1), 22.
6. Robbins, B., Field, R., Kolaczkowski, S., Lockett, A. (1996). Rationalisation of the relationship between proton leakage and water flux through anion exchange membranes. *Journal of Membrane Science*, Vol. 118(1), pp. 101-110.
7. Serdiuk, V. O., Sklavbinskyi, V. I., Bolshanina, S. B., Ivchenko, V. D., Qasim, M. N., Zaytseva, K. O. (2018). Membrane processes during the regeneration of galvanic solution. *Journal of Engineering Sciences*, Vol. 5(2), pp. F1-F6, DOI: 10.21272/jes.2018.5(2).f1.
8. Serdiuk, V., Sklabinskyi, V., Bolshanina, S., Ableyev, A., Dychenko, T. (2020). Prevention of hydrosphere contamination with electroplating solutions through electromembrane processes of regeneration. *Journal of Ecological Engineering*. Vol. 21(4), pp. 61-69, DOI: 10.12911/22998993/119801.
9. Serdiuk, V., Sklabinskyi. V., Bolshanina, S., Ableyev, A., Dychenko, T. (2020). Effect of hydrodynamic parameters on membrane electrolysis enhancement. *In: Ivanov V., Pavlenko I., Liaposhchenko O., Machado J., Edl M. (eds) Advances in Design, Simulation and Manufacturing III. DSMIE 2020. Lecture Notes in Mechanical Engineering. Springer, Cham*, DOI: 10.1007/978-3-030-50491-5_22.
10. Serdiuk, V., Zaytseva, K., Sklabinsky, V., Ivchenko, V., Ponomarova, L. (2018). Laboratory and industrial testing of membrane electrochemical devices for purification and regeneration of chromium containing galvanic solutions. *In: Membrane and Sorption Materials and Technologies: Present and Future, Dzyazko Yu. S., Plisko T. V., Chaban M. O. (eds.)*, pp. 40-45.
11. Xing, Y., Chen, X., Wang, D. (2007). Electrically regenerated ion exchange for removal and recovery of Cr(VI) from wastewater. *Environmental Science and Technology*. Vol. 41(4), pp. 1439-1443.
12. Ye, Z., Yin, X., Chen, L., He, X., Lin, Z., Liu, C., Ning, S., Wang, X., Wei, Y. (2019). An integrated process for removal and recovery of Cr(VI) from electroplating wastewater by ion exchange and reduction–precipitation based on a silica-supported pyridine resin. *Journal of Cleaner Production*, Vol. 236, 117631, https://doi.org/10.1016/j.jclepro.2019.117631

JOURNAL OF ENGINEERING SCIENCES

Volume 9, Issue 2 (2022)

Mbah, O. M., Madueke, C. I., Umunakwe, R., Okafor, C.O. (2022). Machine learning approach for solar irradiance estimation on tilted surfaces in comparison with sky models prediction. Journal of Engineering Sciences, Vol. 9(2), pp. G1-G6, doi: 10.21272/jes.2022.9(2).g1

Machine Learning Approach for Solar Irradiance Estimation on Tilted Surfaces in Comparison with Sky Models Prediction

Mbah O. M.[1*], Madueke C. I.[2], Umunakwe R.[2], Okafor C. O.[3]

[1*] Department of Mechanical Engineering, Federal University Oye-Ekiti, Ikole, City, 370105, Ekiti-State, Nigeria;
[2] Department of Material and Metallurgical Engineering, Federal University Oye-Ekiti, Street, Ikole, 370105, Ekiti -State, Nigeria;
[3] Department of Mechanical Engineering, Grundtvig Polytechnic, Street, Oba, 434116, Anambra State, Nigeria

Article info:
Submitted: April 14, 2022
Accepted for publication: August 29, 2022
Available online: September 4, 2022

***Corresponding email:**
oguejiofor.mbah@fuoye.edu.ng

Abstract. In this study, two supervised machine learning models (Extreme Gradient Boosting and K-nearest Neighbour) and four isotropic sky models (Liu and Jordan, Badescu, Koronakis, and Tian) were employed to estimate global solar radiation on daily data measured for one year period at the National Center for Energy, Research and Development (NCERD) at the University of Nigeria, Nsukka. Two solarimeters were employed to measure solar radiation: one measured solar radiation on a tilted surface at a 15° angle of tilt, facing south, and the other measured global horizontal solar radiation. The measured global horizontal solar radiation and the time and day number were used as input for the prediction process. Python computational software was used for model prediction, and the performance of each model was assessed using statistical methods such as mean bias error (MBE), mean absolute error (MAE), and root mean square error (RMSE) (RMSE). Compared to the measured data, it was discovered that the Extreme Gradient Boosting (XGBoost) algorithm offered the best performance with the least inaccuracy to sky models.

Keywords: machine learning, sky models, solar energy, solar radiation, tilted surface.

1 Introduction

The sun generates electromagnetic radiation known as solar irradiance, and the quantity of the radiation received in a given area is determined by geographical location, daytime, season, and local weather. The dearth of solar radiation data has necessitated the development of several mathematical models (Isotropic and Anisotropic sky models).

However, it has been observed that mathematical models offer an approximate solution, have high computational cost, and consume time during the solving process. The development of machine and deep learning algorithms is being viewed as a feasible option for estimating solar radiation. This study aims to compare the predicting accuracy of sky models to machine learning models on a tilted surface. Measured solar radiation data on a tilted surface at a 15° angle of tilt, facing south, will be used to train and validate the models.

2 Literature Review

Many researchers have utilized several empirical models to estimate global solar irradiance. For example, three isotropic sky models were utilized to estimate global solar irradiance on a tilted surface, and their performance was compared to experimental data using a statistical method [1]. Similarly, two anisotropic empirical models developed by Perez and Hay, Davies, Klucher, and Reindl (HDKR) were utilized to predict solar radiation on tilted surfaces in Sub-Saharan Africa Climate [2]. According to the results, the Perez model fared better regarding statistical measures. Shourehdeli et al. [3] used four empirical models with isentropic coefficients to estimate injector performance in critical mode. In Biskra, Algeria, Chabane et al. [4] established a model for solar irradiance forecasting dependent on the aerosol optical depth between two wavelengths of 550 and 1250 nm.

Machine learning algorithms have also been utilized in forecasting since they allow more data to be incorporated into the forecast. For example, Piryonesis and El-Diraby [5] used a machine learning algorithm to anticipate

pavement deterioration and assess long-term pavement performance. With various input data, the Support Vector Machine Regression (SVM-R) model has been effectively utilized to estimate global sun radiation [6-9]. Similarly, the Artificial Neural Network (ANN) approach has been used to forecast and predict historical experimental data [10-14]. In addition, many researchers have employed hybrid models to estimate global solar radiation.

For example, Torabi et al. [15] proposed a Cluster-Based Approach (CBA) that estimates daily global solar radiation on the horizontal surface using a support vector machine and an Artificial Neural Network. The results demonstrate that the hybrid model outperformed the separate models in terms of mean absolute percentage error. Similarly, Gala et al. [16] used three hybrid models to forecast global solar radiation in seven different sites in Spain: support vector machine, gradient boosted regression, and random forest. The outcome demonstrates that the hybrid model is extremely effective. Achour et al. [17] utilized a hybrid mode to estimate Southern Algeria's solar radiation. Furthermore, Herath et al. [18] developed a mathematical model for daily global solar radiation forecast and compared its performance to that of artificial neural network prediction.

Some international findings on the use of machine learning algorithms in forecasting horizontal solar radiation have been published.

Quej et al. [19] assessed the performance of an "adaptive neuro-fuzzy inference system (ANFIS), an artificial neural network (ANN), and a support vector machine (SVM) in calculating daily global horizontal solar radiation from collected data in Mexico". SVM fared better, according to the results. Similarly, Marzo et al. [20] forecasted daily solar radiation data from deserts in Chile, Israel, Saudi Arabia, South Africa, and Australia using an artificial neural network (ANN) model trained on daily minimum and maximum temperatures as well as extraterrestrial radiation. The model was tested using a statistical tool and data. ANN produced an average relative root mean square derivation (RRMSD) of 0.13 and a correlative coefficient of 0.8. In Turkey, Augbulut et al. [21] employed four different machine learning methods (Support Vector Machine (SVM), Artificial Neural Network (ANN), Kernel and Nearest-Neighbor (KNN), and Deep Learning (DL)) to forecast power output system. In addition, the four machine learning approaches were used to predict daily global solar radiation in four Turkish districts. (Kirklareli, Tokat, Nevsehir and Karamam) [22]. The result indicated that ANN has a higher prediction than other models. Haciouglu Rifat [23] built a linear and gaussian regression model for solar irradiance estimation in Turkey's Zonguldak province. The input parameters were wind speed, temperature, pressure, and humidity; statistically, the gaussian model performed better. Various machine learning algorithms based on linear and nonlinear regression approaches were also examined [24-28].

In addition, multiple empirical models for estimating solar radiation were examined using the average monthly mean value of solar radiation in Bhopal, India [29].

However, several researchers have observed that empirical models do not accurately forecast solar radiation data because they do not capture the complicated and nonlinear relationship between the response and the covariate variable in humid regions [30-32].

3 Research Methodology

3.1 Site and measurement

The solar radiation data were measured at the National Center for Energy Research and Development (NCERD) in the University of Nigeria, Nsukka. Nsukka is a town and Local Government Area in South East Nigeria in Enugu State with latitude $6°51'28''$ North and longitude $7°23'44''$ East. Nsukka has a tropical savanna climate with the highest average temperature of 36° in February and 28° lowest in July. Two solarimeters were used to measure solar radiation data for one year (Febrary2017 - January 2018). One solarimeter monitored hourly global solar radiation on a horizontal surface, whereas the other measured it on a tilted surface with a 15° inclination heading south.

3.2 Description of machine learning models

Machine learning is an aspect of artificial intelligence that uses algorithms to build a model from data. They are employed in the estimation of the target function to predict the output variable given the input variables. The following is a brief description of the two machine learning algorithms used.

3.2.1 Extreme gradient boosting (XGBoost)

Extreme gradient boosting is a machine learning approach that describes the gradient and how the loss function can be minimized using second partial derivatives of the loss function. It is a technique used for regression and classification which produces a prediction model in the form of a decision tree. The XGBoost model on prediction of *i*-th instance at the *t*-th iteration is given as

$$L^{(t)} = \sum_{i=1}^{n} l\left(y_i, y_i^{\Lambda(t-1)} + f_t(X_i)\right) + \Omega(f_t) \qquad (1)$$

where l is the loss function, f_t is the t'^{th} tree output; Ω – the regularization and $y_i^{\Lambda(t)}$ – the prediction of the *i*-th instance at the *t*-th iteration. XGBoot loss function approximation with Taylor expansion is given as

$$L^{(t)} = \sum_{i=1}^{n} l\left(y_i, y_i^{\Lambda(t-1)}\right) + g_t f_t(X_i) + \frac{1}{2} h_i f_t^2(X_i) + \\ + \Omega(f_t) \qquad (2)$$

where g_i and h_i – the first and second derivatives of the loss function.

3.2.2 K-nearest neighbor (KNN)

K-nearest neighbor is a supervised machine learning algorithm to solve classification and regression problems.

It locates the k-nearest neighbor to the test data and performs classification with the class label. The average nearest neighbor ratio is given as:

$$ANN = \frac{\overline{D}_o}{\overline{D}_E} \quad (3)$$

where $\overline{D_o}$ – the observed mean distance between each feature and its nearest neighbor is given as:

$$\overline{D_o} = \frac{\sum_{i=1}^{n} d_i}{n} \quad (4)$$

and $\overline{D_E}$ – the expected mean distance for the features given in a random pattern.

$$\overline{D_E} = \frac{0.5}{\sqrt{\frac{n}{A}}} \quad (5)$$

in the above equations, d_i – the distance between feature i and its nearest neighboring feature, n corresponds to the total number of features; A – the area of the minimum enclosing rectangle around all features.

3.3 Solar radiation on the horizontal surface

Horizontal solar radiation (global irradiance) is the summation of direct(beam) and diffuse(scattered) irradiance. Direct irradiance comes directly from the sun to the earth's surface, while diffused irradiance is the scattered solar radiation that reaches the earth's surface.

$$I_H = I_{H,b} + I_{H,d} \quad (6)$$

where $I_{H,b}$ – the beam(direct) irradiance; $I_{H,d}$ – the diffuse irradiance and I_H – horizontal solar radiation.

3.4 Solar radiation on the tilted surface

The incident solar radiation on a tilted surface is composed of three components (direct irradiance, diffuse irradiance, and ground reflectance):

$$I_T = I_{T,b} + I_{T,d} + I_{T,r} \quad (7)$$

where $I_{T,b}$ is the beam irradiance (tilted surface); $I_{T,d}$ is the diffuse irradiance (tilted surface); $I_{T,r}$ – the ground reflectance and I_T – solar radiation on the tilted surface.

3.5 Isotropic models that are commonly utilized are described

To estimate solar irradiance on a tilted surface, isotropic and anisotropic sky models are utilized. Four isotropic sky models were utilized in this investigation, and their findings were compared to machine learning models. The isotropic sky models are described briefly below.

3.5.1 Badescu model

Badescu model has a view factor of $F = \left(\frac{3+\cos\beta}{4}\right)$ and can be expressed as

$$I_T = I_{H,b}R_b + I_{H,d}\left(\frac{3+\cos\beta}{4}\right) + I_{H,\rho}\left(\frac{1-\cos\beta}{2}\right) \quad (8)$$

3.5.2 Tian model

This model evaluated three components of solar radiation on a slanted surface (beam, diffuse, and ground reflectance):

$$I_T = I_{H,b}R_b + I_{H,d}\left(1 - \frac{\beta}{180}\right) + I_{H,\rho}\left(\frac{1-\cos\beta}{2}\right) \quad (9)$$

3.5.3 Koronakis model

Koronakis model incorporated the circumsolar and horizontal brightening and proposed the slope $\beta = 90^0$ and is proposed to be

$$I_T = I_{H,b}R_b + I_{H,d}\left(\frac{2+\cos\beta}{3}\right) + I_{H,\rho}\left(\frac{1-\cos\beta}{2}\right) \quad (10)$$

3.5.4 Liu-Jordan model

This model assumes that circumsolar and horizon brightening are both zero and that diffuse radiation is exclusively isotropic:

$$I_T = I_{H,b}R_b + I_{H,d}\left(\frac{1+\cos\beta}{2}\right) + I_{H,\rho}\left(\frac{1-\cos\beta}{2}\right) \quad (11)$$

3.6 Methods of models evaluation

In this work, the prediction of machine learning models and isotropic sky models was compared to the experimental data using three statistical tests: Mean Absolute Error (MAE), Mean Bias Error (MBE), and Root Mean Square Error (RMSE) (RMSE).

3.6.1 Mean bias error (MBE)

The mean bias error evaluates the whole bias and detects if the model is producing overestimation ($MBA > 0$) or underestimation when ($MBA < 0$). Mean bias error is given as

$$MBE = \frac{1}{n}\sum_{i=1}^{n}(Hpi - H_{mi}) \quad (12)$$

where H_{pi} – the predicted value; H_{mi} – the measured value; n – the number of observations.

3.6.2 Mean absolute error (MAE)

Mean absolute error is a measure of model evaluation metric used with regression models and can be expressed as:

$$MAE = \frac{1}{n}\sum_{i=1}^{n}\left(\frac{H_{pi}-H_{mi}}{n}\right) \quad (13)$$

where n is the number of data points.

3.6.3 Root mean square error (RMSE)

The fluctuation of the anticipated values around the observed data is quantified by the root mean square error. It is computed using the following equation:

$$RMSE = \sqrt{\frac{1}{n}\sum_{i=1}^{n}(H_{pi} - H_{mi})^2} \quad (14)$$

where H_{pi} – the predicted value; H_{mi} – the measured value; n – the number of observations.

4 Results

Figure 1 depicts the correlation between the models and the measured solar radiation data on a tilted surface using scattered plots. The greater the association between the models and the measured data, the closer the data points are to the line of best fit. The models and the measured data have a high, positive, linear correlation. By offering a tighter grouping of data points, the Extreme gradient boosting (Xgboost) model provided the most significant correlation among the models, followed by K-nearest neighbor, Badescu, Koronakis, Tian and Liu, and Jordan models, in that order.

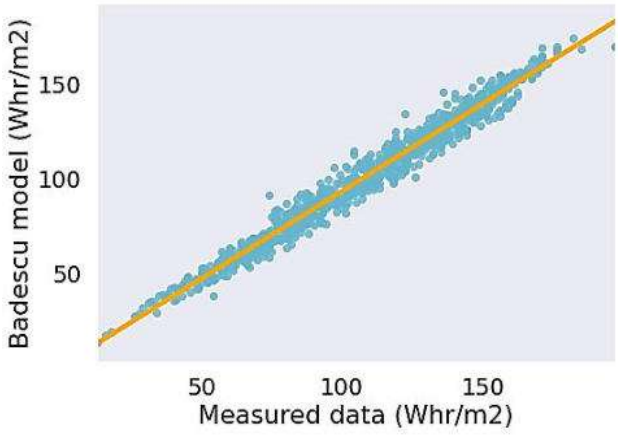

a

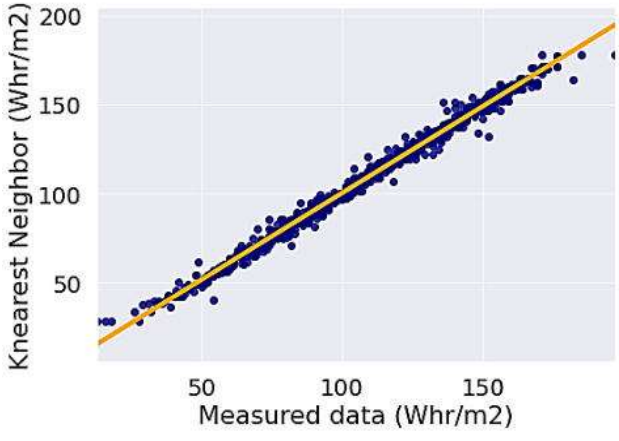

b

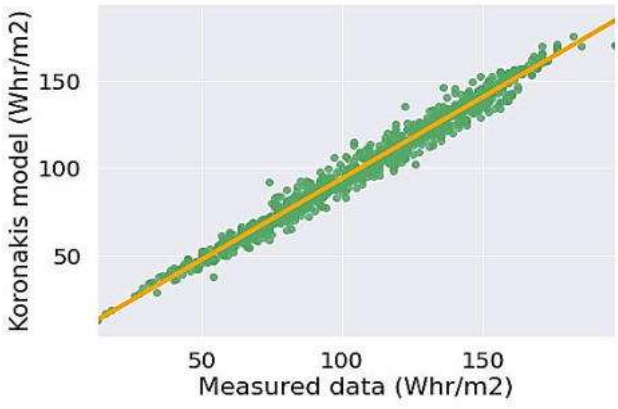

c

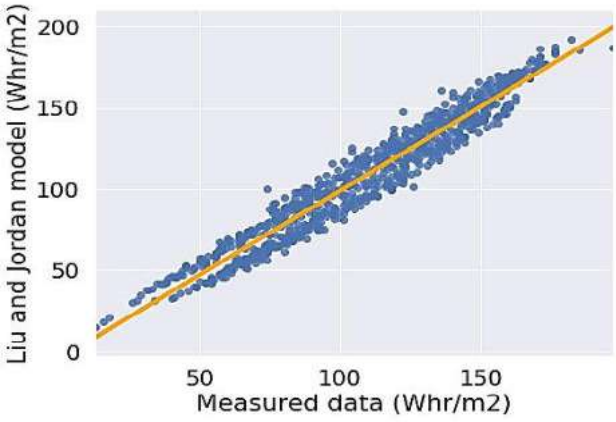

d

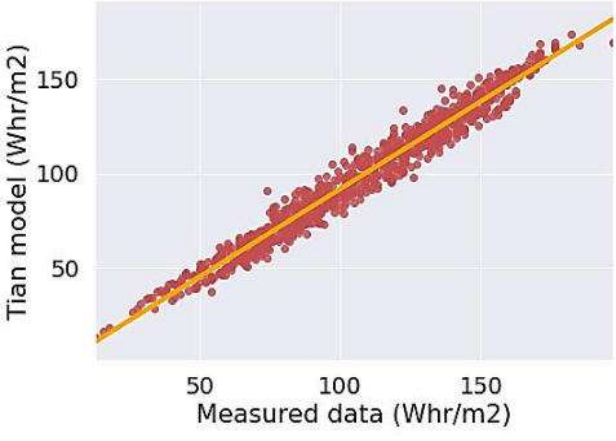

e

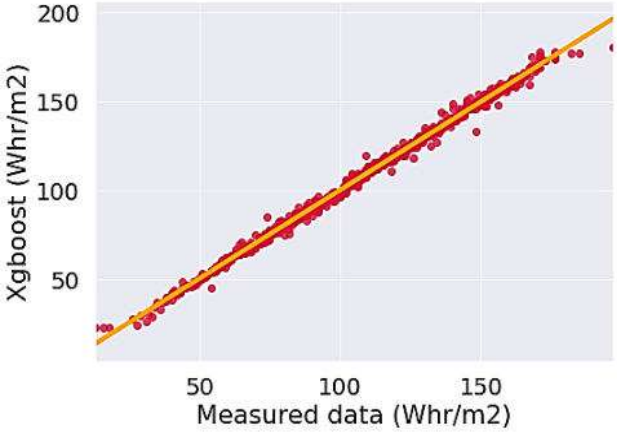

f

Figure – Predicted versus measured solar radiation data on titled surfaces for the six models, W·hr / m^2: a – Badescu model; b – K-nearest neighbor; c – Koronakis model; d – Liu-Jordan model; e – Tian model; f – XGBoost

Figure 2 compares each model forecast with the measured solar radiation data on day 329 with the most significant clearness index. The graph demonstrates that the two machine learning models (Extreme gradient boosting and K-nearest neighbor) provided nearly identical results closer to the measured solar radiation data, while the Liu and Jordan model produced the highest projected values across all models.

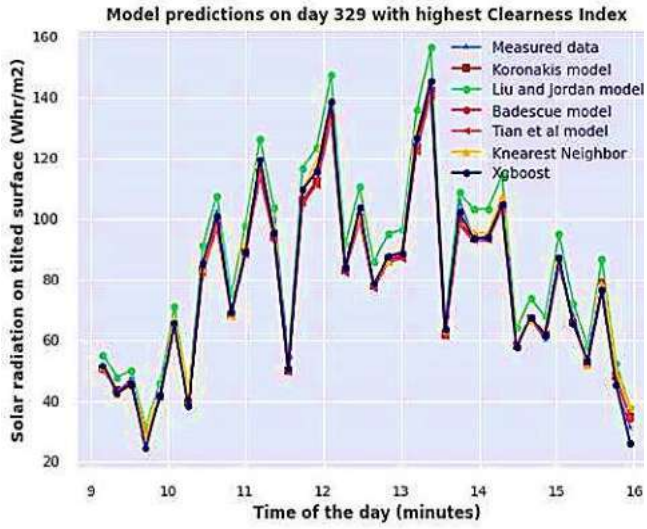

Figure 2 – Comparison of different models' estimation with measured data

In addition, the Koronakis model had the lowest predicted values of all the isotropic sky models.

5 Discussion

The Root Mean Square Error quantifies the volatility of expected values around the measured data (RMSE). The model's performance improves as the value decreases. Extreme gradient boosting (XGBoost) had the lowest RMSE of 2.11 W·hr/m^2, and the Tian model had the highest RMSE of 11.20 W·hr/m^2. Other models, such as Koronakis, Liu and Jordan, Badescu, and K-nearest Neighbor, achieved RMSEs of 8.71 W·hr/m^2, 9.23 W·hr/m^2, 9.46 W·hr/m^2, and 3.35 W·hr/m^2.

Mean Absolute Error (MAE) is a model evaluation metric. The XGBoost model had the lowest MAE of 1.37 W·hr/m^2, followed by the K-nearest neighbor at 2.34 W·hr/m^2, and the Koronakis, Liu-Jordan, and Badescu models had an MAE of 7.22 W hr/m^2, 8.06 W·hr/m^2, and 7.90 W·hr/m^2, respectively. The Tian model had the highest MAE of 9.44 W·hr/m^2.

Mean Bias Error (MBE) provides information on the models' long-term performance. It tells whether the model is over or underestimating. When MBE is more than zero, the model overestimates. When MBE is less than zero, the model underestimates.

XGBoost and K-nearest neighbor models had a positive MBE of 0.00647Whr/m^2 and 0.16430W hr/m^2, respectively. Other models, such as Koronakis, Liu-Jordan, Badescu, and Tian, have negative values of MBE errors: –6.51 W·hr/m^2, –0.71 W·hr/m^2, –7.26 W·hr/m^2 and –8.95 W·hr/m^2, respectively.

6 Conclusions

The efficiency of sky models and machine learning models for estimating solar radiation on a tilted surface was compared to observed solar radiation data on a tilted surface. The findings are based on comparing four isotropic sky models and two machine learning models.

The statistical analysis found that extreme gradient boosting (XGBoost) had the lowest RMSE (2.11 W·hr/m^2), MAE (1.37 W·hr/m^2), and MBE (0.01 W·hr/m^2) among the six models, whereas Tian had the greatest RMSE (11.20 W·hr/m^2), MAE (9.44 W·hr/m^2), and MBE (–8.95 W·hr/m^2).

The two machine learning models (Extreme gradient boosting and K-nearest neighbor) outperformed the isotropic sky models in terms of RMSE, MAE, and MBE.

Extreme gradient boosting (XGBoost) and the K-nearest neighbor model can estimate global solar radiation on a tilted surface, where observed data is scarce.

7 Acknowledgments

The authors appreciate the National Centre for Energy, Research and Development (NCERD), University of Nigeria, Nsukka, where the solar radiation data was measured.

References

1 Mbah, O. M., Mgbemene, C. A., Enibe, S. O., Ozor, P. A., Mbohwa, C. (2018). Comparison of experimental data and isotropic sky models for global solar radiation estimation in Eastern Nigeria. *Proceedings of the World Congress on Engineering*, pp. 581-585.

2 Mbah, O. M., Ozor, P., Mgbemene, C., Enibe, S. O., Mbohwa, C. (2018). Comparative analysis of anisotropic sky models and experimental data in estimating solar radiation on tilted surface in Sub-Saharan African climate. *IEOM Conference. IEOM 2018*, pp. 592-598.

3 Shourehdeli, S. A., Mobini, K., Asakereh, A. (2022). Modeling of isentropic coefficients used in one dimensional model to predict ejector performance at critical mode. *Iranian (Iranica) Journal of Energy & Environment*, Vol. 13, pp. 111-123.

4 Chabane, F., Arif, A., Moummi, N., Brima, A. (2020). Prediction of solar radiation according to aerosol optical depth. *Iranian (Iranica) Journal of Energy & Environment*, Vol. 11, pp. 271-276.

5 Piryonesi, S. M., El-Diraby, T. E. (2020). Data analytics in asset management: Cost-effective prediction of the pavement condition index. *Journal of Infrastructure Systems*, Vol. 26, 04019036.

6 Guermoui, M., Rabehi, A., Gairaa, K., Benkaciali, S. (2018). Support vector regression methodology for estimating global solar radiation in Algeria. *The European Physical Journal Plus*, Vol. 133, pp. 1-9.

7 Chen, J. L., Li, G. S. (2014). Evaluation of support vector machine for estimation of solar radiation from measured meteorological variables. *Theoretical and Applied Climatology*, Vol. 115, pp. 627-638.
8 Chen, J. L., Li, G. S., Wu, S. J. (2013). Assessing the potential of support vector machine for estimating daily solar radiation using sunshine duration. *Energy Conversion and Management*, Vol. 75, pp. 311-318.
9 Chen, J. L., Liu, H. B., Wu, W., Xie, D. T. (2011). Estimation of monthly solar radiation from measured temperatures using support vector machines – A case study. *Renewable Energy*, Vol. 36, pp. 413-420.
10 Mahdavi Jafari, M., Khayati, G. R., Hosseini, M., Danesh-Manesh, H. (2017). Modeling and optimization of roll-bonding parameters for bond strength of Ti/Cu/Ti clad composites by artificial neural networks and genetic algorithm. *International Journal of Engineering*, Vol. 30, pp. 1885-1893.
11 Motameni, H. (2020). Determining the composition functions of Persian non-standard sentences in terminology using a deep learning fuzzy neural network model. *International Journal of Engineering*, Vol. 2020, Vol. 33, pp. 2471-2481.
12 Benmouiza, K., Cheknane, A. (2013). Forecasting hourly global solar radiation using hybrid k-means and nonlinear autoregressive neural network models. *Energy Conversion and Management*, Vol. 75, pp. 561-569.
13 Rahimikhoob, A. (2010). Estimating global solar radiation using artificial neural network and air temperature data in a semi-arid environment. *Renewable Energy*, Vol. 35, pp. 2131-2135.
14 Çelik, Ö., Teke, A., Yıldırım, H. B. (2016). The optimized artificial neural network model with Levenberg–Marquardt algorithm for global solar radiation estimation in Eastern Mediterranean Region of Turkey. *Journal of Cleaner Production*, Vol. 116, pp. 1-12.
15 Torabi, M., Mosavi, A., Ozturk, P., Varkonyi-Koczy, A., Istvan, V. (2018). A hybrid machine learning approach for daily prediction of solar radiation. *International Conference on Global Research and Education*, pp. 266-274.
16 Gala, Y., Fernández, Á., Díaz, J., Dorronsoro, J. R. (2016). Hybrid machine learning forecasting of solar radiation values. *Neurocomputing*, Vol. 176, pp. 48-59.
17 Achour, L., Bouharkat, M., Assas, O., Behar, O. (2017). Hybrid model for estimating monthly global solar radiation for the Southern of Algeria:(Case study: Tamanrasset, Algeria). *Energy*, Vol. 135, pp. 526-539.
18 Herath, H., Ariyathunge, S., Karunasena, G. (2021). *Development of a Mathematical Model to Forecast Solar Radiation and Validating Results Using Machine Learning Technique*. Available online: https://doi.org/10.21203/rs.3.rs-669429/v1.
19 Quej, V. H., Almorox, J., Arnaldo, J. A., Saito, L. (2017). ANFIS, SVM and ANN soft-computing techniques to estimate daily global solar radiation in a warm sub-humid environment. *Journal of Atmospheric and Solar-Terrestrial Physics*, Vol. 155, pp. 62-70.
20 Marzo, A., Trigo-Gonzalez, M., Alonso-Montesinos, J., Martínez-Durbán, M., López, G., Ferrada, P., Fuentealba, E., Cortés, M., Batlles, F. J. (2017). Daily global solar radiation estimation in desert areas using daily extreme temperatures and extraterrestrial radiation. *Renewable Energy*, Vol. 113, pp. 303-311.
21 Ağbulut, Ü., Gürel, A. E., Ergün, A., Ceylan, İ. (2020). Performance assessment of a V-Trough photovoltaic system and prediction of power output with different machine learning algorithms. *Journal of Cleaner Production*, Vol. 268, 122269.
22 Ağbulut, Ü., Gürel, A. E., Biçen, Y. (2021). Prediction of daily global solar radiation using different machine learning algorithms: Evaluation and comparison. *Renewable and Sustainable Energy Reviews*, Vol. 135, 110114.
23 Hacioğlu, R. (2017). Prediction of solar radiation based on machine learning methods. *The Journal of Cognitive Systems*, Vol. 2, pp. 16-20.
24 Alizamir, M., Kim, S., Kisi, O., Zounemat-Kermani, M. (2020). A comparative study of several machine learning based non-linear regression methods in estimating solar radiation: Case studies of the USA and Turkey regions. *Energy*, Vol. 197, 117239.
25 Bamisile, O., Oluwasanmi, A., Ejiyi, C., Yimen, N., Obiora, S., Huang, Q. (2021). Comparison of machine learning and deep learning algorithms for hourly global/diffuse solar radiation predictions. *International Journal of Energy Research*, Vol. 2021, doi: 10.1002/er.6529.
26 Üstün, İ., Üneş, F., Mert, İ., Karakuş, C. (2020). A comparative study of estimating solar radiation using machine learning approaches: DL, SMGRT, and ANFIS. *Energy Sources, Part A: Recovery, Utilization, and Environmental Effects*, Vol. 2020, pp. 1-24.
27 Aslam, M., Lee, J. M., Kim, H. S., Lee, S. J., Hong, S. (2020). Deep learning models for long-term solar radiation forecasting considering microgrid installation: A comparative study. *Energies*, Vol. 13, 147.
28 Fan, J., Wang, X., Wu, L., Zhou, H., Zhang, F., Yu, X., Lu, X., Xiang, Y. (2018). Comparison of support vector machine and extreme gradient boosting for predicting daily global solar radiation using temperature and precipitation in humid subtropical climates: A case study in China. *Energy Conversion and Management*, Vol. 164, pp. 102-111.
29 Shukla, K. N., Rangnekar, S., Sudhakar, K. (2015). Comparative study of isotropic and anisotropic sky models to estimate solar radiation incident on tilted surface: A case study for Bhopal, India. *Energy Reports*, Vol. 1, pp. 96-103.
30 Feng, Y., Gong, D., Zhang, Q., Jiang, S., Zhao, L., Cui, N. (2019). Evaluation of temperature-based machine learning and empirical models for predicting daily global solar radiation. *Energy Conversion and Management*, Vol. 198, 111780.
31 Sharifi, S. S., Rezaverdinejad, V., Nourani, V. (2016). Estimation of daily global solar radiation using wavelet regression, ANN, GEP and empirical models: A comparative study of selected temperature-based approaches. *Journal of Atmospheric and Solar-Terrestrial Physic*s, Vol. 149, pp. 131-145.
32 Khosravi, A., Nunes, R. O., Assad, M. E. H., Machado, L. (2018). Comparison of artificial intelligence methods in estimation of daily global solar radiation. *Journal of Cleaner Production*, Vol. 194, pp. 342-358.

JOURNAL OF ENGINEERING SCIENCES

Volume 9, Issue 2 (2022)

Chernysh, Y., Bataltsev, Y., Shen, X.-J., Bohdanovych, O., Yakhnenko, O. (2022). Electro-fermentation for biopolymers production: trends determination with bioinformatics data analysis. Journal of Engineering Sciences, Vol. 9(2), pp. H1-H8, doi: 10.21272/jes.2022.9(2).h1

Electro-Fermentation for Biopolymers Production: Trends Determination with Bioinformatics Data Analysis

Chernysh Y.[1*[0000-0003-4103-4306]], Bataltsev Y.[1[0000-0003-2035-2014]], Shen X.-J.[2[0000-0003-1951-0927]], Bohdanovych O.[1[0000-0002-5812-1169]], Yakhnenko O.[1[0000-0001-8455-1536]]

[1] Sumy State University, 2, Rymskogo-Korsakova St., 40007, Sumy, Ukraine;

[2] Key Laboratory of Yarn Materials Forming and Composite Processing Technology of Zhejiang Province, Jiaxing University, 314001, Jiaxing, China

Article info:

Submitted: June 17, 2022

Accepted for publication: September 5, 2022

Available online: September 8, 2022

***Corresponding email:**

e.chernish@ssu.edu.ua

Abstract. The paper is devoted to the study of directions of application of combined systems for obtaining biofuels and biopolymers using electro-oxidative processes, namely electro-fermentation. In the course of the work, a step-by-step methodology of research is shown, and the relationship between different bioinformatic databases in their combined use is described, which made it possible to identify trends in electro-fermentation systems with the production of bio-based products. A review of possible electro-fermentation systems with major bio-product production was performed. The possibility of including anaerobic producers of organic acids, namely lactic acid, for the needs of biopolymerization, with bioinformatic databases was substantiated. The model of the process of anaerobic fermentation with the production of organic acids for biopolymerization has been formed. The analysis of bioinformatic databases showed that the strains Anaerotignum propionicum X2, isolated from silty bottom sediments, and Anaerotignum propionicum 19acry 3, isolated from an operating anaerobic reactor, have the most significant indicators of lactate productivity. The conditions for their cultivation with an indication of nutrient media and modification of their composition are considered.

Keywords: biofuels, biopolymers, electro-fermentation, bioinformatic databases, nutrient medium.

1 Introduction

Modern advances in the efficient use of waste to create value-added products can ensure the sustainability of food systems and become a tool for solving the global problem of conserving fossil resources and minimizing environmental risks for the biosphere.

Synthetic polymeric materials are derived from the processing of non-renewable natural carbon sources - oil or products of its processing. After use, such products do not decompose for a long time in the environment due to the lack of enzymatic systems capable of destroying chemical bonds in the synthetic polymer molecule and become the cause of environmental pollution, both micro- and macroplastics, and the release into the environment of dioxin and other highly toxic substances, the release of large amounts of CO_2, increasing the greenhouse effect, destructive effect on living organisms of different levels of organization in the ecosystems.

There is increasing interest in obtaining biopolymers as substitutes for synthetic polymeric materials from recycling secondary raw materials [1-4].

The advantages of this direction are the reduction or in the future, even rejection of non-renewable raw material sources, the extraction of which causes environmental pollution, and obtaining bioplastics from renewable raw material sources (biomass of plant origin, agricultures, organic waste in the form of low-grade sewage and lignocellulose biomass), reduction of greenhouse gas emissions and harmful effects on the climate change in the production of bioplastics compared to the production of synthetic plastics.

Considering that the obtained bioplastic is also compost-resistant like synthetic bioplastic and is not automatically biodegradable, recycling it after use is possible. As a result, we can conclude that the production and use of bioplastic will have less impact on the environment than the production of traditional synthetic plastic and can replace it in a wide range of human economic activities.

Thus, biopolymers are vital substitutes for petroleum-based plastics due to environmentally safe production methods, biocompatibility, and biodegradability [5]. The use of biopolymers for 3D printing technologies and their promising applications in various areas of the aerospace, textile, food, biomedical and bioindustrial industries has a significant academic, environmental and social interest. Additive manufacturing includes a subset of processes that convert a computer-aided design into a metal, polymer, ceramic, or composite structure layer by layer. For example, materials such as starch can be extruded, while some inherently non-printable products such as meat, vegetables, and rice must be processed into a powder/paste before being 3D printed. The biomedical field requires a material to have consistent performance in terms of printability, biocompatibility, degradability, and mechanical properties [6]. At the same time, bioelectrochemical systems (BES) can be used to generate electricity directly from the treatment of waste or wastewater, together with the production of valuable chemicals such as biopolymer, various alcohols, acetate, butyrate, as well as for the production of biogas, such as CH_4 and H_2.

The work aims to study the directions of application of combined systems for producing biofuels and biopolymers using electro-oxidative processes, namely electro-fermentation. In connection with this aim, two tasks were solved:

– overview of possible systems for electro-fermentation with the production of bio-basic products;

– analysis of anaerobic processes of organic acids using various bioinformatic databases.

2 Research Methodology

Bioinformation technologies implement methods that allow the administration of data on biological objects. A biological object is an open system consisting of highly organized systems of perception, sorting, and distribution of information from the environment. This ensures a biological object's organizational, structural, and functional development, which can be considered a complex structure of a multi-stage hierarchical sequence of interacting systems and subsystems in close contact with the environment.

This study used the following bioinformatics databases: GenBank, KEGG (Kyoto Encyclopedia of Genes and Genomes), EzBioCloud Database, and BacDive (The Bacterial Diversity) Metadatabase.

Figure 1 shows the dynamics in time for databases of sequences and three-dimensional structures, which indicates a significant potential for the development of information about the genome of various ecological and trophic groups of microorganisms. At the same time, GenBank and KEGG databases have free access and are most convenient for the tasks set in this study in combination with other bioinformatics platforms.

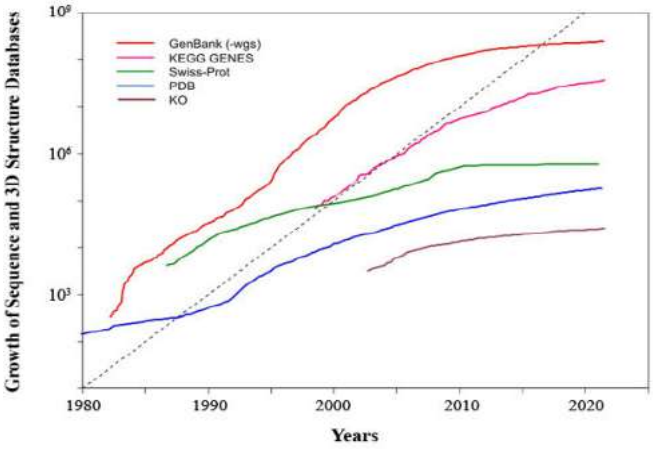

Figure 1 – Growth of Sequence and 3D Structure Databases

The step-by-step methodology of the study is shown in Fig. 2 and describes the relationship between different bioinformatic databases when they are used together.

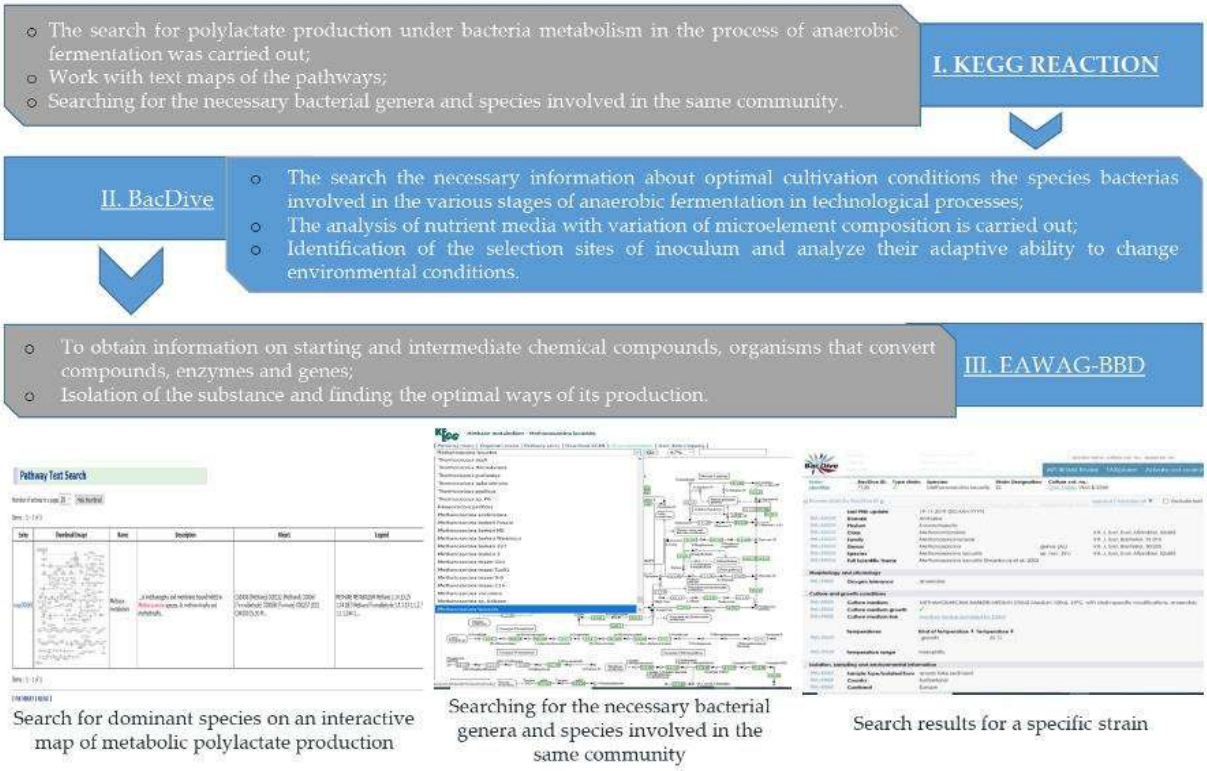

Figure 2 – Search in bioinformatic databases

3 Results and Discussion

3.1 Determination of trends in electro-fermentation systems with obtaining bio-basic products

The rapid uptake of glucose enhances lower Parallel fermentations in nature's food chains to produce numerous products, including molecular hydrogen (H_2), carbon dioxide (CO_2), formate, acetate, ethanol, lactate, succinate, and propionate. Facultative aerobes associated with *Aeromonadaceae* and obligate anaerobes associated with *Lachnospiraceae, Veillonellaceae, and Ruminococcaceae* have been related to various fermentations.

Methanogenesis continued during incubation, and 13C CH_4 labeling confirmed that the extra [13C]glucose carbon had been dissimilated to CH_4. Hydrogenotrophic methanogens belonging to the *Methanobacteriaceae* and *Methanoregulaceae* have been associated with methanogenesis, and acetogens belonging to the *Peptostreptoccocaceae* are participants in the methanogenic food web. Electrochemical processes based on renewable electricity sources at ambient temperature are an attractive alternative [7].

Dark fermentation produces hydrogen with a relatively low yield (maximum $4H_2$ per glucose) with an accumulation of metabolites such as volatile fatty acids (VFAs). On the other hand, the dark fermentation process is still attractive because of its high productivity and simple reactor design. In this regard, hybrid systems that add a second process for treating dark fermentation effluents are the subject of much research interest. By adding a second process, hybrid systems can have a potentially attractive high hydrogen yield while solving the dark fermentation wastewater treatment problem.

There are several possible combinations of a hybrid system [8]:

1) dark fermentation + photofermentation. VFAs, which are formed during dark fermentation, are ideal substrates for photofermentation;

2) dark fermentation + cell for microbial electrolysis;

3) dark fermentation + cell-free enzyme system.

4) dark fermentation + anaerobic fermentation in a fermenter. VFAs in dark fermentation effluents can be substrates for methanogens. In this process, a mixture of hydrogen and methane can be formed.

The first three combinations have the potential to achieve the maximum yield of $12H_2$ on glucose.

Many bacteria can release hydrogen as a result of dark fermentation using organic compounds: $[CH_2O]_n \rightarrow CO_2 + H_2$. It is microorganisms that can be used to dispose of various organic wastes.

A possible attractive application of the electrochemical oxidation reaction is its use to intensify the metabolism of the necessary eco-trophic groups of bacteria in the process of dark fermentation [9]. Considering the possibility of increasing the yield of organic acids in dark fermentation, interest in the electrolyzer increases.

Thus, electro-fermentation (EF) is based on electrochemical processes affecting microbial metabolism. Electron transfer during anodic or cathodic electrolysis can regulate ORP and the NAD+/NADH ratio, affecting intracellular metabolism. Recently, anodic electro fermentation using Corynebacterium glutamicum was

performed to obtain L-lysine. The results showed that using anodic electro fermentation can balance the oxidation-reduction and energy states of C. glutamicum and thus improve the anaerobic production of L-lysine. Cathodic electro fermentation was also carried out to simultaneously increase biogas and biochemical production, while the highest biogas content [96 % (v/v)] and acetate production (358 mg/l) were achieved [11].

Regulation of the kinetics of the EF processes due to the action of electrodes in the microbial environment is a mechanism of electrocatalysis (Fig. 3) aimed at the regulated formation of biobased products.

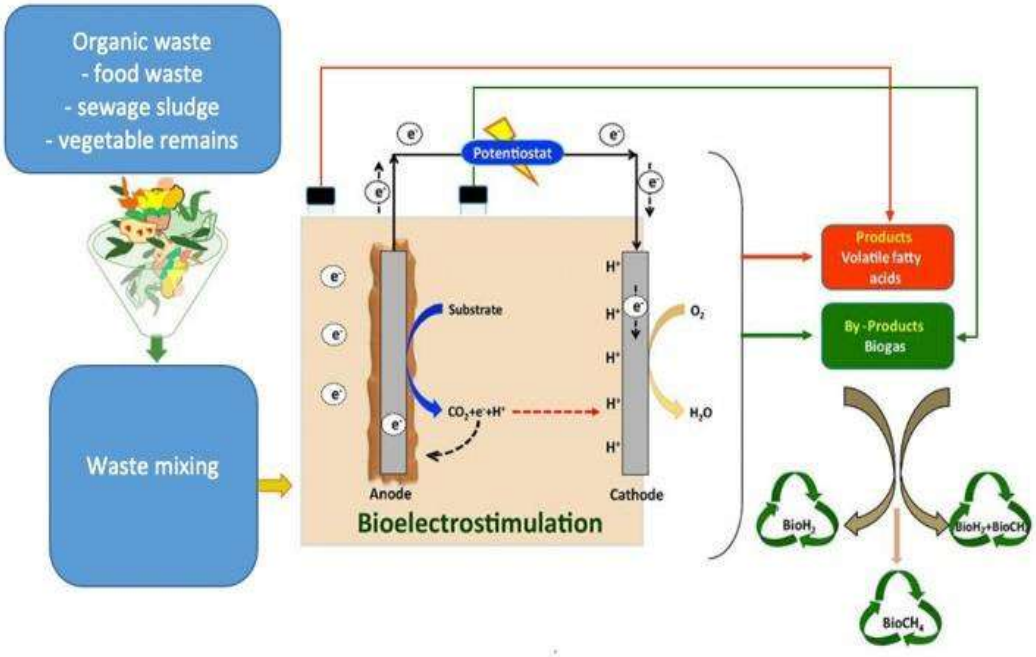

Figure 3 – Electro-fermentation under the anaerobic condition with the production of biobased products

Such organic waste, including low-grade wastewater and lignocellulosic biomass, was converted into electricity with the help of microbial fuel cells (MFC). Thus, electrical energy was used to produce hydrogen in microbial electrolysis cells (MEC) or other products, including caustic and peroxide and several organic acids. The variety of microbial and enzymatic catalysts that nature offers provides many potential applications. Compared to conventional fuel cells, bioelectrochemical systems (BES) operate under relatively mild conditions and do not use expensive precious metals as catalysts. Recently discovered microbial electrosynthesis (MES) of high-value chemicals has significantly expanded the horizons of BES application.

New application concepts, developing alternative materials for electrodes, separators, and catalysts, and innovative design have made BES a promising technology [10].

The co-production of various biofuels and organic compounds using waste and CO_2 as direct substrates points to a promising future for microbial fuel cell technologies. Likewise, an electrodialysis system can be used to extract organic acids from the dark fermentation of glucose for H_2 production by E. coli. This process was later successfully demonstrated on food waste hydrolysates. This extractive fermentation is expected to be maintained indefinitely. However, membrane fouling, the requirement for constant ionic composition, pH imbalance, etc., are major obstacles. Microbial electrolysis cells were also integrated with reverse electrodialysis, which showed a natural generation of H_2 by combining the momentum from the oxidation of organics at the anode and the energy of the salinity gradient; in addition, saline solutions can be continuously regenerated with waste heat (~38–40 °C) [12].

The work [13] performed a series of experiments using a range of commercial electron donors with varying degrees of lactate (polylactate) polymerization. These experiments were carried out using sediments from the Hanford Formation (coarse sand and gravel) submerged in Hanford groundwater, to which Cr(VI) and several types of lactate-based electron donors (Hydrogen Release Compound, HRC; primer-HRC, pHRC; extended-release HRC) and polylactate-cysteine form (Metal Remediation Compound, MRC) were added. The results showed that polylactate compounds increased bacterial biomass and activity more than sodium lactate when applied at equivalent carbon concentrations. At the same time, the concentration of hydrogen and methane in the headspace increased and correlated with changes in the microbial community [13].

Figure 4 provides an integrated flowchart of the anaerobic fermentation process, showing the bio-basic products produced at different stages of fermentation. The emphasis is on the production of organic acids that can be used to obtain biodegradable polymers, in particular, in the process of using a combination of dark fermentation (acidogenic phase of anaerobic digestion) and electrochemical processes (Fig. 3).

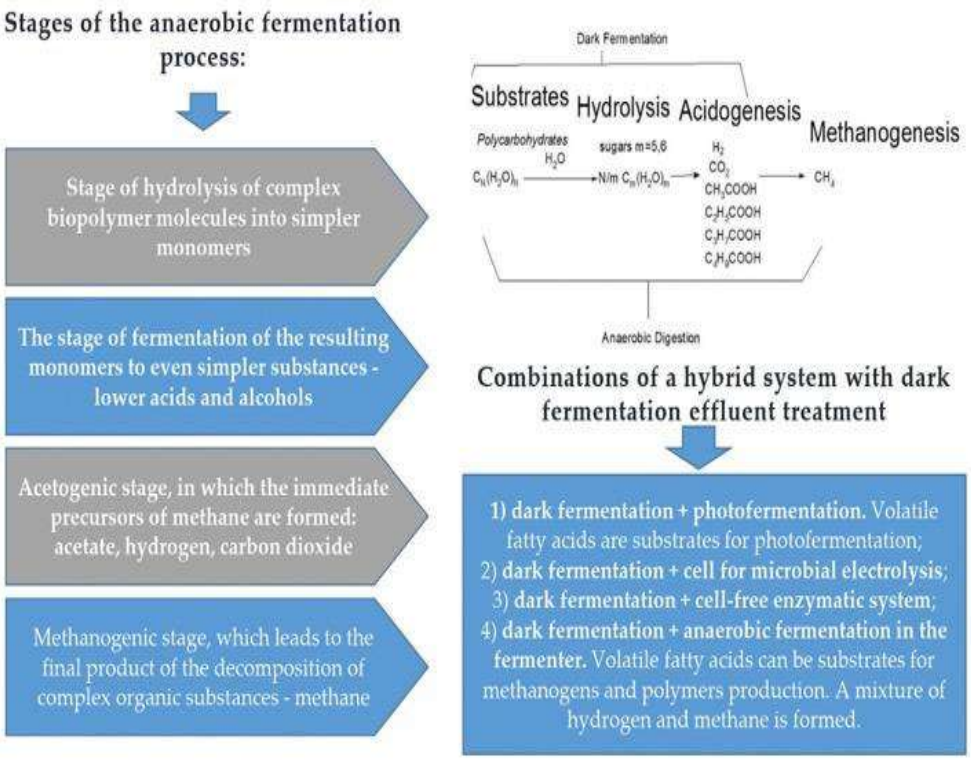

Figure 4 – Model of the anaerobic fermentation process with the production of organic acids for biopolymerization

Modern additive manufacturing (AM) of biopolymers, with a particular focus on cellulose, lignin, alginate, chitosan, starch, polylactic acid (PLA), and polycaprolactone (PCL), is increasing of interest to manufacturers of environmentally friendly polymers [6].

3.2 Analysis of anaerobic processes of organic acids using various bioinformatic databases

This paper considers the bioproduction of lactic acid for the needs of biopolymerization. Initially, GenomNet was used to identify the metabolic activity of anaerobic microorganisms for their production during dark fermentation (Fig. 5).

Polylactate (PLA) is a representative biodegradable polymer derived from lactate and is a polymer having high applicability as a general-purpose polymer or a medical polymer.

Currently, PLA is produced by the polymerization of lactate obtained from microbial fermentation. To synthesize PLA over 100,000 daltons, there is a polymerization method from low molecular weight PLA obtained by lactate direct polymerization into higher molecular weight PLA using a chain joining agent but using an organic solvent or a pair of chains. The addition of ring agents complicates the process and has the disadvantage that they are not easily removed.

Currently, a commercially available high molecular weight PLA manufacturing process is used to convert lactate to lactide and then synthesize PLA via a lactide ring condensation reaction [14].

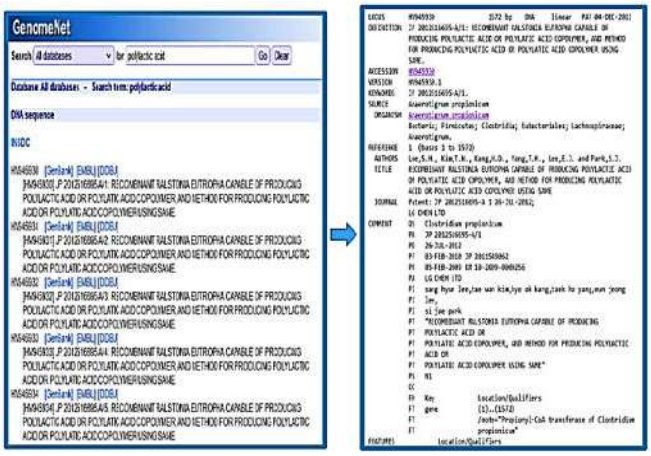

Figure 5 – Search for producers of lactic and polylactic acids

It has been determined that anaerobic strains of bacteria isolated from the methanogenic reactor have significant productivity indicators for lactate (Fig. 6).

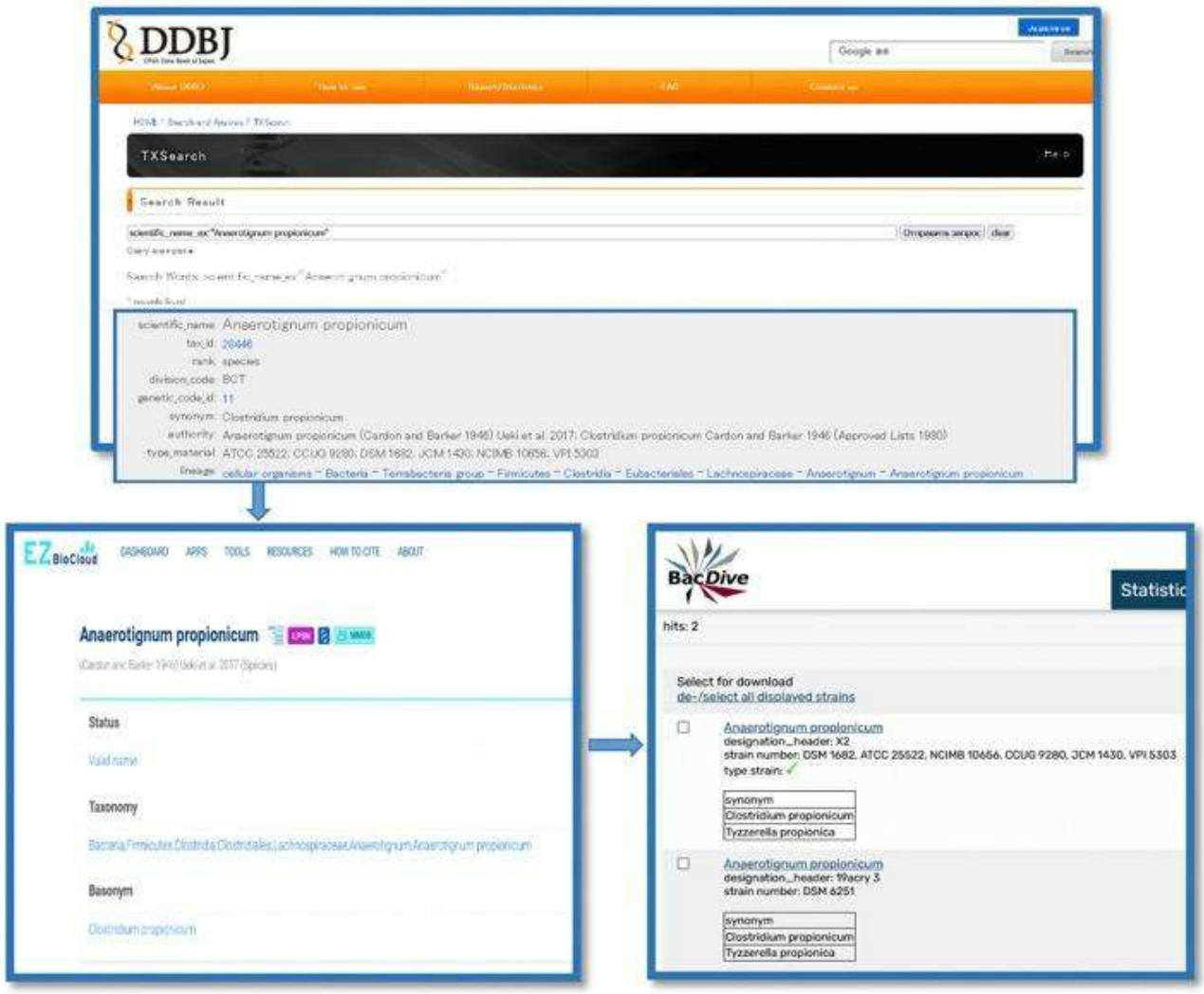

Figure 6 – Search in bioinformatic databases for the required types of anaerobic bacteria

Anaerotignum propionicum X2 is an anaerobic, chemoorganotrophic, spore-forming bacterium that was isolated from silty bottom sediments. *Anaerotignum propionicum* 19acry 3 is an anaerobe, a mesophilic bacterium, which has been isolated from an active anaerobic reactor. The conditions for their cultivation with an indication of nutrient media are shown in Figure 7.

Both strains can be cultivated on an identical nutrient medium. Dissolve the ingredients (except bicarbonate and cysteine), adjust the pH to 7.0, then saturate the medium with 100 % N_2 gas for 30–45 minutes to make it anoxic. Add and dissolve the bicarbonate and cysteine, then dispense the medium under 100 % N_2 gas into anoxic Hungat or sulfur tubes and autoclave. If necessary, adjust the pH of the whole medium to 7.0–7.2.

Based on previous studies [15], it was proposed to modify the nutrient medium for cultivating the desired anaerobic species by introducing phosphogypsum instead of calcium sulfate (Table 1).

Phosphogypsum is a multi-ton industrial waste from phosphate fertilizer production and when accumulated, can cause the alienation of vast areas of functioning ecosystems and contamination of the air, soil, and groundwater with acidic compounds containing fluorine, sulfur, phosphorus, and heavy metals.

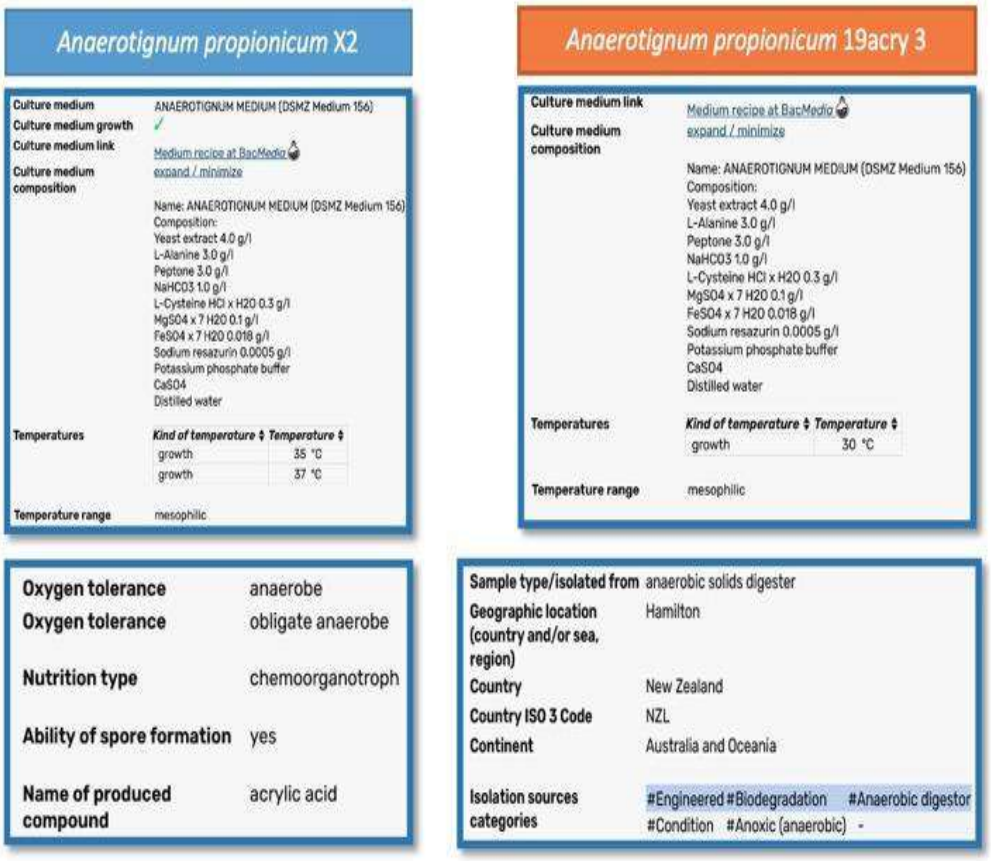

Figure 7 – Culture conditions

But it is the presence in phosphogypsum of calcium, phosphorus, residual traces of sulfur, and rare-earth elements, which are essential biogenic components for many species of living organisms, including microorganisms, makes it a source of additional macro- and microelements for bacteria used in biotechnology processes [15].

Table 1 – Culture medium for Anaerotignum propionicum

Compound	Amount	Unit	Conc. [g/L]	Conc. [mM]
L-Alanine	3.0	g	3	33.674
Peptone	3.0	g	3	–
Yeast extract	4.0	g	4	–
$MgSO_4$ x 7 H_2O	0.1	g	0.1	0.406
$FeSO_4$ x 7 H_2O	18.0	mg	0.018	0.065
Potassium phosphate buffer (1 M, pH 7.1)	5.0	ml	–	5
Phosphogypsum $CaSO_4 \times 2H_2O$ (saturated aq. solution)	2.5	ml	–	–
Sodium resazurin (0.1 % w/v)	0.5	ml	$5 \cdot 10^{-4}$	0.002
$NaHCO_3$	1.0	g	1	11.904
L-Cysteine HCl x H_2O	0.3	g	0.3	1.708
Distilled water	1000.0	ml	–	–

An important direction is the selection of the necessary types of anaerobes from local systems of anaerobic digestion of waste and effluents for their effective introduction into bioelectrochemical systems for the production of biobased products.

4 Conclusions

The article provides an overview of possible directions for using electro fermentation to intensify the processes of obtaining biobased products, such as biohydrogen, biomethane, and organic acids for producing biopolymers.

The analysis of anaerobic lactic acid processes for biopolymerization was carried out using various bioinformatic databases, namely the GenBank, KEGG, EzBioCloud, and BacDive Metadatabase. The analysis of bioinformatic databases showed that the strains *Anaerotignum propionicum* X2, isolated from silty bottom sediments, and *Anaerotignum propionicum* 19acry 3, isolated from an operating anaerobic reactor, have the most significant indicators of lactate productivity. The conditions for their cultivation with an indication of nutrient media and modification of their composition are considered.

5 Acknowledgments

We are thankful for the support of International Innovation and Applied Center "Aquatic Artery" (Sumy, Ukraine), which allowed this scientific cooperation to start. This research project was carried out as a planned research project of the Department of Ecology and Environmental Protection Technologies of Sumy State University, related to the topic "Assessment of the technogenic load of the region with changes in industrial infrastructure" according to the scientific and technical program of the Ministry of Education and Science of Ukraine (state registration No 0121U114478).

References

1. Armistead, S. J., Smith, C. C., Staniland, S. S. (2022). Sustainable biopolymer soil stabilization in saline rich, arid conditions: a 'micro to macro' approach. *Scientific Reports*, Vol. 12(1), 2880. https://doi.org/10.1038/s41598-022-06374-6.
2. Saleh, A. K., El-Gendi, H., Soliman, N. A., El-Zawawy, W. K., Abdel-Fattah, Y. R. (2022). Bioprocess development for bacterial cellulose biosynthesis by novel Lactiplantibacillus plantarum isolate along with characterization and antimicrobial assessment of fabricated membrane. *Scientific Reports*, Vol. 12(1), 2181. https://doi.org/10.1038/s41598-022-06117-7.
3. Wang, Q., Chen, W., Zhu, W., McClements, D. J., Liu, X., Liu, F. (2022). A review of multilayer and composite films and coatings for active biodegradable packaging. *Npj Science of Food*, Vol. 6(1), 18. https://doi.org/10.1038/s41538-022-00132-8.
4. Yamada, M., Kawamura, M., Yamada, T. (2022). Preparation of bioplastic consisting of salmon milt DNA. Scientific Reports, Vol. 12(1), 7423. https://doi.org/10.1038/s41598-022-11482-4.
5. Banu, J. R., Kumar, M. D., Gunasekaran, M., Kumar, G. (2019). Biopolymer production in bio electrochemical system: Literature survey. *Bioresource Technology Reports*, Vol. 7, 100283. https://doi.org/10.1016/j.biteb.2019.100283.
6. Pradhan, R. A., Rahman, S. S., Qureshi, A., Ullah, A. (2021). Biopolymers. *In Biopolymers and their Industrial Applications*, pp. 281-303. Elsevier. https://doi.org/10.1016/B978-0-12-819240-5.00012-2.
7. Schulz, K., Hunger, S., Brown, G. G., Tsai, S. M., Cerri, C. C., Conrad, R., Drake, H. L. (2015). Methanogenic food web in the gut contents of methane-emitting earthworm Eudrilus eugeniae from Brazil. *The ISME Journal*, Vol. 9(8), pp. 1778-1792. https://doi.org/10.1038/ismej.2014.262.
8. Ding, C., Yang, K.-L., He, J. (2016). Biological and fermentative production of hydrogen. *In Handbook of Biofuels Production*, pp. 303-333. Elsevier. https://doi.org/10.1016/B978-0-08-100455-5.00011-4.
9. Hauke, P., Klingenhof, M., Wang, X., De Araújo, J. F., Strasser, P. (2021). Efficient electrolysis of 5-hydroxymethylfurfural to the biopolymer-precursor furandicarboxylic acid in a zero-gap MEA-type electrolyzer. *Cell Reports Physical Science*, Vol. 2(12), 100650. https://doi.org/10.1016/j.xcrp.2021.100650.
10. Bajracharya, S., Sharma, M., Mohanakrishna, G., Dominguez Benneton, X., Strik, D. P. B. T. B., Sarma, P. M., Pant, D. (2016). An overview on emerging bioelectrochemical systems (BESs): Technology for sustainable electricity, waste remediation, resource recovery, chemical production and beyond. *Renewable Energy*, Vol. 98, pp. 153-170. https://doi.org/10.1016/j.renene.2016.03.002.
11. Zheng, T., Li, J., Ji, Y., Zhang, W., Fang, Y., Xin, F., Dong, W., Wei, P., Ma, J., Jiang, M. (2020). Progress and Prospects of Bioelectrochemical Systems: Electron Transfer and Its Applications in the Microbial Metabolism. *Frontiers in Bioengineering and Biotechnology*, Vol. 8, 10. https://doi.org/10.3389/fbioe.2020.00010.
12. Kumar, P., Chandrasekhar, K., Kumari, A., Sathiyamoorthi, E., Kim, B. (2018). Electro-Fermentation in Aid of Bioenergy and Biopolymers. *Energies*, Vol. 11(2), 343. https://doi.org/10.3390/en11020343.
13. Brodie, E. L., Joyner, D. C., Faybishenko, B., Conrad, M. E., Rios-Velazquez, C., Malave, J., Martinez, R., Mork, B., Willett, A., Koenigsberg, S., Herman, D. J., Firestone, M. K., Hazen, T. C. (2011). Microbial community response to addition of polylactate compounds to stimulate hexavalent chromium reduction in groundwater. *Chemosphere*, Vol. 85(4), pp. 660-665. https://doi.org/10.1016/j.chemosphere.2011.07.021.
14. Yang, T. H., Park, S. J., Lee, E. J., Kang, H. O., Kim, T. W., Lee, S. H. (2010). Recombinant ralstonia eutropha capable of producing polylactic acid or polylatic acid copolymer, and method for producing polylactic acid or polylatic acid copolymer using same. Patent No. WO2010090436A2.
15. Chernysh, Y., Yakhnenko, O., Chubur, V., Roubík, H. (2021). Phosphogypsum Recycling: A Review of Environmental Issues, Current Trends, and Prospects. *Applied Sciences*, Vol. 11(4), 1575. https://doi.org/10.3390/app11041575.

JOURNAL OF ENGINEERING SCIENCES

Volume 9, Issue 2 (2022)

Ablieieva I. Yu., Plyatsuk L. D., Liu T., Berezhna I. O., Yanchenko I. O. (2022). Decontamination of oil-polluted soils: Power of electronic bioinformatic databases. Journal of Engineering Sciences, Vol. 9(2), pp. H9-H16, doi: 10.21272/jes.2022.9(2).h2

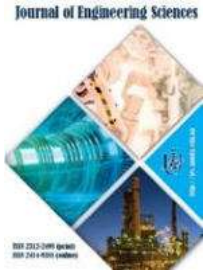

Decontamination of Oil-Polluted Soils: Power of Electronic Bioinformatic Databases

Ablieieva I. Yu.[1*[0000-0002-2333-0024]], Plyatsuk L. D.[1[0000-0003-0095-5846]], Liu T.[2[0000-0002-6456-4767]], Berezhna I. O.[1[0000-0001-9606-4241]], Yanchenko I. O.[1[0000-0002-7833-5690]]

[1] Sumy State University, 2, Rymskogo-Korsakova St., 40007, Sumy, Ukraine;

[2] Swedish University of Agricultural Sciences, 5, Almas Allé, Box 7015, 75007 Uppsala, Sweden

Article info:

Submitted: May 11, 2022

Accepted for publication: September 5, 2022

Available online: September 9, 2022

***Corresponding email:**

i.ableyeva@ecolog.sumdu.edu.ua

Abstract. The main idea was to solve the problem related to oil contamination of soil using bioremediation with bioaugmentation with modeled microorganism strains. The paper aimed to develop a bacterial consortium for petroleum hydrocarbon degradation during the biological treatment of oil-contaminated soils using electronic databases. The research methodology included an analysis of the mechanisms and metabolic pathways of petroleum hydrocarbon degradation and an assessment of the possible reaction modulus and enzymatic systems for the degradation of aromatic compounds. The taxonomic classification and review of oil compound transformation metabolic pathways were carried out using electronic KEGG, MetaCyc, and EzTaxon databases. The KEGG database was used to create a microbiological consortium of certain strains of bacteria that improved hydrocarbon degradation process performance. Identification of bacteria's complete genome using Island Viewer 4 allowed to create of a consortium of oil-destructive bacteria consisting of such strains: *Pseudoxanthomonas spadix BD-a59*, *Rhodococcus jostii RHA1*, *Rhodococcus aetherivorans IcdP1*, *Pseudomonas putida ND6*, *Pseudomonas stutzeri 19SMN4*, *Pseudomonas fluorescens UK4*, *Acinetobacter lactucae OTEC-02*, *Bacillus cereus F837/76.7.9*. The ratio between the mentioned strains of microorganisms in the consortium was set at 20 % : 20 % : 15 % : 10 % : 10 % : 5 % : 5 % : 15 %. This bacterial consortium for aromatic hydrocarbons was created according to the metabolic information of basic enzymatic systems and the predominant transformation of particular oil compounds using the BacDive database.

Keywords: soil pollution, bioremediation, oil biodegradation, synergism.

1 Introduction

The microbiological degradation of organic substances after the ingress of oil and oil products into the soil is very relevant from the point of view of ensuring the environmental safety of oil-producing territories. At the same time, the decomposition of linear hydrocarbons is much easier than aromatic hydrocarbons due to the complexity of the chemical structure of arenes, which requires more thorough study to develop approaches to intensify the process. In this regard, the main focus of this article is the study of polycyclic aromatic hydrocarbons (PAH) and their biodegradation processes. It is known that *Pseudomonas* [1], *Sphingomonas*, *Mycobacterium* [2], *Bacillus* [3, 4], and *Rhodococcus* [5] genera consist of bacteria with the capacity for PAH degradation. Jain and Bajpai [6] claimed that genetically modified microorganisms have exhibited enhanced destructive capabilities encompassing a large number of chemical pollutants, in particular petroleum hydrocarbons and even polycyclic aromatic hydrocarbons. Consequently, it could be potentially used for the biological treatment of oil-contaminated soils and other environments.

Scientists have studied the patterns and mechanisms of chemical reactions with the participation of microorganism's strain *Aspergillus glaucus* belonging to the genus *Aspergillus*. The final and intermediate oxidation products of naphthalene and anthracene have been determined in the study [7].

Heterotrophic aerobes bacteria get carbon and energy from petroleum hydrocarbons during oxidative processes resulting in the degradation of the aforementioned organic substances [8]. Developing a complex of special enzymes promotes the absorption of hydrophobic substrate and microorganisms' decomposition of organic matter. Bacteria-producing enzymes from the oxygenase group could destroy substances with hydrophobic properties. The enzyme group of dehydrogenases acts in the oxidative

processes of hydrophilic compounds [9]. According to a study by the authors [10], *Basillus* sp. strain X6 produced dehydrogenase with the capacity to biodegradation rate of 50 % and other enzymes had a lower value.

2 Literature Review

According to plenty of research, the enzymatic activity of the soil directly depends on the oil content. In this point, the paper [11] indicates that the concentration of oil up to 10 % positively affects catalase, dehydrogenase and urease activity; up to 17 % – on phosphatase and lipolytic activity. However, the amount of oil in the soil above these values inhibits the activity of all types of enzymes.

The maximum effective result can be achieved if it is used a consortium of bacteria capable of the destruction of organic substances of certain chemical composition and nature [12]. According to the obtained results by [13], bacterial consortium consisting of *Stenotrophomonas acidaminiphila*, *Bacillus megaterium*, *Bacillus cibi*, Pseudomonas aeruginosa and Bacillus cereus showed a good degradation ability for oil wastes as well as bio-surfactant production capacity, compared with isolates. The problem of creating favorable living conditions for consortium is partially solved by bioaugmentation, biostimulation and the use of biologics, primarily, mentioned above biosurfactants in the implementation of the In-situ method that means without removing the soil, which enhances the metabolism of microflora [14–17].

Strains of microorganisms capable of oxidizing oil produce biosurfactants that provide the dispersion process of oil and oil products and increase the selective membrane permeability, which has a positive effect on the entry of PAHs into the cell from the outside. Such substances must be a high-molecular-weight bioemulsifier such as extracellular biosurfactant of lipopolysaccharide nature produced by A*cinetobacter calcoaceticus, Acinetobacter radioresistens* KA53 [18].

Despite the presented research results on the pathways of decomposition of aromatic substances, poor structuring of information and gaps in methodological approaches to creating appropriate bacterial consortia exist. Most of the publicly available databases do not contain the results of experimental studies of protein sequences of microorganisms [19].

The present research has been focused on the electronic bioinformatic databases, aiming to develop bacterial consortium for petroleum hydrocarbons degradation during bioremediation of oil-contaminated soils.

To accomplish the aim, the tasks have been set as follows:

1) to analyze the mechanisms and metabolic pathways of aromatic petroleum hydrocarbons degradation based on electronic KEGG databases use;

2) theoretically substantiate and simulate the composition of the oil-degradable bacterial consortium capable for bioaugmentation in the case of soil bioremediation.

3 Materials and Methods

Electronic KEGG databases (the Kyoto encyclopedia of genes and genomes), MetaCyc and the EzTaxon database were used for taxonomic classification and study of metabolic pathways for the decomposition of petroleum compounds. Bacterial Diversity Metadatabase BacDive was used to study the application and interaction of oil degradable microorganisms, their physiology, morphology, isolation, culture and growth conditions, and sampling and environmental information.

Well-known and widespread among specialists, webserver IslandViewer 4 (http://www.pathogenomics.sfu.ca/islandviewer/) was used to predict and visualize genomic islands "(GIs, regions of probable horizontal origin) in bacterial genomes". GIs contain information about medically or ecologically necessary adaptation factors that increase the ability to compete with microorganisms in the ecological niche, including different factors [20].

"The exploration of the catalytic activities of microbial communities involved in the degradation of persistent PAHs in contaminated sites was carried out using MAGICPAH stands for Molecular Approaches and MetaGenomic Investigations for Cleanup of Polyaromatic Hydrocarbon" (http://aromadeg.siona.helmholtz-hzi.de/). MAGICPAH is a database on a core catabolic enzymes that allows an adequate scheme of reactions and enzymes responsible for the destruction of aromatic hydrocarbons. MetaCyc (https://MetaCyc.org) is a massive database including practically identified metabolism reactions of all living beings. MetaCyc contains the pathways related to metabolism and reactions, enzymes, metabolites, and genes [21].

The subject of research was the study of metabolic pathways for the decomposition of polycyclic aromatic products by certain microorganisms, with the release of important biosurfactants that affect the efficiency of a given process. KEGG database (https://www.kegg.jp/kegg/pathway.html#xenobiotics) was used as specific research to achieve this goal. KEGG is a computer visualization of the living systems, including genomic information (molecular structure sets of genes and proteins) and chemical information (different chemicals). Genomic information is combined with systems information (dates on schemes for combining networks of interactions, reactions and relationships at the molecular level) and increase biochemical reaction speed [22].

Thus, various ecological and trophic groups of microorganisms can be part of a bacterial consortium under the conditions of a specific ratio to achieve the set goal of the destruction of specific hydrocarbons [13].

4 Results and Discussion

4.1 Mechanisms and metabolic pathways of petroleum hydrocarbons degradation

For today various databases have simplified the process of constructing metabolic pathways for various organic substances. Particularly, the KEGG database simulates metabolic pathways for different substances, petroleum hydrocarbons, to determine the types of involved microorganisms and enzymatic systems. For instance, the result of such modeling for toluene conversation to benzoic acid is shown in Figure 1.

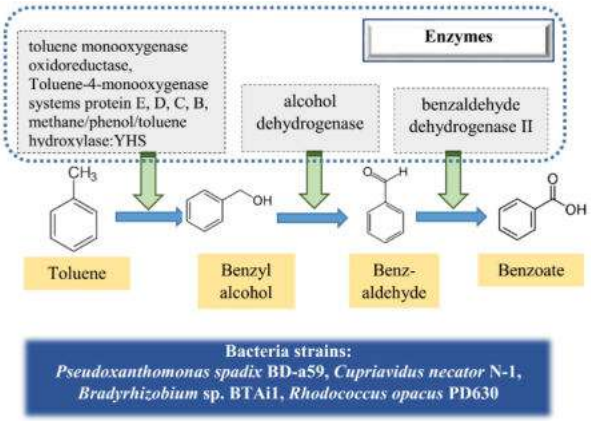

Figure 1 – Toluene degradation, toluene => benzoate: methyl to carboxyl conversion on the aromatic ring

It is known that microorganisms can include in their metabolic reactions not only nutrients but also various anthropogenic chemicals, including aromatic compounds, which contribute to their degradation in the environment [23]. The capacity of toluene degradation by *Rhodococcus opacus* sp. has been confirmed in the research [24]. The diagram of the degradation of PAHs demonstrates complex models of reaction pathways for biodestruction of aromatic substances, including three basic types of ring dihydroxylation modules, followed by meta- or ortho-cleavage modules and joint dihydroxylation and cleavage of aromatic ring, together with an optional pretreatment modulus to convert a methyl group to a carboxyl group on an aromatic ring (Figure 2, a).

Biochemical conversion shown in Figure 2 (a) is supported by 2-formylbenzoate dehydrogenase enzyme belonging to the class of Oxidoreductases that can influence the aldehyde or oxo group of donors, with acceptors NAD+ or NADP+. This enzyme is produced by the following strains of bacteria: *Mycobacterium sp. MCS, Mycobacterium sp. KMS*, *Mycobacterium sp. JLS, Mycolicibacterium vanbaalenii, Mycolicibacterium gilvum PYR-GCK, Mycolicibacterium gilvum Spyr1, Mycolicibacterium rhodesiae, Pseudarthrobacter phenanthrenivorans*.

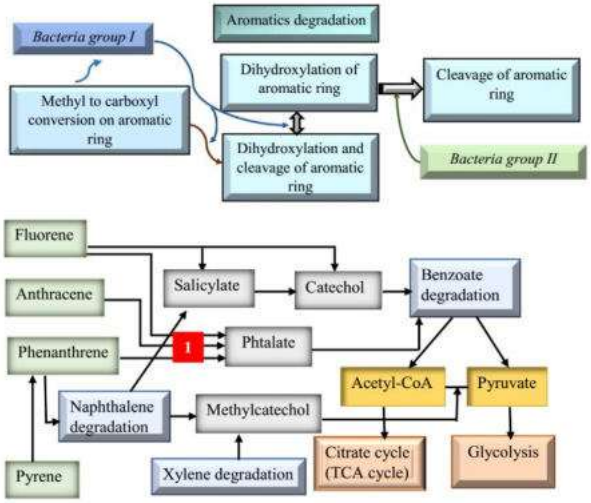

Figure 2 – Flowchart of aromatic compounds degradation with different pathways modules (a), simplified scheme of Polycyclic aromatic hydrocarbon degradation (b)

Such a group of petroleum hydrocarbons as PAHs is the most stable in relation to microbiological degradation. References pathways analysis of some chemicals, particularly fluorene, anthracene, phenanthrene, pyrene, toluene, and xylene, indicate Polycyclic aromatic hydrocarbon degradation transition into Benzoate degradation (Figure 2, b). Moreover, the first four PAH from the above-mentioned list has interconnected pathways. In this case, phthalate acts as a link, the metabolic pathway of transformation that also closes to Benzoate degradation.

A pathways analysis of the degradation of the aromatic compounds indicated that main degradation modules include Toluene and Benzoate degradation, Catechol ortho-cleavage and Catechol meta-cleavage, Xylene, Naphthalene, Phthalate degradation (Figure 2, b). The flowchart for the transformation of 2-Carboxybenzaldehyde during the bacterial biodestruction, indicated by the number 1 in the Polycyclic aromatic hydrocarbon degradation (see Figure 2, b), is shown in Figure 3.

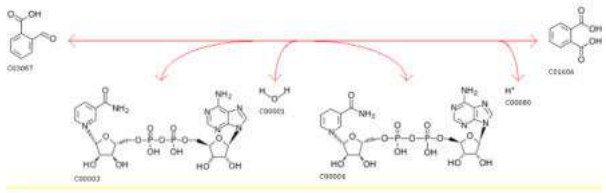

Figure 3 – 2-formylbenzoate (2-Carboxybenzaldehyde) (C03057) to o-phthalic acid (Phthalate) (C01606) conversion scheme: C00003 – NAD^+, C00001 – H_2O, C00004 – NADH, C00080 – H^+

Based on the study of metabolic schemes for the transformation of aromatic hydrocarbons, many different pathways for their destruction have been determined, as well as connections with other chains, in relation with which several enzyme systems can participate in the transformation of one substance.

The oxidation process of benzoate is provided by benzoate, benzoic enzymes, as well as dioxygenase, hydroxylase, and oxidoreductase enzymes classes acting on paired donors to reduce molecular oxygen. On the basis of the study of cultural and morphological signs, markers of resistance related to the genomic fingerprints method, scientists managed to find out the fate of microorganisms capable of oil degradation and prove their sustainability. Microorganisms-destructors of *Rhodococcus* and *Pseudomonas* strains are selective for individual oil products. It is necessary to form an influential association of microorganisms-destructors, a biological product for cleaning the soil from oil pollution [25, 26].

4.2 Modeling of oil-degradable bacteria consortium capable for bioaugmentation

The essential principle of bacteria consortium successful functioning is based on the synergetic effect in the relationship between different ecological trophic groups of microorganisms because one's metabolites have to be a carbon source for others [27, 28]. Analysis of degradation modules of main aromatic compounds shows intermediate and final products and the necessary enzymatic systems to accelerate these transformations (Figure 4).

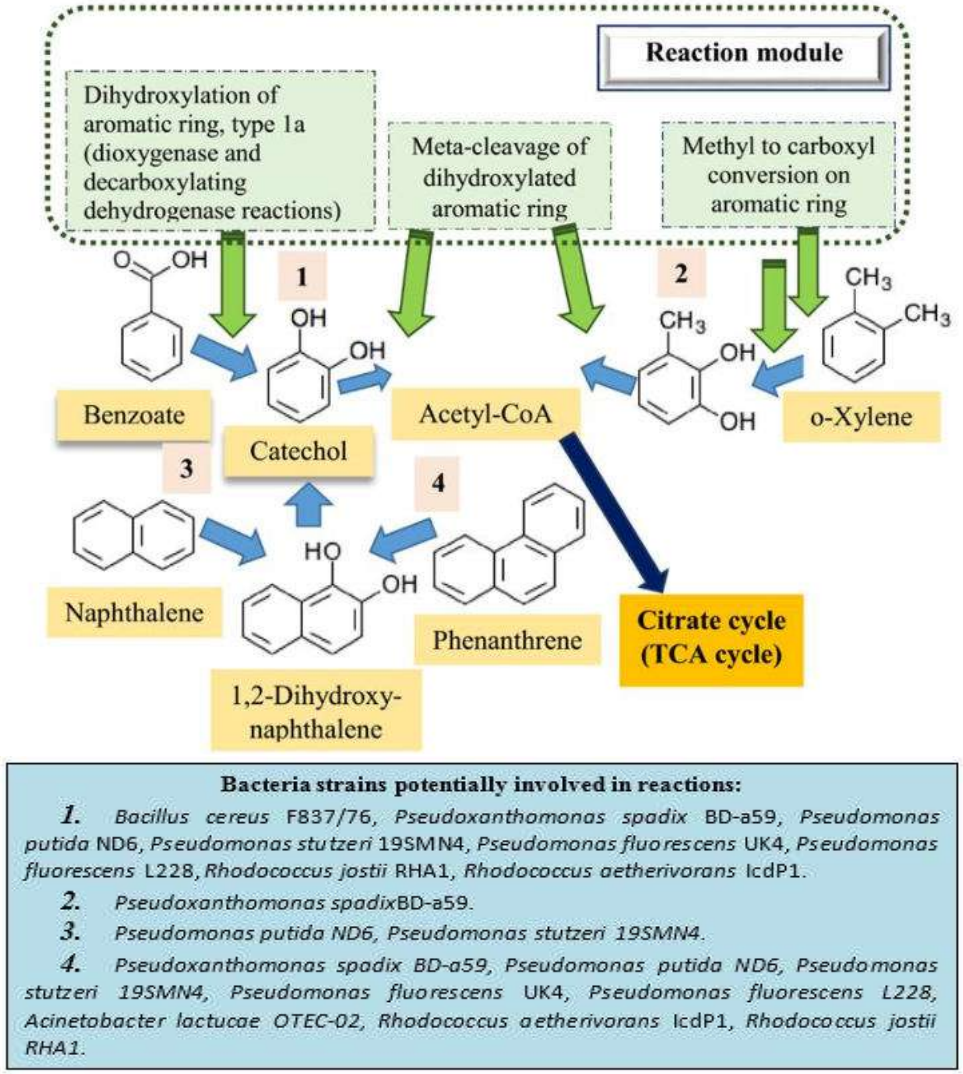

Figure 4 – Reaction modulus for degradation of aromatic compounds

Legend: Green boxes are different reaction types of aromatic compounds destruction; green arrows demonstrate conversions for appropriate reactions; blue arrows indicate a such conversion one aromatic compounds into others. Numbers signify certain pathways: 1 – benzoate=> catechol; 2 – o-xylene => 3-methylcatechol; 3 – naphthalene => 1,2-dihydroxynaphthalene; 4 – phenanthrene => 1,2-dihydroxynaphthalene.

The first conversion belongs to Benzoate degradation due to the reaction of dihydroxylation of the aromatic ring involving enzymes benzene 1,2-dioxygenase and dihydroxycyclohexadiene carboxylate dehydrogenase

from the class of Oxidoreductases. Enzyme catechol 1,2-dioxygenase (class Oxidoreductases) effected on sole donors with inclusion of oxygenases (molecular oxygen) starts the meta-cleavage pathway of catechol degradation. Naphthalene 1,2-dioxygenase is related to the ring-hydroxylating dioxygenase (RHD) that significantly impacts the destruction of aromatic substances, including PAHs. Aryl alcohol dehydrogenase includes enzymes with a broad specificity for alcohols with an aromatic or cyclohex-1-ene ring. At the same time, this enzyme has little or no activity against short-chain aliphatic alcohols (https://www.genome.jp/dbgetbin/www_bget?K00055+1.1.1.90+R05348).

Alcaligenes sp. strain PPH degrades phenanthrene via 1-hydroxy-2-naphthoic acid hydroxylase, salicylic acid, and catechol [29]. Pseudoxanthomonas spadix BD-a59 must be involved in the degradation of all six BTEX (benzene, toluene, ethylbenzene, and o-, m-, and p-xylene) compounds. It is isolated from gasoline-contaminated sediment. *Pseudoxanthomonas spadix* BD-a59 complete genome information was successfully obtained using simulating tool IslandViewer 4 (http://www.pathogenomics.sfu.ca/islandviewer/accession/NC_016147.2/) it has to be potentially involved in mostly PAH degradation reactions. In this relation, *Pseudoxanthomonas spadix* BD-a59 was determined as the dominant species in the consortium model.

The complete set of enzymatic systems involved in PAH biodegradation has to be provided by including bacteria strains into consortium: *Pseudoxanthomonas spadix BD-a59, Pseudomonas putida ND6, Pseudomonas stutzeri 19SMN4, Pseudomonas fluorescensc UK4, Pseudomonas fluorescens L228, Acinetobacter lactucae OTEC-02, Rhodococcus aetherivorans IcdP1, Rhodococcus jostii RHA1*.

Figure 5 shows a bacterial consortium that was created for the degradation of aromatic hydrocarbons, based on data on metabolism, diversity, the presence of certain enzymes, and the main transformation pathways.

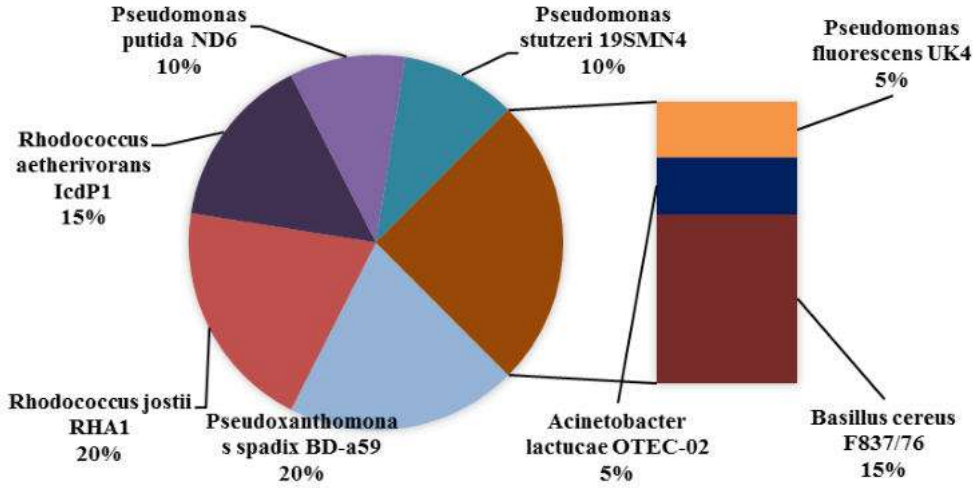

Figure 5 – The diagram of different bacteria related to the bio destruction of aromatic hydrocarbons

The created consortium includes bacteria strains in a different ratio based on the bacteria group is 100 %. The difference in the mass ratio between the strains used for this model is due to differences in the necessary enzymes. The creation of such a consortium became possible based on data on the enzymes required to decompose aromatic hydrocarbons, mainly oxidoreductase and oxygenase. Bioinformatic databases made it possible to select such bacterial strains that are characterized by synergy, that is, an increase in the overall effect regarding the use of carbon in oil products as an energy source for bacteria such as *Pseudoxanthomonas* and *Pseudomonas* strains. In this case, the intermediate decay products are a substrate for other bacteria (*Acinetobacter* and *Rhodococcus* strains) from the consortium.

For instance, *Pseudoxanthomonas spadix* BD-a59 and *Rhodococcus aetherivorans* IcdP1 are more capable of cyclic hydrocarbon destruction. *Rhodococcus aetherivorans* IcdP1 was retrieved from polluted soil of the abandoned Beijing Coking Plant in China" (doi:10.13145/bacdive11035.20190402.4). "The genome highlights important features for bioaugmentation, including the genes involved in the degradation of methyl-ethyl-ketone" [30].

Rhodococcus jostii RHA1 has been reported to be soil actinomycete, capable of decomposition of polychlorinated biphenyls in soil and includes a wide range of compounds in metabolism (doi:10.13145/bacdive11034.20190402.4).

Under PAH pollution, PAH-catabolic genes, particularly aromatic hydroxylating dioxygenase gene fragments in both α- and γ-Proteobacteria were close to nahAc and phnAc genes, whereas the predominantly actinobacteria were isolated in the study area.

It was reported [31] that *Acinetobacter, Achromobacter*, *Bacillus, Flavobacterium, Klebsiella, Micrococcus, Pseudomonas,* and *Staphylococcus* consortium application contributed a 62.08 % decrease in the concentration of total petroleum hydrocarbons. Moreover, such result was recorded at 42 day of the experiment.

Okafor et al. [32] have determined that bacterial strains such as *Pseudomonas, Bacillus, Klebsiella,* and *Enterobacter* could produce biosurfactants for PAH degradation (benzene and naphthalene) while a consortium of *Pseudomonas, Bacillus, Lysinibacillus,* and *Enterobacter* had the highest rate of oil degradation.

Jahir et al. [33] postulated that Bacillus spp. has resistant endospores to be more tolerant to high levels of hydrocarbons in soil that has been proved according to the research [34]. High biodegradation capacity at the level above 93 % of crude oil was recorded for the bacterial consortium of Bacillus cereus and Pseudomonas putida bacteria [35].

Jussila et al. [36] reported *Pseudomonas aeruginosa* JI104 must be an effective utilizing and catechol-positive bacteria having the xylEgene participated in the destruction of aromatic hydrocarbons (xylE, BTEX destruction).

Pseudomonas strains, as well as the xylEgene was determined in other *Proteobacteria* isolates, such as *Acinetobacter, Achromobacter, Enterobacter,* and *Stenotrophomonas*. The GC-MS analysis showed that a consortium of such bacteria *Acinetobacter, Pseudomonas, Enterobacter, Cronobacter, Stenotrophomonas, Achromobacter, Ochrobactrum, Paenibacillus, Bacillus, Microbacterium, Curtobacterium,* and *Sphingobacterium* was able to reduce the crude oil content of the liquid culture by 40.5 % after 10 days [37].

Another author also reported a consortium of bacteria strains such as *Bacillus cereus BL01, Pseudomonas sruzeri BL02, Acinetobacter sp. BL03, Bacillus sp. BL04* provided removal efficiency at the level of 46 %, while the consortium mentioned above application supplemented by *Azotobacter vinelandii AV01* producing surfactant increase this indicator up to 85 % [38]. Consortium of *Bacillus aerius B2, Psuedomonas stutzeri B3, Ochrobactrum intermedium B4, Micrococcus lylae B5, and Acinetobacter calcoaceticus B9* could increase the rate of oil degradation by 88 % [39].

Strains belonging to the *Bacillus* species show mixed resistance to antibiotics and heavy metals. The study [26] results proclaimed that isolates *Aneurini bacillus migulanusstra* in KTPP was the most effective in degrading the wide range of petroleum hydrocarbons. Bacillus cereus strain BSP showed multiple resistance against heavy metals and presented a high ability to degrade the selected hydrocarbons.

Thus, the bacteria included in the proposed consortium have a high ability to degrade hydrocarbons, which the studies of other scientists have reliably confirmed.

5 Conclusions

A scheme for the degradation of aromatic compounds has been developed, shown with combination schemes of reaction modules for the biodestruction of aromatic compounds. The investigated reactions consist of three basic ring dihydroxylation modulus, followed by meta- or ortho-cleavage modulus and co-dihydroxylation and aromatic ring cleavage, together with a pretreatment modulus to convert a methyl group to a carboxyl group on the aromatic ring.

A pathways analysis of the degradation of the aromatic compounds indicated that main degradation modulus includes Toluene and Benzoate destruction, Catechol ortho-cleavage and Catechol meta-cleavage, Xylene, Naphthalene, Phthalate destruction. Modelling of oil-degradable bacteria consortium capable for bio augmentation was carried out based on reaction modulus for degradation of aromatic compounds, exploration of different enzymatic systems that catalyse certain reactions, and definition of bacteria capable of producing appropriate enzymes. Identification of bacteria complete genome using IslandViewer 4 allowed to create of a consortium of oil-destructive bacteria consisting of such strains: *Pseudoxanthomonas spadix BD-a59, Rhodococcus jostii RHA1, Rhodococcus aetherivorans IcdP1, Pseudomonas putida ND6, Pseudomonas stutzeri 19SMN4, Pseudomonas fluorescens UK4, Acinetobacter lactucae OTEC-02, Basillus cereus F837/76*. The ratio between the mentioned strains of microorganisms in the consortium was set at 20 % : 20 % : 15 % : 10 % : 10 % : 5 % : 5 % : 15 %.

The scientific novelty of this study is the determination of the necessary bacteria in the consortium, which are capable of decomposing polycyclic aromatic hydrocarbons in the course of their vital activity. This approach makes it possible to effectively use the bioaugmentation method on oil-contaminated soils due to accidental oil spills, which often occur and require immediate application of measures to eliminate and clean up the soil.

For the future study, investigation of the native overall microbial community, regarding the impact of oil contamination and bioremediation related to the decontamination efficiency is needed.

Acknowledgments

Research Project also was carried out as planned research projects of the Department of Ecology and Environmental Protection Technologies, Sumy State University, connected with subjects “Reduction of technogenic loading on the environment of enterprises of chemical, machine-building industry and heat and power engineering” and “Reduction of the technogenic load on the environment from oil production facilities: prospects for the application of biotechnology” according to the scientific and technical program of the Ministry of Education and Science of Ukraine (state registration No 0116U006606 and 0121U114460).

References

1. Zhang, X., Xu, D.J., Zhu, C.Y., *et al*. (2012). Isolation and identification of biosurfactant producing and crude oil degrading Pseudomonas aeruginosa strains. *Chem. Eng. J.*, Vol. 209, pp. 138-146, doi: 10.1016 j.cej.2012.07.110.
2. Azadi, D., Shojaei, H., Mobasherizadeh, S.et al. (2017). Screening, isolation and molecular identification of biodegrading mycobacteria from Iranian ecosystems and analysis of their biodegradation activity. *AMB Express*, Vol. 7(180), doi: 10.1186/s13568-017-0472-4.
3. Dai, X., Lv, J., Yan, G., Chen, C., Guo, S., Fu, P. (2020). Bioremediation of intertidal zones polluted by heavy oil spilling using immobilized laccase-bacteria consortium. *Bioresource Technology*, Vol. 309, doi: 10.1016/j.biortech.2020.123305.
4. Das, K., Mukherjee, A. K. (2007). Crude petroleum-oil biodegradation efficiency of Bacillus subtilis and Pseudomonas aeruginosa strains isolated from a petroleum-oil contaminated soil from North-East India. *Bioresource Technology*, Vol. 98(7), pp. 1339-134, doi: 10.1016/j.biortech.2006.05.032.
5. Liu, Y., Li, C., Huang, L., He, Y., Zhao, T., Han, B., Jia, X. (2017). Chinese Journal of Chemical Engineering Combination of a crude oil-degrading bacterial consortium under the guidance of strain tolerance and a pilot-scale degradation test. *Chinese Journal of Chemical Engineering*, Vol. 25(12), pp. 1838-1846, doi: 10.1016/J.CJCHE.2017.02.001.
6. Jain, P., Bajpai, V. (2012). Biotechnology of bioremediation - a review. *International journal of environmental sciences*, Vol. 3(1), pp. 535-549, doi: 10.6088/ijes.2012030131053.
7. Stoyanova, K., Gerginova, M., Dincheva, I., Peneva, N., Alexieva, Z. (2022). Biodegradation of Naphthalene and Anthracene by *Aspergillus glaucus* Strain Isolated from Antarctic Soil. *Processes*, Vol. 10, pp. 873, doi: 10.3390/pr10050873.
8. Sierra-Garcia, I. N., Oliveira, V. M. (2013). Microbial Hydrocarbon Degradation: Efforts to Understand Biodegradation in Petroleum Reservoirs. in Chamy R, Biodegradation Engineering Technology, Intech Open London, pp. 47-72, doi: 10.5772/55920.
9. Ramadass, K., Megharaj, M., Venkateswarlu, K., Naidu, R. (2018). Bioavailability of weathered hydrocarbons in engine oil-contaminated soil: Impact of bioaugmentation mediated by *Pseudomonas spp.* on bioremediation. *Science of The Total Environment*, Vol. 636, pp. 968-974, doi: 10.1016/j.scitotenv.2018.04.379.
10. Yan, S., Wang, Q., Qu, L. et al. (2013). Characterization of Oil-Degrading Bacteria from Oil-Contaminated Soil and Activity of their Enzymes. *Biotechnology & Biotechnological Equipment*, Vol. 27(4), pp. 3932-3938, doi: 10.5504/BBEQ.2013.0050.
11. Das, P., Yang, X.-P., Ma, L. (2014). Analysis of biosurfactants from industrially viable *Pseudomonas* strain isolated from crude oil suggests how rhamnolipids congeners affect emulsification property and antimicrobial activity. *Frontiers in microbiology*, Vol. 5(696), article ID 696, doi: 10.3389/fmicb.2014.00696.
12. Patowary, K., Patowary, R., Kalita, M. C., Deka, S. (2016). Development of an Efficient Bacterial Consortium for the Potential Remediation of Hydrocarbons from Contaminated Sites. *Frontiers in Microbiology*, Vol. 7(1092), doi: 10.3389/fmicb.2016.01092.
13. Cerqueira, V. S., Hollenbach, E. B., Maboni, F., Vainstein, M. H., Camargo, F. A. O., Peralba, M. do C. R., Bento, F. M. (2011). Biodegradation potential of oily sludge by pure and mixed bacterial cultures. *Bioresource Technology*, Vol. 102(23), pp. 11003-11010, doi: 10.1016/j.biortech.2011.09.074.
14. Adhikari, D., Araki, K. S., Mukai, M., Kai, T., Kubota, K., Kawagoe, T., Kubo, M. (2015). Development of an Efficient Bioremediation System for Petroleum Hydrocarbon Contaminated Soils Based on Hydrocarbon Degrading Bacteria and Organic Material Control. *Austin Journal of Biotechnology & Bioengineering*, Vol. 2(3), pp. 1048–1054.
15. Lladó, S., Solanas, A. M, de Lapuente, J., Borràs, M., Viñas, M. (2012). A diversified approach to evaluate biostimulation and bioaugmentation strategies for heavy-oil-contaminated soil. *Science of the Total Environment*, Vol. 435-436, pp. 262-269, doi: 10.1016/j.scitotenv.2012.07.032.
16. Mrozik, A., Piotrowska-Seget, Z. (2009). Bioaugmentation as a strategy for cleaning up of soils contaminated with aromatic compounds. *Microbiological Research*, Vol. 165, pp. 363-375, doi: 10.1016/j.micres.2009.08.001.
17. Varjani, S. J., Upasani, V. N. (2017). Crude oil degradation by *Pseudomonas aeruginosa* NCIM 5514 : Influence of process parameters. *Indian Journal of Experimental Biology*, Vol. 55, pp. 493-497.
18. Uzoigwe, C., Burgess, J. G., Ennis, C. J. et al (2015). Bioemulsifiers are not biosurfactants and require different screening approaches. *Front Microbiology*, Vol. 6(245), doi: 10.3389/fmicb.2015.00245.
19. Duarte, M., Jauregui, R., Vilchez-Vargas, R., Junca, H., Pieper, D. H. (2014). Aroma Deg, a novel database for phylogenomics of aerobic bacterial degradation of aromatics. *Database: the journal of biological databases and curation*, 2014 (bau118), doi: 10.1093/database/bau118.
20. Bertelli, C., Laird, M. R., Williams, K.P. et al (2017). Island Viewer 4: expanded prediction of genomic islands for larger-scale datasets. *Nucleic Acids Research*, Vol. 45(W1), pp. W30-W35, doi: 10.1093/nar/gkx343.
21. Caspi, R., Billington, R., Fulcher, C. A., Keseler, I. M., Kothari, A., Krummenacker, M., et al. (2018). The MetaCyc database of metabolic pathways and enzymes. *Nucleic Acids Research*, Vol. 46(1), pp. D633-D639, doi:10.1093/nar/gkv1164.
22. Kanehisa, M., Furumichi, M., Tanabe, M., Sato, Y., Morishima, K. (2017). KEGG: new perspectives on genomes, pathways, diseases and drugs. *Nucleic Acids Research*, Vol. 45(D1), pp. D353-D361, doi:10.1093/nar/gkw1092.
23. Lhotský, O, Krákorová, E., Linhartová, L., Křesinová, Z., Steinová, J., Dvořák, L., Rodsand, T., Filipová, A. Kroupová, K., Wimmerová, L., Kukačka, J., Cajthaml, T. (2017). Assessment of biodegradation potential at a site contaminated by a mixture of BTEX, chlorinated pollutants and pharmaceuticals using passive sampling methods - Case study. *Science of The Total Environment*, Vol. 607-608, pp. 1451-1465, doi: 10.1016/j.scitotenv.2017.06.193.

24. Pathak, A., Chauhan, A., Blom, J. et al. (2016). Comparative Genomics and Metabolic Analysis Reveals Peculiar Characteristics of *Rhodococcus opacus* Strain M213 Particularly for Naphthalene Degradation. *PLOS ONE*, Vol. 11(8), pp. e0161032, doi: 10.1371/journal.pone.0161032.
25. Auffret, M. D., Yergeau, E., Labbe, D. et al (2015). Importance of *Rhodococcus* strains in a bacterial consortium degrading a mixture of hydrocarbons, gasoline, and diesel oil additives revealed by metatranscriptomic analysis. *Applied Microbiology Biotechnology*, Vol. 99, pp. 2419-2430, doi: 10.1007/s00253-014-6159-8.
26. Godheja, J., Shekhar, S.K., Satyanarayan, G. N. V. et al. (2017). Antibiotic and Heavy Metal Tolerance of Some Indigenous Bacteria Isolated From Petroleum Contaminated Soil. *International Journal of Current Microbiology and Applied Sciences*, Vol. 6(3), pp. 194-211, doi:10.20546 / ijcmas.2017.603.021.
27. Shankar, S., Kansrajh, C., Dinesh, M. G., Satyan, R. S., Kiruthika, S., Tharanipriya, A. (2014). Application of indigenous microbial consortia in bioremediation of oil-contaminated soils. *International Journal of Environmental Science and Technology*, Vol. 11, pp. 367-376, doi:10.1007/s13762-013-0366-1.
28. You, Z., Xu, H., Zhang, S., Kim, H., Chiang, P. (2018). Comparison of Petroleum Hydrocarbons Degradation by *Klebsiell apneumoniae* and *Pseudomonas aeruginosa*. *Applied Science*, Vol. 8(12), pp. 2551, doi: 10.3390/app8122551.
29. Deveryshetty, J., Phale, P. S. (2010). Biodegradation of phenanthrene by Alcaligenes sp. strain PPH: partial purification and characterization of 1-hydroxy-2-naphthoic acid hydroxylase. *FEMS Microbiology Letters*, Vol. 311(1), pp. 93-101, doi: 10.1111/j.1574-6968.2010.02079.x.
30. Dueholm, M. S., Albertsen, M., D'Imperio, S. et al. (2014). Complete genome of Rhodococcus pyridinivorans SB3094, a methyl-ethylketone-degrading bacterium used for bioaugmentation. *Genome Announcements*, Vol. 2(3), pp. e00525-14, doi: 10.1128/genomeA.00525-14.
31. Nwogu, T. P., Azubuike, C. C., Ogugbue, C. J. (2015). Enhanced Bioremediation of Soil Artificially Contaminated with Petroleum Hydrocarbons after Amendment with Capra aegagrushircus (Goat) Manure. *Biotechnology Research International*, Article ID 657349, 7 pages, doi: 10.1155/2015/657349.
32. Okafor, C. P., Udemang, N. L., Chikere, C. B., Akaranta, O., Ntushelo, K. (2021). Indigenous microbial strains as bioresource for remediation of chronically polluted Niger delta soils. *Scientific African*, Vol. 11, pp. e00682, doi: 10.1016/j.sciaf.2020.e00682.
33. Jahir, A. K., Syed, H. A. R. (2011). Isolation and characterization of micro-organism from oil contaminated sites. *Advances in Applied Science Research*, Vol. 2(3), pp. 455-460.
34. Kidibule, P. E., Sosovelem, E. M., Mshandetem, A. M. (2014). Isolation and Identification of Microorganisms from Crude Oil Contaminated Soils of Dar es Salaam, Tanzania. *British Biotechnology Journal*, Vol. 4(8), pp. 918-931, doi: 10.9734/BBJ/2014/11780.
35. Tuhuloula, A., Suprapto, S., Altway, A., Juliastuti, S. R. (2019). Biodegradation of Extractable Petroleum Hydrocarbons by Consortia *Bacillus cereus* and *Pseudomonas putida* in Petroleum Contaminated-Soil. *Indonesian Journal of Chemistry*, Vol. 19(2), pp. 347-355, doi: 10.22146/ijc.33765.
36. Jussila, M. M., Zhao, J., Suominen, L. et al. (2007). TOL plasmid transfer during bacterial conjugation in vitro and rhizoremediation of oil compounds in vivo. *Environmental Pollution*, Vol. 146(2), pp. 510-524.
37. Rajaei, S., Seyedi, S. M., Raiesi, F. et al. (2013). Characterization and Potentials of Indigenous Oil-Degrading Bacteria Inhabiting the Rhizosphere of Wild Oat (Avena Fatua L.) in South West of Iran. *Iran Journal of Biotechnology*, Vol. 11(1), pp. 32-40, doi: 10.5812/ijb.9334.
38. Helmy, Q., Laksmono, R., Kardena, E. (2015). Bioremediation of Aged Petroleum Oil Contaminated Soil: From Laboratory Scale to Full Scale Application. *Procedia Chemistry*, Vol. 14, pp. 326-333, doi: 10.1016/j.proche.2015.03.045.
39. Iyobosa, E., Fang, Z. S., Jun, N. H., Jiehao, S., Gang, M. X. (2021). Development of a robust bacterial consortium for petroleum hydrocarbon degradation. *Fresenius Environmental Bulletin*, Vol. 30(3), pp. 2356-2367.

JOURNAL OF ENGINEERING SCIENCES

Volume 9, Issue 2 (2022)

Copyright Agreement

We, the Authors of the Article publishing in the Journal of Engineering Sciences, in the case of acceptance for publication, transfer to Founders and Editorial Board the underlined rights:

– publishing this article in English and distribution of the printed version;

– English translation of the article and distribution of the hard copy of the translation;

– distribution of the electronic version of the article through any electronic means (by hosted on the official website of the Journal, in electronic databases, repositories, etc.).

We reserve the rights without the consent of the Editorial Board or Founders:

– to use the article materials partially or in whole for educational purposes;

– to use the article materials partially or in whole to write own dissertations;

– to use the article materials for thesis preparing, conference materials, as well as for presentations;

– to post electronic copies (including the final electronic version downloaded from the official website of the Journal):

– on the personal web-sources of all the co-authors (websites, webpages, blogs, etc.);

– on the web-sources of authors working organizations (including electronic institutional repository);

– on the International scientometric databases;

– on non-commercial open-access sources.

In all cases, the presence of citations to the article or hyper-link to the electronic copy of the journal's official website is obligatory.

By this agreement, we also certify that the submitted article:

– does not violate the copyrights of other persons or organizations;

– has not been published previously in other publishing houses and submitted for publication in other Journals.

JOURNAL OF ENGINEERING SCIENCES

Volume 9, Issue 2 (2022)

Dear Authors of the Journal of Engineering Sciences!

The Editorial Board of the Journal of Engineering Sciences pays special attention to the structure of the articles according to the **List of Scientific Professional Editions of Ukraine** (Category "B", Minutes No. 1208 of 07.11.2018, Appendix No. 8). Only original articles by the authorship of up to 5 authors are accepted for publication according to the **Template** with the following elements:

– general statement of the problem and its relationship with the essential scientific or practical problems;
– analysis of the recent investigations and publications in the same research field;
– statement of the significance of the general problem that was not solved before;
– statement of the purpose of the research article;
– description of the initial data of the research with the justification of the achieved scientific results;
– conclusions and ways for further development of the research.

All the articles are reviewed by the independent double-blind procedure.

All the authors should send via e-mail **jes@teset.sumdu.edu.ua** the electronic version of the following materials:
– article **in English** according to the **Template**;
– information about authors and their affiliation with the related address.

ATTENTION!
If one of the mentioned components is not sent or there are many stylistic, orthographic, and grammatical errors, the article will not be considered by the Editorial Board and will not be reviewed.

The minimum size of the materials:
1. Scientific – theoretical articles (up to 25,000 symbols; about 14 pages) that deal with the theoretical research and descriptions of physical laws concerning the investigated phenomena; theoretical generalizations and fundamental principles proved by the experimental research data.
2. Scientific-practical articles (up to 10,000 symbols; about 6 pages) that deal with scientific experiments and recent experience. They include the proposed methods for the experimental research or means to observe the studied phenomena. An essential part of these articles is the description of the achieved results and their explanation acquired in immediate interaction with the object of investigations, its significance, and practical implementations.
3. Scientific-methodological articles (up to 15,000 symbols; about 8 pages) that deal with the review of processes, methods, instruments for solving scientific and applied problems; the statement of the new methodology, results of which allow creating more precise methodology based on an up-to-date methodology for the implementation of discovered laws.

Ministry of Education and Science of Ukraine
Sumy State University

JOURNAL OF ENGINEERING SCIENCES

Scientific Journal

Volume 9, Issue 2 (2022)

Відповідальний за випуск
І. В. Павленко

Комп'ютерне складання та верстання:
Х. В. Берладір

Обкладинка:
В. О. Іванов

Коректор:
С. М. Симоненко

Responsible for release:
Ivan Pavlenko

Computer design and typesetting:
Kristina Berladir

Cover page:
Vitalii Ivanov

Corrector:
Svitlana Symonenko

Підписано до друку 30.06.2021. Формат 60x84/8.
Папір офс. Друк офс.
Ум. друк. арк. 17,45. Обл.-вид. арк. 23,72.
Наклад 100 прим. Замовлення №
Сумський державний університет, вул. Римського-Корсакова, 2, 40007, м. Суми, Україна
Свідоцтво про внесення суб'єкта видавничої справи до Державного реєстру
ДК № 3062 від 17.12.2007.

Надруковано у друкарні Сумського державного університету,
вул. Римського-Корсакова, 2, 40007, м. Суми, Україна

Editorial Board: 2, Rymskogo-Korsakova St., 40007, Sumy, Ukraine; Apt. M-211
Contact Phones: +380-993-845-740
E-mail: jes@teset.sumdu.edu.ua
Website: https://jes.sumdu.edu.ua

State registration certificate of the print mass-media No. 20499-10299 PR.